Neutron scattering study of charge-ordering in $R_{1/3}Sr_{2/3}FeO_3$ (R = La, Pr, Nd, Sm, and Y)

by

Jie Ma

A dissertation submitted to the graduate faculty
in partial fulfillment of the requirements for the degree of
DOCTOR OF PHILOSOPHY

Major: Condensed Matter Physics

Program of Study Committee:
Robert J. McQueeney, Major Professor
Alan I. Goldman
Gordon J. Miller
Marzia Rosati
Alejandro Travesset-Casas
Edward Yu

Iowa State University

Ames, Iowa

2010

DEDICATION

To my parents, Chengguo Ma, and Zhihong Ma.

TABLE OF CONTENTS

LIST OF TABLES

LIST OF FIGURES

ACKNOWLEDGEMENTS

I would like to take this opportunity to express my thanks to those who helped me with various aspects of conducting research and the writing of this thesis.

I'd like to give words of gratitude to all those who helped to make this thesis possible. First of all, It is difficult to overstate my gratitude to my Ph.D. supervisor, Dr. Robert J. McQueeney. His enthusiasm and profound knowledge of the rare earth oxides and neutron scattering have inspired me. His patience during the discussion of my experiments and data have encouraged me. His scientific and linguistic insights through hundreds and thousands corrections of the drafts of my papers, thesis proposal, and thesis have edified me. To have been a student of him is one of my best experiences in my life.

I would like to thank the professors in my program of study committee, Drs. Alan I. Goldman, Gordon J. Miller, Marzia Rosati, Alejandro Travesset-Casas, and Edward Yu, for their time and energy put into my thesis.

I wish to thank all the members and collaborators of the McQueeney group. I am particularly indebted to previous postdoctoral research fellow and current associate Dr. Jiaqiang Yan, whose steps I have followed into: you tremendously impressed me and inspired me. I extend special thanks to my long-time officemates, Drs. Haifeng Li, Souleyman Omar-Diallo, and Mr. Daniel K. Pratt. They have been sharing not only their knowledge in academic area with me, but also much of their lives. Their presence has made my life in Ames bright and colorful.

I wish to acknowledge the help and support of our collaborators at Ames Laboratory: Drs. David C, Johnston and William R. McCallum, all the sample characterization and part of the sample synthesis were used the facilities of their lab; at Los Alamos and Oak Ridge National Laboratories: Anna Llobet-Megias, Frans Trouw, Matthew B. Stone, and Douglas Abernathy. They made our elastics neutron diffraction and inelastic neutron scattering experiments possible through their advice and unrelenting support and were always willing to share their deep knowledge and understanding of neutron scattering.

Finally, I would like to dedicate this thesis to my grandfather Jiude Ma. I also have much graitude for the emotional support from my wife Yang and my son Leon without whose support I would not have been able to complete this work. I would also like to thank my family, Yang's family, and my friends for their loving guidance and financial assistance during the writing of this work.

This work was performed at Ames Laboratory under Contract No. DE-AC02-07CH11358 with the U.S. Department of Energy.

CHAPTER 1. Introduction

1.1 Introduction

The complicated physical phenomena in complex transition-metal oxides (TMO), such as high T_c superconductivity, colossal magnetoresistivity, metal-insulator transitions, etc., have long been the focus of intense inquiry and debate in condensed matter science, since they are related to strong electronic correlations and cannot be explained within the ‘standard model’ of solid state physics. These novel functionalities of the correlated electron systems have a wide range of potential for applications in industry, such as information storage, energy transportation, and so on. The charge-ordering (CO) transition is very common in TMO and there is a specific CO transition temperature, T_{CO}. Above T_{CO}, the charge is not ordered, which means that the electrons in a compound are itinerant and the positions of the electrons are not fixed. Below T_{CO}, the charge is ordered, which means that the electrons are localized and the positions of the electrons are settled. Hence, the electrical conductivity of a material is changed at T_{CO} and this transition is classified as metal-insulator transition. Usually the CO with commensurate hole doping in TMO is thought to play an important role in various cases, including the superconducting cuprates, where the spin/charge stripe formation competes with superconducting states [1], colossal-magnetoresistive manganites, where CO competes with ferromagnetic metallic state stabilized by an external magnetic field [2], layered nickelates, where CO takes the form of the small polaron lattices [3], and layered manganites, where CO could be bothered by the correlated dynamics of spins and charges [4]. Therefore understanding the causes and implications of CO phenomena is significantly important.

The first research on the metal-insulator transition with the CO ground state was made by Verwey in 1939 [5]. Following his attempts, many efforts have been extended to elucidate the CO mechanism and its consequences. However, in spite of this effort, a theory that sufficiently explains all of the experimental observations has eluded us due to the complex interaction among structural, magnetic, and electronic states. Up to now, it has been widely recognized that CO arises from the coupling or the competition among Coulomb interaction, magnetic energy, and electron-lattice interaction. However, the interrelation of these interactions or the dominance of one over the others is not understood.

As one of the most advanced techniques in condensed matter physics, neutron scattering can not only reveal the crystalline and magnetic structures, but also probe the microscopic dynamics: how nuclei and magnetic moments move and interact. Therefore, it is a perfect tool for studying the CO system, for which the coupling of magnetism and structural distortions are the key [6, 7].

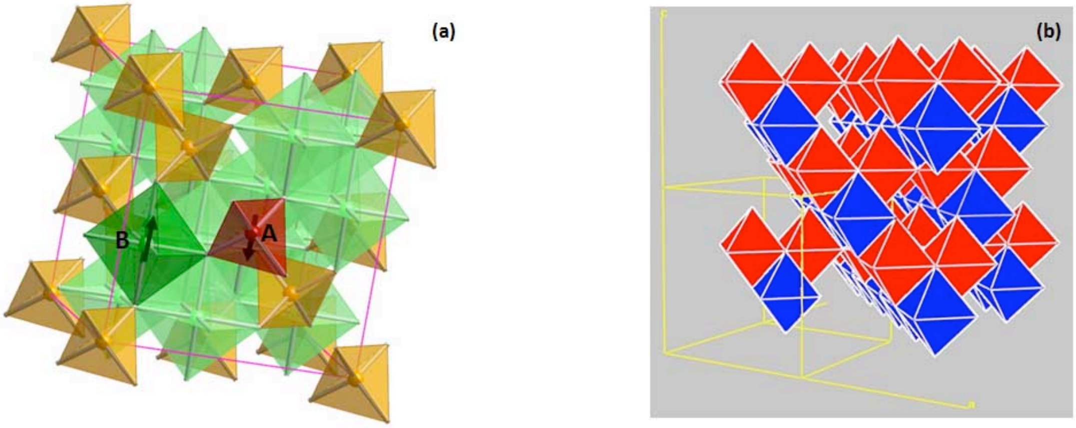

Figure 1.1 (a) The crystal structure and ferrimagnetic ordering of Fe_3O_4 above the transition temperature, the *A*-site (red) is tetrahedral sublattice and completely occupied by Fe^{3+} ions, and *B*-site (green) is the octahedral sublattice and has an average valence of $Fe^{2.5+}$. The directions of the spins are labeled with the arrows; (b) The crystal structure and charge ordering of Fe_3O_4 below the transition temperature in Verwey's model, the octahedrons (blue and red) are Fe^{2+}/Fe^{3+} ions, which stack along the *c*-axis.

The compound that Verwey studied was Fe_3O_4. It is a mixed valence compound with a cubic spinel structure: the tetrahedral (*A*) sublattice is completely occupied by ferric ions (Fe^{3+}), while the octahedral (*B*) sublattice has an average valence of $Fe^{2.5+}$, Fig. 1.1(a). The resistivity increases weakly as temperature decreases, and the material becomes much more insulating below ~ 122 *K*, which means that the metal-insulator transition occurs [5]. Verwey suggested that conduction at high temperatures was due to mixed valence of the *B*-site irons, while below the transition temperature the *B*-site irons formed distinct Fe^{2+} and Fe^{3+} ions that order in real space along the cubic axis with a corresponding sharp drop in conductivity, Fig. 1.1(b). This kind of transition is called Verwey transition and is one of the earliest instances of invoking many-body effects to explain a solid-state phase transition. The specific temperature at which CO occurs is called the Verwey temperature, T_V. Verwey built the following model to explain the mechanism: In a unit cell, there are eight Fe^{3+} and Fe^{2+} ions respectively distributed over the 16 *B*-sites, and electron exchange between equivalent *B*-sites occurs on the tetrahedral corner-shared network according to the relation, Fe^{2+} - e^- $\rightleftharpoons$ Fe^{3+}, giving rise to the electrical conductivity [8].

In Fe_3O_4, the Verwey transition would not appear to be driven by the magnetic energy due to the large difference between the temperatures of the ferrimagnetic ($\sim$ 860 *K*) and first-order Verwey transitions ($\sim$ 120 *K*): The magnetic structure is insensitive to the long-range CO [9]. Furthermore, it is also argued that the electron-lattice interaction is not an important factor because of the small crystalline distortions [10]. Thus, the large Coulomb repulsion should be the main driving force and Verwey transition can be thought of as a long-range CO of Fe^{3+} and Fe^{2+} produced in a process reminiscent of the Wigner crystallization that occurs at low electron densities in the free electron gas [11, 12]. Although Verwey's original hypothesis explains many of the features in the CO system, intense research challenged this speculation over years: In 1956, Anderson presented that the short-range ordering of Fe^{2+} and Fe^{3+} existed above T_V due to significant intersite Coulomb repulsion and frustration on the *B*-site sublattice [13]; Due to the local charge "neutrality" (2.5+ average valence on each tetrahedron) from the short-ranged electron correlations, the charge hopping and conductivity were restricted [14]. The importances of electron-lattice interactions were also reconsidered since the monoclinic lattice distortions can be induced by the elastic and orbital interactions [15], and its complexity has made the characterization of the Verwey state difficult [16]. The neutron techniques have helped us to refine our understanding of Fe_3O_4: In 1975, G. Shirane *et. al.* disproved Verwey's CO model by the high resolution neutron diffraction: a superlattice peak was observed at (2, 0, *l*+1/2) refer to the cubic lattice (O_h^7-$Fd\bar{3}m$), but not at (0, 0, 2) as expected for Verwey ordering scheme, which suggested more complex 3D pattern of CO in contrast to the Fe^{2+}/Fe^{3+} alternating along the *c*-axis as Verwey proposed [17]. Recently, even the validity of the CO model has been questioned [18]. Although the neutron and resonant X-ray diffraction measurements dispute this result, the concept of an integral CO state with full charge disproportionation in Fe_3O_4 is challenged [19, 20]. Theoretical calculations in the local spin density approximation (*LSDA*) and generalized gradient approximation (*GAA*) with local coulomb interaction (*U*) support the existence of fractional charge disproportionation [21, 22]. Thus, it is suggested that the simple ionic mechanism proposed by Anderson cannot explain the Verwey transition and the verdict that the Coulomb interaction is the sole driving force of Fe_3O_4 is not convincing [23]. Our group has pioneered studies that uses investigations of spin-wave spectra to learn more about CO. We analyzed the spectra of inelastic neutron scattering for Fe_3O_4 and observed that spin-wave stiffening above T_V provides strong evidence for Anderson's short-ranged electron correlations in the mixed valent (MV) phase and indirectly supports the idea that the intersite Coulomb interactions are important to the Verwey transition. The optical spin waves of Δ_5 symmetry ($\sim$ 80 *meV*) are shifted upwards above T_V due to the occurrence of *B*-*B* ferromagnetic (F) double exchange while the other modes are not affected [24], which indicates that super exchange interaction is insensitive to the details of long-range CO below T_V. Therefore, the intersite Coulomb interactions play an important role in the system, even if full charge disproportionation does not occur [23, 25].

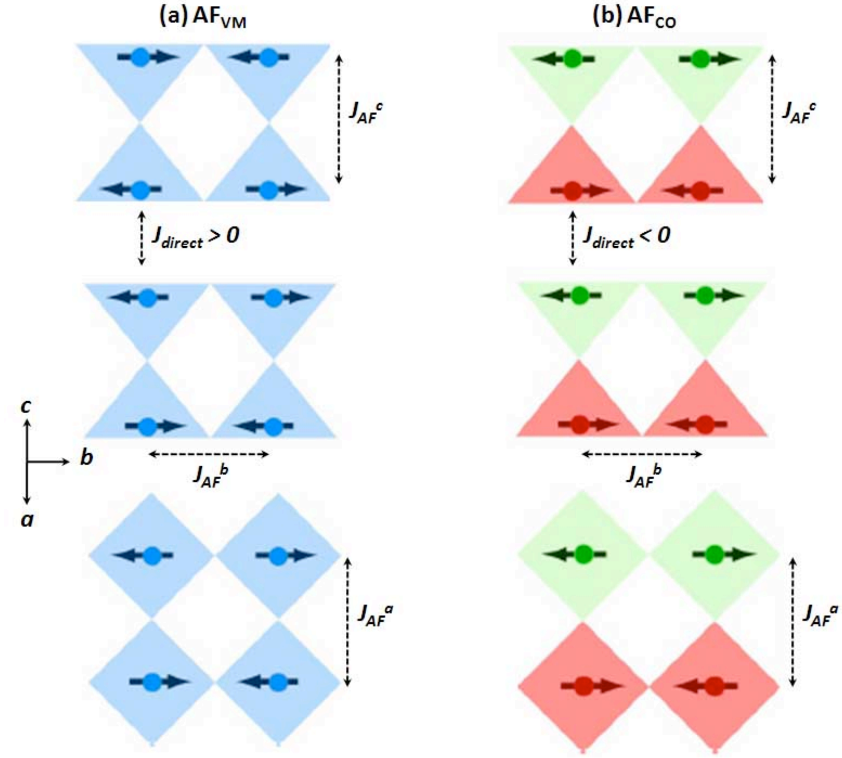

Figure 1.2 Schematic representations of charge and magnetic order [28] in $YBaFe_2O_5$. The upper and lower panels are projections onto the *bc* and *ab* planes, respectively. Fe ions are shown as balls and oxygen square pyramids as triangles or squares. Arrows indicate magnetic moments. (a) For 308 $K < T <$430 K (AF_{MV}), the Fe ions are valence mixed (blue). (b) For $T <$ 308 K (AF_{CO}), Fe^{2+} (green) and Fe^{3+} (red) chains run along the *b* axis and alternate along the *a* and *c* directions.

$YBaFe_2O_5$ (YBFO) is another Verwey transition compound with a fractional valence of 2.5+. The perovskite-based crystal structure consists of FeO_2-BaO-FeO_2 double layers, in which five coordinated Fe sites form apex-shared square pyramids with the double layers separated by an oxygen-vacant Y layer [26]. At high temperatures, a single iron site, $Fe^{2.5+}$, is detected in YBFO by Mössbauer spectroscopy [27, 28], while no superlattice peak is observed by the synchrotron X-ray powder diffraction (SXPD) and neutron powder diffraction (NPD), Fig. 1.2(a) [26, 29]; On cooling, the compound reveals a three-step CO processes: i) the Fe ions order antiferromagnetically at $T_N \sim 432$ *K*, and remain the valence mixed; ii) based on the Mössbauer data, two different iron signals, $Fe^{2.5+\delta}$ and $Fe^{2.5-\delta}$, are observed as a premonitory CO transition; iii) the complete transition into nearly full charge disproportionation of Fe^{2+} and Fe^{3+} is found with the further cooling below the Verwey temperature ($T_V \sim 308$ *K*), Fig. 1.2(b). The Fe charge disproportionation of the last transition can be expressed as, $2Fe^{2.5+} \rightarrow Fe^{2+} + Fe^{3+}$, and detected by SXPD and NPD. The main difference between the two antiferromagnetic (AF) structures(step ii) and iii)) is the sign of the direct exchange between double layers (across the Y layer): F in AF_{MV} and AF in AF_{CO}. Furthermore, the lattice symmetry changes from *Pmmm* to *Pmma*. Consequently, a three-dimensional charge-ordered arrangement of the two ions is revealed, Fig. 1.2 [30,31], and an unusual opportunity to study MV transition is provided by a cooperative Jahn-Teller distortion and a magnetic phase transition [32].

Both $YBaFe_2O_5$ and Fe_3O_4 have a magnetic transition temperature (T_N) that is larger than the CO temperature (T_{CO}). However, the difference between the temperatures (ΔT) of the magnetic and CO transition varies: In YBFO, ΔT is ~ 124 *K*, which is much smaller than Fe_3O_4 (~ 740 *K*). Thus, there is a great possibility that the magnetic energy contributes to the stability of CO state in YBFO. In order to prove this, our group has applied the inelastic neutron scattering to study the CO of YBFO. Based on the magnetic excitation energies, we found that the charge-ordered insulating ground state below T_V can be well explained with e_g superexchange (SE) interactions, while the conduction state above T_V can be well explained with the addition t_{2g} double exchange (DE) interactions within AE FeO_2-BaO-FeO_2 double layers by an electron hopping process [30]. Thus, the magnetic energy is important to the CO state of YBFO. In addition, the *GGA + U* method has been applied to simulate both the low-temperature CO and the high-temperature MV phase in good agreement with INS data and other experimental results [33]. Therefore, both the magnetic energy and electron-lattice interaction play some role in the ordered ground state.

The subject of this dissertation addresses the origin of the CO transition of $R_{1/3}Sr_{2/3}FeO_3$(*R*: rare

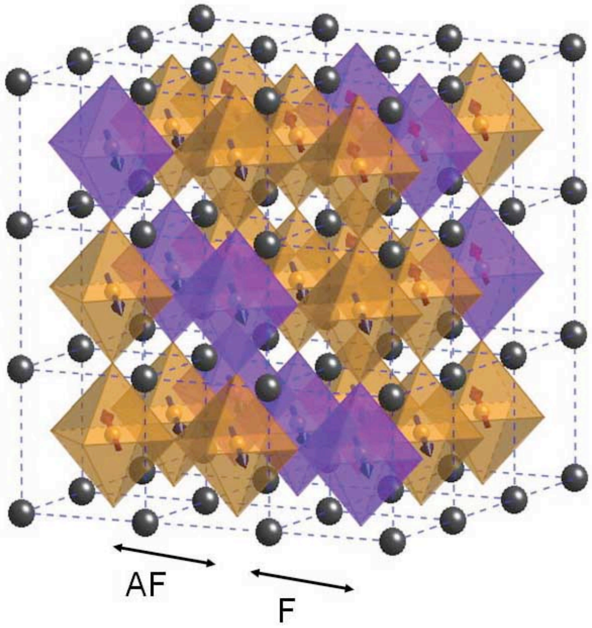

Figure 1.3 Crystal structure and magnetic ordering in *R*SFO below the Verwey transition temperature. The black dots are the R^{3+} ions, the brown (purple) octahedra are the Fe^{3+}-O_6 (Fe^{5+}-O_6), whose center-site is occupied by Fe^{3+}(Fe^{5+}) ion and corner-sites are occupied by O^{2-} anion. Arrows indicate magnetic moments.

earth metal) (*R*SFO). *R*SFO is a perovskite-based crystal with a fractional valence 3.67+ at high temperature. The parent lattice structure is relatively simple and is based on the standard single layer perovskite ABO_3. Below the transition temperature, it is proposed that charge disproportionation occurs in *R*SFO according to $3Fe^{3.67+} \rightleftharpoons 2Fe^{3+} + Fe^{5+}$, and the different iron valences order along the body diagonal $[111]_c$. In order to describe the magnetic structure easily, it is noted that the antiferromagnet (AFM) spins are $\cdots \uparrow\downarrow\downarrow\downarrow\uparrow\uparrow \cdots$ with the CO $\cdots$ Fe^{3+}, Fe^{3+}, Fe^{5+}, Fe^{3+}, Fe^{3+}, Fe^{5+}, $\cdots$ along the cubic [100] direction. The magnetic transition temperature (T_N) is the same as the CO temperature (T_{CO}). This is distinct from Fe_3O_4 and YBFO, where the magnetic order occurs first followed by CO, Fig. 1.3 [34, 35, 36]. Furthermore, it is also reported that the Coulomb interaction is very small due to the small charge-transfer gap, and can be tuned by a smaller rare earth ion substitution on the *R*-site [37]. Thus, these compounds provide a great opportunity to study the different factors for the CO stability [36]. Under the assumption that Coulomb interaction is weak, T. Mizokawa and A. Fujimori calculated the magnetic energies for different CO states and claimed that the observed CO pattern depended on the ratio of magnetic exchange energies [38]. This still needs to be proven by further experimental evidence and is the main topic of this thesis. In addition, the exact contribution of coulomb interaction, magnetic energy, and electron-phonon interaction to this CO system is still not clarified. The purpose of this dissertation is to explore the original driving force of the CO ground state of *R*SFO by the methods of neutron scattering (elastic and inelastic).

1.2 Dissertation Layout

The dissertation will begin with a brief review of the three driving forces for CO in TMO: magnetic energy, Coulomb interaction, and election-lattice interaction.

In the following two chapters, chapter 3 and 4, the sample synthesis, experimental techniques and instruments are presented. Since the central technique used is neutron scattering, chapter 3 introduces the theoretical background, instruments, and data reduction of the techniques. The lab characterization and magnetic order measurement by neutron diffraction on these compounds *R*SFO(R = Pr, Nd, Sm, and Y) are shown in chapter 4. The magnetic ordering phase of SSFO is observed by NPD for the first time.

Chapter 5 discusses magnetic properties of the parent compounds RFeO$_3$(R = La, Pr, Nd, Sm, and Y) (*R*FO). After introducing the magnetic structure and lab characterization of *R*FO compounds, the magnetic exchange energies of *R*FO are deduced by the Heisenberg Model analysis of the neutron scattering data. Because Pr^{3+}, Nd^{3+}, and Sm^{3+} are magnetic ions, the crystal electric field (CEF) contributions are also analyzed. Besides fitting the magnetic excitation data in energy verse intensity, Q-cut fitting is introduced as another data reduction method. (CEF) excitations from these two different methods agree well with each other. CEF data obtained in this chapter are used to separate the magnetic signals of R^{3+} and Fe^{3+} in Sr-doped compounds as described in the following chapter.

Chapter 6 discusses the effect of the magnetic energy and Coulomb interaction on the CO in *R*SFO (R = La, Pr, and Nd). The theoretical basis for this research is introduced. The contributions of the magnetic energy to the Fe ions ordering in *R*SFO are discussed by subtracting the CFE, which is based on the study of *R*FO presented in chapter 5. Some plausible results are concluded: the magnetic energy could stabilize the CO itself in LSFO and PSFO, while the role of Coulomb interaction can be deduced upon the *R*-site substitution from La to Nd.

Chapter 7 extends the investigation of the CO driving force in *R*SFO to the electron-lattice interaction. With the comparison of the phonon density-of-state (DOS) of parent and Sr-doped compounds at different temperatures, the *R*-site substitution, Sr introduction, and temperature varying influences on electron-lattice interaction are discussed.

Finally, chapter 8 summarizes the main results of this dissertation and proposes some new perspectives which are worthy being the subjects of future work.

Bibliography

[1] J. M. Tranquada, B. J. Sternlieb, J. D. Axe, Y. Nakamura, and S. Uchida, Nature (London) **375** (1995) 561

[2] Z. Jirák, S. Krupička, Z. Šimša, M. Dlouhă, S. Vratislav, Journal of Magnetism and Magnetic Materials 53 (1985) 153; H. Kuwahara, Y. Tomioka, A. Asamitsu, Y. Moritomo, and Y. Tokura, Science 270 (1995) 961

[3] C. H. Chen, S-W. Cheong, and A. S. Cooper, Physical Review Letters, 71 (1993) 2461; S-W. Cheong, H. Y. Hwang, C. H. Chen, B. Batlogg, L. W. Rupp, Jr., and S. A. Carter, Physical Review B 49 (1994) 7088

[4] Y. Moritomo, Y. Tomioka, A. Asamitsu, Y. Tokura, and Y. Matsui, Physical Review B 51 (1995) 3297

[5] E. J. W. Verwey, Nature (London) 144 (1939) 327

[6] G. L. Squires, *Introduction to the theory of thermal neutron scattering*, Cambridge University Press. 1996

[7] R. J. McQueeney, *Lattice effcts in high-temperature superconductors*, UMI, 1997

[8] F. Walz, Journal of Physics: Condensed Matter 14 (2002) R285

[9] J. Garcia and G. Subias, Journal of Physics: Condensed Matter 16 (2004) R145

[10] T. Okamura, Science reports of the Tohoku Imperial University 21 (1932) 231

[11] E. J. Verwey, P. W. Haayman, and F. C. Romeijn, Journal of Chemical Physics 15 (1947) 181

[12] N. F. Mott, Advances in Physics 16 (1967) 49

[13] P. W. Anderson, Physics Review 102 (1956) 1008

[14] D. Ihle and B. Lorenz, Journal of Physics C 19 (1986) 5239

[15] I. Leonov, A. N. Yaresko, V. N. Antonov, M. A. Korotin, and V. I. Anisimov, Physical Review Letters 93 (2004) 146404

[16] J. M. Zuo, J. C. H. Spence, and W. Petuskey, Physical Review B 42 (1990) 8451

[17] G. Shirane, S. Chikazumi, J. Akimitsu, K. Chiba, M. Matsui, and Y. Fuji, Journal of the Physical Society of Japan 39 (1975) 949

[18] J. García, G. Subías, M. G. Proietti, H. Renevier, Y. Joly, J. L. Hodeau, J. Blasco, M. C. Sánchez, and J. F. Bérar, Physical Review Letters 85 (2000) 578

[19] J. P. Wright, J. P. Attfield, and P. G. Radaelli, Physical Review B 66 (2002) 214422

[20] E. Nazarenko, J. E. Lorenzo, Y. Joly, J. L. Hodeau, D. Mannix, and C. Marin, Physical Review Letters 97 (2006) 056403

[21] G. K. H. Madsen and P. Novak, Europhysics Letters 69 (2005) 777

[22] H.-T. Jeng, G. Y. Guo, and D. J. Huang, Physical Review Letters 93 (2004) 156403

[23] P. Piekarz, K. Parlinski, and A. M. Oleś, Physical Review B 76 (2007) 165124

[24] R. J. McQueeney, M. Yethiraj, W. Montfrooij, J. S. Gardner, P. Metcalf, and J. M. Honig, Physical Review B 73 (2006) 174409

[25] R. J. McQueeney, M. Yethiraj, S. Chang, W. Montfrooij, T. G. Perring, J. M. Honig, and P. Metcalf, Physical Review Letters 99 (2007) 246401

[26] P. M. Woodward, E. Suard, and P. Karen, Journal of the American Chemical Society 125 (2003) 8889

[27] P. Karen, P. M. Woodward, J. Lindén, T. Vogt, A. Studer, P. Fisher, Physical Review B 64 (2001) 214405

[28] J. Lindén, P. Karen, A. Kjekshus, J. Miettinen, T. Pietari, M. Karppinen, Physical Review B 60 (1999) 15251

[29] P. Karen, P. M. Woodward, P. N. Santhosh, T. Vogt, P. W. Stephens, S. J. Pagola, Journal of Solid State Chemistry 167 (2002) 480

[30] S. Chang, P. Karen, M. P. Hehlen, F. R. Trouw, and R. J. McQueeney, Physical Review Letters 99 (2007) 037202

[31] P. M. Woodward and P. Karen, Inorganic Chemistry 42 (2003) 1121

[32] Y. Tokura, Reports on Progress in Physics 69 (2006) 797

[33] C. Spiel, P. Blaha, and K. Schwarz, Physical Review B 79 (2009) 115123

[34] P. D. Battle, T. C. Gibb, and P. Lightfoot, Journal of Solid State Chemistry 84 (1990) 271

[35] S. E. Dann, D. B. Currie, M. T. Weller, M. F. Thomas and A. D. Al-Rawwas, Journal of Solid State Chemistry 109 (1994) 134

[36] J. Q. Li, Y. Matsui, S. K. Park, and Y. Tokura, Physical Review Letters 79 (1997) 297

[37] S. K. Park, T. Ishikawa, Y. Tokura, J. Q. Li and Y. Matsui, Physical Review B 60 (1998) 10788

[38] T. Mizokawa and A. Fujimori, Physics Review Letter 80 (1998) 1320

CHAPTER 2. Overview of the charge-ordering driving forces of Coulomb interaction, magnetic energy, and electron-phonon interaction

In this chapter, I will present the important concepts which palya role in the phenomenon of CO. Electrons in solids possess three attributes: charge (e^-), spin ($S=\pm\frac{1}{2}$) and orbital symmetry. Interaction among these can account for CO transitions and a variety of other novel phenomena. Many of the details of charge and magnetic state are mainly determined by the crystal structure of the compound, and $R_{1/3}Sr_{2/3}FeO_3$ (R: rare earth) materials are based on RFeO$_3$ perovskite materials [1], the structure of ABO_3 need to be introduced at first. Then, the role of Coulomb interaction, magnetic energy, and electron-lattice interaction will be reviewed.

2.1 Structural Considerations

2.1.1 Structure of ABO_3

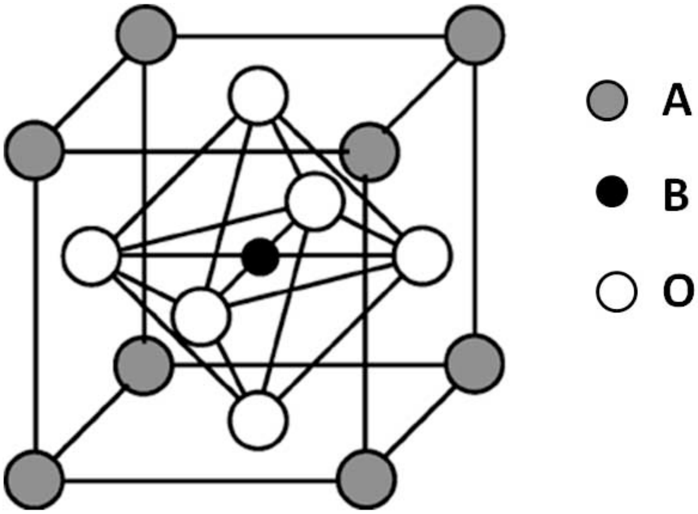

Figure 2.1 Ideal ABO_3 cubic-provskite structure.

The ideal ABO_3 perovskite TMOs has the cubic structure of Fig. 2.1. The ABO_3 cubic-perovskite structure *A* cations and *B* cations are in twelvefold and sixfold oxygen coordination respectively.

Normally, *A*-site is occupied by rare earth/IIA-metal ions and *B*-site is occupied by transition-metal ions (we simplify it as '*M*' ion). In our case, the *A*-site is occupied by *R*/Sr (*R*: rare earth metal) ions and the *M*-site is occupied by Fe.

The perovskite structure is often distorted, typically by cooperative tilting of MO_6 octahedra, due to steric effects caused by the different radii of *A* and *B* ions. The bond length of *Fe-O* and the degree of ∠ *Fe-O-Fe* are modified by the distortion. If the ionic sizes of *A*, *M*, and *O* have certain ideal ratio in the perovskite structure, Fig. 2.1, and there is no tilting in the system, it results in a bond angle of 180° (*M-O-M*). However, this is just the ideal case, the ionic radii are different and there is no way to avoid octahedral tilting in the general case. The propensity for lattice distortions are described by the Geometric Tolerance Factor which is related to the effect of different distances between the ions/anions,

$$t = \frac{< A - O >}{\sqrt{2} < M - O >}, \tag{2.1}$$

where <*A-O*> and <*M-O*> are the average bond lengths of *A-O* and *M-O* which are typically estimated from the standard ionic radii obtained from diffraction data and are available in tables [2].

If $t < 1$, the *A-O* bonds are under tension and the *M-O* bonds are under compression. Normally, the lattice stresses are relieved by the cooperative rotations of the corner shared MO_6 octahedra about a cubic crystallographic axis, which leads to the *M-O-M* bond angles bending from 180° to (180° - ϕ) along with a shortening *A-O* bond. The crystal symmetry is reduced by these cooperative rotations: for example, rotations about a [1 1 1] axis give rhombohedral ($R\bar{3}c$) symmetry, where t is from ~ 0.956 to ~ 1.012 as reported; those about a [110] axis give orthorhombic (*Pbnm* or *Pnma*) symmetry, where t is from ~ 0.87 to ~ 0.99 as reported.

The perovskite structure is very robust and amenable to a wide variety of chemical modifications on *A*- and *B*-site. Substituting the *A*-site ion with an ion of different radius is an effective method to control the distortion and thereby control fundamental electronic parameters, such as electron hopping interaction. Heterovalent doping on the *B*-site modifies the average valence of oxidation state and can lead to CO as discussed below. The range of t values is also related to the oxidation state of the *B* cation: t vary from 0.886 to 1.139 for $A^{+}B^{5+}O_3$-type perovskite compounds, from 0.822 to 1.061 for $A^{2+}B^{4+}O_3$-type compounds, and from 0.832 to 1.012 for $A^{3+}B^{3+}O_3$-type compounds. Obviously, the tolerance factor value of ABO_3-type perovskite compounds sharply increases as the oxidation state of the *B* cation increases [3, 4, 5, 6, 7, 8].

In this thesis, the perovskite structure of *R*FO is orthorhombic and the structure of *R*SFO is rhombohedral. For the parent compound, the neighbors of oxygen ion are same, Fe^{3+}, thus the distortion of oxygen is small and just happens in the plane. The environment of oxygen ion in *R*SFO is more complicated: there are two kinds of the oxygen-atom displacements, Fe^{3+}-O^{2-}-Fe^{3+} and Fe^{3+}-O^{2-}-Fe^{5+}. In mixed valent systems where a CO transition occurs, the oxygen ions are displaced by the neighbor charges, which are superimposed on these cooperative rotations [9]. Therefore, it is similar *R*FO for the first one; the charges are alternating (Fe^{3+}/Fe^{5+}) and the Fe ions themselves have different ionic sizes for the second case, the central oxygen-atom moves away from one Fe atom near neighbor toward the other.

In addition, the effect of CO on structure contributes to the lattice distortion. Usually, *A-O* bond is more sensitive than *M-O* bond on this factor due to the environment of the A^{3+} ion is more flexible than the perovskite center-site *M*. In LSFO, the bond lengths (in Å) of *A-O* and *M-O* are listed at 50 *K* and room temperature, Table 2.1 [10].

Table 2.1 The bond lengths (in Å) of *A-O* and *M-O* for LSFO at 50 *K* and 300 *K*.

	50 *K*	300 *K*
Fe-O	1.936(1) × 6	1.938(1) × 6
La/Sr-O	2.591(1) × 3	2.635(1) × 3
	2.883(1) × 3	2.843(1) × 3
	2.733(1) × 6	2.738(1) × 6

The tolerance factors of *R*FO and *R*SFO at room temperature are listed in Table 2.2. The values of both lines are the data of X-ray measurement, the first line is the results of our samples and the '$*$'s show the reference one. So it can be clearly seen: i) the distortion is increasing with the substituting of the smaller rare earth metal, from La to Y; ii) compared to the related *R*FO, *t* of *R*SFO is larger due to the higher oxidation state of Fe ions, from Fe^{3+} to $Fe^{3.67+}$. The above discussion is based on the assumption that there are no oxygen defects. Fig. 2.2 shows the phase of $La_{1-x}Sr_xFeO_{3-\delta}$ with the oxygen stoichiometry [1]: If the oxygen content is 3.0, the space group is changing from the low symmetry (othorhombic) to high symmetry (cubic) with Sr doping due to the average covalent radius of Sr^{2+}, $\langle Sr^{2+} \rangle$, is 1.12 Å, which is smaller than $\langle La^{3+} \rangle$ and close to $\langle Fe^{4+} \rangle$; If the oxygen content is

Table 2.2 The tolerance factor of *R*FO and *R*SFO as measured by X-ray diffraction.

	LFO	PFO	NFO	SFO	YFO
R^{3+} radius (Å)	1.216	1.178	1.162	1.13	1.07
Space group	*Pnma*	*Pnma*	*Pnma*	*Pnma*	*Pnma*
Tolerance factor	0.951 ± 0.002	0.925 ± 0.002	0.918 ± 0.002	0.910 ± 0.002	0.890 ± 0.002
(t)	0.954*	0.925*	0.918*	0.907*	0.889*
	LSFO	PSFO	NSFO	SSFO	
Space group	$R\bar{3}c$	$R\bar{3}c$	$R\bar{3}c$	$R\bar{3}c$	
Tolerance factor	0.999 ± 0.002	0.997 ± 0.002	0.996 ± 0.002	0.993 ± 0.002	
(t)	1.003*	0.996*	0.992*	0.989*	

* reference 11, 12, 13, 14, 15, 16.

less than 3.0, the phase transition even can reverse the sequence from the high symmetry (cubic) to low symmetry (tetragonal) with Sr doping. In the case of the thesis, the oxygen stoichiometry was maintained at 2.95 at a minimum.

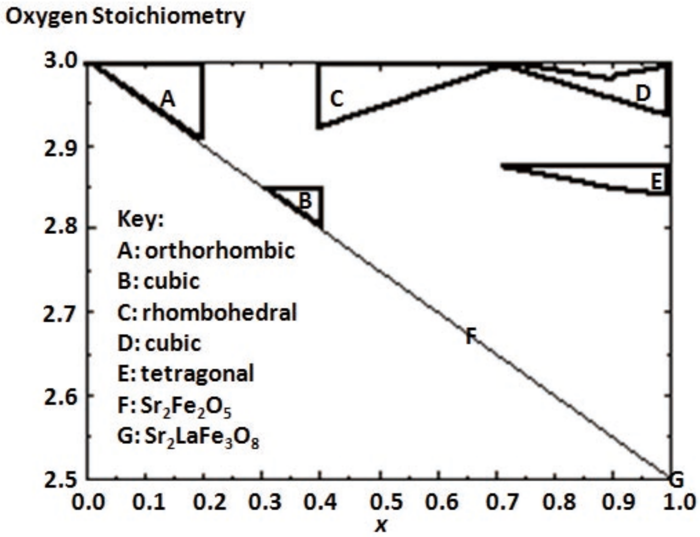

Figure 2.2 The phase diagram of $La_{1-x}Sr_xFeO_{3-\delta}$, which describes the full range of x and δ. The labeled regions are identified in the key, while the unlabeled regions are multiphase.

2.2 Coulomb Interaction

In the ionic systems, the Coulomb interaction is responsible for much of the total energy. Especially in ionic insulators, such as the parent compound *R*FO, it can represent even up to 90 % of the total cohesive energy. The expression of Coulomb interaction is quite simple, just being given by Coulomb's law,

$$U_{ij}^{Coulomb} = \frac{q_i q_j}{4\pi\epsilon_0 r_{ij}}\,, \tag{2.2}$$

where q_i and q_j are the charges of *i* and *j* ions, r_{ij} is the distance between them.

From above equation, we could clearly find that the Coulomb interaction is determined by the values and positions of charges. However, the mixed valent materials in the Verwey system, such as *R*SFO, are on the boundary of metallic and insulating (semiconducting) behavior, and the ionic valence and degree of charge localization can change dramatically at temperatures above and below T_V, which lead to the complications to calculate the Coulomb interactions and the metallic screening. In this section, I will introduce the Hubbard model due to metal-insulator transition at first; then a simple case of the Coulomb interaction stabilizing the CO in a free electron gas, Wigner Crystal, will be presented; at last, I am going to discuss the energy of CO on a lattice and Madelung energy.

2.2.1 Metal-Insulator Transition (MIT) and Hubbard Model

As the first successful theoretical and experimental descriptions of metals, semiconductors, and insulators, electronic band theory is based on noninteracting or weakly interacting electron systems. In the theory, it makes a general distinction on the filling of the electronic bands at zero temperature: For metals, the highest filled band (conduction band) is partially filled; For semiconductors, it is completely filled, but the gap between the highest filled band (valence band) and the nearest empty band is small (order *kT*); For insulators, the filled state of the bands are same as semiconductor, but the band gap is large (typically 1 *eV* or more). In other words, the Fermi level lies in a band gap in insulators and semiconductors while the level is inside a band for metals [17, 18, 19]. However, de Boer and Verwey reported: Although many transition-metal oxides have a partially filled *d*-electron band, they are nonetheless poor conductors and indeed often insulators [20]. Concerning the report, Peierls proposed the electron-electron correlation: the origin of the insulating behavior could be the strong Coulomb repulsion between electrons [21].

In 1949, Mott first tried to explain this kind of insulator in the band structure [22]: A lattice model was built by a single electronic orbital on each site without electron-electron interactions. Then, a single band would be formed from the overlap of the atomic orbitals, where the band became full when two

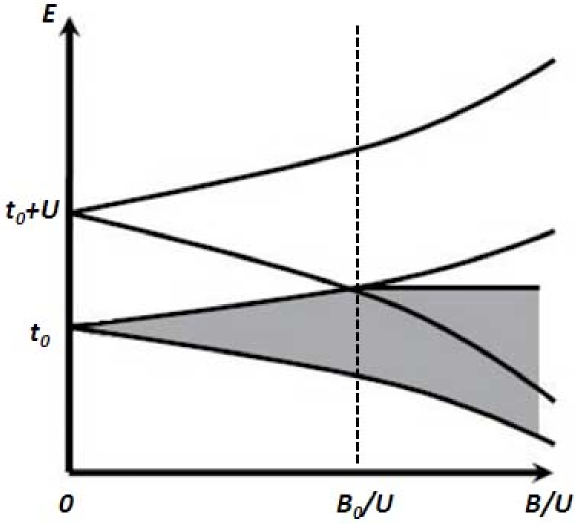

Figure 2.3 Hubbard model from localized state to extended state in half filled energy bands.

electrons, one with spin-up and the other with spin-down, occupied each site. Due to the large Coulomb repulsion between the electrons, the band would split into two: The lower one was formed from electrons that occupied an empty site and the upper one from electrons that occupied a site already taken by another electron. Thus, the lower band would be full, and the system an insulator. In addition to the insulating phase, describing and understanding the metallic phases in this system is a still challenging subject. The earlier pioneering work on MIT was done by Hubbard and based on the tight-binding approximation [23, 24]. J. Hubbard introduced two items: i) the electron band width, t, which is the kinetic energy gained from hybridization; ii) the coulomb energy, U, which is the energy cost for double occupancy of an atomic site. In the Hamiltonian, these two are competitive: a band term decreasing the kinetic energy and an electron localized term decreasing the Coulomb correlation energy,

$$H = \sum_{i,j,\sigma} t_{ij} c^{+}_{i\sigma} c_{j\sigma} + U \sum_{i} n_{i\sigma} n_{i\bar{\sigma}} \, , \tag{2.3}$$

where $n_{i\sigma} = c^{+}_{i\sigma}\, c_{i\sigma}$ is particle operator, $c^{+}_{i\sigma}$ and $c_{i\sigma}$ are the creation and annihilation operators of paticles with spin σ located on site i. Assuming $t_0 = t_{ii}$ and $t = t_{ij}$. Since t_0 is the lowest energy of the conduction band, $t_0 + U$ is the potential energy of the other electrons with the antiparallel spin.

The total electron band width is related to the coordination number and hopping integral and expressed as B. Assuming z is the coordination number, $B = 2zt$. If $B \gg U$, the ground state of the Hamilto-

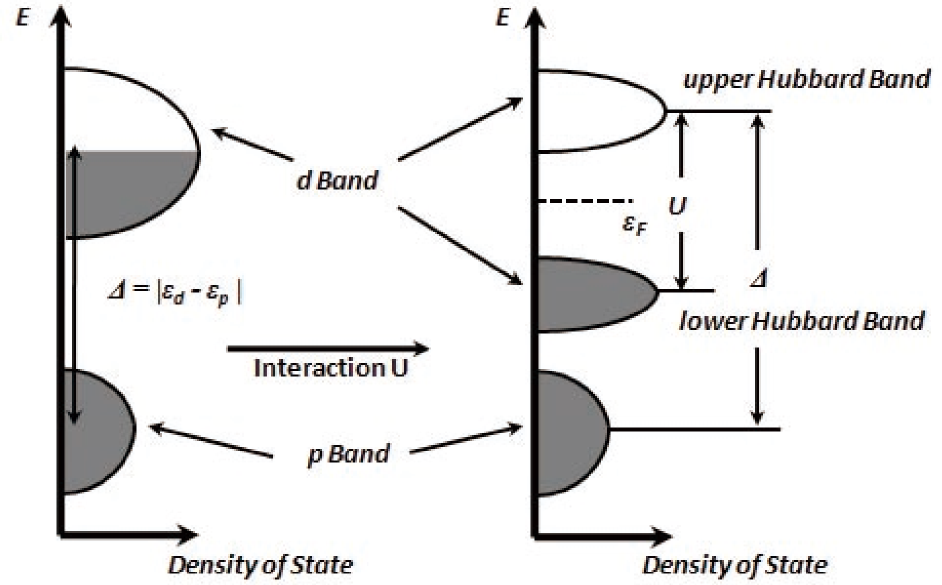

(a) ***Mott – Hubbard Insulator***

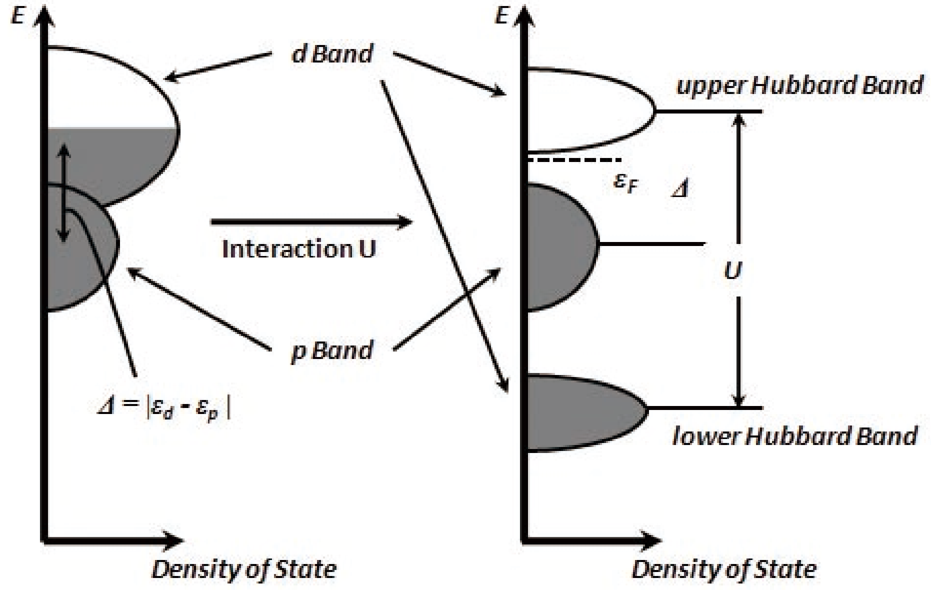

(b) ***Charge Transfer Insulator***

Figure 2.4 Schematic illustration of energy levels for (a) a Mott-Hubbard insulator and (b) a charge-transfer insulator generated by the d-site interaction effect. ε_F is the fermi level.

nian is metallic and unless band is filled. If $B \ll U$, the ground state of the Hamiltonian is localized due to the half-filled band; If $B \approx U$, the material is a poor metal or semiconductor. Therefore, the electronic conduction of a compound is decided by the ratio of B/U as shown in Fig. 2.3 and the critical value is B_0/U.

In TMO, the energy band of *3d* orbital of transition metal ion is typically narrow (B is small) and will be split into the upper and lower Hubbard bands. The energy level of *2p* orbital of oxygen anion (E_p) relative to the metal *d*-bands (E_d) outlines two extreme cases: Mott-Hubbard (MH) insulator, $E_p < E_d$, and Charge Transfer (CT) insulator, $E_d < E_p < E_d + U$. If the energy gap between the *2p* orbital of oxygen anion and the upper Hubbard bands of the transition metal is Δ, those two insulators can be defined as MH insulator ($U < \Delta$) and CT insulator ($U > \Delta$) [25, 26], Fig. 2.4.

Usually the *2p* orbital of oxygen anion and the Hubbard bands of transition metal ions do not separate as significantly as in Fig. 2.4, there are overlaps between them, which produce the covalence between the *d* electron of metal ion and *p* electron of oxygen anion. In such a case, we label the metal-oxygen hybridization as t_{pd}, the modfied *d* electron phase diagram can be plotted in Fig. 2.5 by D. D. Sarma [27].

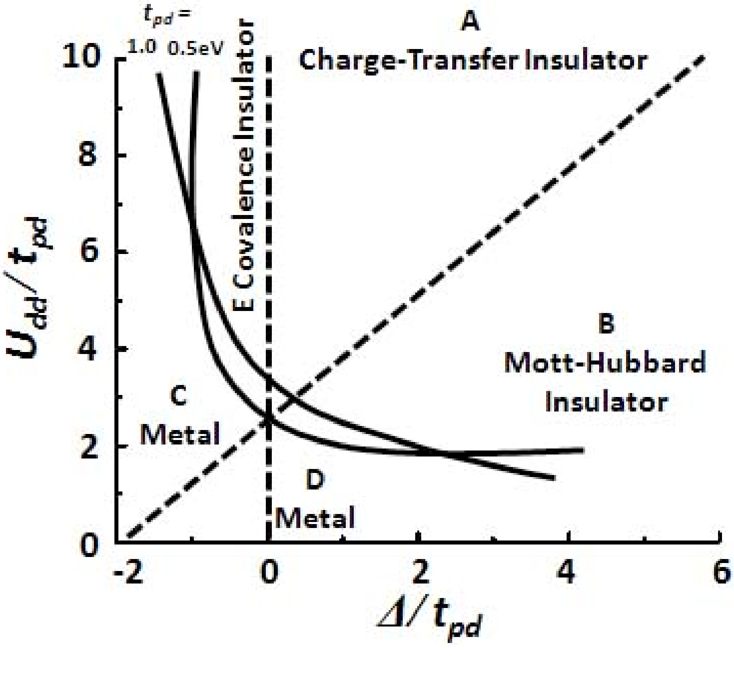

Figure 2.5 The *d* electron phase diagram. t_{pd} is hybridization between the *d* electron of transition metal ion the *p* electron of oxygen anion.

Based on the Hubbard model, the metallic or insulating phases are a function of *U*/*t* and doping, and a generic phase diagram is shown in Fig. 2.6. Although it is an insulator at large *U*/*t* and 1/2 filling, a metallic phase can be obtained by either doping or changing the hybridization (smaller *U*/*t*). In the shaded region near the Mott insulator, the charge carriers are nearly localized and charge transport is complicated due to the mixing of charge fluctuations with spin and lattice distortions. In those regions, the properties like high temperature superconductor (HTSC) appear and the mechnism still is not fully understood [25].

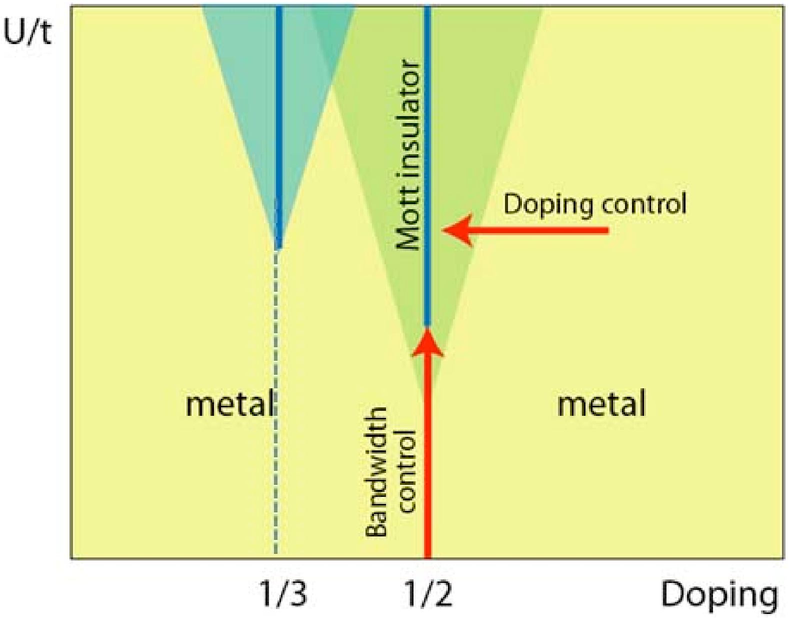

Figure 2.6 Metal-insulator phase diagram based on the Hubbard model in the plane of *U*/*t* and filling *n* (*n* = 1/3 and 1/2). Although the shaded area means the principle metallic state, it is strongly influenced by the metal-insulator transition, in which carriers are easily localized by extrinsic forces such as randomness and electron-lattice coupling.

In the thesis, *R*FO is a CT insulator [28] and the electronic state can be modified by doping different atom into the parent compounds. In the parent compound, the electron state of Fe ion is half filled $3d^5$, and the orbital filling state will move to the less doping direction gradually with the Sr^{2+} doping on R^{3+}-site, Fig. 2.6. Then, the *U*/*t* value will determine the first order transition: i) If *U*/*t* is small and there is no shared shaded region as the doping crosses different doping states, the metal-insulator, semiconductor-insulator, and semiconductor-semiconductor transition can be observed: For example, with the *x* increasing, the electronic conductivity is changing from the insulator to metal for

$La_{1-x}Sr_xFeO_{3-\delta}$ [29, 30, 31], Fig. 2.7(a); ii) If *U*/*t* is not small and there is a probability that the doping will pass through the shared shaded region of different states, the metal-insulator transition will be bothered a lot and even be destroyed: For example, if R^{3+}-site substitution from La^{3+} to Sm^{3+} as the doping level *x* is fixed on 2/3, the hybridization will decrease (larger *U*/*t*), the semiconductor-insulator transition temperature is decreasing until no electrical resistivity transition observed in Gd sample [15], Fig. 2.7(b).

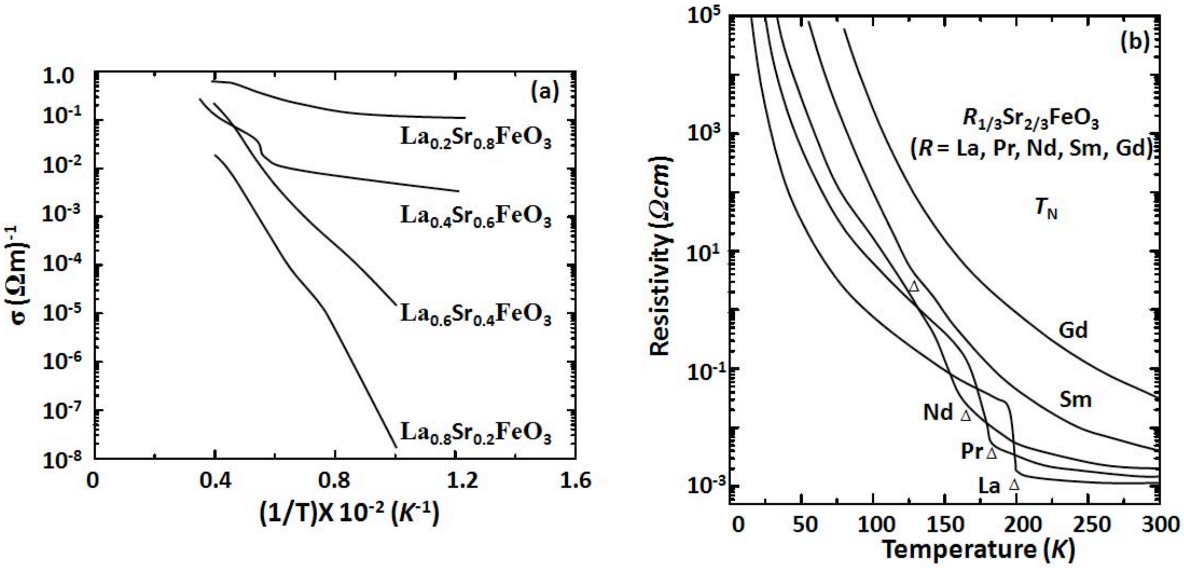

Figure 2.7 (a) Relationship of electronic conductivity (σ) and temperature ($1/T$) for various composition of $La_{1-x}Sr_xFeO_3$; (b) Temperature dependence of resistivity for $R_{1/3}Sr_{2/3}FeO_3$ system in a cooling process, the resistivity abnormality is marked by the triangle sign Δ.

2.2.2 Coulomb Interaction on the CO

2.2.2.1 Wigner Crystal

Wigner Crystal is a model that describes how Coulomb interaction between electrons in a metal can lead to CO. It was first studied by Wigner in the 1930s [32, 33]. He considered an effect which was neglected in free electron model: if the electron density is less than a critical value, the electron will not move randomly through space as what it behaves in most metal. The Coulomb repulsion between electrons results in charge localization and the electrons will crystallize and form a lattice. This crystalline phase is named Wigner Crystal. In this crystal, the overlap of the localized electronic wave functions will be so small that the formation of energy band with delocalized electrons will be overcome by the long-range Coulomb interaction leading to crystallization of the electrons. Although Wigner Crystal is an ideal model, these crystallized electrons still can be observed in some critical compound, such as lanthanum-doped calcium hexaboride [34].

2.2.2.2 Madelung Energy of CO State

Wigner Crystal is just a relative simple CO model and studies the case of free electrons. Normally, CO system is electrons are localized to ionic sites determined by crystal lattice. The Madelung energy is a factor that describes the stability of such kind long-range interaction between ions [35]. It is the main contribution to the binding energy of ionic crystals. As the total energy of all ions of the compound attracting or repulsing the ion *i*, the expression of Madelung energy is based on the Coulomb's law,

$$U_i = \sum_j U_{ij} = \frac{q_i}{4\pi\epsilon_0} \sum_j \frac{q_j}{r_{ij}}, \tag{2.4}$$

where q_i and q_j are the charges of *i* and *j* ions, r_{ij} is the distance between them.

If the distances r_{ij} are normalized to the nearest neighbor distance r_0 the potential may be written

$$U_i = \frac{q_i}{4\pi\epsilon_0 r_0} \sum_j \frac{q_j}{r_{ij}/r_0} = \frac{q_i}{4\pi\epsilon_0 r_0} M_i\,, \tag{2.5}$$

with M_i being the (dimensionless) Madelung constant of the *i*th ion

$$M_i = \sum_j \frac{q_j}{r_{ij}/r_0}, \tag{2.6}$$

In the thesis, the Madelung constant of the Sr doped compound, *R*SFO, has been roughly calculated: In the whole compound, the charges of O^{2-} anions and La^{3+}/Sr^{2+} ions are -2.0 and +2.333333, their positions do not change on different CO directions; The ionic positions on different CO directions of Fe^{5+} and Fe^{3+} ions are different, just Fe^{5+} and Fe^{3+} ions are calculated with the charges of +5.0 and +3.0. Since the system is electroneutral, the values of M_i are converge. Therefore, M_i on [111] and [100] are 1.647 and 1.696, respectively. Consequently, the Coulomb interaction will stabilize the CO on [100] in the ideal condition without considering the screen and lattice distortion effects. (the M_i will be oscillating on [110] direction due to the symmetry).

2.3 Magnetic Energy

In the previous section, the Coulomb interaction (charge effect) contribution to CO has been discussed. Spin is another intrinsic property of an electron besides charge, and its contribution to CO will be introduced. The interaction between spins is described by magnetic energy. Due to the close energy levels, the orbitals of the bonding atom will reorganize and form new hybrid ones, and magnetic energy between the spins of unpaired electrons in those orbitals originates from quantum mechanical exchange. If the energy band of the compound is narrow and the unpaired electrons exist, the whole system can be magnetic: For example, it is AFM for MH insulator. In *R*SFO, the energy level of *2p* orbitals of O anion is very close to the energy of *3d* orbitals of Fe ion in the CO system and the energy band is narrow, thus the magnetic energy might play an important role in the CO state.

In this section, the local spin state of Fe ions will be introduced at first; then, the magnetic interaction and the Goodenough-Kanamori rule will be discussed; at last, magnetic energy contribution to the CO of $La_{1/3}Sr_{2/3}FeO_3$ will be presented.

2.3.1 Local Spin State of Fe ions

Since the spin exchange is related closely to the hybridization, the energy levels of each bonding electron should be clarified. In the octahedral structure, the six ligands, O^{2-}, occupy the corner and surround the *M*-site Fe ion. Due to the cubic symmetry, the energy degeneracy of the free ion is destroyed: the $3d_{z^2}$ and $3d_{x^2-y^2}$ orbitals of Fe ions will form σ-bonds with the *2p* orbitals of the O^{2-}, which will have higher energy, and the $3d_{xy}$, $3d_{xz}$ and $3d_{yz}$ orbitals of Fe ions will form π-bonds with the *2p* orbitals of the O^{2-}, which will have lower energy. The two higher-energy orbitals are collectively referred to as e_g and three lower-energy orbitals as t_{2g}. The energy difference is expressed as Δ_{oct}, which is the crystal-field splitting parameter. It is around several *eV*. The excitation of the *3d*-orbitals from the free ions to the octahedral environment is shown in Fig. 2.8.

The Hamiltonian can be expressed as

$$H_{3d}(\mathbf{r}) = H_0(\mathbf{r}) + \sum_{j=1}^{6} V^{(O)}(\mathbf{r} - \mathbf{R}_j)\,, \tag{2.7}$$

where $H_0(\mathbf{r})$ is the Coulomb potential of the central metal ions and $V^{(O)}(\mathbf{r}\text{-}\mathbf{R}_j)$ is the interactions between the central metal ions at site $\mathbf{r}$ and the environment O^{2-} ligands at site $\mathbf{R}_j$.

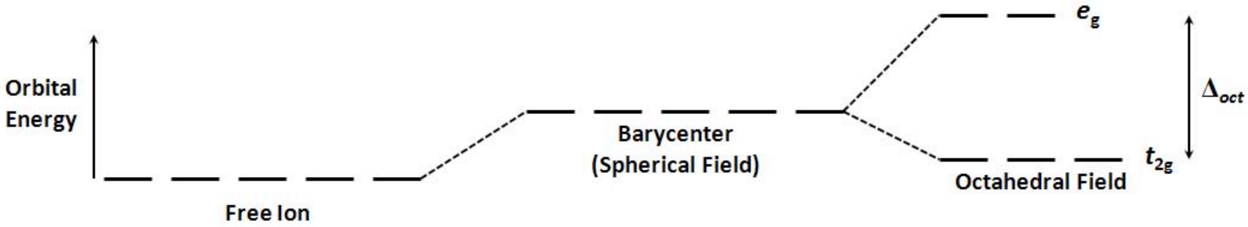

Figure 2.8 Octahedral crystal field stabilization energy.

The local spin states of ions are not just determined by the Pauli exclusion principle and Hund's rules, the crystal-field splitting parameter will be another factor. For *R*FO and *R*SFO, the local spin state of Fe^{3+} is so called high-spin states due to $\Delta_{oct} < J_{Hund}$ and is expressed in Fig. 2.9(b).

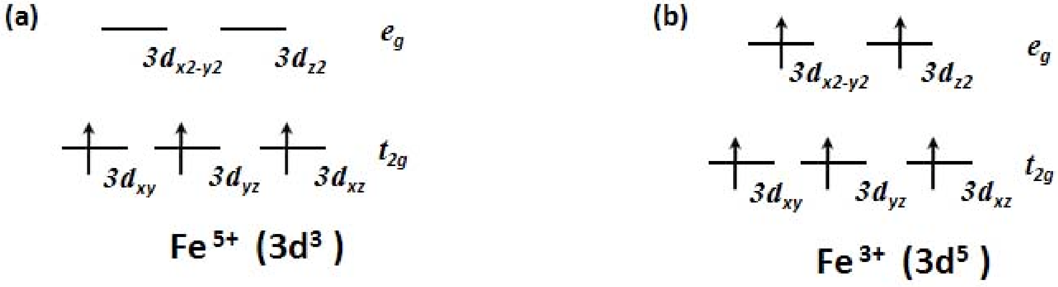

Figure 2.9 The local spin states of Fe^{3+} (a) and Fe^{5+} (b) in the cubic environment.

Furthermore, the above discussion is the normalest case of the crystal electric field (CEF) excitations for the Fe ions in the cubic symmetry, the peroviskite distortion will lead to the further lifting of degeneracy and energy level splitting on the e_g and t_{2g} energy levels is expected to be small [36, 37, 38, 39].

2.3.2 Magnetic Interaction

2.3.2.1 Superexchange

In an insulator, such as *R*FO, the magnetic interaction between Fe spins mediated by the common nonmagnetic oxygen neighbors by a process called superexchange (SE). For the SE interaction, the electrons are shared between metal ions via virtual excitations or intermediate states involving oxygen. In homovalent insulators with the perovskite structure, SE typically leads to AF order. However, as discussed below, SE can be either AF and ferromagnetic (F) in the mixed valent or CO compounds. This competition between F and AF exchanges can affect the stabilities and total energy of the CO state. In the thesis, the parent compounds, *R*FO, and the doped compounds, *R*SFO, are two perfect examples.

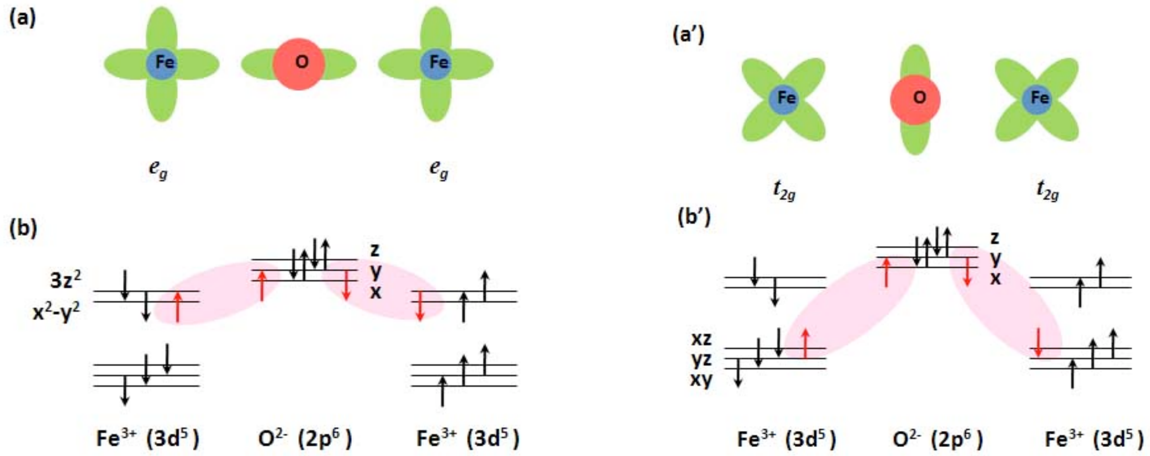

Figure 2.10 Antiferromagnetic illustrations of the superexchange mechanism for Fe^{3+}($3d^5$) ions with the straight bonds by O^{2-}($2p^6$) anion. (left) The σ bond is formed in Fe-O-Fe system; (right) The π bond is formed in Fe-O-Fe system.

Fig. 2.10 explains the mechanism of AF exchange in *R*FO. As the half filled $3d$ orbitals of Fe^{3+} can have strongly overlapping with the filled $2p$ orbital of O^{2-}, hybridization will allow the sharing of electrons between them and two kinds of bonds are formed from the Pauli exclusion principal and Hund's rules: i) As illustrated in the left figure, a σ-bond is formed by the overlap of the e_g orbitals of Fe, such as $3d_{x^2-y^2}$, with $2p_x$ orbital of O. An AFM is strongly favored since O can simultaneously share both of its $2p_x$ electrons only when neighboring Fe ions have oppositely aligned spins. ii) In the right figure, the t_{2g} orbitals of Fe ions can interact with the $2p_x$ orbital of O to produce a π-bond, and it is also AF. However, this kind of interaction between t_{2g} orbitals is very weak compared to the σ-bond and can usually be ignored if both bonds exist. Furthermore, the ground state F for the two Fe^{3+} ions is forbidden by the Pauli principle, Fig. 2.11. Therefore, the SE interaction results in G-type AF coupling in the straight bonds of Fe^{3+} ions [40].

In heterovalent systems displaying CO, the SE interaction can also lead to the F interaction in the straight bonds. In our case, Fe^{3+} and Fe^{5+} of *R*SFO is stated in Fig. 2.12. A spin up Fe^{3+} ion will share a spin down oxygen electron since there is no more room for spin up electrons; In the Fe^{5+} ion, the x^2-y^2

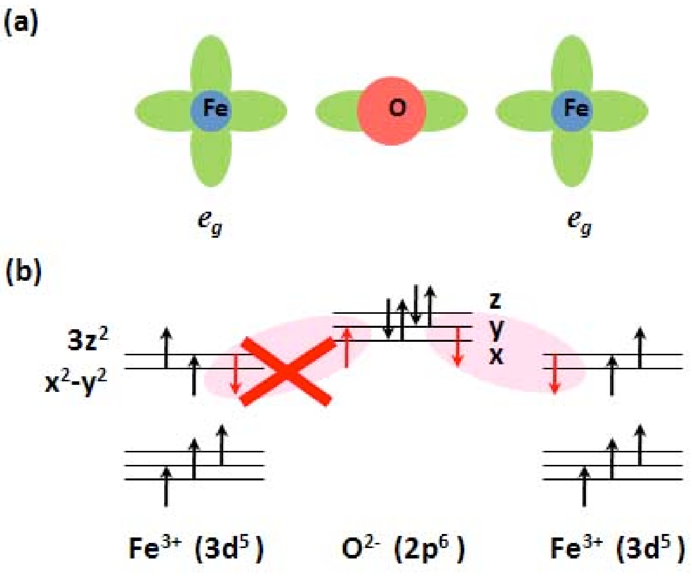

Figure 2.11 Ferromagnetism is rejected assuming non-orthogonal Fe^{3+} orbitals.

orbital is empty and the Hund coupling is large, thus Pauli exclusion principle favors that the oxygen ion share an electron that has the same spin as the other spins. Since the Fe^{3+} ion is already sharing the spin down electron, the Fe^{5+} ion must be spin up. Therefore, the resulting exchange between Fe^{3+} and Fe^{5+} is F.

In addition, the spin directions of the hopping electrons between Fe^{3+} and Fe^{5+} do not have to change in order to conform with Hund's rules when they are on the accepting ions. Hence, the electron movement on the bond Fe^{3+}-O-Fe^{5+} will be facilitated more easily and the kinetic energy expended on the whole processing will be reduced. The total saving energy could lead to ferromagnetic alignment of neighboring ions. This gives the explanation to the higher electron conductivity in *R*SFO compared to *R*FO at the same temperature.

2.3.2.2 Goodenough-Kanamori Rule

As the particularly important indirect interactions of electrons via an intermediary in TMO, superexhange effect is strongly dependent on the magnetic moments of transition metal ions, the overlap integral between orbitals of transition metal and oxygen ions, and the bond angle of M-O-M. A rough estimate of the size and sign (AF or F) of exhange interaction in insulators is summarized by Goodenough-Kanamori Rule. In 1955, J. Goodenough first proposed the idea of 'partial bond formation' of the ligand with the

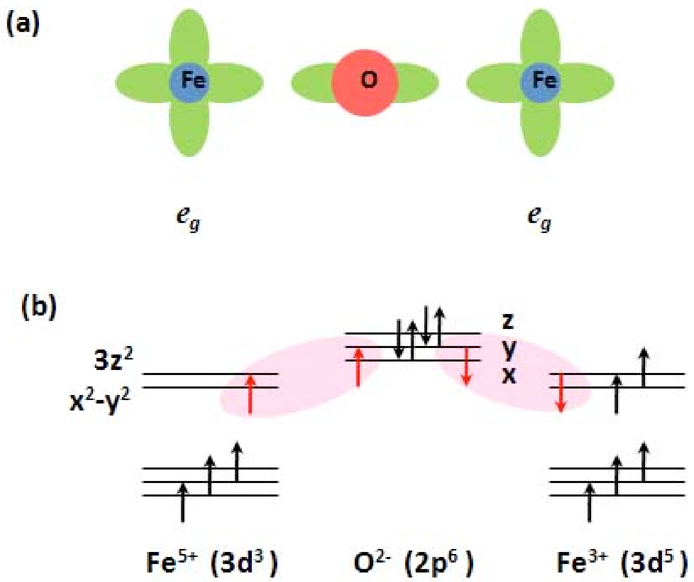

Figure 2.12 Illustration of the ferromagnetic mechanism by SE interaction for Fe ions with different valence (Fe^{3+} and Fe^{5+}). The relative orbitals (a) and energy levels (b) in the Fe-O-Fe system.

metals on both sides of the exchanges and the rough formula; in 1959, Kanamori provided more rigorous mathematical underpinning [41, 42].

This rule assumes that a virtual electron transfer occurs between the overlapping orbitals of electronic states that are separated by an energy, ΔE, in an interatomic spin-spin interactions system. And the theoretical basis of it rests on four preconditions:

- The spin angular momentum is conserved in the electron transfer;
- The Pauli exclusion principal restricts the electron transfer from the same anion *p*-orbital;
- The intraatomic spin-spin potential exchange interaction is ferromagnetic and is determinative where the Pauli exclusion principle is not restrictive;
- The inter-site hopping parameter between the neighboring site can be roughly calculated by

$$t^{\uparrow\uparrow} = t_0 cos(\frac{\theta}{2}) \, , \, or \;\; t^{\uparrow\downarrow} = t_0 sin(\frac{\theta}{2}) \;\; , \tag{2.8}$$

where θ is the relative angle between the neighboring spins, and t_0 is the maximum value of the hopping parameter.

$$t_0 = (\psi_i, H'\psi_j) = \varepsilon_{ij}(\psi_i, \psi_j)\,, \tag{2.9}$$

where ε_{ij} is a one-electron energy, H' is the potential perturbation of the electron with orbital ψ_j by the presence of the other cation orbital ψ_i, and (ψ_i, ψ_j) is the overlap integral for the two orbitals. In orthogonal orbitals, (ψ_i, ψ_j) = 0.

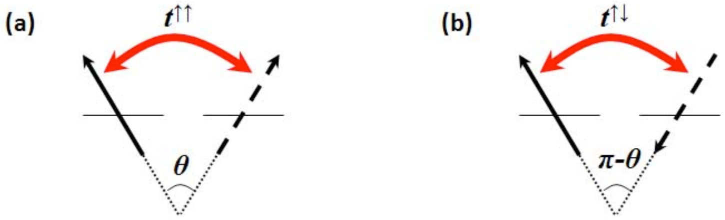

Figure 2.13 (a) and (b) the illustration of the hopping in ferromgnetism and anti-ferromgnetism with the parameter, $t^{\uparrow\uparrow}$ and $t^{\uparrow\downarrow}$.

As a virtual electron transfer between states of different energy, ΔE is treated in higher-order perturbation theory and the ratio, $\frac{t_0}{\Delta E}$, is much less than unity.

i) Due to the Pauli exclusion principle, the virtual electron transfer between half-filled orbitals is AF, so the $t^{\uparrow\downarrow}$ must be the second-order perturbation for the near-neighbor interaction

$$\Delta\varepsilon \approx -\frac{|t^{\uparrow\downarrow}|^2}{\Delta E} = -\frac{t_0^2}{\Delta E} sin^2(\frac{\theta}{2}) = -const. + (\frac{t_0^2}{2\Delta E})cos\theta\,, \tag{2.10}$$

In antiferromagnetism (J^{ex} < 0), the spin-dependent part of this energy is

$$\Delta\varepsilon_{ex} = -J^{ex} S_i \cdot S_j\,, \tag{2.11}$$

Hence,

$$J^{ex} \approx -\frac{t_0^2 cos\theta}{2 S_i S_j \Delta E}\,, \tag{2.12}$$

If S_i = S_i= S = 1/2 and they have the same direction (θ = 180°), the interaction between two electrons is $J^{ex} \approx \frac{2t_0^2}{\Delta E}$, which is the same result as the one derived by P. W. Anderson by the

'Virtual processes' assumption in 1950. Therefore, the Goodenough-Kanamori rule is also named as Goodenough-Kanamori-Anderson rule [40, 41, 42].

ii) Although a virtual electron transfer from a half-filled to an empty orbital is not restricted by the Pauli exclusion principle, the transfered spin is favored by the ferromagnetic Hund's intraatomic potential exchange. Hence, $t^{\uparrow\uparrow}$ is used and the ferromagnetic interaction (J^{ex}>0) is treated in third-order perturbation theory, which adds a factor $\frac{\Delta_{ex}}{\Delta E}$

$$J^{ex} = \frac{t_0^2 \Delta_{ex} cos\theta}{2 S_i S_j (\Delta E)^2}\,, \tag{2.13}$$

where Δ_{ex} is the intraatomic exchange energy.

For example,

To a 180° *M-O-M* CT insulator, ΔE is the CT gap Δ and *U* is the Coulomb interaction, the ground state energy will be

$$E_0(AF) \approx 2t_0^2/\Delta\,, \tag{2.14}$$

and

$$E_0(F) \approx \frac{2t_0^2}{\Delta}(1 + \frac{t_0^2}{\Delta} + \frac{t_0^2}{\Delta U})\,, \tag{2.15}$$

Then, the total antiferromagnetic energy will be

$$J \approx \frac{2t_0^4}{\Delta^2}(1/U + 1/\Delta)\,, \tag{2.16}$$

Based on above calculation, the magnetic ground state of the major transition metals with the octahedral structures could be listed by the Goodenough-Kanamori rule. For example, Table 2.4 shows the interaction between cations in octahedral sites with 180°.

Table 2.3 180° Interaction between Cations in Octahedral Sites.

number of d electrons	Examples	Bonds and Mechanism	Superexchange
d^5 - d^5	Mn^{2+} - Mn^{2+} Fe^{3+} - Fe^{3+}	σ and π	AFM
d^5 - d^3	Fe^{3+} - Cr^{3+} Fe^{3+} - Fe^{5+}	σ and π	FM

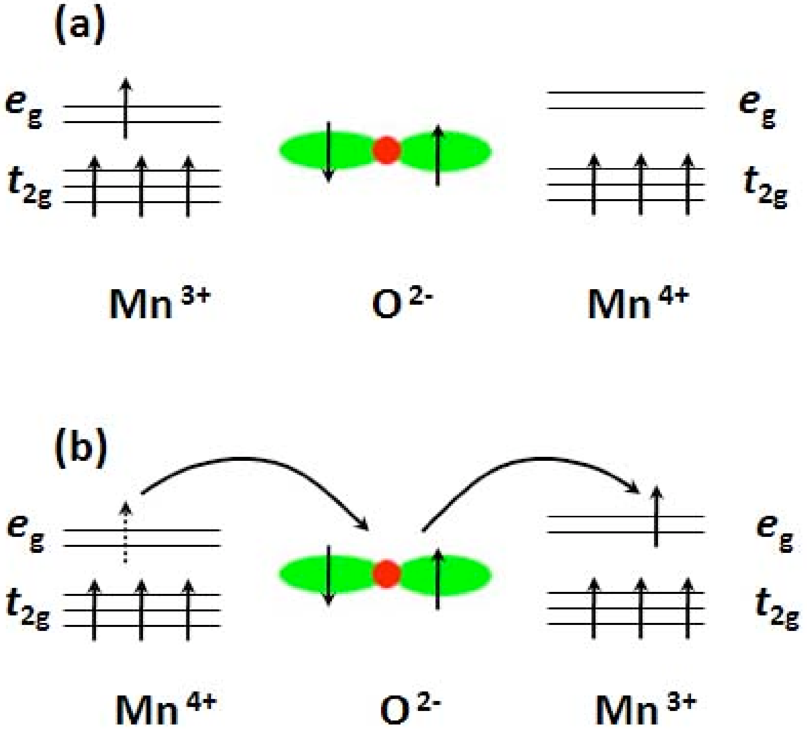

Figure 2.14 (a) and (b) are the processing of the double exchange mechanism for Mn ions with different valence (Mn^{3+} and Mn^{4+}).

2.3.2.3 Double Exchange

Another common magnetic coupling interaction that can occur in the mixed valent materials is double exchange (DE), which was first studied by C. Zener in 1951 [43] and usually occurs in Verwey system above T_V in metallic state. Compared to superexchange coupling, this interaction mechanism proposes a relative easy way by which an electron may be exchanged between two metal ions: in SE, the electrons do not actually move between the two metal positive ions as it is a virtual process; in DE, the conduction electrons in mixed valent state jump between the two positive ions via the intermediate ligand and it is a real process. Therefore, a material with the DE coupling requires that the system display some metallic conductivity behavior. DE was first introduced to describe manganites, Fig. 2.14 is one possibility of the figures of the DE in $La_{1-x}A_xMnO_3$ (A: Ca, Sr, or Ba) [43]: the single e_g electron of Mn^{3+} can hop to the unoccupied e_g orbitals of Mn^{4+} through an intervening of O^{2-} anion.

From Fig. 2.14, we could observe that double exchange is always ferromagnetic and requires Hund's coupling to local spin states. The spin directions of the binding electrons do not change between the hopping and accepting ions, so the kinetic energy expended on the whole processing will be reduced and the electron will move from one species to another more easily. The ground state will favor the ferromagnetic alignment between the neighboring ions.

Since both superexchange and double-exchange interaction can drive ferromagnetism and the resistivity sometimes is not very sensitive especially in powder sample, it is very hard to difference them intuitively. Experimentally, a popular method to difference those exchange is based on the valences of metal ions: in DE, ions are same on average; in SE, they are not same [43, 44].

2.3.2.4 Superexchange in metal center domain wall of $La_{1/3}Sr_{2/3}FeO_3$

From the previous review on the concepts and rules related to the magnetic energy, the contribution of the magnetic energy of $La_{1/3}Sr_{2/3}FeO_3$ to the CO ground state will be analyzed in this section.

Since the parent compound, *R*FO, is a CT insulator and the G-type AFM is driven by SE, the doped holes will be shared between Fe and O ions as Sr^{2+} substituting La^{3+}. Based on the position of the doped-hole in the CO states, there are two kinds of domain walls (DWs) separating the AF domains: the metal-centered domain wall (MCDW) and oxygen-centered domain wall (OCDW) [45]. And the different CO structures are possible depending on the relative strength of F and AF magnetic interactions and Coulomb interactions.

In 1998, T. Mizokawa and A. Fujimori examined the CO transition in LSFO in detail. They first excluded the long range Coulomb interaction contribution to the CO ground state in LSFO. Compared to the calculation of local-spin-density approximation (LSDA) + U in Fe_3O_4, where the intersite Coulomb interaction is well screened to $\sim 0.2\ eV$ [46], the intersite Coulomb interaction in LSFO is expected to be more thoroughly screened due to the longer metal-metal distance than in the spinel-type structure and the small CT gap of LSFO. Then, the electron-lattice coupling term was excluded due to lack of a detectable lattice distortion in the CO state [47].

Therefore, only the effect of magnetism on CO via the superexchange interaction is discussed in the

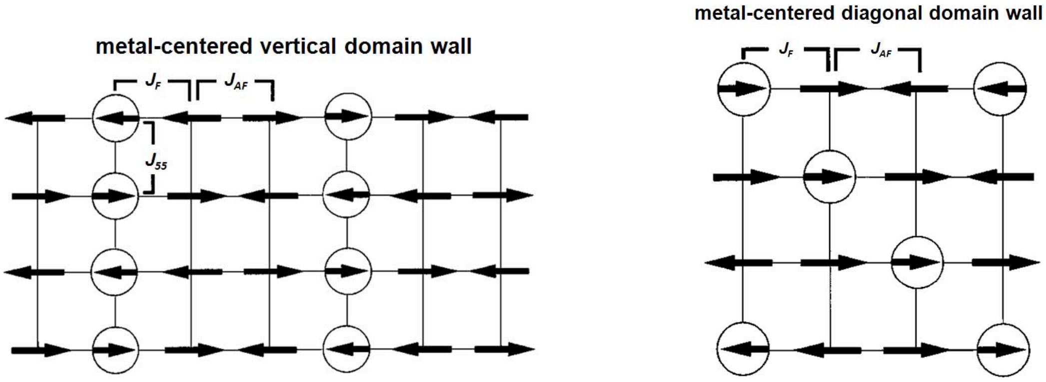

Figure 2.15 MCDW along the (1, 0) and (1, 1, 1) directions for the F coupling between the domain edge and the DW. The circle is the location of hole, and the arrows are the spins of Fe ions: the spin of Fe^{5+} is the short arrow and the spin of Fe^{3+} is the long one. The two neighboring domains are in phase [47].

doped perovskite-type Fe oxides. The two possible charge and magnetic structures for the MCDW and OCDW case in 2D and 3D are shown in Fig. 2.15 and Fig. 2.16, respectively. The magnitudes and the directions of the spins are expressed by the size and direction of the arrows and circle shows the hole position.

For the case of the nearest neighbor-exchange interactions in Fig. 2.15, if the MCDW is along the [1 0 0] direction, there are J_F between Fe^{3+} (long arrows) and Fe^{5+} (short arrows), J_{AF} between Fe^{3+} and Fe^{3+}, and J_{55} between Fe^{5+} and Fe^{5+}. In 3D system: For Fe^{5+}, there are 4 J_{55} and 2 J_F between the nearest neighbors; For Fe^{3+}, there are 5 J_{AF} and 2 J_F between the nearest neighbors. Since there are one Fe^{5+} ion and two Fe^{3+} ions in each magnetic unit cell, the total magnetic energy will be -[10J_{AF} + 4J_F + 4J_{55}]/18 ($E_{tot} = \sum_{i,j} J_{i,j}$). If the MCDW is along the [1 1 1] direction, the situation is simple due to the vanishing of J_{55}: there is no nearest neighbors between Fe^{5+} and Fe^{5+}. With the assumption of nearest neighbor, each Fe^{3+} has 3 J_F and 3 J_{AF}, and each Fe^{5+} has 6 J_F, thus the magnetic energy will be -[6J_{AF} + 12J_F]/18. Hence, the other magnetic energies in different CO directions and DWs are listed in Table 2.5 and Table 2.6 with the same method.

In OCDW, the SE coupling in the DW (J_{55}) does not exist, which simplifies the expression of the magnetic energy. Compared to the magnetic energy of MCDW in the same direction, it is found that the magnetic exchange energies depend on the center of DW. From the M$\ddot{o}$ssbauer measurement, the magnetic moments and actual charges are around 4.1μ_B and +3.2 for ‘Fe^{3+}’ ions and 2.1μ_B and +4.2

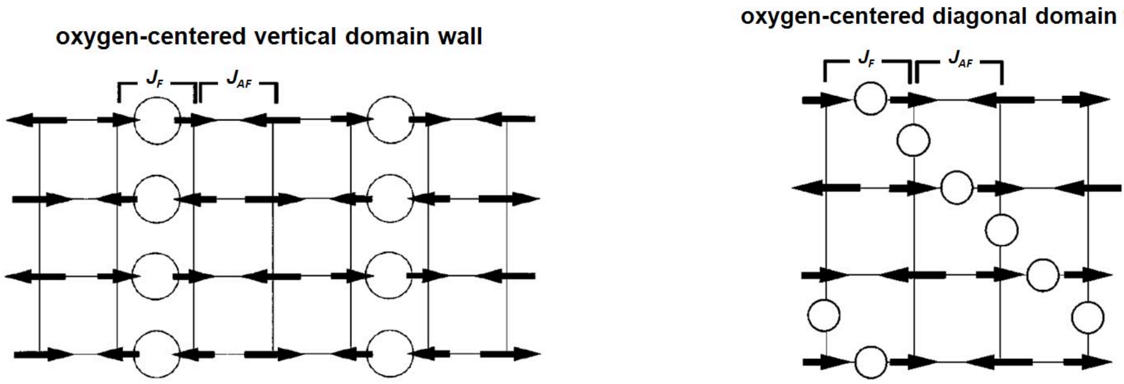

Figure 2.16 OCDW along the (1, 0) and (1, 1, 1) directions. The neighboring domains are in antiphase [47].

for ‘Fe^{5+}’ ions, so it is expected that the maximum of the hole density modulation coincides with a minimum of spin density wave, which is consistent with the MCDW.

Table 2.4 Magnetic energies per metal-oxygen-metal bond of the CO states with the MCDW for the hole concentration x = 1/3.

2D		3D	
(1, 0)	-[6J_{AF} + 4J_F + 2J_{55}]/12	(1, 0, 0)	-[10J_{AF} + 4J_F + 4J_{55}]/18
(1, 1)	-[4J_{AF} + 8J_F]/12	(1, 1, 0)	-[8J_{AF} + 8J_F + 2J_{55}]/18
		(1, 1, 1)	-[6J_{AF} + 12J_F]/18

Based on Table 2.6, the direction of the ordering domain in 3D is decided by the total contribution of the magnetic exchange energies, J_{AF}, J_F, and J_{55}, Fig. 2.17. J_{55} need to be explained before the magnetic energies on different directions are compared. As the former introduction of magnetic interaction, J_{55} should be much less than J_{AF} since it originates from the t_{2g} π-bond SE. It is conservative to assume that J_{55} = J_{AF}, then CO will be stable along [1 1 1] direction when $|$ J_F / J_{AF} $|$ > 1; If J_{55} = 0, CO remains along the [1 1 1] direction unless $|$ J_F / J_{AF} $|$ < 1/2.

Table 2.5 Magnetic energies per metal-oxygen-metal bond of the CO states with the OCDW for the hole concentration x = 1/3.

2D		3D	
(1, 0)	-[10J_{AF} + 2J_F]/12	(1, 0, 0)	-[16J_{AF} + 2J_F]/18
(1, 1)	-[8J_{AF} + 4J_F]/12	(1, 1, 0)	-[14J_{AF} + 4J_F]/18
		(1, 1, 1)	-[12J_{AF} + 6J_F]/18

Actually, this hypothesis of the magnetic energy to CO can be tested by INS. From the powder average magnetic spectrum, the relative magnetic exchange energies is measured. Consequently, the ratio of the magnetic energy can be determined and the direction of CO is decided: if it agrees with the experimental data, which means that CO is on [1 1 1] direction for LSFO, the magnetic energy can stabilize the CO alone; if it does not fit the experimental result, which means that CO is not on [1 1 1] direction for LSFO, there is another contribution to CO besides the magnetic energy.

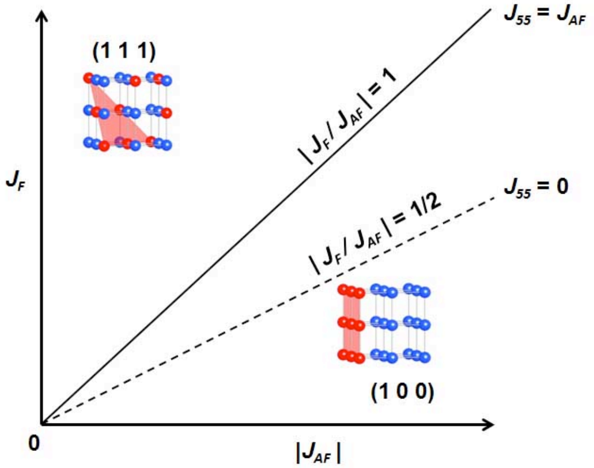

Figure 2.17 Phase diagram of LSFO as a function of the magnetic exchange energies. The phase boundary moves upward as J_{55} increases.

2.4 Electron-lattice Interaction

The Coulomb interaction and the magnetic energy on the CO ground state have been discussed, we now turn to the electron-lattice interaction. Usually, CO accompanies the changing of the dynamic and static displacements of the charges to lower the system energy, thus an interaction between charge and phonon/lattice can be involved in the stabilization of the CO state. In fact, the influence of the electron-phonon/electron-lattice interaction on CO has been observed in many cases: In $\mathrm{La}_{2-x}\mathrm{Sr}_x\mathrm{CuO}_4$, the INS measurement presented an abrupt development of new oxygen lattice vibrations with CO, and a direct correlation between these lattice modes and the electronic susceptibility inferred the mixing of such modes and charge fluctuations [48]; In $\mathrm{La}_{2-x}\mathrm{Sr}_x\mathrm{NiO}_4$, the band of phonons corresponding to the in-plane oxygen vibrations (80-90 *meV*) were observed to split into two subbands centered at 75 and 85 *meV* by the INS measurement as the charges were ordered, and these changes were associated with the coupling of oxygen vibrations to doped holes, which resided in the NiO_2 planes and were a signature of strong electron-lattice coupling [49].

For a crystal, the general hamiltonian is

$$\hat{H} = \hat{T}_e + \hat{V}_{e-e} + \hat{T}_n + \hat{V}_{n-n} + \hat{V}_{e-n}\,, \tag{2.17}$$

where $\hat{T}_e$ is the kinetic energy of the electrons, $\hat{V}_{e-e}$ is the electron-electron interaction, $\hat{T}_n$ is the kinetic energy of the nuclei, $\hat{V}_n$ is the Coulombic repulsion energy of the nuclei, and $\hat{V}_{e-n}$ is the Coulombic attraction between electrons and nuclei.

With the Born-Oppenheimer approximation, the total wavefunction, Ψ, is broken into the electronic and nuclear components, so a series expansion of $\hat{H}$ in Eq. (2.17) is performed and the perturbation theory will be applied. As we solve this quantum problem, the eigenstate is normally separated into radial and angular parts,

$$\Psi(\mathbf{r}, \mathbf{R}) = \sum_k \chi_k(\mathbf{R})\psi_k(\mathbf{r}, \mathbf{R})\,, \tag{2.18}$$

where **r** and **R** are the electronic and nuclear coordinates of atom *k*.

And the electron-phonon/lattice interaction occurs through the action of $\hat{T}_n$ on ψ_k(**r**, **R**). Therefore, the material structure and composition are the two dominant factors contributing to electron-phonon interaction [50, 51].

However, the electron-phonon/electron-lattice is complicated and many details about these lattice anomalies are still unclear. It is difficult to ascertain whether the lattice is intimately involved in the CO, or merely passively responding in a general case. Therefore, I will introduce the concept of electron-phonon/electron-lattice interaction with some simpler cases, such as Kohn anomaly, magnetite, and manganites, by analyzing the phonon/lattice spectrum in this section.

2.4.1 Electron-phonon interactions on the CO

2.4.1.1 Kohn Anomaly

In 1959, W. Kohn studied the phonon spectrum of a metal and proposed that there is a discontinuity in the derivative of the dispersion at $q = 2k_F$ due to the abrupt change in the screening of lattice vibrations by conduction electrons. This singularity is called Kohn anomaly and is a consequence of the electron-phonon interaction [52].

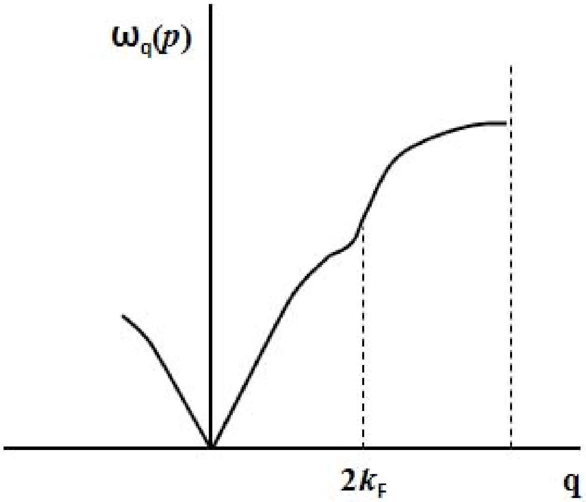

Figure 2.18 The kohn anomaly in the phonon dispersion curve when the phonon wavenumber q equals the diameter of the Fermi surface [55].

Kohn anomalies arise from a homogeneous electron gas and are obtained in the real part of the dielectric function by the Lindhard model: a logarithmic term yelds a singularity for $\mathbf{q} = 2\ \mathbf{k}_F$, where $\mathbf{k}_F$ is the Fermi wavevector. Although this singularity is 'small' in reciprocal space, a strong oscillation can be observed in real space by Fourier transform. The structure of the singularity is consistent with the Fermi surface geometry and $\omega(\mathbf{q})$ can be measured by inelastic neutron scattering [53, 54, 55].

2.4.1.2 Magnetite

Magnetite is the prototypical example of Verwey system and has been discovered nearly 80 years, however, the driving forces behind the Verwey transition are still not completely understood as discussed in chapter 1 [56, 57]. Recent studies demonstrated that pure electrostatics cannot be the sole factor responsible for the observed charge-ordered state below the Verwey transition [58, 59]. As the CO is a cooperative phenomenon including an interplay between lattice, charge, and orbital degrees of freedom, the electron-lattice interaction to the CO state of magnetite has received considerable attention [60].

In 2007, P. Piekarz *et. al.* applied the *GGA + U* calculations with realistic parameters for Fe ions to simulate the phonon energy spectrum, and the agreement is qualitative with the experimental data obtained by Raman and infrared spectroscopy. In order to test the contribution of the electron interaction effects, it was neglected and the phonon spectra are even qualitatively different from the observed ones

[60]. Thus, this *ab initio* calculation demonstrate the involvement of lattice distortions and electron-phonon interaction in the CO state.

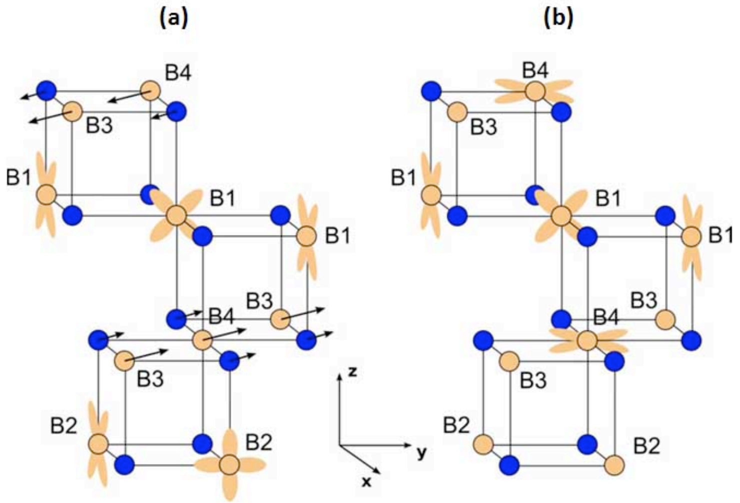

Figure 2.19 Orbital order in the t_{2g} states of Fe(B) ions in magnetite for (a) the $Fd3m$ cubic structure distorted by the X_3 phonon, and (b) the structure of $P2/c$ symmetry. Fe and O ions are presented by orange and blue balls. Fe(B) ions have six O neighbors, while each O anion has three Fe(B) and one Fe(A) neighbor. The arrows represent the atomic displacements in the X_3 mode. [59].

Fig. 2.19 shows one possible CO model based on the *LSDA*+U-like method. The four Fe(B) sites split into two subclasses due to the lattice distortion in the X_3 mode at the high and low temperatures. Fig. 2.19(a) shows the high temperature cubic structure, electrons occupy the $B1$ and $B2$ Fe ions and are empty at the $B3$ and $B4$ Fe ions for t_{2g} band. While Fig. 2.19(b) shows the low temperature monoclinic structure, the electrons density increases for $B1$ and $B2$ Fe ions and reduced for $B3$ and $B4$ Fe ions which is responsible for the charge disproportionation and leads to the occupied states at the $B1$ and $B4$ Fe ions and empty states at the $B2$ and $B3$ Fe ions. Since the average Fe-O distances for the bonds to the $B2$- and $B3$-sites are significantly smaller than those for the $B1$- and $B4$-sites, the CO can change from the promoted by the X_3 mode itself.

Furthermore, this X_3 mode also stabilizes the orbital ordering(OO) in the t_{2g} states. At the high temperature, if the mode is considered to be limited to single Fe-O planes: Fe(B) ions move along with O anions in one plane, while atoms in neighboring planes do not move at all. As indicated in the Fig. 2.19(a), the electrons occupy orthogonal d_{yz} and d_{xz} orbitals. For the low temperature one, Fig. 2.19(b), the alternating OO is formed by the occupied states on $B1$ and $B4$ ions with the orthogonal orbitals on the NN. Thus, the orbitals of $\frac{1}{2}(d_{xz} \pm d_{yz})$ and $d_{x^2-y^2}$ are preferred. [59]

2.4.1.3 $La_{1.2}Sr_{1.8}Mn_2O_7$

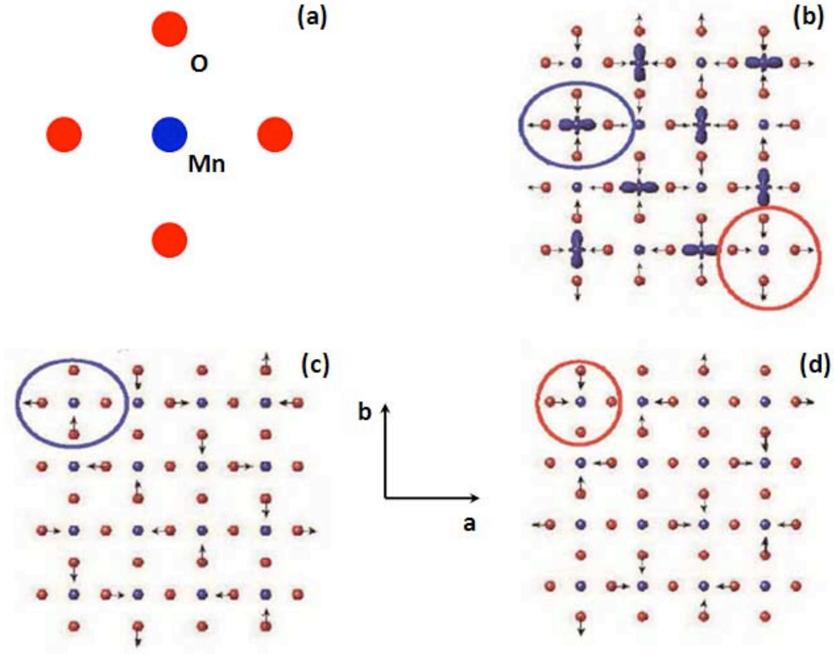

Figure 2.20 Correspondence between CE-order and phonon vibration patterns. (a) Schematic of homogeneus electron in *ab* plane with Mn (blue) and O (red). (b) Schematic of the displacements of oxygens from the ideal unordered structure in long-range CE ordered $La_{1.2}Sr_{1.8}Mn_2O_7$. Drawn e_g orbitals indicate the Mn^{3+} ions. (c), (d) Eigenvectors of the transverse (c) and longitudinal (d) bond-stretching phonons with $\mathbf{q}$ = (0.25, 0.25, 0). Small Mn displacements are not shown. The colorful lines indicate the partial matching of oxygen displacements of the CE order and of the phonon eigenvectors [61].

Based on the homogeneus electron gas approximation, the electron-phonon interaction is observed by Kohn anomaly. However, the electron-phonon interaction still can be witnessed in compounds with the inhomogeneus electron distribution, such as the Jahn-Teller (JT) effect in the distorted TMOs. It was reported in $La_{1.2}Sr_{1.8}Mn_2O_7$ that the polarons (charge carriers which can distort the atomic lattice and trap themselves) were observed in the metallic phase by inelastic neutron scattering and may originate from a competing insulating charge-ordered phase [61].

The ideal environment of Mn ions in MnO_2 layers is shown in Fig. 2.20(a): there are 4 O^{2-} anions homogeneously distributed around Mn. However, when the insulator is the charge and orbitally ordered (CE-type), the e_g charge is localized on alternate Mn sites where the first order phase transition differentiate Mn^{3+} and Mn^{4+} sites, Fig. 2.20(b) [62, 63]. Furthermore, the short range CE fluctuations should couple strongly to both the longitudinal and transverse phonons and can be figured out in the marked zones: the lattice deformation around the Mn^{3+} site corresponds to a part of the eigenvector of the transverse phonon, whereas the deformation around the Mn^{4+} site corresponds to a part of the eigenvector of the longitudinal one, Fig. 2.20(c) and (d).

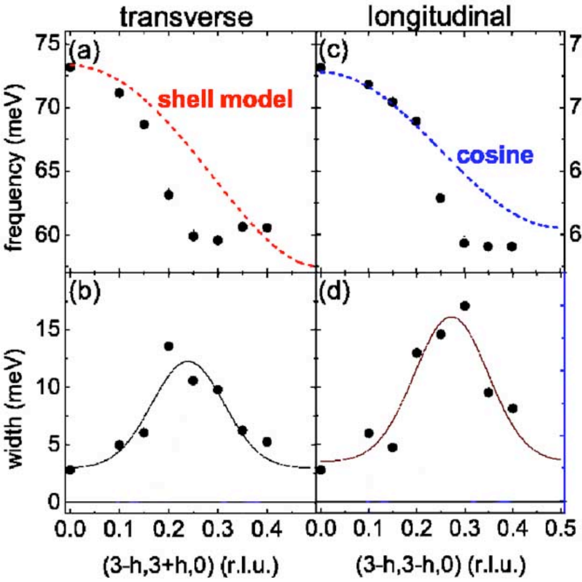

Figure 2.21 Dispersions and linewidths of transverse and longitudinal bond-stretching phonons in [1, 1, 0] direction of $\mathrm{La}_{1.2}\mathrm{Sr}_{1.8}\mathrm{Mn}_2\mathrm{O}_7$. (a), (c) Data points represent measured phonon energies; red dashed line is the dispersion calculated by the shell model; blue dashed line is a cosine function. (b), (d) Data points are phonon FWHM after correction for the experimental resolution [61].

Measuring the directions, $\mathbf{q}$ = (-h, -h, 0) and (-h, +h, 0) at 10 K, the longitudinal and transverse branches were obtained. Fig. 2.21 presents the dispersions and linewidths of transverse and longitudinal bond-stretching phonons in [1, 1, 0] direction. It indicates the strong electron-phonon coupling deep in the metallic state due to the sharp dipping and maximum linewidth near $\mathbf{q}_{CE}$ (1/2, 1/2, 0) of both branches.

2.4.1.4 $\mathbf{La_{1/3}Sr_{2/3}FeO_3}$

Since there is no detectable lattice distortion below T_{CO} [16, 45], the electron-lattice coupling is not expected to be as important as the superexchange coupling in the CO state. However, there is still an argument on the CO stabilization by the electron-lattice interaction based on the study of the longitudinal ultrasonic velocity (*V*) [64], and the scenario is supported by two theoretical and experimental results: i) *V* is softening above T_{CO} and hardening below T_{CO}, which is comparable to the calculation of small *JT* polarons in manganites [65]; ii) above T_{CO}, the experimental data of the longitudinal modulus *C*(*T*) agrees with the theoretical calculation, which is modeled by the dynamic *JT* effect of Fe ion. The details are presented in the followings.

i) JT polarons

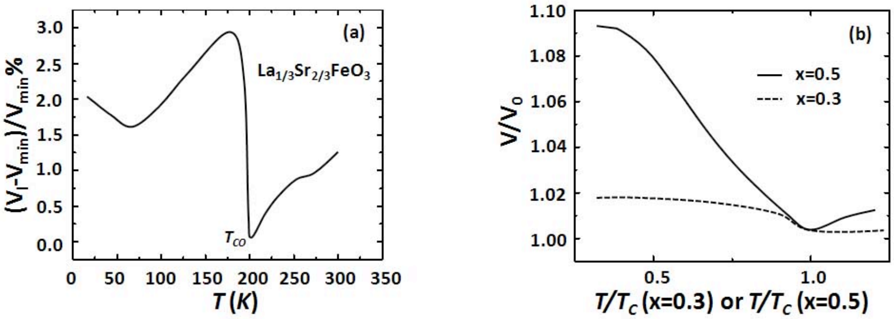

Figure 2.22 (a) The temperature dependence of longitudinal ultrasonic velocity for $La_{1/3}Sr_{2/3}FeO_3$ [64]; (b) The behaviors of the renormalized sound velocity in the metallic (x = 0.3, dashed line) and in the CO of $La_{1-x}Ca_xMnO_3$(x = 0.5, solid line) phase [65].

In 1998, B. I. Min *et al.* theoretically calculated the renormalized sound velocity in metallic state and CO state, which include the electron-phonon coupling constant, Fig. 2.22(b). The Hamiltonians in both cases incorporating the electron-acoustic phonon coupling will be expressed as [66, 67, 68],

In metallic phase

$$H_{el-ph} = \sum_{iq} c_i^\dagger c_i e^{i\mathbf{q}\cdot\mathbf{R}_i} D_q (b_q + b_{-q}^\dagger)\,, \tag{2.19}$$

where n_i = $c_i^\dagger$ (c_i) is the local electron density, $e^{i\mathbf{q}\cdot\mathbf{R}_i}$ $\mathbf{D}_q$ is the dynamic matrix at site $\mathbf{R}_i$, and $b_{-q}^\dagger(b_q)$ are annihilation (creation) operators for phonons.

In CO phase

The Hamiltonian of electron-phonon interaction is simplified,

$$H_{el-ph} = \frac{1}{\sqrt{N}} \sum_i \sum_k \omega_0(k) g(k) \sigma_i Q_k e^{i\mathbf{q}\cdot\mathbf{R}_i}\,, \tag{2.20}$$

where $\omega_0(c)$ = v_0 k (v_0 is the bare longitudinal sound velocity), $g(k)/\sqrt{N}$ is the electron-phonon coupling constant for k, σ_i is related to the local electron density, and Q_k $e^{i\mathbf{q}\cdot\mathbf{R}_i}$ is related to the dynamic matrix at site $\mathbf{R}_i$.

Since the temperature dependence of the longitudinal ultrasonic velocity for LSFO is qualitatively similar to the case of $La_{1-x}Ca_xMnO_3$, which is interpreted by the *JT* effect of Mn^{3+}, it is possible that the small *JT* polarons with strong electron-phonon coupling play a role in CO inLSFO.

ii) JT theory

According to the *JT* theory, the coupling between the *JT* ions and the lattice distortion can be described by the mean field approximation, and the relationship between the longitudinal modulus $C(T)$ ($T > T_{CO}$) can be expressed as [69],

$$C(T) = C_0(T - T_C^0)/(T - \theta)\,, \tag{2.21}$$

where $C(T) = \rho\ V^2$ [70]. ρ is the mass density, C_0 is the elastic modulus in the absence of *JT* coupling, and the characteristic temperature of T_C^0 and θ can be determined by the ultrasonic measurements of the elastic modulus softening.

Fig. 2.23 shows the temperature dependence of the experimental (dash line) and theoretical (solid line) $C(T)$ for $La_{1/3}Sr_{2/3}FeO_3$ above T_{CO}, the good agreement suggests the existence of the electron-phonon coupling via the JT effect.

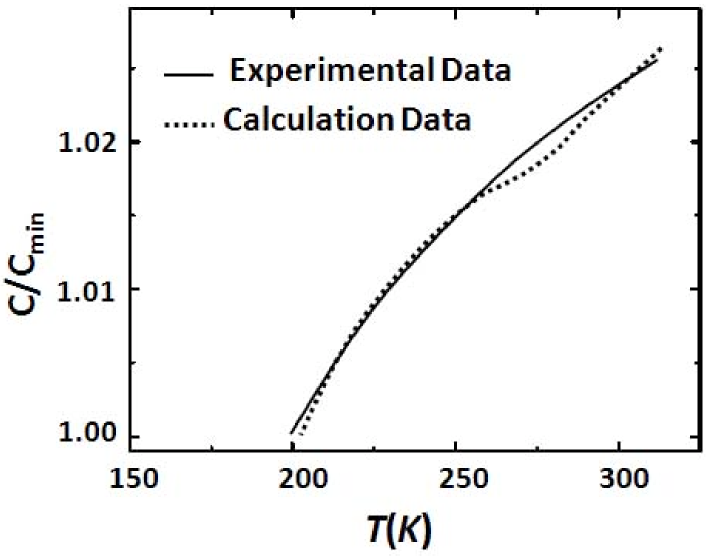

Figure 2.23 The temperature dependence of the $C(T)$ for $La_{1/3}Sr_{2/3}FeO_3$ above T_{CO} (dash line is experimental data, solid line is the results calculated using Eq. (21)) [65].

This hypothesis of the electron-phonon/electron-lattice to CO can be tested by inelastic neutron scattering. Based on the analyzing of the powder average phonon spectrum by the phonon models, such as rigid ionic model, shell model, and so on, the spring constants, effective valence and radii are simulated. Then, the coupling between the electron and phonon/lattice can be inferred. The details of measurement of phonons and their analysis will be discussed in Chapter 7.

Bibliography

[1] S. E. Dann, D. B. Currie, M. T. Weller, M. F. Thomas and A. D. Al-Rawwas, Journal of Solid State Chemistry 109 (1994) 134

[2] R. D. Shannon, and C. T. Prewitt, Acta Crystallographic B 26 (1970) 1046

[3] Huan Zhang, Na Li, Keyan Li and Dongfeng Xue, Acta Crystallographica B 63 (2007) 812

[4] *Inorganic Crystal Structure Database*(ICSD) Version 1.3.3 (2004)

[5] Muller and Roy *The Major Ternary Structural Families*, New York, Springer-Verlag, 1974

[6] H. Mizoguchi, P. M. Woodward, S. H. Byeon and J. B. Parise, Journal of the American Chemical Society 126 (2004) 3175

[7] K. Ito, K. Tezuka, and Y. Hinatsu, Journal of Solid State Chemistry 157 (2001) 173

[8] A. A. Belik, S. Y. Stefanovich, B. I. Lazoryak and E. Takayama-Muromachi, Chemistry of Materials 18 (2006) 1964

[9] M. W. Lufaso and P. M. Woodward, Acta Crystallographica B 57 (2001) 725

[10] P. D. Battle, T. C. Gibb, and P. Lightfoot, Journal of Solid State Chemistry 84 (1990) 271

[11] H. Falcón, A. E. Goeta, G. Punte, and R. E. Carbonio, Journal of solid state chemistry 133 (1997) 379

[12] S. K. Pandey, R. Bindu, P. Bhatt, S. M. Chaudhari, and A. V. Pimpale, Physica B 365 (2005) 47

[13] W. Slawinski, R. Przenioslo, I. Sosnowska, and E. Suard, Journal of Physics: Condensed Matter 17 (2005) 4605

[14] E. N. Maslen, V. A. Streltsov, and N. Ishizawa, Acta Crystallographica B 52 (1996) 406

[15] D. Du Boulay, E. N. Maslen, and V. A. Streltsov, Acta Crystallographica B 51 (1995) 921

[16] S. K. Park, T. Ishikawa, Y. Tokura, J. Q. Li, and Y. Matsui, Physics Review B 60 (1999) 10788

[17] H. Bethe, Annals of Physics (Leipzig) 87 (1928) 55.

[18] F. Bloch, Zeitschrift für Physik 57 (1929) 545.

[19] A. Sommerfeld, Zeitschrift für Physik 47 (1928) 1.

[20] J. H. de Boer, and E. J. W. Verway, Proceedings Physical Society London, Series A 49 (1937) 59.

[21] R. Peierls, Proceedings Physical Society London, Series A 49 (1937) 72.

[22] N. F. Mott, Proceedings Physical Society London, Series A 49 (1937) 72.

[23] J. Hubbard, Proceedings of the Royal Society London, Series A 276 (1963) 238

[24] J. Hubbard, Proceedings of the Royal Society London, Series A 277 (1964) 237.

[25] M. Imada, A. Fujimori, and Y. Tokura, Reviews of Modern Physics, 70 (1998) 1039

[26] J. Zaanen, G. A. Sawatzky, and J. W. Allen, Physics Review Letters 55 (1985) 418

[27] C. N. R. Rao, Chemical Communications 19 (1996) 2217

[28] T. Arima, Y. Tokura, and S. Uchida, Physics Review B 48 (1993) 6597

[29] J. Mizusaki, T. Sasamoto, W. R. Cannon and H. K. Bowen, Journal of the American Ceramic Society 66 (1983) 247

[30] G. Chern, W. K. Hsieh, M. F. Tai, and K. S. Hsung, Physics Review B 58 (1998) 1252

[31] E. V. Tsipis, M. V. Patrakeev, V. V. Khartona, A. A. Yaremchenko, G. C. Mather, A. L. Shaula, I. A. Leonidov, V. L. Kozhevnikov, and J.R. Frade, Solid State Sciences 7 (2005) 355

[32] E. Wigner, Physics Review 46 (1934) 1002

[33] E. Wigner, Transactions of the Faraday Society 34 (1938) 678

[34] D. P. Young, D. Hall, M. E. Torelli, Z. Fisk, J. L. Sarrao, J. D. Thompson, H. R. Ott, S. B. Oseroff, R. G. Goodrich and R. Zysler, Nature 397 (1998) 412

[35] E. Madelung Phys. Zs. XIX (1918) 524

[36] J. H. Van Vleck, Physics Review 41 (1932) 208

[37] S. S. Zumdahl, *Chemical Principles Fifth Edition* Boston: Houghton Mifflin Company, 2005

[38] D. F. Shriver and P. W. Atkins, *Inorganic Chemistry 3rd edition*, Oxford University Press, 2001

[39] H. L. Schläfer and G. Gliemann, *Basic Principles of Ligand Field Theory* Wiley Interscience: New York, 1969

[40] P. W. Anderson, Physics Review 79 (1950) 350

[41] J. B. Goodenough, Physics Review 100 (1955) 564

[42] J. Kanamori, Journal of Physics and Chemistry of Solids 10 (1959) 87

[43] C. Zener, Physics Review 82 (1951) 403

[44] P. -G. de Gennes, Physics Review 118 (1959) 141

[45] J. Q. Li, Y. Matsui, S. K. Park, and Y. Tokura, Physical Review Letters 79 (1997) 297

[46] V. I. Anisimov, I. S. Elfimov, N. Hamada, and K. Terakura, Physics Review B 54 (1996) 4387

[47] T. Mizokawa and A. Fujimori, Physics Review Letter 80 (1998) 1320

[48] R. J. McQueeney, J. L. Sarrao, P. G. Pagliuso, P.W. Stephens, and R. Osborn, Physics Review Letter 87 (2001) 077001

[49] R. J. McQueeney, J. L. Sarrao, and R. Osborn, Physics Review B 60 (1999) 80

[50] J. M. Ziman, *Electrons and phonons*, Oxford Univ. Press, Oxford, (1960)

[51] G. Grimvall, *The electron-phonon interaction in metals*, North-Holland, Amsterdam, (1981)

[52] W. Kohn, Physics Review Letter 2 (1959) 393

[53] R. M. Martin, *Electronic Structure, Basic Theory and Practical Methods*, Cambridge University Press, 2004

[54] N. W. Ashcroft, and N. D. Mermin, *Solid State Physics*, Thomson Learning, Inc., 1976

[55] P. L. Taylor, and O. Heinonen, *A Quantum Approach to Condensed Matter Physics*, Cambridge University Press, 2002

[56] F. Walz, Journal of Physics: Condensed Matter 147 (2002) R285

[57] J. García and G. Subías, Journal of Physics: Condensed Matter 16 (2004) R145

[58] P. Piekarz, K. Parlinski, and A. M. Oleś, Physics Review Letter 97 (2006) 156402

[59] P. Piekarz, Krzysztof Parlinski, and Andrzej M. Oleś, Physics Review B 76 (2007) 165124

[60] K. Parlinski, Z.-Q. Li, and Y. Kawazoe, Physics Review Letter 78 (1997) 4063

[61] F. Weber, N. Aliouane, H. Zheng, J. F. Mitchell, D. N. Argyriou, and D. Reznik, arXiv:1001 4636 (2010)

[62] P. G. Radaelli, D. E. Cox, M. Marezio, and S-W. Cheong, Physics Review B 55 (1997) 3015

[63] D. N. Argyriou, H. N. Bordallo, B. J. Campbell, A. K. Cheetham, D. E. Cox, J. S. Gardner, K. Hanif, A. dos Santos, and G. F. Strouse, Physics Review B 61 (2000) 15269

[64] Hui Kong, and Changfei Zhu, Europhysics Letters 86 (2009) 54001

[65] B. I. Min, J. D. Lee and S. J. Youn, Journal of Magnetism and Magnetic Materials 177 (1998) 881

[66] Y. Motome, and M. Imada, Physics Review B 60 (1999) 7921

[67] M. Capone, C. Castellani, and M. Grilli, arXiv:1003.1042v1 (2010)

[68] Xian-Sheng Cao, and Chang-Le Chen, Physica B: Condensed Matter 404 (2009) 65

[69] R. L. Melcher, *Physical Acoustics*, Vol. 12, Academic Press, New York, 1970

[70] M. Cankurtaran, G. A. Saunders, K. C. Goretta, and R. B. Poeppel, Physics Review B 46 (1992) 1157

CHAPTER 3. Neutron Scattering

3.1 Introduction

The neutron scattering technique is a valuable tool for investigating many features of materials, molecules, and condensed matter. Due to the specific properties of neutron, the static and dynamic properties of a sample can be measured. i) based on the mass of neutron, the de Broglie wavelength of a thermal neutron can be calculated, and it is on the same order of interatomic distances in solid and liquids; ii) the neutron is charge neutral, which has the advantage of deep penetration and interaction with nuclei rather than electronic cloud; iii) the neutron has a magnetic moment, which means that it can interact with magnetic atoms, thus providing information about magnetic structure; iv) the energy and momenta of thermal neutrons match well those of a range of thermal excitations, such as phonons and magnons, thus the dynamics of materials can be studied [1].

In this chapter, I will review some basic concepts related to neutron scattering at first; then, I will talk about the elastic and inelastic neutron scattering and introduce the instrumentation used in this research; at last, the data analysis of the inelastic neutron scattering in this thesis will be introduced [1, 2, 3].

3.2 Scattering of neutrons from system

3.2.1 Elastic and inelastic scattering

A general geometry for scattering experiment is shown in Fig. 3.1, where an incident neutron beam with the wave vector $\vec{k}$ is scattered by the sample and the final neutron beam with the wave vector $\vec{k}'$ is counted by the detectors. The direction of the scattered neutrons is recorded by θ and ϕ. $d\Omega$ is the relative solid angle. r is the distance from the target to the detector and dS is the differential area of the scattered neutrons. The incident and final neutron energies are $E = \hbar^2| \vec{k} |^2/2m$ and $E' = \hbar^2| \vec{k}' |^2/2m$, where m is the mass of the neutron, and the energy transferred to the sample is $\Delta E = E - E' = \hbar^2(| \vec{k} |^2 - | \vec{k}' |^2)/2m$;

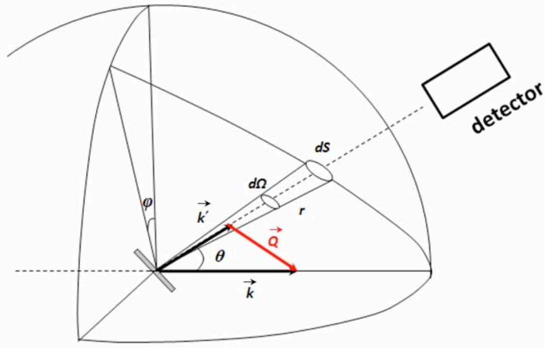

Figure 3.1 Neutron Scattering geometry.

The incident and final neutron momenta are $\vec{p} = \hbar\vec{k}$ and $\vec{p'} = \hbar\vec{k'}$, and the momentum transferred to the sample is $\hbar\vec{Q} = \Delta\vec{p} = \vec{p} - \vec{p'} = \hbar(\vec{k} - \vec{k'})$. If the incident energy equals the final energy, which means that $\Delta E = 0$ *meV*, the scattering is elastic scattering; If the incident energy does not equal the final energy, $\Delta E \neq 0$ *meV*, the scattering is inelastic scattering.

For a typical powder scattering experiment, neutrons are measured which have scattered through an angle 2θ. The magnitude of the momentum transfer is then given by

$$Q^2 = k^2 + k'^2 - 2kk'cos2\theta \, , \tag{3.1}$$

3.2.2 Scattering Cross Section

The central quantity in a scattering experiment is the cross-section. If the measured neutron is in a given direction as a function of their energy E' and the direction of the scattered neutron are θ, ϕ, which are included in $d\Omega$, the *partial differential cross-section* is defined by

$$\begin{aligned} \frac{d^2\sigma}{d\Omega dE'} = (&number\, of\, neutrons\, scattered\, per\, second\, into \\ &a\, small\, solid\, angle\, d\Omega\, in\, the\, direction\, \theta\, , \phi\, with \\ &final\, energy\, between\, E'\, and\, E' + dE')/(\Phi d\Omega dE') \end{aligned} \quad , \tag{3.2}$$

where Φ is the flux of the incident neutrons.

If we do not consider the energy of the scattered neutrons, but count all neutrons scattered into $d\Omega$. The cross-section will be the *differential cross-section*

$$\frac{d\sigma}{d\Omega} = \begin{matrix}(number\, of\, neutrons\, scattered\, per\, second \\ into\, d\Omega\, in\, the\, direction\, \theta\,,\phi)/(\Phi d\Omega)\end{matrix}\,, \tag{3.3}$$

and the *total scattering cross-section* is

$$\sigma = \; (total\, number\, of\, neutrons\, scattered\, per\, second)/\Phi\,, \tag{3.4}$$

In the following sections, a general case will be analyzed to deduce the cross-section from the initial and final neutron states.

Suppose the initial and final states of the sytem are ($\vec{k}$, λ) and ($\vec{k}'$, λ') respectively, as the neutron traverses the scattering potential *V* in the sample. λ denotes an aggregate quantum number for the state of the sample. In an experiment, we are usually interested in the scattering cross-section corresponding to neutrons being scattered into final states $\vec{k}'$ within a small solid angle $d\Omega$ around the direction $\hat{\Omega}$. Hence, the *differential cross-section* is

$$(\frac{d\sigma}{d\Omega})_{\lambda\rightarrow\lambda'} = \frac{1}{\Phi}\frac{1}{d\Omega}\sum_{k'\, in\, d\Omega} W_{k,\,\lambda\rightarrow k',\,\lambda'}\,, \tag{3.5}$$

where $W_{k,\,\lambda\rightarrow k',\,\lambda'}$ is the number of transitions per second from the initial state to final state. Based on Fermi′s golden rule, we can express it into the terms of the matrix element of the potential, which is the coupling of the initial and final states

$$\sum_{k'\, in\, d\Omega} W_{k,\,\lambda\rightarrow k',\,\lambda'} = \frac{2\pi}{\hbar}\rho_{k'} \mid \langle k'\lambda' \mid V \mid k\lambda\rangle \mid^2\,, \tag{3.6}$$

where $\rho_{k'}$ is the density of final states within $d\Omega$ per unit energy. Working out $\rho_{k'}$ from the energy relation for free final particles $E' = \hbar^2 \mid \vec{k}' \mid ^2/2m$ and using the fact that Φ is proportional to the velocity of incident neutrons ($\vec{k}$),

$$(\frac{d\sigma}{d\Omega})_{\lambda\rightarrow\lambda'} = \frac{k'}{k}(\frac{m}{2\pi\hbar^2})^2 \mid \langle k'\lambda' \mid V \mid k\lambda\rangle \mid^2\,, \tag{3.7}$$

If the final states is within $d\Omega$ and of energy between E' and $E' + dE'$, we also obtain the differential cross-section for scattering of neutrons, by requiring that the energy of the system (neutron + sample) be conserved:

$$(\frac{d^2\sigma}{d\Omega\, dE})_{\lambda\to\lambda'} = \frac{k'}{k}(\frac{m}{2\pi\hbar^2})^2 \mid \langle k'\lambda' \mid V \mid k\lambda\rangle \mid^2 \delta((E_\lambda + E) - (E_{\lambda'} + E'))\,, \tag{3.8}$$

3.3 Nuclear Scattering

Due to the special physical properties of neutron, such as static mass and electroneutrality, the related information on nuclear scattering can be obtained. Since nuclei can occur in different isotopes or nuclear spins, which have different scattering lengths, the scattering is classified into coherent and incoherent processes.

3.3.1 Coherent and Incoherent Scattering

The first step in evaluating the matrix element, $\langle\, k'\ \lambda' \mid V \mid k\ \lambda\,\rangle$, is to integrate with respect to the neutron coordinate, $\mathbf{r}$. For the *l*th nucleus with the position vector, $\mathbf{R}_l$, the potential of the neutron has the form V_j($\mathbf{r}$ - $\mathbf{R}_l$), then the total potential for the scattering system is,

$$V(\mathbf{r}) = \sum_l V_l(\mathbf{r} - \mathbf{R}_l)\,, \tag{3.9}$$

Fermi pseudopotential is usually applied to describe the scattering of a free neutron by a nucleus and the potential is given as a function of radius,

$$V(\mathbf{r}) = \frac{2\pi\hbar^2}{m} b\delta(\mathbf{r})\,, \tag{3.10}$$

where b is the scattering length.

Therefore, the time-dependent partial differential cross-section will be

$$\begin{aligned}\frac{d^2\sigma}{d\Omega dE} = \frac{k'}{k}\frac{1}{2\pi\hbar}\sum_{l,l'} b_l b_{l'} \int_{-\infty}^{\infty} &\langle exp(-i\mathbf{Q}\cdot\mathbf{R}_{l'}(0))exp(i\mathbf{Q}\cdot\mathbf{R}_l(t))\rangle \\ &\times exp(-i\omega t)dt\end{aligned}\;, \tag{3.11}$$

where the quantity in brackets represents a space-time correlation function for the displacements projected along the momentum transfer. And the '< >' denote the thermal average where $\hbar\omega$ is the energy transferred to the sample.

Actually, there are two scattering processes distinguished at this view: coherent scattering, which preserve the phase in the scattering by each center coherently, and incoherent scattering, which loses the coherency. The coherent scattering includes the interference effects, and these effects build up over the whole sample. On the other hand, the incoherent scattering is random in the phase of each scattered wave and prevents any macroscopic interference. In the case of coherent scattering, the Fourier transform of the correlation functions is between different atoms at different times, whereas in the incoherent case, each atom is considered separately and the correlation function is for the same atom at different times. In addition, both of the scatterings occur regardless Bravais/non-Bravais lattice and depend on isotopic and nuclear spin populations of nuclei in lattice, thus, they occur in both elastic and inelastic scattering experiments.

$$\begin{aligned}(\frac{d^2\sigma}{d\Omega dE})_{coh} = \frac{\sigma_{coh}}{4\pi}\frac{k'}{k}\frac{1}{2\pi\hbar}\sum_{l,l'}\int_{-\infty}^{\infty}\langle exp(-i\mathbf{Q}\cdot\mathbf{R}_{l'}(0))exp(i\mathbf{Q}\cdot\mathbf{R}_{l}(t))\rangle \\ \times\, exp(-i\omega t)dt\end{aligned}, \tag{3.12}$$

and

$$\begin{aligned}(\frac{d^2\sigma}{d\Omega dE})_{inc} = N\frac{\sigma_{inc}}{4\pi}\frac{k'}{k}\frac{1}{2\pi\hbar}\sum_{l}\int_{-\infty}^{\infty}\langle exp(-i\mathbf{Q}\cdot\mathbf{R}_{l}(0))exp(i\mathbf{Q}\cdot\mathbf{R}_{l}(t))\rangle \\ \times\, exp(-i\omega t)dt\end{aligned}, \tag{3.13}$$

where $\sigma_{coh} = 4\pi(\bar{b})^2$ and $\sigma_{inc} = 4\pi(\bar{b^2}$ - $(\bar{b})^2)$ with the bar denoting averages over all nuclei in the sample.

3.3.2 Scattering Function

Based on the above discussion, the cross-section (σ) is determined by the energy (*E*) and the geometry (Ω). However, a scattering state is recorded in reciprocal space as the energy and momentum experimentally, a variable named *scattering function* is applied for convenience and it is expressed as

$S(\mathbf{Q}, \omega)$. The relations between $S(\mathbf{Q}, \omega)$ and the cross-sections for coherent and incoherent scattering of Bravais lattice are,

$$\begin{aligned}(\frac{d^2\sigma}{d\Omega dE})_{coh} &= \frac{\sigma_{coh}}{4\pi}\frac{k'}{k}S_{coh}(\mathbf{Q},\omega) \\ (\frac{d^2\sigma}{d\Omega dE})_{inc} &= \frac{\sigma_{inc}}{4\pi}\frac{k'}{k}S_{inc}(\mathbf{Q},\omega)\end{aligned}, \tag{3.14}$$

From Fourier transfers, a more general formulation of neutron scattering was derived by van Hove in terms of correlation functions [4]. He defined a variable named *time-dependent pair-correlation function*, $G(\mathbf{r}, \mathrm{t})$, and all the information on the system available from a neutron scattering experiment is encoded in it for the scattering centers. The relationship between $G(\mathbf{r}, \mathrm{t})$ and $S_{coh}(\mathbf{Q}, \omega)$ will be

$$S_{coh}(\mathbf{Q},\omega) = \frac{1}{2\pi\hbar}\int G(\mathbf{r},t)exp(i(\mathbf{Q}\cdot\mathbf{r}-\omega t))d^3r dt\,, \tag{3.15}$$

The self intermediate function

$$I_S(\mathbf{Q},t) = \frac{1}{N}\sum_j\langle exp(-i\mathbf{Q}\cdot\mathbf{R}_j(0))exp(i\mathbf{Q}\cdot\mathbf{R}_j(t))\rangle\,, \tag{3.16}$$

leads tothe incoherent scattering function, S_{inc} $(\mathbf{Q}, \omega)$, corresponds to the self-correlations, $G(\mathbf{r}, \mathrm{t})$,

$$G_S(\mathbf{r},t) = \frac{1}{(2\pi)^3}\int I_S(\mathbf{Q},t)exp(-i\mathbf{Q}\cdot\mathbf{r})d\mathbf{Q}\,, \tag{3.17}$$

and

$$S_{inc}(\mathbf{Q},\omega) = \frac{1}{2\pi\hbar}\int I_S(\mathbf{Q},t)exp(-i\omega t)dt\,, \tag{3.18}$$

3.3.3 Bravais and Non-Bravais lattice

Due to the number of atoms per unit cell, the crystal can be classified in Bravais lattice and non-Bravais lattice, and the time-dependent position operators are different in the non-Bravais case:

i) Bravais lattice, there is one atom per unit cell and the instantaneous position is,

$$\mathbf{R}_l(t) = \mathbf{l} + \mathbf{u}_l(t)\,, \tag{3.19}$$

where $\mathbf{l}$ is the equilibrium position and $\mathbf{u}_l(t)$ is the displacement from the equilibrium position.

In a harmonic system, the forces are linear functions of the displacements. Thus, the displacements $\mathbf{u}_l$ are the sum of displacements due to a series of normal modes,

$$\mathbf{u}_l = (\frac{1}{2MN})^{1/2} \sum_s \frac{\mathbf{e}_s}{\sqrt{\omega_s}} (\hat{a}_s exp(i\mathbf{q}\cdot\mathbf{l}) + \hat{a}_s^{+} exp(-i\mathbf{q}\cdot\mathbf{l}))\,, \tag{3.20}$$

where $\mathbf{q}$ is the wavevector of the mode, *s* stands for the index $\mathbf{q}$ and *j*. ω_s is the angular frequency and $\mathbf{e}_s$ is the polarization vector of mode *s*. *M* is the mass of a nucleus and *N* is the number of nuclei.

ii) Non-Bravais lattice, there are more than one atom per unit cell and the position of atom *d* in unit cell is,

$$\mathbf{R}_{ld} = \mathbf{l} + \mathbf{d} + \mathbf{u}_{ld}\,, \tag{3.21}$$

where $\mathbf{l}$ + $\mathbf{d}$ is the equilibrium position of the atom *d* in unit cell *l*, and $\mathbf{u}_{ld}$ is the displacement from equilibrium.

Corresponding to the Bravias crystal, the $\mathbf{u}_{ld}$ can be expressed as

$$\mathbf{u}_{ld} = (\frac{1}{2M_dN})^{1/2} \sum_s \frac{1}{\sqrt{\omega_s}} (\mathbf{e}_{ds}\hat{a}_s exp(i\mathbf{q}\cdot\mathbf{l}) + \mathbf{e}_{ds}^{*}\hat{a}_s^{+} exp(-i\mathbf{q}\cdot\mathbf{l}))\,, \tag{3.22}$$

where *N* is the number of unit cells in the crystal, and M_d is the mass of the atom at position *d*. *s* stands for the index $\mathbf{q}$ and *j*. $\mathbf{e}_{ds}$ is the polarization vector for the atom at position *d* for the mode *s*.

In general, the nucleus is different at each *d* position in the unit cell. Therefore, the factor need to be taken inside the double sum over the atoms and the partial differential cross-section is,

$$\begin{aligned}(\frac{d^2\sigma}{d\Omega dE'})_{coh} =& \frac{k'}{k}\frac{1}{2\pi\hbar}\sum_{ld}\sum_{l'd'}\bar{b}_d\bar{b}_{d'}exp[i\mathbf{Q}\cdot(\mathbf{l}+\mathbf{d}-\mathbf{l}'-\mathbf{d}')] \\ &\times\int_{-\infty}^{\infty}\langle exp(-i\mathbf{Q}\cdot(\mathbf{u}_{l'd'}(0))exp(i\mathbf{Q}\cdot(\mathbf{u}_{ld}(t))\rangle exp(-i\omega t)dt\end{aligned}, \quad (3.23)$$

Hence, the corresponding incoherent cross-section is obtained for *ld* = *l'd'* and replacing $\bar{b}_d^2$ with $\bar{b}_u^2$.

Fig. 3.2 shows a pictorial representation of a scattering process: i) If the energy $\hbar\omega$ = *E* - E' is zero, the scattering is elastic, which can be used to determine the lattice structure of the crystal; ii) If the energy $\hbar\omega$ > 0 (< 0), the excitation(s) of wave vector $\mathbf{Q}$ and the energy $\hbar\omega$ is created (absorbed) with the neutron-nucleus interaction. Only in small $\mathbf{Q}\cdot\mathbf{u}$ limit, the occupation number of phonons in the compound is raising (decreasing) from $n_{\mathbf{q}\omega}$ to $n_{\mathbf{q}\omega}$ + 1 or $n_{\mathbf{q}\omega}$ - 1. Otherwise, multiphonon is obtained.

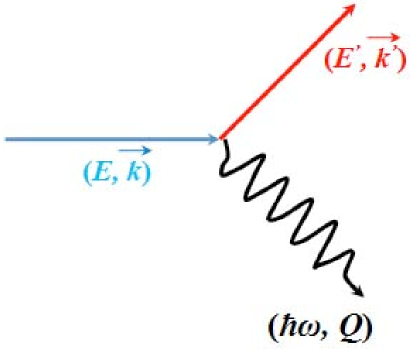

Figure 3.2 Schematic of a scattering process.

In the following sections, the diffraction and inelastic scattering from phonons of Bravais (Non-Bravais) lattice will be discussed in separately. In addition, the signal will include coherent and incoherent parts from Eq. (3.12) and (3.13).

3.3.3.1) Bravais lattice

From Eq. (3.11) and (3.19), the space-time correlation function for the displacements along the momentum transfer, $\langle$*exp*(-*i*$\mathbf{Q}\cdot\mathbf{R}_{l'}$*(0)*) *exp*(*i*$\mathbf{Q}\cdot\mathbf{R}_l$*(t)*)$\rangle$, can be simplified to $\langle$*exp*(-*i*$\mathbf{Q}\cdot\mathbf{u}_{l'}$*(0)*) *exp*(*i*$\mathbf{Q}\cdot\mathbf{u}_l$(*t*))$\rangle$ due to the time-independent equilibrium position, $\mathbf{l}$ ($\mathbf{l}'$).

Defining the operators *U* and *V* as -*i*$\mathbf{Q}\cdot\mathbf{u}_0$(*0*) and *i*$\mathbf{Q}\cdot\mathbf{u}_l$(*t*) respectively. Then, both cross-sections will have the correlation function $\langle$ *expU expV* $\rangle$ and a static structure factor can be pulled out of the time integral in harmonic model,

$$\langle expU expV \rangle = exp\langle U^2 \rangle exp\langle UV \rangle \,, \tag{3.24}$$

where the first factor on the right corresponds to the well-known Debye-Waller factor.

Then, the scattering function will be,

$$S = \frac{N}{2\pi\hbar} exp\langle U^2 \rangle \sum_{\mathbf{l}} exp(i\mathbf{Q}\cdot\mathbf{l}) \int_{-\infty}^{\infty} exp\langle UV \rangle exp(-i\omega t) dt \,, \tag{3.25}$$

exp⟨ *UV* ⟩ can be expanded by a Taylor series,

$$exp\langle UV \rangle = 1 + \langle UV \rangle + \frac{1}{2!}\langle UV \rangle^2 + \cdots \,, \tag{3.26}$$

I) Diffraction

If *exp*⟨ *UV* ⟩ = 1, the energy-independent scattering function can be expressed by the static structure factor (| k' | = | k |) multiplied by the Debye-Waller factor.

a.) Coherent scattering, which $\mathbf{l} \neq 0$,

$$\begin{aligned} S_{coh\,el} &= N exp\langle U^2 \rangle \sum_{l} exp(i\mathbf{Q}\cdot\mathbf{l}) \delta(\hbar\omega) \\ &= N \frac{(2\pi)^3}{v_0} exp\langle U^2 \rangle \sum_{\tau} \delta(\mathbf{Q} - \tau) \delta(\hbar\omega) \end{aligned} \,, \tag{3.27}$$

where v_0 is the volume of the unit cell of the crystal, τ is a vector in the reciprocal lattice, and *N* is the number of nuclei.

b.) Incoherent scattering, which $\mathbf{l} = 0$,

$$S_{inc\,el} = N exp\langle U^2 \rangle \,, \tag{3.28}$$

II) Inelastic scattering from one phonon

If *exp*⟨ *UV* ⟩ = ⟨ *UV* ⟩, the scattering function is related to one phonon scattering,

a.) Coherent scattering, which $\mathbf{l} \neq 0$,

$$\begin{aligned}
S_{coh\,1ph} =& \frac{N}{2\pi\hbar} exp\langle U^2\rangle \sum_l exp(i\mathbf{Q}\cdot\mathbf{l}) \int_{-\infty}^{\infty} \langle UV\rangle exp(-i\omega t)dt \\
=& \frac{N}{4\pi M} exp\langle U^2\rangle \sum_l exp(i\mathbf{Q}\cdot\mathbf{l}) \sum_s \frac{(\mathbf{Q}\cdot\mathbf{e}_s)^2}{\omega_s} \\
& \times \int_{-\infty}^{\infty} [exp\{-i(\mathbf{q}\cdot\mathbf{l}-\omega_s t)\}\langle n_s+1\rangle \\
& + exp\{-i(\mathbf{q}\cdot\mathbf{l}-\omega_s t)\}\langle n_s\rangle] exp(-i\omega t)dt \\
=& \frac{(2\pi)^3}{v_0}\frac{1}{2M} exp\langle U^2\rangle \sum_s\sum_\tau \frac{(\mathbf{Q}\cdot\mathbf{e}_s)^2}{\omega_s} \\
& [\langle n_s+1\rangle \times \delta(\omega-\omega_s)\delta(\mathbf{Q}-\mathbf{q}-\tau) \\
& + \langle n_s\rangle \times \delta(\omega+\omega_s)\delta(\mathbf{Q}+\mathbf{q}-\tau)]
\end{aligned} , \qquad (3.29)$$

b.) Incoherent scattering, which $\mathbf{l} = 0$,

$$\begin{aligned}
S_{inc,1-phonon} = \frac{1}{2M} exp\langle U^2\rangle \sum_s \frac{(\mathbf{Q}\cdot\mathbf{e}_s)^2}{\omega_s} \\
\times [\langle n_s+1\rangle\delta(\omega-\omega_s) + \langle n_s\rangle\delta(\omega+\omega_s)]
\end{aligned} , \qquad (3.30)$$

where $\langle\ n(\omega)\ \rangle$ is the Bose-Einstein distribution, and the two delta functions correspond to the creation and annihilation of one phonon of energy $\hbar\omega$, respectively.

III) Inelastic scattering from multi-phonon

From the expansion of $exp\langle\ UV\ \rangle$, the higher-order terms result in the multiphonon scattering. For the two-phonon term, $\frac{1}{2!}\langle\ UV\ \rangle^2$, obtained from Eq. (3.26), the energy and momentum will be

a.) Coherent scattering, which $\mathbf{l} \neq 0$,

$$\begin{aligned}
\frac{\hbar^2}{2m}(k^2 - k'^2) = \hbar(\pm\omega_{s1} \pm \omega_{s2}) \\
\mathbf{k} - \mathbf{k}' = \tau \pm \mathbf{q}_1 \pm \mathbf{q}_2
\end{aligned} , \qquad (3.31)$$

Two phonons are created or annihilated in the two different normal modes as the neutrons are scattered. In the one-phonon process, the scattering occurs only for discrete value of $\mathbf{k}'$ with the fixed $\mathbf{k}$, scattering angle, and crystal orientation. However, in the two-phonon process, the final $\mathbf{k}$-vector $\mathbf{k}'$ will be arbitrary with a certain range, which can satisfy Eq. (3.31). Therefore, it gives a continuous spectrum, which adds to the back ground. For the higher phonon processes, the energy and momentum equations keep similar as Eq. (3.31) with additional terms ω_{s_3}, $\mathbf{q_3}$ and so on.

b.) Incoherent scattering, which **l** = 0.

Although the incoherent multiphonon scattering is not same as the analysis in coherent scattering case and it is not easy to estimate the contribution, it also gives over a continuous range of $\mathbf{k}'$ and adds to the background scattering.

3.3.3.2) Non-Bravais lattice

With the similar derivation method of the scattering function of Bravais crystal, the diffraction and one-phonon partial differential cross-section will be presented.

I) Diffraction

a.) Coherent scattering

$$(\frac{d\sigma}{d\Omega})_{coh\,el} = N\sum_{l} exp(i\mathbf{Q}\cdot\mathbf{l}) \mid \sum_{d} \bar{b}_d exp(i\mathbf{Q}\cdot\mathbf{d}) exp(-W_d) \mid^2 , \qquad (3.32)$$

where

$$W_d = \frac{1}{2}\langle[\mathbf{Q}\cdot\mathbf{u}_{ld}(t)]^2\rangle , \qquad (3.33)$$

Summing over *l*,

$$(\frac{d\sigma}{d\Omega})_{coh\,el} = N\frac{(2\pi)^3}{v_0}\sum_{\tau} \delta(\mathbf{Q}-\tau) \mid F_N(\mathbf{Q}) \mid^2 , \qquad (3.34)$$

where $F_N(\mathbf{Q})$ is the *nuclear unit-cell structure factor*,

$$F_N(\mathbf{Q}) = \sum_{d} \bar{b_d} exp(i\mathbf{Q}\cdot\mathbf{d}) exp(-W_d) , \qquad (3.35)$$

b.) Incoherent scattering

For the incoherent scattering of non-Bravais crystal, the elastic cross-section can be expressed as

$$(\frac{d\sigma}{d\Omega})_{inc\,el} = N \sum_{d} [(\bar{b_d^2}) - (\bar{b_d})^2] exp(-W_d)\,, \tag{3.36}$$

II) Inelastic scattering from one phonon

a.) Coherent scattering

The one-phonon coherent partial differential cross-section of non-Bravais crystal can be straightforward to calculate,

$$\begin{aligned} (\frac{d^2\sigma}{d\Omega dE'})_{coh\,1ph} = & \frac{k'}{k}\frac{(2\pi)^3}{2v_0}\sum_{s}\sum_{\tau}\frac{1}{\omega_s} \\ & \mid \sum_{d}\frac{\bar{b}_d}{\sqrt{M_d}} exp(-W_d) exp(i\mathbf{Q}\cdot\mathbf{d})(\mathbf{Q}\cdot\mathbf{e}_{ds}) \mid^2 \\ & \times [\langle n_s+1\rangle \delta(\omega-\omega_s)\delta(\mathbf{Q}-\mathbf{q}-\tau) \\ & + \langle n_s\rangle \delta(\omega+\omega_s)\delta(\mathbf{Q}+\mathbf{q}-\tau)] \end{aligned} \,, \tag{3.37}$$

b.) Incoherent scattering

The incoherent one-phonon cross-section is,

$$\begin{aligned} (\frac{d^2\sigma}{d\Omega dE'})_{inch\,1ph} = & \frac{k'}{k}\sum_{d}\frac{1}{2M_d}[(\bar{b_d^2}) - (\bar{b_d})^2] exp(-W_d) \\ & \times \sum_{s,q}\frac{\mid \mathbf{Q}\cdot\mathbf{e}_{ds}\mid^2}{\omega_s}[\langle n_s+1\rangle \delta(\omega-\omega_s) \\ & + \langle n_s\rangle \delta(\omega+\omega_s)] \end{aligned} \,, \tag{3.38}$$

III) Powder Average Scattering

i) Incoherent Scattering

Our samples are powders and there is an interference condition like $\mathbf{k}$ - $\mathbf{k}'$ = $\mathbf{Q}$ + $\mathbf{q}$, where $\mathbf{q}$ is the wavevector of the normal mode s. However, the phonon density-of-states (DOS), $Z(\omega)$, is usually used to describe measurements using a powder sample. DOS is the summation over the whole Brillouin zone and contains only one δ function, $\delta(\omega$-$\omega_s)$

for the emission cross-section.

$$Z(\omega) = \sum_{s,k} \delta(\omega - \omega_s(k))\,, \tag{3.39}$$

Only the energy condition

$$\omega = \omega_s \;\; or \;\; \frac{\hbar^2}{2m}(k^2 - k'^2) = \hbar\omega\,, \tag{3.40}$$

needs to be satisfied.

For a given $\mathbf{k}$, θ, and crystal orientation, incoherent one-phonon scattering occurs for a continuous range of k' values; For a given k', we get scattering from all normal modes whose ω_s values satisfy the energy condition, Eq. (3.40). Actually, there is no difference scattering function between single crystal ans powders. Therefore, the cross-section depends on the *number* of modes that have the correct frequency and can be expressed as [4, 5]

$$S_{inc,+1-phonon} = \frac{3}{2M} exp(-W_d) \frac{\langle(\mathbf{Q}\cdot\mathbf{e}_s)^2\rangle_{av}}{\omega} Z(\hbar\omega)\langle n(\omega)+1\rangle\,, \tag{3.41}$$

where

$$\langle n+1\rangle = \frac{1}{2}[coth(\frac{1}{2}\hbar\omega\beta)+1]\,, \tag{3.42}$$

The $\langle\, (\mathbf{Q}\cdot\mathbf{e}_s)^2\,\rangle_{av}$ is the value of $(\mathbf{Q}\cdot\mathbf{e}_s)^2$ averaged over all the modes with frequency ω. For a cubic crystal,

$$\langle(\mathbf{Q}\cdot\mathbf{e}_s)^2\rangle_{av} = \frac{1}{3}Q^2 \tag{3.43}$$

then,

$$S_{inc,\pm1-phonon} = \frac{1}{4M} exp(-W_d) \frac{Q^2}{3\omega} Z(\hbar\omega)[coth(\frac{1}{2}\hbar\omega\beta) \pm 1]\,, \tag{3.44}$$

The phonon DOS may be determined by measuring the incoherent one-phonon scattering as a function of E' for a cubic crystal, which is the lattice structure of the samples in this thesis.

ii) Coherent Scattering

Unlike the incoherent scattering, there is no general expression for the powder-averaged coherent scattering. We do not sum over the whole Brillouin zone, rather average the coherent scattering over all directions of $\vec{Q}$,

$$S(\mid \mathbf{Q} \mid, \omega) = \int d\Omega_{\mathbf{Q}} S(\mathbf{Q}, \omega)\,, \tag{3.45}$$

where

$$d\Omega_{\mathbf{Q}} = sin\theta d\theta d\phi\,, \tag{3.46}$$

From Eq. (3.37), (3.45), and (3.46), the coherent scattering of powder sample depends on not only the angle average of the transfered momentum $\mathbf{Q}$ and the polarization vector $\mathbf{e}_s$, but also the angle average of the transfered momentum $\mathbf{Q}$ and the position vector $\mathbf{d}$.

3.4 Magnetic Scattering

In this section, the scatterings from magnetic structure and the ordered spin-wave, magnon, are introduced. Because there are many kinds of interactions between different domains, such as ferromagnet, antiferromagnet, helical arrangement of spins, and so on, it is hard to find a common expression to describe all possible ordered magnetic systems. Furthermore, the spin operator σ makes the case more complicated than nuclear scattering.

$$(\frac{d^2\sigma}{d\Omega dE'})_{\sigma\lambda\to\sigma'\lambda'} = (\frac{m}{2\pi\hbar^2})^2\frac{k'}{k} \mid \langle k'\sigma'\lambda' \mid V \mid k\sigma\lambda\rangle \mid^2 \delta(E_\lambda - E_{\lambda'} + \hbar\omega)\,, \tag{3.47}$$

We now consider a regular case: in a crystal, there is an ion *i* (*l*, *d*) at the position R_{ld}. *l* denotes the unit cell in which the ion locates, and *d* is the specific ion inside the unit cell. The magnetic potential energy will be expressed as,

$$V = W_{Si} + W_{Li}\,, \tag{3.48}$$

where W_{Si} and W_{Li} are spin and orbital parts, respectively.

$$\begin{aligned} W_{Si} &= curl(\frac{\mathbf{s_i} \times \hat{R}}{R^2}) \\ W_{Li} &= \frac{1}{\hbar}\frac{\mathbf{p_i} \times \hat{R}}{R^2} \end{aligned} \,, \tag{3.49}$$

Assuming

$$\sum_i \langle k' \mid W_{Si} + W_{Li} \mid k \rangle = 4\pi \mathbf{Q}_\perp \,, \tag{3.50}$$

where

$$\mathbf{Q}_\perp = \sum_{\mathbf{i}} \mathbf{exp}(\mathbf{iQ} \cdot \mathbf{r_i})[\hat{\mathbf{Q}} \times (\mathbf{s_i} \times \hat{\mathbf{Q}}) + \frac{\mathbf{i}}{\hbar \mathbf{Q}}(\mathbf{p_i} \times \hat{\mathbf{Q}})] \,, \tag{3.51}$$

Thus, the differential cross-section will be

$$(\frac{d^2\sigma}{d\Omega dE'})_{\sigma\lambda \to \sigma'\lambda'} = (\gamma r_0)^2 \frac{k'}{k} \mid \langle \sigma'\lambda' \mid \sigma \cdot \mathbf{Q}_\perp \mid \sigma\lambda \rangle \mid^2 \delta(E_\lambda - E_{\lambda'} + \hbar\omega) \,, \tag{3.52}$$

$\mathbf{Q}_\perp$ is the vector projection of $\mathbf{Q}$ on to the plane perpendicular to $\hat{Q}$, which is related to the magnetization of the scattering system,

$$\begin{aligned} \mathbf{Q}_\perp^* \cdot \mathbf{Q}_\perp &= [\mathbf{Q}^* - (\mathbf{Q}^* \cdot \hat{Q})\hat{Q}][\mathbf{Q} - (\mathbf{Q} \cdot \hat{Q})\hat{Q}] \\ &= \mathbf{Q}^* \cdot \mathbf{Q} - (\mathbf{Q}^* \cdot \hat{Q})(\mathbf{Q} \cdot \hat{Q}) \\ &= \sum_{\alpha\beta} (\delta_{\alpha\beta} - \hat{Q}_\alpha \hat{Q}_\beta) \mathbf{Q}_\alpha^* \mathbf{Q}_\beta \end{aligned} \,, \tag{3.53}$$

If p_σ is the probability of the initial neutron state in σ, the total cross-section over the final (σ', λ') and initial states (σ, λ) will be,

$$\sum_{\sigma\sigma'} p_\sigma \mid \langle \sigma'\lambda' \mid \sigma \cdot \mathbf{Q}_\perp \mid \sigma\lambda \rangle \mid^2 \,, \tag{3.54}$$

Since

$$\sum_\sigma p_\sigma \mid \langle \sigma \mid \sigma_x^2 \mid \sigma \rangle = 1 \,, \tag{3.55}$$

and

$$\sum_\sigma p_\sigma \mid \langle \sigma \mid \sigma_x \sigma_y \mid \sigma \rangle = 0 \,, \tag{3.56}$$

the differential cross-section can be expressed by the dipole scattering and related to the magnetic momentum factors, $\mathbf{Q}_\alpha$ and $\mathbf{Q}_\beta$,

$$\begin{aligned}\frac{d^2\sigma}{d\Omega dE'} = (\gamma r_0)^2\frac{k'}{k}\sum_{\alpha\beta}(\delta_{\alpha\beta} - \hat{Q}_\alpha\hat{Q}_\beta) \\ \times\sum_{\lambda\lambda'}p_\lambda\langle\lambda \mid Q_\alpha^+ \mid \lambda'\rangle\langle\lambda' \mid Q_\beta \mid \lambda\rangle\delta(E_\lambda - E_{\lambda'} + \hbar\omega)\end{aligned}, \tag{3.57}$$

Similar as the time-dependent nuclei position operator, the time-dependent spin position operator is defined with the time related and spin position factors,

$$\hat{S}^\alpha_{ld}(t) = exp(iHt/\hbar)\hat{S}^\alpha_{ld}exp(-iHt/\hbar)\,, \tag{3.58}$$

Furthermore, the time-dependent spin density is expressed as

$$\hat{S}^\alpha_Q(t) = \sum_{ld} f_d(Q)exp(-i\mathbf{Q}\cdot(\mathbf{l}+\mathbf{R}_{ld}))\hat{S}^\alpha_{ld}(t)\,, \tag{3.59}$$

where $\hat{S}^\alpha_{ld}$(t) is the α component of the time-dependent spins for the ion (*l*, *d*). For the magnetic ion, the amplitude prefactor, f_d(Q), depends on the Lande g-factor, the magnetic form factor, F_d(Q), and the Debye-Waller factor, W$_d$(Q),

$$f_d(Q) = \frac{1}{2}gF_d(Q)exp(-W_d(Q))\,, \tag{3.60}$$

Then, the magnetic scattering cross section is (in order to not misunderstand the scattering function and spin momentum symbol, we will replace the scattering function by the partial differential cross section, $\frac{d^2\sigma}{d\Omega dE'}$, in this magnetic scattering section)

$$\begin{aligned}\frac{d^2\sigma}{d\Omega dE'} =& \frac{(\gamma r_0)^2}{2\pi\hbar}\frac{k'}{k}\sum_{ld,l'd'}\sum_{\alpha\beta}(\delta_{\alpha\beta} - \hat{Q}_\alpha\hat{Q}_\beta)\frac{1}{4}g_{d'}g_dF^*_{d'}(\mathbf{Q})F_d(\mathbf{Q}) \\ &\times\int_{-\infty}^{\infty}dt\langle exp(-i\mathbf{Q}\cdot\mathbf{R}_{l'd'}(0))exp(i\mathbf{Q}\cdot\mathbf{R}_{ld}(t))\rangle\langle S^\alpha_{l'd'}(0)S^\beta_{ld}(t)\rangle exp(-i\omega t)\end{aligned}, \tag{3.61}$$

where γ equals 1.913 and r$_0$ is the classical radius of electron,

$$r_0 = \frac{\mu_0}{4\pi}\frac{e^2}{me} = 2.818 \times 10^{-15} m\,, \tag{3.62}$$

And $\frac{k'}{k}$ $(\gamma\, r_0)^2$ $F^*_{d'}(\mathbf{Q})$ $F_d(\mathbf{Q})$ is scattering cross-section; $\langle\, S^{\alpha}_{l'd'}(0) S^{\beta}_{ld}(t)\,\rangle$ is the spin-spin correlation function.

3.4.1 Magnetic Diffraction

From Eq. (3.61), it is found that the magnetic cross-section is not only related to the spin momenta, but also the positions of the spins. For magnetic diffraction, $\hbar\omega$ = 0 and $|k|$ = $|k'\;|$. As the discussions on the nuclear diffraction, the studies on the magnetic diffraction will be based on the Bravais and non-Bravais crystals in the following.

i) Bravais crystal

For a Bravais crystal, the magnetic cross-section will become

$$\begin{aligned}\frac{d^2\sigma}{d\Omega dE'} = \frac{(\gamma r_0)^2}{2\pi\hbar} N[\frac{1}{2} g F(\mathbf{Q})]^2 \sum_{\alpha\beta}(\delta_{\alpha\beta} - \hat{Q}_\alpha \hat{Q}_\beta) \sum_l exp(i\mathbf{Q}\cdot\mathbf{l}) \\ \times \int_{-\infty}^{\infty} \langle exp(-i\mathbf{Q}\cdot\mathbf{u}_0(0)) exp(i\mathbf{Q}\cdot\mathbf{u}_l(t))\rangle \\ \langle S^\alpha_0(0) S^\beta_l(t)\rangle exp{-}i\omega t dt\end{aligned}\;, \tag{3.63}$$

where N is the number of magnetic unit cells, and $\mathbf{u}_l(t)$ is the displacement of nucleus **l** from its equilibrium position.

As $t \to \infty$, $\langle\, S^{\alpha}_{0}\; (0)\; S^{\beta}_{l}\; (t)\,\rangle$ becomes independent of time,

$$\lim_{t\to\infty} \langle S^\alpha_0(0) S^\beta_l(t)\rangle = \langle S^\alpha_0(0)\rangle\langle S^\beta_l(t)\rangle\,, \tag{3.64}$$

Integrating with respect to E', the elastic cross-section is

$$\begin{aligned}(\frac{d^2\sigma}{d\Omega})_{el} = (\gamma r_0)^2 N[\frac{1}{2}gF(\mathbf{Q})]^2 exp(-2W)\sum_{\alpha\beta}(\delta_{\alpha\beta} - \hat{Q}_\alpha\hat{Q}_\beta) \\ \times\sum_l exp(i\mathbf{Q}\cdot\mathbf{l})\langle S_0^\alpha(0)\rangle\langle S_l^\beta(t)\rangle\end{aligned}, \tag{3.65}$$

Ferromagnet

Assuming the magnetic direction is *z*-axis, $\langle S_l^z\rangle$ is independent of the site position *l*,

$$\langle S_l^z\rangle = \langle S^z\rangle\,, \tag{3.66}$$

then,

$$(\frac{d^2\sigma}{d\Omega})_{el} = (\gamma r_0)^2 N[\frac{1}{2}gF(\mathbf{Q})]^2 exp(-2W)(1-\hat{Q}_z^2)\langle S^z\rangle^2\sum_l exp(i\mathbf{Q}\cdot\mathbf{l})\,, \tag{3.67}$$

Usually,

$$\sum_l exp(i\mathbf{Q}\cdot\mathbf{l}) = \frac{(2\pi)^3}{v_0}\sum_\tau\delta(\mathbf{Q}-\tau)\,, \tag{3.68}$$

As

$$\mathbf{Q} = \tau\ ,\ \hat{Q}_z = \hat{\tau}\cdot\hat{\eta}\,, \tag{3.69}$$

where $\hat{\tau}$ is a unit vector in the direction of τ, and $\hat{\eta}$ is a unit vector in the mean direction of the spins. The cross-section with many domains is

$$\begin{aligned}(\frac{d^2\sigma}{d\Omega})_{el} = (\gamma r_0)^2 N\frac{(2\pi)^3}{v_0}\langle S^\eta\rangle^2\sum_\tau[\frac{1}{2}gF(\tau)]^2 exp(-2W) \\ \times[1-(\hat{\tau}\cdot\hat{\eta})_{av}^2]\delta(\mathbf{Q}-\tau)\end{aligned}, \tag{3.70}$$

where $\langle S^\eta\rangle$ is the mean value of the component of the spin in the direction of $\hat{\eta}$ for each domain.

If all directions in space are equally likely for $\hat{\eta}$,

$$[1-(\hat{\tau}\cdot\hat{\eta})^2]_{av}=2/3\ ,\ \hat{Q}_z=\hat{\tau}\cdot\hat{\eta}\,, \tag{3.71}$$

The nuclear Bragg peaks and the magnetic Bragg peaks of a ferromagnetic crystal occur at the same reciprocal point. However, there are several differences between them: i) the magnetic scattering is proportional to $\langle S^{\eta}\rangle^2$ and temperature dependent. It falls to zero at T_c, while the only temperature factor in nuclear peak is Debye-Waller factor; ii) Since the magnetic potential is long range and the nuclear potential is short range, the magnetic form factor $F(\tau)$ falls rapidly with increasing $\mid \tau \mid$, while the only factor including $\mid \tau \mid$ in nuclear peak is again Debye-Waller factor.

More generally, the magnetization $\langle \mathbf{M}(\mathbf{r})\rangle$ is periodic in the unit cell of the crystal. With the Fourier transform of magnetization density, the cross-section is

$$(\frac{d^2\sigma}{d\Omega})_{el}=(\frac{\gamma r_0}{2\mu_B})^2\frac{(2\pi)^3}{v_0}\sum_{\tau}exp(-2W)\delta(\mathbf{Q}-\tau)\mid\hat{\tau}\times[\mathbf{M}(\tau)\times\hat{\tau}]\mid^2\,, \tag{3.72}$$

ii) Non-Bravais crystal

Magnetic unit cell usually contains more than one sublattice, such as antiferromagnets. In such kind of complicate magnetic systems, assuming one specific sublattice is *A*. If the mean spin direction in this sublattice *A* is $\hat{\eta}$ and $\langle S^{\eta}\rangle$ is the staggered mean spin, the relative position and spin momentum function for the single domain will be

$$\begin{aligned}&\sum_{l,l'}exp[i\mathbf{Q}\cdot(\mathbf{l}-\mathbf{l}')]\langle S^{\eta}_{l'}\rangle\langle S^{\eta}_{l}\rangle\\&\qquad=\langle S^{\eta}\rangle^2N_m\sum_{A}exp(i\mathbf{Q}\cdot\mathbf{l})\sum_{d}\sigma_d exp(i\mathbf{Q}\cdot\mathbf{d})\end{aligned}\ , \tag{3.73}$$

and

$$\sum_{A}exp(i\mathbf{Q}\cdot\mathbf{l})=\frac{(2\pi)^3}{v_{0m}}\sum_{\tau_m}\delta(\mathbf{Q}-\tau_m)\,, \tag{3.74}$$

where N_m is the number of magnetic unit cells in the crystal, v_{0m} is the volume of the magnetic unit cell, and τ_m is a vector in the magnetic reciprocal lattice. $\sum_A$ and $\sum_d$ mean the sums over the ions in sublattice A and in the magnetic unit cell, respectively. σ_d is direction of the spins: in AF, the value +1 is for spin up and -1 is for spin down. Therefore, the cross-section can be expressed as,

$$\begin{aligned}(\frac{d^2\sigma}{d\Omega})_{el} = (\gamma r_0)^2 N_m \frac{(2\pi)^3}{v_{0m}} \sum_{\tau_m} \mid F_M(\tau_m) \mid^2 exp(-2W) \\ \times [1 - (\hat{\tau} \cdot \hat{\eta})^2_{av}] \delta(\mathbf{Q} - \tau)\end{aligned}, \tag{3.75}$$

where $F_M(\tau_m) = \frac{1}{2} g \langle S^\eta \rangle F(\tau_\mathbf{m}) \sum_d \sigma_d exp(i\tau_\mathbf{m} \cdot \mathbf{d})$.

Antiferromagnet-LaFeO$_3$

LaFeO$_3$ is G-type antiferromagnetic, Fig. 3.3. The nuclear lattice is perovskite and a vector in the lattice will be expressed by the unit-cell vectors of the nuclear reciprocal lattice $\tau_\mathbf{1}$, $\tau_\mathbf{2}$, $\tau_\mathbf{3}$,

$$\tau = \mathbf{t_1}\tau_\mathbf{1} + \mathbf{t_2}\tau_\mathbf{2} + \mathbf{t_3}\tau_\mathbf{3}\,, \tag{3.76}$$

where t_1, t_2, t_3 are integers. As $\mathbf{Q} = \tau$, the nuclear Bragg scattering can be observed.

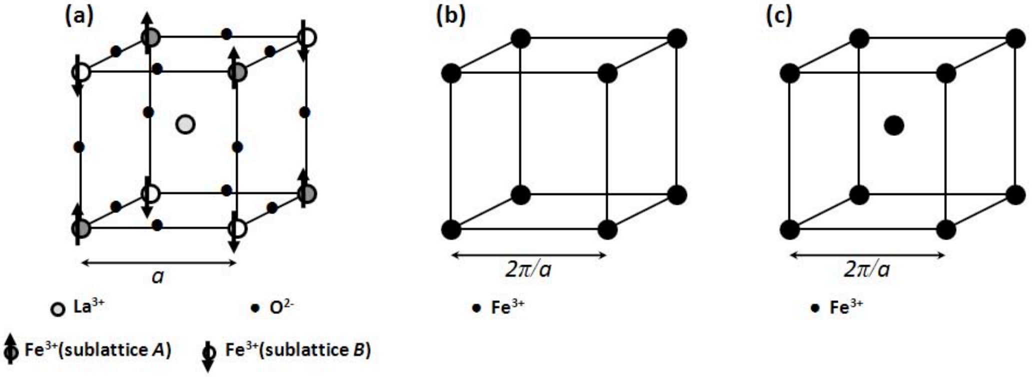

Figure 3.3 (a) Structure of LaFeO$_3$, arrows show the spin directions of Fe^{3+} ions; (b) nuclear reciprocal lattice (all Fe^{3+} ions are treated as identical); (c) magnetic reciprocal lattice (obtained by taking account of the spin directions of the Fe^{3+} ions).

The magnetic lattice is face-center cubic, the vector τ_m will be

$$t_1,\ t_2,\ t_3\ \ or\ \ t_1+\frac{1}{2},\ t_2+\frac{1}{2},\ t_3+\frac{1}{2}\,, \tag{3.77}$$

where t_1, t_2, t_3 are integers. As $\mathbf{Q} = \tau_{\mathbf{m}}$, the magnetic Bragg scattering can be observed.

Summing over d in$F_M(\tau_m)$ of Eq.(70) for a pair of neighboring antiferromagnet A and B ions,

$$\begin{aligned}\sum_d \sigma_d exp(i\tau_{\mathbf{m}}\cdot\mathbf{d}) = 0\ \ for\ \ \tau_{\mathbf{m}}\ &=\ t_1,\ t_2,\ t_3, \\ = 2\ \ for\ \ \tau_{\mathbf{m}}\ &=\ t_1+\frac{1}{2},\ t_2+\frac{1}{2},\ t_3+\frac{1}{2}.\end{aligned} \tag{3.78}$$

So nuclear and magnetic Bragg scattering peaks are observed at different points in reciprocal space. However, it is not always the case that both scattering peaks occur at different phase for an antiferromagnet, such as MnF_2. Usually, the staggered mean spin $\langle\, S^{\eta}\rangle$ is measured to difference the nuclear and magnetic Bragg scatterings: for magnetic scattering, the intensity is proportional to $\langle\, S^{\eta}\rangle^2$, which is temperature dependent and falls down to zero at T_N.

3.4.2 Inelastic Magnetic Scattering

Figure 3.4 Spin-spin correlation of different ions j and j'.

In ordered magnets at low temperature, excitations are described by collective modes of spin-waves, Fig. 3.4. The cross-section expression is same as Eq. (3.61), while the energy and momenta requirements are different: $\hbar\omega \neq 0$ and $|k| \neq |k'|$.

$$\begin{aligned}\frac{d^2\sigma}{d\Omega dE'} =& \frac{(\gamma r_0)^2}{2\pi\hbar}\frac{k'}{k}\sum_{ld,l'd'}\sum_{\alpha\beta}(\delta_{\alpha\beta}-\hat{Q}_\alpha\hat{Q}_\beta)\frac{1}{4}g_{d'}g_dF^*_{d'}(\mathbf{Q})F_d(\mathbf{Q}) \\ &\times\int_{-\infty}^{\infty}dt\langle exp(-i\mathbf{Q}\cdot\mathbf{R}_{l'd'}(0))exp(i\mathbf{Q}\cdot\mathbf{R}_{ld}(t))\rangle\langle S^{\alpha}_{l'd'}(0)S^{\beta}_{ld}(t)\rangle exp(-i\omega t)\end{aligned}, \quad (3.79)$$

Powder average

For a powder sample, the cross-section is the result of not only average spin orientations, but also average of $\vec{Q}$ direction,

$$\frac{d^2\sigma}{dE'} = \int\frac{d^2\sigma}{d\Omega dE'}d\Omega\,, \quad (3.80)$$

and

$$\begin{aligned}\int\frac{d^2\sigma}{d\Omega dE'}d\Omega =& \frac{(\gamma r_0)^2}{2\pi\hbar}\frac{k'}{k}\sum_{ld,l'd'}\int\sum_{\alpha\beta}(\delta_{\alpha\beta}-\hat{Q}_\alpha\hat{Q}_\beta)\frac{1}{4}g_{d'}g_dF^*_{d'}(\mathbf{Q})F_d(\mathbf{Q}) \\ &\times\int_{-\infty}^{\infty}dt\langle exp(-i\mathbf{Q}\cdot\mathbf{R}_{l'd'}(0))exp(i\mathbf{Q}\cdot\mathbf{R}_{ld}(t))\rangle\langle S^{\alpha}_{l'd'}(0)S^{\beta}_{ld}(t)\rangle exp(-i\omega t)d\Omega\end{aligned}, \quad (3.81)$$

Therefore, we can find that the inelastic cross-section is not only determined by the Fourier transform in time and space of $\langle S^{\alpha}_{l'd'}(0)S^{\beta}_{ld}$(t) $\rangle$, but also the angle average.

3.4.3 Linear spin-wave theory

If spin waves are in an ordered system (ferromagnet or antiferromagnet), the coupling between spins is often described by a Heisenberg model,

$$H_{ex} = -\sum_{ld,l'd'}J(ld,l'd')\mathbf{S}_{ld}\cdot\mathbf{S}_{l'd'}\,, \quad (3.82)$$

where J (ld,l' d') is the pair-wise exchange values between the spin of ion (ld), S_{ld}, and the spin of ion (l' d'), $S_{l'd'}$.

If the spin-waves originate from the same type of ion with spin S. Then, the spin-wave dispersion relations are

a) ferromagnet:

$$\hbar\omega_q^{ferro} = S[J(0) - J(q)]\,, \tag{3.83}$$

b) antiferromagnet:

$$\hbar\omega_q^{anti} = S\sqrt{J^2(0) - J^2(q)}\,, \tag{3.84}$$

where J (q) is the function of the pairwise exchange;

$$J(q) = \sum_{ld,l'd'} J(ld, l'd')exp(-i\mathbf{q} \cdot (\mathbf{R}_{ld} - \mathbf{R}_{l'd'}))\,, \tag{3.85}$$

From Eq. (3.83), (3.84), and (3.85), we can get that the excitation energies are Q-dependent. Therefore, the partial differential inelastic magnetic cross-section mainly depends on Q-dependent magnetic form factors which can be found in the International Crystallography Tables. Furthermore, the magnetic form factor is the Fourier transform of the magnetization density, it falls steadily with increasing Q.

To determine the spin wave cross-section in more completed structures, the spin operator in Heisenberg Hamiltonian, Eq. (3.82), is separated into two parts: magnitude, S_d ($S_{d'}$) and sign, $\sigma_d(\sigma_{d'})$. Hence, S_d ($\mathrm{S}_{d'}$) is positive and $\sigma_d(\sigma_{d'})$ = ± 1 with +1 (-1) parallel (antiparallel) to the z-quantization axis. For the antiferromagnetic perovskite structure, σ_A = -1 and σ_B = +1. (Here, A and B have different meaning than ABO_3. They are the same ion but have opposite spin directions.) With the Holstein-Primakoff transformation, the angular momentum operators are mapped to boson creation and annihilation operators. Then, the equation for the magnetic system can be expressed in matrix form: ($\mathbf{M}$ - γ $\mathbf{I}$) $\mathbf{T}$ = 0 where $\mathbf{M}$ is the transfer martix,

$$\mathbf{M}_{dd'}(\mathbf{q}) = \delta_{d,d'} \sum_{lk} J(0d; lk)\sigma_k S_k - \sigma_{d'}\sqrt{S_d S_{d'}} \sum_{l} J(0d; ld')exp(i\mathbf{q} \cdot \mathbf{R}_l)\,, \tag{3.86}$$

From the diagonaliztion of the matrix $\mathbf{M}(\mathbf{q})$ at wavevector $\mathbf{M}$, we can obtain the eigenvalues, $\gamma_n(\mathbf{q})$, and eigenvectors, $\mathbf{T}_n(\mathbf{q})$, where *n* labels the spin wave branch. Here, it should be noticed that the matrix is not Hermitian due to $\sigma_{d'}$. However, the eigenvalues for this matrix are real and there is no branch across zero (i.e. an entire branch must be completely positive or negative) with the number of the negative branches equal to the number of antiparallel spin sites. The spin-wave dispersion for branch *n* is $\hbar\omega_n(\mathbf{q})$ = $|\gamma_n(\mathbf{q})|$. The normalized eigenvector is

$$T_{nd} = \frac{\sqrt{S_d}\xi_n d}{\sqrt{\sum_d S_d \xi_{nd}^2}}\,, \tag{3.87}$$

where ξ_{nd}^2 is the fraction of the *d*th spin contained in the eigenvector and $\Sigma_d\, T_{nd}^2$ =1 for each branch.

When we expand the local spin deviation into the terms of plane waves, $\hat{S}_{ld}^{\alpha}$(t) (in Eq.(3.81)) is rewritten as

$$\hat{S}_{ld}^{\alpha}(t) = \frac{1}{N}\sum_q exp(i\mathbf{q}\cdot\mathbf{l})\hat{S}_{\mathbf{q},d}^{\alpha}(t)\,, \tag{3.88}$$

then, the spin-spin correlation function in Eq. (3.81), $\langle$ $S_{l',d'}^{\alpha}$(0) S_{ld}^{β}(t) $\rangle$ which can be expressed as $\langle$ $S_{\mathbf{Q}}^{\alpha}$(0) $S_{-\mathbf{Q}}^{\beta}$(t) $\rangle$, becomes

$$\begin{aligned}\langle\hat{S}_{\mathbf{Q}}^{\alpha}\hat{S}_{-\mathbf{Q}}^{\beta}(t)\rangle = \sum_{dd'} f_d(Q)f_{d'}(Q)exp(i\mathbf{Q}\cdot(\mathbf{d}-\mathbf{d}'))\sum_q\delta(\mathbf{Q}-\mathbf{q}-\mathbf{r})\\ \times\,\langle\hat{S}_{\mathbf{q},d}^{\alpha}\hat{S}_{-\mathbf{q},d'}^{\beta}(t)\rangle\end{aligned}\,, \tag{3.89}$$

Therefore, the thermal average of the spin-spin correlation functions (spin-spin fluctuation) are performed in the type $S^+S^-$for each branch (labeled *n*)

$$\langle\hat{S}_{\mathbf{q},d}^{+}\hat{S}_{-\mathbf{q},d'}^{-}(t)\rangle_n = \frac{\sigma_d\sigma_{d'}}{2N}\sqrt{S_dS_d'}T_{nd}T_{nd'}^{*}[n_{\mathbf{q},n}exp(-i\omega_n(\mathbf{q})t)]\,, \tag{3.90}$$

$$\langle\hat{S}_{-\mathbf{q},d}^{-}\hat{S}_{-\mathbf{q},d'}^{+}(t)\rangle_n = \frac{\sigma_d\sigma_{d'}}{2N}\sqrt{S_dS_d'}T_{nd}T_{nd'}^{*}[(n_{-\mathbf{q},n}+1)e^{-i\omega_n(-\mathbf{q})t}]\,, \tag{3.91}$$

where n_{qn} is the Bose occupation factor and T_{nd} is the contribution of the *d*th atom to the spin wave eigenvector of branch *n*.

For the collinear magnet, Fig. 3.5, the spins aligned to the $\hat{\mu}$ direction, the partial differential inelastic

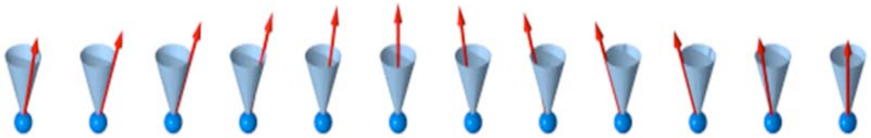

Figure 3.5 Schematic of the linear spin wave.

cross section can be written (q = - $\mathbf{q}$) as

$$\begin{aligned}\frac{d^2\sigma}{d\Omega dE'} = (\gamma r_0)^2\frac{k'}{k}(1+\frac{(\hat{\mu}\cdot\mathbf{Q})^2}{Q^2})\sum_n |\sum_d F_d(\mathbf{Q})\sigma_d\sqrt{S_d}T_{nd}(\mathbf{q})e^{-i\mathbf{Q}\cdot\mathbf{d}_d}|^2 \\ \times\,\delta(\mathbf{Q}-\mathbf{q}-\tau)[n(\omega)\delta(\omega+\omega_n(\mathbf{q}))+(n(\omega)+1)\delta(\omega-\omega_n(\mathbf{q}))]\end{aligned}, \tag{3.92}$$

In the antiferromaget, the dispersion and associated eigenvectors can be used to calculate the spin wave structure factor for unpolarized neutron energy loss scattering from a single crystal sample,

$$\begin{aligned}\frac{d^2\sigma}{d\Omega dE'} =& \frac{1}{2}(\gamma r_0)^2\frac{k'}{k}(1+\frac{(\hat{\mu}\cdot\mathbf{Q})^2}{Q^2}) \\ &\times\sum_n |\sum_i F_i(\mathbf{Q})\sigma_i\sqrt{S_i}T_{ni}(\mathbf{q})e^{-i\mathbf{Q}\cdot\mathbf{d}_i}|^2\times(n(\omega)+1)\delta(\omega-\omega_n(\mathbf{q}))\end{aligned}, \tag{3.93}$$

For the simple perovskite magnets, all ions in the magnetic cell are considered to be equivalent. The structure factor can then be written,

$$\begin{aligned}\frac{d^2\sigma}{d\Omega dE'} = \frac{1}{2}(\gamma r_0)^2\frac{k'}{k}SF^2(\mathbf{Q})(1+\frac{(\hat{\mu}\cdot\mathbf{Q})^2}{Q^2}) \\ \times\sum_n |\sum_d \sigma_d T_{nd}(\mathbf{q})e^{-i\mathbf{Q}\cdot\mathbf{d}_d}|^2\times(n(\omega)+1)\delta(\omega-\omega_n(\mathbf{q}))\end{aligned}, \tag{3.94}$$

To compare Heisenberg model spin wave results to the powder INS data, powder-averaging of $S_{mag}(\mathbf{Q},\ \omega)$ is performed by Monte-Carlo integration over a large number of Q-vectors lying on a constant-Q sphere, giving the orientationally averaged $S_{mag}(\mathbf{Q},\ \omega)$ which depends only on the magnitude of $\mathbf{Q}$.

Due to the anisotropy from orthorhombic distortion, the exchange within the perovskite *ab*-plane (J_{ab}) and that along the *c*-axis (J_c) have different values, and can even have different signs. The Heisenberg Hamiltonian becomes,

$$H = -J_{ab} \sum_{\langle i,j\rangle \| a,b} \mathbf{S}_i \cdot \mathbf{S}_j - J_c \sum_{\langle i,j\rangle \| c} \mathbf{S}_i \cdot \mathbf{S}_j - g\mu_B H_a \sum_i \sigma_i S_i \,, \tag{3.95}$$

where $\mathbf{S}_i$ is the spin vector on the *i*th site and sums are restricted to nearest neighbor spins in the *ab*-plane and along the *c*-axis. Exchange energies are defined such that a positive *J* represents ferromagnetic exchange. Uniaxial single-ion anisotropy is represented by an anisotropy field H_a that acts on spin $\mathbf{S}_i$ and points along the local spin direction (given by σ_i = ± 1).

LFO is *G*-type antiferromagnet, J_{ab} < 0; J_c < 0. When the single ion anisotropy is zero, the dispersion is [6],

$$\omega(\mathbf{q}) = 2S\{(2 \mid J_{ab} \mid + \mid J_c \mid)^2 - [2 \mid J_{ab} \mid \gamma_+(\mathbf{q}) + \mid J_c \mid \gamma_z(\mathbf{q})]^2\}^{1/2} \,, \tag{3.96}$$

where $\gamma_+(\mathbf{q})$ = $\frac{1}{2}$ (cos q_xa + cos q_ya), $\gamma_z(\mathbf{q})$ = cos q_za, $\mathbf{q}$ is the spin wave momentum, and $\mathbf{a}$ is the cubic perovskite lattice constant.

The dispersions for each magnetic structure are shown in Fig. 3.6 for the case where $|J_{ab}|$ = $|J_c|$.

The spin-wave density-of-state (SWDOS) is summed over all wavevectors in the Brillouin zone ($\mathbf{q}$),

$$g(\omega) = \frac{1}{N} \sum_{q,n} \delta(\omega - \omega_n(\mathbf{q})) \,, \tag{3.97}$$

where q is the spin wave wavevector in the first Brillouin zone.

Therefore, the SWDOS of LFO is shown in Fig. 3.6.

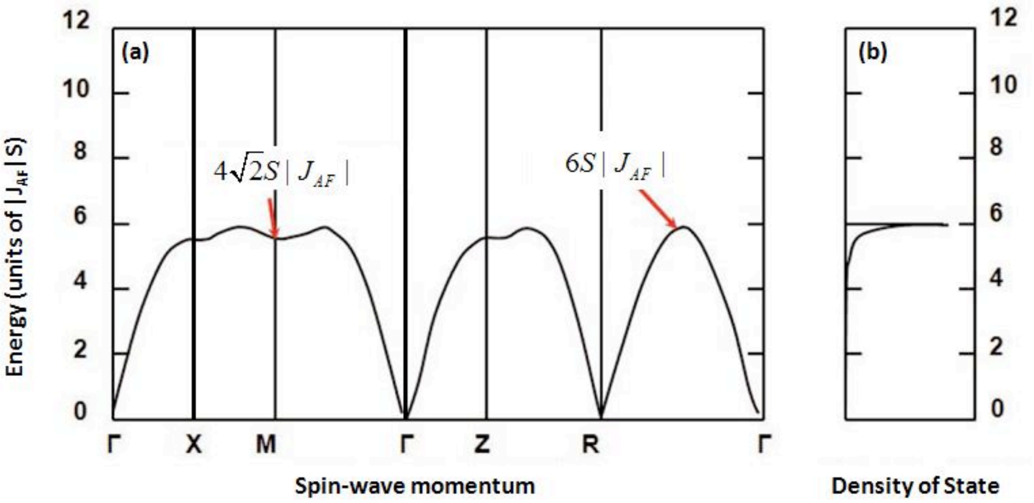

Figure 3.6 The spin wave dispersion along various symmetry directions (left panels) and the spin wave density of states (right panel) for LFO. Red arrows and labels indicate the energies of the extrema in the dispersion that give rise to Van Hove singularities in the density-of-states.

3.5 Density of States and Time-of-Flight Neutron Spectrometer

3.5.1 Dispersion and Density of States

INS is a perfect tool to collect the dispersion and DOS data. Dispersion shows the relationship between the angular frequency, ω, and wavenumber, k, which are related to the energy and the momentum. While DOS shows the total number of states at each energy of the system and is the average of the dispersion over all wavevectors. Because of the preciseness of the dispersion, there are some extra requirements in a dispersion measurement compared to DOS measurement: i) the measurement time of full dispersion can take much longer than the case of DOS; ii) the sample for the dispersion measurement need to be a single crystal and must be aligned before it is loaded in the sample chamber. However, DOS can quickly determine the magnetic exchange interactions and allow for rapid systematic studies of the evolution of magnetism in perovskite systems.

3.5.2 Principal of Time-of-Flight

The time-of-flight (TOF) technique was first employed to perform energy-dependent neutron measurements (Dunning et al., 1935). The technique has been greatly refined over the last 75 years with the advent of reactors and pulsed sources [7]. Due to the high peak flux and inherent time structure, all pulsed-source spectrometers are TOF spectrometers. The TOF technique has the following advantages: i) it can measure the high excitation energies; ii) the measurements of the momentum and energy transfers, $\mathbf{Q}$ and ω, are performed simultaneously; iii) Due to those broad surveys of $\mathbf{Q}$ and ω measurements, the instrument is effective for powders; iv) the fixed geometry of the instruments has the advantages for time dependent measurements or when measuring under difficult sample environment conditions [7].

Figure. 3.7 is the schematic of a typical TOF instrument for inelastic neutron scattering, which is a direct-geometry chopper spectrometer.

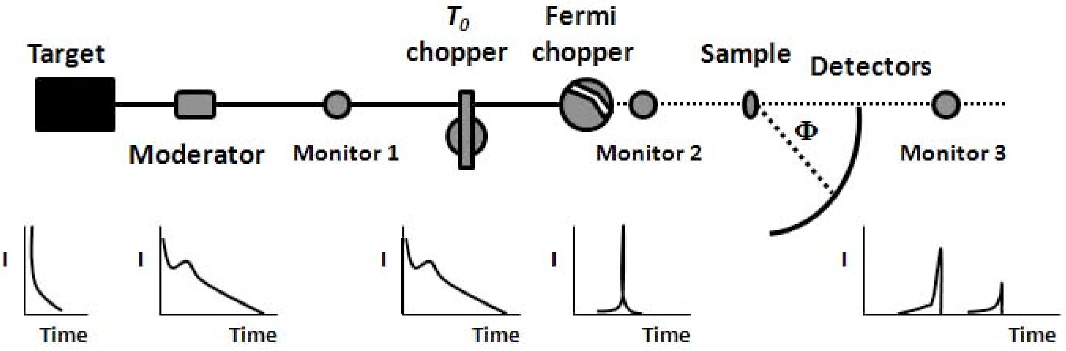

Figure 3.7 Direct-geometry TOF neutron spectrometer.

The neutrons are produced by a spallation source which produces of neutrons by accelerating pulses of protons into a tungsten target (Lujan Center, Los Alamos National Laboratory) or liquid mercury target (Spallation Neutron Source, Oak Ridge National Laboratory). The interaction of the protons with the target produces showers of pulsed neutrons. The high energy neutrons emitted from the spallation source pass through a moderator, which is a tank filled with water and slows down some of the neutrons to thermal energies. However, this equilibration process is thermal equilibrium, not reacted, and the final neutron spectrum will contain a tail of the epithermal neutrons of higher energy. In order to prevent those fast neutrons from entering the instrument, which will undergo a series of inelastic collisions inside the instrument and produce an undesired, spectrally broad background, a T_0 chopper is used, which is a thick and heavy metal to absorb or scatter fast neutrons. The rotating velocity of T_0 chopper is phased to be closed when proton strike target. The monochromatic neutrons of a specific energy are selected by Fermi chopper, which is phased to pass the desired energy. This energy selection depends on the energy-velocity relationship for the free neutrons, $E = (1/2)mv^2$. As the neutrons are incident on a sample and scattered, the momentum and energy of them are transferred, and collected by a set of detectors, which cover a large angular range. The 3He neutron detectors absorb an incoming neutron thereby emitting a photon which is measured by standard photon detectors (proportional counters). The time of the initial neutron pulse and the arrival time on the detector, τ, is recorded, Fig. 3.8.

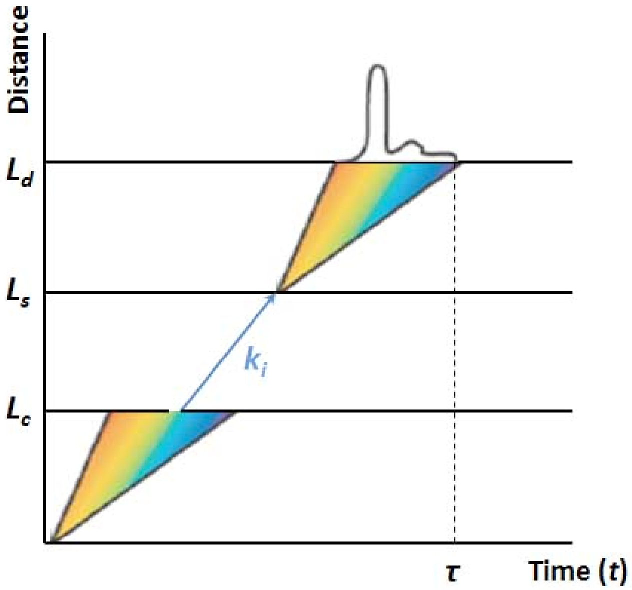

Figure 3.8 Time vs position of pulsed TOF neutron. L_c, L_s, and L_d are the positions of Fermi chopper, sample, and detectors respectively. And k_i is the wavevector of incident neutron beam.

Based on the knowledge of the incident energy and the constant distance between the sample and detectors, the flight time determines velocity of the scattered neutrons. Then, the energy can be obtained from the incident energy (E_i) by Fermi chopper and the positions of detectors by TOF method.

$$\hbar\omega = E_i[1 - (\frac{L_2}{\tau\sqrt{\frac{2E_i}{m}} - L_s})^2] \,, \tag{3.98}$$

where *m* is the neutron mass, and L_2 = L_d - L_s, which is the distance between the sample and detectors.

From the conservation laws of the momentum and energy of the excitation, the momentum transfer can be expressed as,

$$Q^2 = \frac{2mE_i}{\hbar^2}(2 - \frac{\hbar\omega}{E_i} - 2\sqrt{1 - \frac{\hbar\omega}{E_i}cos2\theta) \,, \tag{3.99}$$

and can be determined by substituting Eq. (3.98) into Eq. (3.99).

In this thesis, polycrystalline samples are discussed and only the magnitude of the momentum transfer is relevant,

$$Q = \frac{1}{\sqrt{2.072}}[2E_i(1 - cos2\theta\sqrt{1 - \frac{\hbar\omega}{E_i}}) - \hbar\omega]^{1/2}\,, \tag{3.100}$$

In this TOF approach, the longer the neutron flight path, the better resolution. However, the total surface of detectors is finite due to the spatial and monetary constraints and there is a trade-off between the length of the flight path and the solid-angle coverage.

Because the flux of neutrons in a monochromatic beam is low, the quantities of samples need to be several grams or tens of grams. The typical beam sizes are on the order of a few centimeters. However, another problem comes out from this sample size, the multiple scattering events must be minimized. Typically, the elastic cross-section is much larger than its inelastic part, hence the multiple scattering mostly involves several elastic scattering or a combination of one elastic scattering and one inelastic scattering. Due to the neutrons involved in an apparent elastic scattering event travel extra distances inside the sample, they will reach the detector with a delay and there exists an apparent energy loss. Multiple scattering is very hard to correct, and as a result the thin samples will reduce the number of such processes. A typical value is to make samples that scatter 10% of the incident neutrons, limiting double elastic scattering events to less than 1%. This important and unfortunate consequence waste most of the already scarce incident neutrons.

3.5.3 Pharos and ARCS

4.4.2.1) Pharos

Pharos is a direct-geometry TOF spectrometer at the Lujan Center of Los Alamos Neutron Science Center (LANSCE), Los Alamos National Laboratory (LANL). In LANSCE, Los Alamos Meson Physics Facility (LAMPF) is one of the world's most powerful linear accelerator, 20Hz, and the facility is capable of accelerating protons up to 800 million electron volts.

Fig. 3.9 is the schematic diagram of Pharos. The instrument is designed for studies of fundamental excitations in condensed-matter systems. The sample is positioned 20 *m* from a chilled-water moderator and the distance from the sample to detectors is 4 *m*. There are 375 meter-long

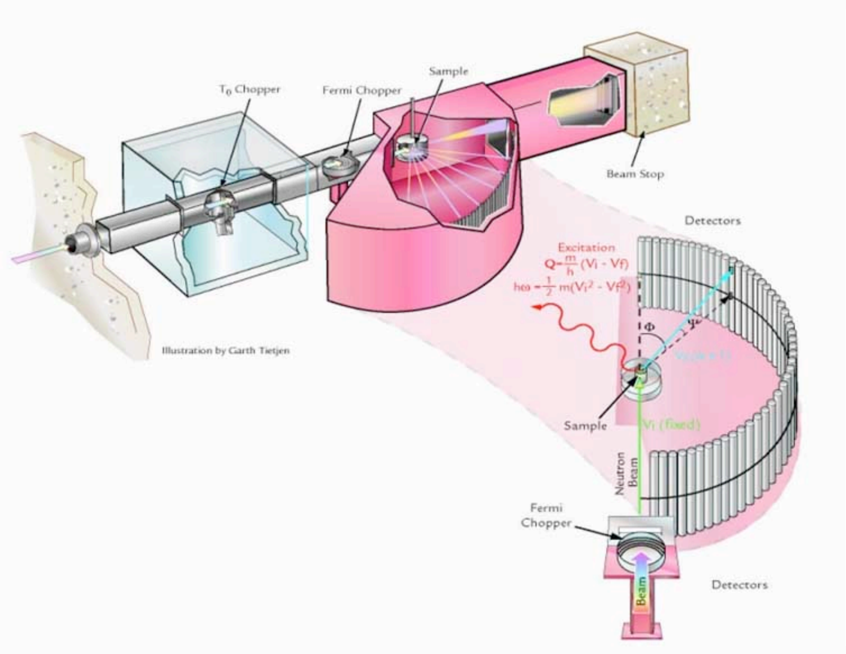

Figure 3.9 Direct-geometry TOF neutron spectrometer, Pharos.

and position-sensitive detectors, which cover a total area of 10 *m*^{2}. The detectors are housed in an evacuated, shielded flight path and covering scattering angles between -10° and 145°. The monochromatic incident energies are selected by a high-speed Fermi chopper, which is effectively a drum with a 10 *cm* diameter. Fermi chopper has a hole through the middle, which is filled with alternating sheets of neutron absorbing material (slats) and transparent material (slits). Both the slits and slats are curved, and the specific energy ranges are optimized by the radius of curvature and the slit(slat) ratio. For Pharos, the incident energies range from 10 *meV* to 2 *eV*. Furthermore, the incident energy resolution is also decided by the rotating velocity of the Fermi chopper. For Pharos, the typical Fermi chopper frequencies should be at multiples of 20 *Hz*, which is the frequency of the neutron pulse, and the resolution is normally in the range from 2% to 4% of E_i.

4.4.2.2) ARCS

ARCS is the acronym for Angular-Range Chopper Spectrometer. It is a direct-geometry TOF spectrometer at the Spallation Neutron Source (SNS) of Oak Ridge National Laboratory (ORNL). For SNS, the neutrons are produced by the following manners: First, the negative hydrogen ions (a proton with two electrons) are generated in pulses; second, the hydrogen ions are accelerated to 1 *GeV* by a linear accelerator; third, the electrons are stripped off the ion and the protons are concentrated into a 2 *MW* proton beam of less than 1 μs pulses at 60 *Hz* in an accumulator ring; fourth, the protons are directed at a liquid mercury target in the target building, which ejects 20 to 30 neutrons per mercury nucleus hit by a proton. Due to the most intense pulsed neutron beams in the world, it can provide a high neutron flux at the sample, which makes it as the best neutron sourse in the world now, and a large solid angle of detector coverage.

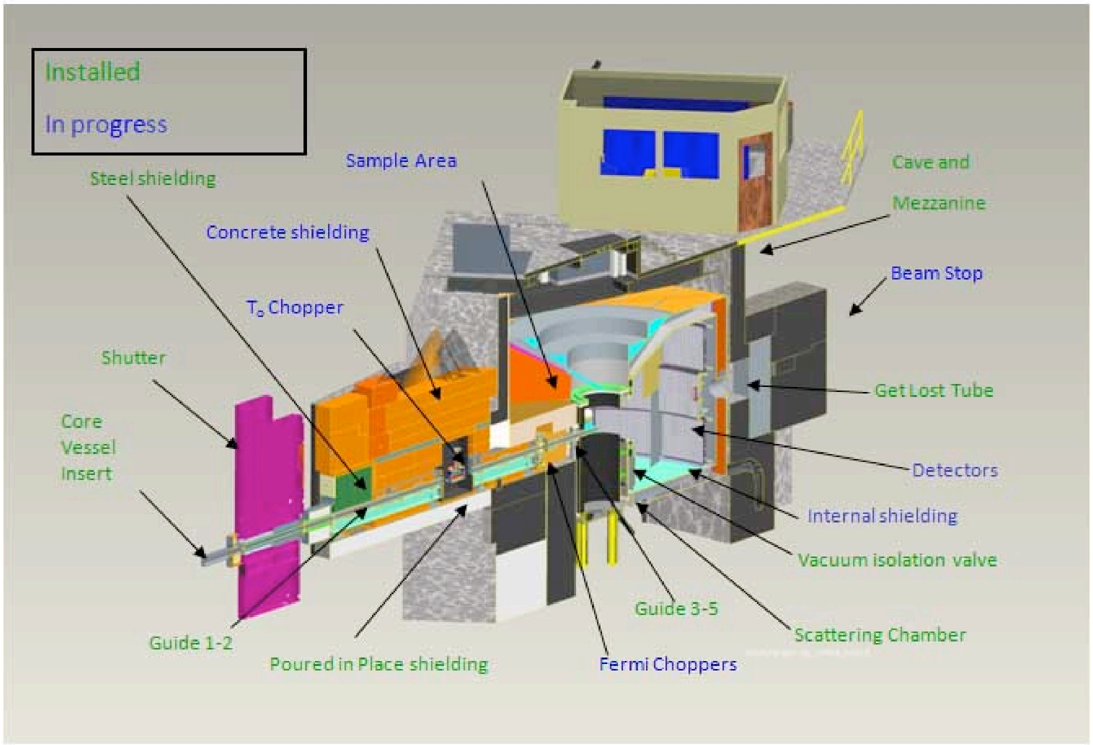

Figure 3.10 Direct-geometry TOF neutron spectrometer, ARCS.

The instrument is used to study the science of dynamical processes in materials. The measured excitation energies in materials and condensed matter are from a few *meV* to several hundred *meV*.

Fig. 3.10 shows the schematic diagram of ARCS. The instrument is very similar to Pharos except the detector shape: The detectors are 3D and set up at 3 levels, e.g. upper, middle, and down, which makes the horizontal detector coverage from -28° to 135° and the vertical detectors coverage from -27° to 26°. Furthermore, the distances between the neutron source and Fermi chopper, between the Fermi Chopper and the sample, and between the sample and the detector are shorter than the relative ones of Pharos, they are 11.6 *m*, 2.0 *m*, and 3.0$\sim$ 3.4 *m* cylindrical geometry respectively. The shorter distances lead to the lower energy resolution of ACRS, 2$\sim$5%

E_i.

LFO have been measured on both Pharos and ARCS and shows in Fig. 3.11. The experiment temperature is T = 10 K and the incident energies are E_i = 160 meV (Pharos) and 177.95 meV (ARCS), respectively. The data spectrum agrees with each other very well.

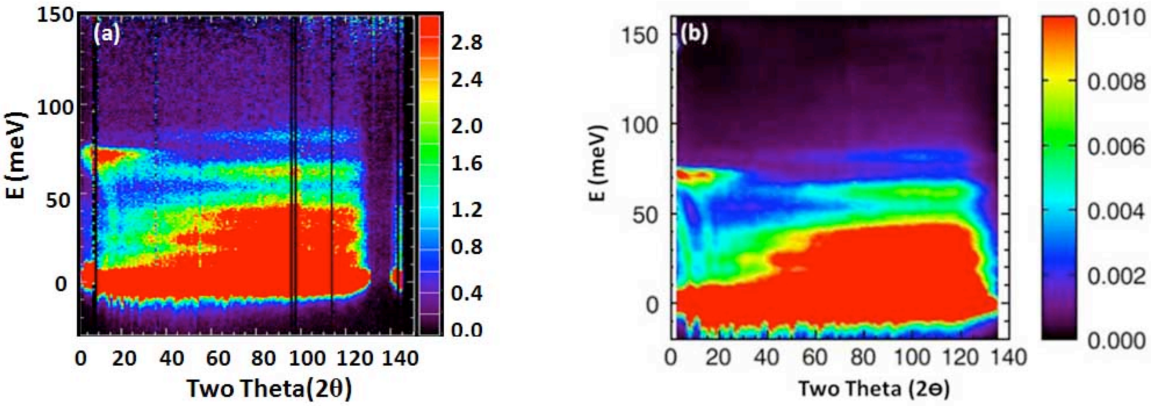

Figure 3.11 Inelastic neutron scattering intensity of LaFeO$_3$ at T = 10 K on (a) Pharos with E_i = 160 meV, and (b) ARCS with E_i = 177.95 meV.

3.6 Data Reduction

Based on the previous discussion in section 3.3 and 3.4, we know the relationship between scattering function, S(Q, ω), and Q (or 2θ): in the low Q (or 2θ) region, spin-wave and phonon scatterings coexist; in the high Q (or 2θ) region, the spin-wave scattering is very weak and phonon scattering is very strong, Fig. 3.12.

However, the measured data (I) is not the exact partial differential inelastic cross section ($\frac{d^2\sigma}{d\Omega dE'}$) data due to the background and instrument resolution. the final intensities is the convolution of the cross section with the experimental resolution function,

$$I(\mathbf{Q}_0, \omega_0) = \int \frac{d^2\sigma}{d\Omega dE'} R(\mathbf{Q} - \mathbf{Q}_0, \omega - \omega_0) d^3\mathbf{Q} d\omega \,, \tag{3.101}$$

where $R(\mathbf{Q}, \omega)$ is the resolution function which can be calculated from the experimental configuration parameters.

Since the integrated data include not only the signal of the sample, but also the signals from the background, such as empty can, sample holder, and so on. In order to get the exact (more accurate) signal of the sample, the empty can was measured alone; then, subtracting the current normalized data of the empty-can run from raw measurement normalized data obtains the sample data,

$$I_{2\theta}(\omega) = I_{2\theta}^{raw}(\omega)/A^{raw} - I_{2\theta}^{can}(\omega)/A^{can}\,, \tag{3.102}$$

where $I_{2\theta}^{raw}(\omega)$ and $I_{2\theta}^{can}(\omega)$ are the current normalized raw total and empty can data, respectively, $I_{2\theta}\,(\omega)$ is current normalized data of the sample, and $A^{raw}(A^{can})$ is the normalized proton current of the neutron source for the related sample(empty can) measurement.

In order to compare data from different samples, the total intensity $I_{2\theta}^{tot}(\omega)$ is normalized from sample raw data ($I_{2\theta}\,(\omega)$) by the sample mole numbers (*M*),

$$I_{2\theta}^{tot}(\omega) = \frac{I_{2\theta}(\omega)}{M}\,, \tag{3.103}$$

The angle integrated intensity can be expressed as,

$$I_{\triangle 2\theta_{1,2}}(\omega) = \int_{2\theta_1}^{2\theta_2} I_{2\theta}^{tot}(\omega) d2\theta\,, \tag{3.104}$$

Actually, $I_{\triangle 2\theta_{1,2}}(\omega)$ is proportional to the scattering function,

$$I_{\triangle 2\theta_{1,2}}(\omega) \propto \int_{2\theta_1}^{2\theta_2} S(2\theta,\omega) d2\theta\,, \tag{3.105}$$

At last, the magnetic scattering in sample was obtained by subtracting the high angle phonon related data from low angle data after scaling by a constant factor,

$$\begin{array}{l} I_{2\theta}^{phonon}(\omega) = I_{2\theta}^{H.A.}(\omega) \\ I_{2\theta}^{mag}(\omega) = I_{2\theta}^{L.A.}(\omega) - \alpha I_{2\theta}^{H.A.}(\omega) \end{array}\,, \tag{3.106}$$

where $I_{2\theta}^{L.A.}\,(\omega)$ is the normalized intensity integrating over low angle range, $I_{2\theta}^{H.A.}\,(\omega)$ is the normalized intensity integrating over high angle range, $I_{2\theta}^{mag}\,(\omega)$ is the normalized magnetic intensity, and α is the scale factor.

Example:

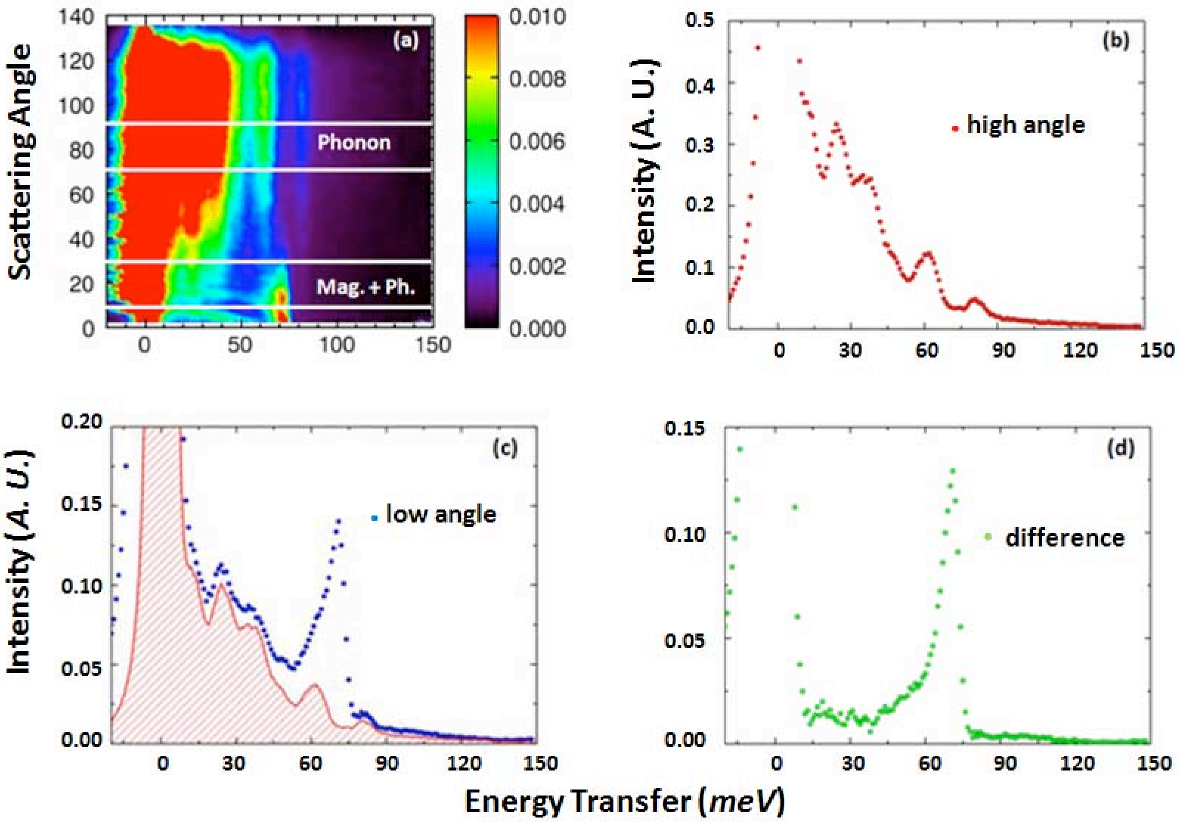

Figure 3.12 (a) Inelastic neutron scattering intensity of $LaFeO_3$ (color scale) versus scattering angle and energy transfer on ARCS at T = 10 K and E_i = 160 meV. Horizontal white lines delineate regions where phonon and magnetic scattering are isolated. (b) Neutron intensity summed over the angle range from 75 - 95° originating from phonons (red dots). (c) Neutron intensity summed over the low angle range from 7 - 30° (blue dots) and phonon background from scaled from high angle sum (red hatched region) (d) Isolated magnetic scattering ($I^{mag}_{2theta}(\omega)$) from LFO (green dots).

The INS data of LFO on Pharos at T = 10 K with E_i = 160 meV is taken as an example, Fig. 3.12(a). The data summed over the high angle range of 2θ = 75° $\sim$ 95° contain only phonon scattering, Fig. 3.12(b), while the data within the low angle range of 10° $\sim$30° contain scattering from both phonons and spin waves, Fig. 3.12(c). The magnetic scattering in LFO sample was obtained by subtracting the high angle phonon related data from low angle data after scaling by a constant factor, Fig. 3.12(d). Since Fe ion is the only magnetic ion in LFO, $I^{mag}_{2\theta}$ $(\omega) = I^{Fe}_{2\theta}$ (ω).

For the resulting magnetic intensity for LFO at 10 K: there is only one peak, ~ 71 meV. The strong peak at 0 meV is elastic scattering.

Bibliography

[1] G. L. Squires, *Introduction to the theory of thermal neutron scattering*, Cambridge University Press. 1996

[2] R. J. McQueeney, *Lattice effcts in high-temperature superconductors*, UMI, 1997

[3] O. Delaire, *The Phonon Entropy of Transition Metals and Alloys*: *Effects of Impurities and of a Martensitic Phase Transition*, http://resolver.caltech.edu/CaltechETD:etd-05262006-160244, 2006

[4] L. V. Hove, Physics Review, 95 (1954) 249

[5] G. Placzek, Physics Review, 86 (1952) 377

[6] R. J. McQueeney, J.-Q. Yan, S. Chang, and J. Ma Physical Review B 78, 184417 (2008)

[7] F. Hippert, E. Geissler, J. L. Hodeau, E. Lelievre-Berna, and, J. Regnard, *Neutron and X-ray Spectroscopy*, Springer 2006

CHAPTER 4. Sample Synthesis and Characterization

4.1 Sample Growth Methods and Description

Polycrystalline $R\mathrm{FeO_3}$ (RFO) and $R_{1/3}\mathrm{Sr_{2/3}FeO_3}$ (RSFO) (R = La, Pr, Nd, Sm, and Y) used in this thesis were prepared by conventional solid-state reaction method. For the parent compounds RFO, the stoichiometric amounts of La_2O_3, Nd_2O_3, Pr_6O_{11}, Sm_2O_3, Y_2O_3, and Fe_2O_3 were mixed by grinding in a mortar with a pestle. Prior to the synthesis, La_2O_3, Nd_2O_3, and Sm_2O_3 were treated at 960°C 20 hours in air to remove absorbed water. The mixtures were transfered to an Al_2O_3 crucible and calcined several times in air at temperatures of 1100 °C and 1200 °C respectively for 24 hours. Then, the press-formed pellets were sintered in air at 1250°C and 1350°C for 30 hours, respectively.

For the doped compounds $R_{1/3}\mathrm{Sr_{2/3}FeO_3}$ (RSFO), the pre-heated La_2O_3, Nd_2O_3, Pr_6O_{11}, Sm_2O_3, or Y_2O_3 were mixed with $SrCO_3$ and Fe_2O_3 stoichiometrically. Then, the homogeneous mixtures were calcined several times in air at temperatures of 1100 °C and 1200 °C respectively for 24 hours. After regrinding, the resulting powder was pressed into pellets and sintered in air at 1250°C and 1350°C for 30 hours each. To form the oxygen content, the pellets were annealed in oxygen atmosphere. As the ionic size decreasing from La^{3+} to Y^{3+}, the oxygen is easy lost from the compound. Hence, the annealing conditions are different for different samples: LSFO was annealed in oxygen environment for 72 hours at 600°C, which is decided by the measurement of thermal gravity analysis(TGA); PSFO and NSFO were annealed under oxygen pressure (10 bar) at 600°C for 72 hours; SSFO and YSFO were annealed under oxygen pressure (100 bar) at 600°C for 24 hours. The 1- and 10-bar annealings were processed in Ames Laboratory, and the 100-bar one used the furnace of Prof. *José A. Alonso* in Spain.

4.2 Sample Characterization

4.2.1 Powder X-ray Diffraction

Room temperature powder X-ray diffraction (XRD) patterns were performed on a Rigaku Miniflex X-ray diffractometer with $Cu\ K_\alpha$ radiation to confirm phase purity and to determine the lattice parameters of the samples. The geometry setup consisted of a fixed x-ray tube, a sample holder, and detector which moved in a horizontal plane. The powders were attached to glass holder and the surface was vertical to the incident beam. The typical measurement of 2θ scan was carried out from 20° to 90° with a step 0.02°. The collected data were analyzed by the Rietica, Rietveld refinement program. In order to reduce the fitting errors, usually silicon powder (a = 5.43088 Å) was added as an internal standard.

The procedures for the specimen preparation were as follows: (i) mark the sample area on a glass rectangle plate by an aluminum mask; (ii) uniformly coat the sample zone with a thin layer of oil or vaseline; (iii) spread the finely ground powders into the sample area by gently tapping or shaking the plate to make the powders spread evenly; (iv) invert the plate to dislodge the excess powder; (v) repeat steps (iii) and (iv) until enough powder adheres to the plate; (vi) clean the powders outside of the marking area.

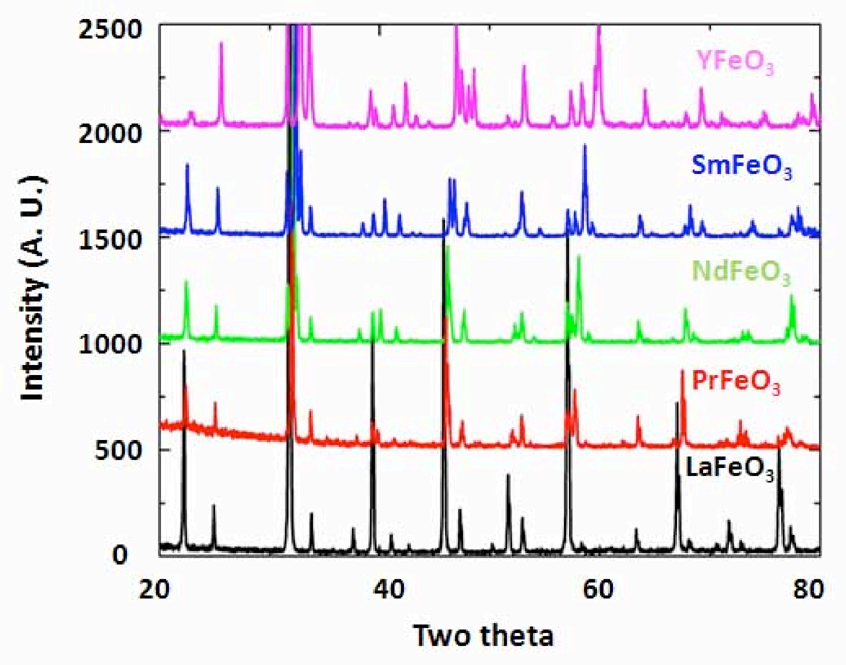

Figure 4.1 X-ray diffraction patterns for *R*FO at room temperature (Cu K_α radiation).

With the above procedure, random orientation of the fine powder could be obtained. However, the amount of powder on the surface of the plate is small and the background contributions from vaseline and glass substrate can not be ignored. In order to get good signals from X-ray spectrum, the oil needs to be less and the amount of the sample powders should have more.

i) X-ray diffraction of $R\mathrm{FeO}_3$ (R = La, Pr, Nd, Sm, and Y)

Room temperature XRD of *R*FO were found to be single phase and could be fitted very well with an orthorhombic structure, Fig. 4.1. The data were analyzed by the GSAS and FullProf Suite refinement programs to determine the nuclear and magnetic structures [1, 2]. The space group is *Pnma* with the lattice constants listed in Table 4.1. The values of unmarked line of each constants are measured ourselves, the labeled lines are reported data. The lattice parameters decreased as the decreasing of R^{3+} ionic size in *R*FO.

Table 4.1 Lattice parameters of rare-earth orthoferrites.

	LaFeO_3	PrFeO_3	NdFeO_3	SmFeO_3	YFeO_3
Space Group	*Pnma*	*Pnma*	*Pnma*	*Pnma*	*Pnma*
Lattice Constant(Å)					
a	5.562 ± 0.011	5.572 ± 0.011	5.588 ± 0.011	5.592 ± 0.011	5.592 ± 0.011
	$5.565^\dagger$	$5.578^\dagger$	$5.587^\ddagger$	$5.592^\dagger$	$5.592^\dagger$
b	7.854 ± 0.016	7.787 ± 0.016	7.762 ± 0.016	7.711 ± 0.015	7.603 ± 0.015
	$7.862^\dagger$	$7.810^\dagger$	$7.761^\ddagger$	$7.711^\dagger$	$7.603^\dagger$
c	5.557 ± 0.011	5.483± 0.011	5.451 ± 0.011	5.394 ± 0.011	5.283 ± 0.010
	$5.556^\dagger$	$5.495^\dagger$	$5.450^\ddagger$	$5.394^\dagger$	$5.283^\dagger$
bond length(Å)					
Fe - O(1)	2.002 ± 0.004	2.004 ± 0.004	2.005 ± 0.004	2.001 ± 0.004	2.001± 0.004
Fe - O(2)	2.004 ± 0.004	2.006 ± 0.004	2.007 ± 0.004	2.007 ± 0.004	2.005 ± 0.004
Fe - O(2)	2.005 ± 0.004	2.015 ± 0.004	2.017 ± 0.004	2.030 ± 0.004	2.032 ± 0.004
bond angle					
∠ Fe - O(1) - Fe	157.6° ± 0.3°	153.3° ± 0.3°	151.2° ± 0.3°	148.9 ° ± 0.3°	143.2° ± 0.3°
∠ Fe - O(2) - Fe	157.5° ± 0.3°	152.4° ± 0.3°	151.4° ± 0.3°	148.8 ° ± 0.3°	145.2° ± 0.3°

† reference [3], ‡ reference [4, 5].

In addition, the bond lengths (Fe - O) and angles (∠ Fe - O - Fe) are also included: the average bond length is increasing, while the angles are decreasing. Therefore, the perovskite of $\mathrm{Fe\text{-}O}_{6/2}$ in *R*FO is distorted more and more with the *R*-site substitution from La to Y.

ii) X-ray diffraction of $R_{1/3}\mathrm{Sr}_{2/3}\mathrm{FeO}_3$ (R = La, Pr, Nd, Sm, and Y)

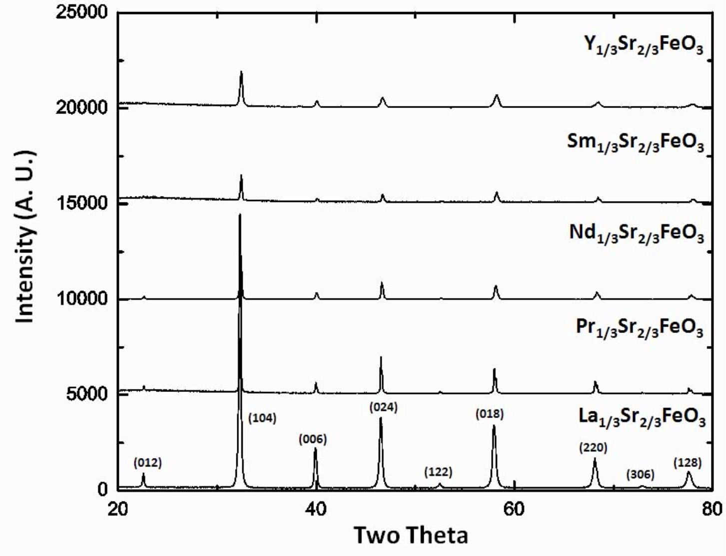

Figure 4.2 X-ray diffraction patterns for *R*SFO at room temperature (Cu K_α radiation).

Room temperature XRD of *R*SFO is shown in Fig. 4.2 and the single phase is observed. Usually, the symmetry of a rhombohedral sample is very close to cubic structure and the phase is labeled by the cubic constant. Fig. 4.3 shows the simulating plot by GSAS with an rhombohedral structure, space group $R\bar{3}c$, Table 4.2. The values of first line are collected by our sample and the data of † line are reference. the Similar to the parent compound *R*FO, the lattice constants decrease with the decreasing ionic size of R^{3+} in *R*SFO from La^{3+} to Sm^{3+}. However, both the

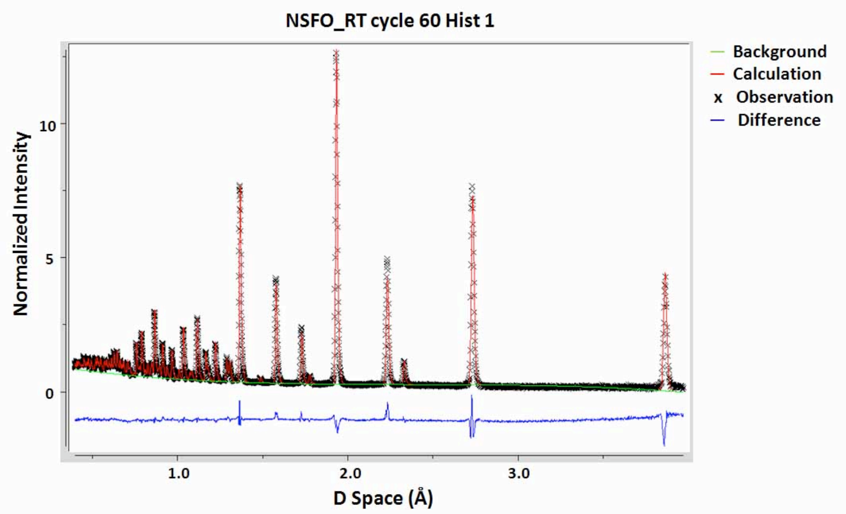

Figure 4.3 Powder neutron diffraction of NSFO at 300 *K*.

bond lengths (Fe-O) and angles (∠ Fe - O - Fe) are decreasing, which is different to the spectra of *R*FO. This is due to the majority *R*-site occupation of Sr^{2+} (2/3), whose ionic radius ($\sim$ 1.12Å) is more close to the radius of Sm^{3+} ($\sim$ 1.13Å) than La^{3+} ($\sim$ 1.22Å). Furthermore, the oxygen stoichiometry can also be fitted with the program, GSAS.

Table 4.2 Lattice parameters of rare-earth orthoferrites *R*SFO.

	LSFO	PSFO	NSFO	SSFO
Space Group	$R\bar{3}c$	$R\bar{3}c$	$R\bar{3}c$	$R\bar{3}c$
Lattice Constant(Å)				
$a = b$	5.482 ± 0.011	5.477 ± 0.011	5.466 ± 0.011	5.459 ± 0.011
	$5.748^{\dagger}$	$5.453^{\dagger}$	$5.468^{\dagger}$	$5.459^{\dagger}$
c	13.413 ± 0.027	13.365 ± 0.027	13.344 ± 0.027	13.318 ± 0.027
	$13.393^{\dagger}$	$13.321^{\dagger}$	$13.356^{\dagger}$	$13.360^{\dagger}$
bond length (Fe - O)	1.941 ± 0.004	1.941 ± 0.004	1.939 ± 0.004	1.939 ± 0.004
bond angle (∠Fe - O - Fe)	$173.2° \pm 0.4°$	$170.5° \pm 0.3°$	$169.3° \pm 0.3°$	$167.6° \pm 0.3°$
Oxygen Deficiency	2.94 ± 0.03	2.97 ± 0.03	2.97 ± 0.03	$--$

†reference 6, 7, 8.

4.2.2 Titration

The oxidation state of iron was determined by iodimetric titration after dissoltion of the samples in hydrochloric acid in closed, carbon dioxide flushed glass containers: the Fe ions with high average valence, +3.67, were reduced into Fe^{2+} ions by I^- ions and I^- ions were oxidized into I_2 molecules or I_3^- ions (I_2 + I^-); the I_2 molecules were reduced into I^- ions by the standard $Na_2S_2O_3$ solution; from the mass of dissolved iron oxide samples and the used volume of $Na_2S_2O_3$ solution, the final valence of Fe ion could be calculated and the oxygen content was obtained. Because I_2 molecules or I_3^- ions were the intermediate products in the whole chemical processing, starch was used as an indicator. (The preparation of the solutions, the experimental procedures, and calculations are attached in appendix.)

Some results are listed:

As the standard $[S_2O_3^{2-}]$ has been decided, the oxygen stoichiometry is decided,

Thus, the average oxygen stoichiometry [9],

$$\bar{y} = \frac{y_1 + y_2 + y_3}{3} = 2.9504 \pm 0.001\,, \tag{4.1}$$

Table 4.3 The pre-titration of $[S_2O_3^{2-}]$ of standard solution.

	V_{init} (*ml*)	V_{end} (*ml*)	$\Delta\ V$ (*ml*)	$[S_2O_3^{2-}]$ (*mol/l*)
1	24.40 ± 0.005	37.25 ± 0.005	12.85 ± 0.010	0.0778 ± 0.0001
2	6.10 ± 0.005	18.95 ± 0.005	12.85 ± 0.010	0.0778 ± 0.0001
3	18.95 ± 0.005	31.77 ± 0.005	12.82 ± 0.010	0.0780 ± 0.0001

Table 4.4 The oxygen stoichiometry of $\mathrm{La}_{1/3}\mathrm{Sr}_{2/3}\mathrm{FeO}_y$.

	m (*g*)	V_{init} (*ml*)	V_{end} (*ml*)	*x*	*y*
1	0.1080 ± 0.0001	26.88 ± 0.005	37.26 ± 0.005	1.564 ± 0.002	2.948 ± 0.001
2	0.1202 ± 0.0001	28.90 ± 0.005	40.57 ± 0.005	1.579 ± 0.002	2.956 ± 0.001
3	0.1229 ± 0.0001	15.31 ± 0.005	27.09 ± 0.005	1.559 ± 0.001	2.946 ± 0.002

Compared to the fitting result of GSAS, 2.94 ± 0.03, the titration result is more accurate.

4.2.3 Magnetization

The dependence of magnetization on the temperature and magnetic field was measured to determine the antiferromagnetic transition (Verwey transition) temperatures and also to determine the sample quality. The instrument is a superconducting quantum interface device (SQUID) magnetometers MPMS-XL manufactured by Quantum Design, Inc. The measurements were performed in the temperature interval $5K \leq T \leq 300K$ with applied field up to 50 *kOe*. The errors in the temperature, magnetic field, and magnetic moment were 0.5%, 1*Oe*, and 1%, respectively. The temperature dependence of magnetization, *M*(*T*), under a fixed magnetic field was measured in two different modes: The first one was called zero-field-cooled (*ZFC*) mode. The sample was first cooled down from a temperature well above its Neel temperature (T_N) under zero magnetic field. Then, a constant magnetic field was applied at the lowest temperature and then the temperature dependence of magnetization was measured while warming up. The second one was called the field-cooled (*FC*). Contrary to the *ZFC* mode, the magnetic field was not zero as the sample was cooled down from a temperature well above T_N. And the same magnetic field was applied while the sample was warmed up from the lowest temperature, then the temperature dependence of magnetization was recorded. The isothermal *M*(*H*) measurement was carried out at 5 *K* after thermal demagnetization at 300 *K* and then zero field cooling down to the measurement temperature.

The SQUID specimen were prepared as follows: (i) select one small piece of the bulk ($\sim$ 50 *mg*) and weight it; (ii) use gelatine capsule as a sample holder and fill the free space of the capsule with cotton to fix the sample; (iii) put the capsule inside a straw and fix the capsule by nonmagnetic material (plastic); (iv) attach the straw to the instrument sample holder and load the sample into an antechamber, where the sample and the deliver chamber are pumped several times to make sure that there is no air inside it; (v) deliver the sample to the measurement chamber and adjust the length of the holder to keep the capsule at the center of magnetic coil of SQUID; (vi) set up the program.

i) Magnetic Susceptibilities of *R*SFO:

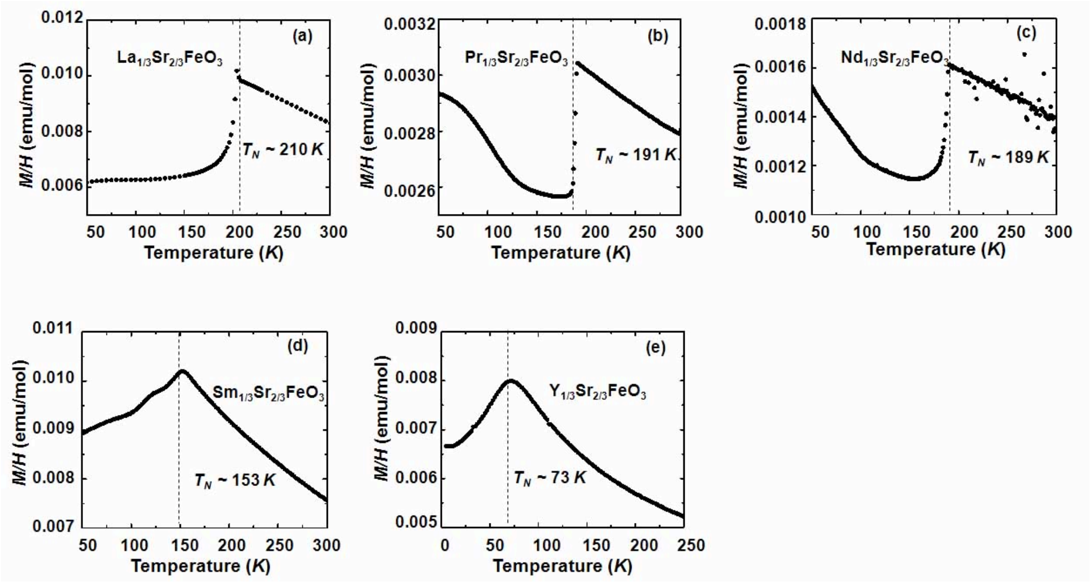

Figure 4.4 Magnetic properties of *R*SFO as determined by ZFC SQUID measurement.

The magnetic susceptibility and magnetization of *R*SFO were measured by ZFC on heating in a magnetic field of 1 *kOe* with the temperature range from 5 *K* to 300 *K*, Fig. 4.4. The signature of a magnetic transition were obtained in LSFO, PSFO, NSFO, SSFO, and YSFO were observed.

ii) Isothermal *M*(*H*) measurement of YSFO:

Because the antiferromagnetic signal of YSFO was very broad, the *M*(*H*) was checked at 5 *K*. From Fig. 4.5, it was observed: i) the values of *M* by increasing field agree with the values of the decreasing field, which means that the major domain of YSFO is antiferromagnetic; ii) there is a jump around zero field, Fig. 4.5(b), hence it is ferromagnetic inside the sample which could be considered as the result of oxygen vacancies.

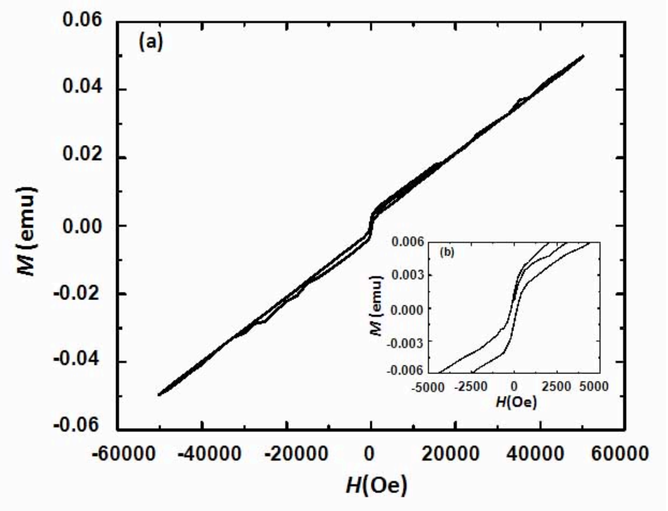

Figure 4.5 *M*-*H* of YSFO at 5 *K*.

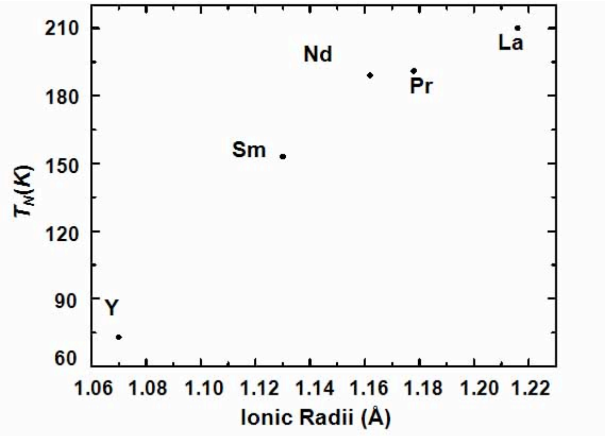

Figure 4.6 The relationship between the radii of the R^{3+} ions with *CN* = 6 and the magnetic transition temperatures of *R*SFO.

Fig. 4.6 showed the relationship between the ionic radii of the rare earth ions and T_N as determined from SQUID measurement. As the the ionic radii decreased, T_N decreased, which agreed previous reports [10].

4.2.4 Electrical Resistivity

Since the Verwey transition is a metal-insulator transition (MIT), the electrical resistivity is measured to determine the first order transition temperature (T_{CO}) of *R*SFO. Based on the following equation, low-temperature resistance can be measured by the Quantum Design Physical Properties Measurement

System PPMS-14 and PPMS-9 instrument.

$$R = \rho \frac{l}{A}\,, \tag{4.2}$$

where ρ is the resistivity constant, *l* is the distance between the voltage probes, and *A* is the vertical area of the sample.

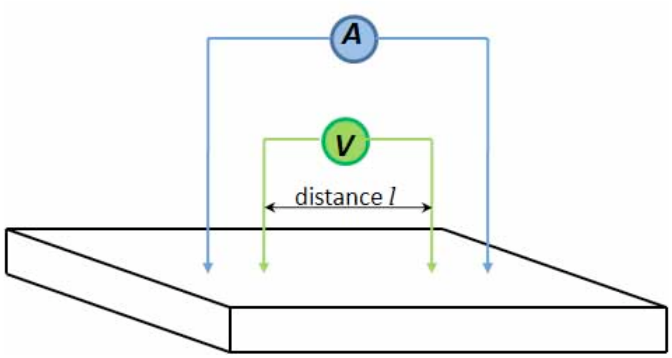

Figure 4.7 Four-probe technique on the electrical resistance measurement.

The four-probe technique was applied, Fig. 4.7, in the interval temperature from $4\ K < T < 300\ K$. The geometry of the specimen was a rectangular with the typical size of $0.5 \times 0.5 \times 3\ mm^3$. Four pieces of the copper wire were attached to the surface of the specimen via an Indium pad or silver epoxy; the inner two copper wires picked up the voltage while the other two applied a small current. The specimen was mounted on a small piece of mica glass with a very small amount of thermal compound. The whole assembly was put on a round thin sheet of copper with a copper cap to shield it. The cooling system was a closed-circle refrigerator with He gas as refrigerant. A Lakeshore silicon diode temperature sensor was put on the cooling head. Temperature was monitored and controlled by a Lakeshore temperature controller Model 340. Current was provided with a Keithley Model 224 Current Source and voltage was recorded with a Keithley 181 nanovoltage meter. Data were recorded under GPIB control of these instruments with a personal computer. To eliminate the contribution of the bias voltage, opposite direction currents were applied at each measuring point.

This four-probe method with rectangle specimen had been found to be accurate for samples with resistivity higher than $10^{-3}\ \Omega{\cdot}cm$; some uncertainty would be encountered for $\rho \leq 5 \times 10^{-4}\ \Omega{\cdot}cm$. The error mainly came from the measurement of the sample size and/or contact size.

Resistivity properties of SSFO

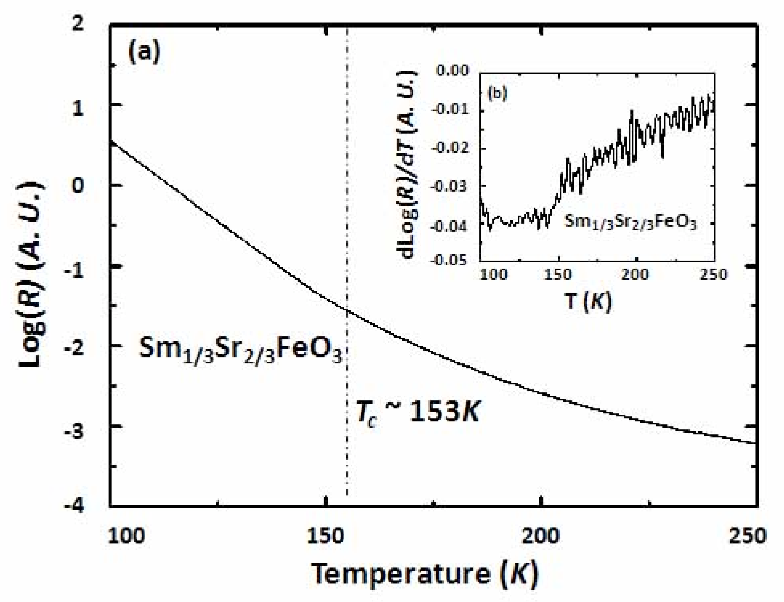

Figure 4.8 Temperature - dependence of the resistivity of SSFO.

The resistivity measurement of SSFO was shown in Fig. 4.8. Because the sample is powder, the resistivity signal was not very clear. We differentiated the logarithm of the resistivity by temperature, Fig. 4.8(b), then the insulator-semiconductor transition temperature is found at $\sim$ 150 *K*, which was as same as T_N obtained from magnetization data.

4.2.5 Specific Heat

The heat capacity is another method to check the phase transition in the *R*SFO compounds. The measurement option of the Quantum Design PPMS instrument was used to measure the temperature dependent specific heat. Usually the data was collected for temperature down to 2 *K*. A relaxation technique was applied in the measurements, in which the sample was briefly heated and then allowed to cool. Then a model that accounted for the thermal relaxation of both the sample and the sample platform was used to fit the thermal response of the samples over the entire temperature response. The samples were attached to the heat capacity platform by Apiezon N grease. In order to subtract the thermal response component of the platform and grease from the final measurement, they were measured separately for the appropriate field and temperature ranges.

Heat capacity of SSFO

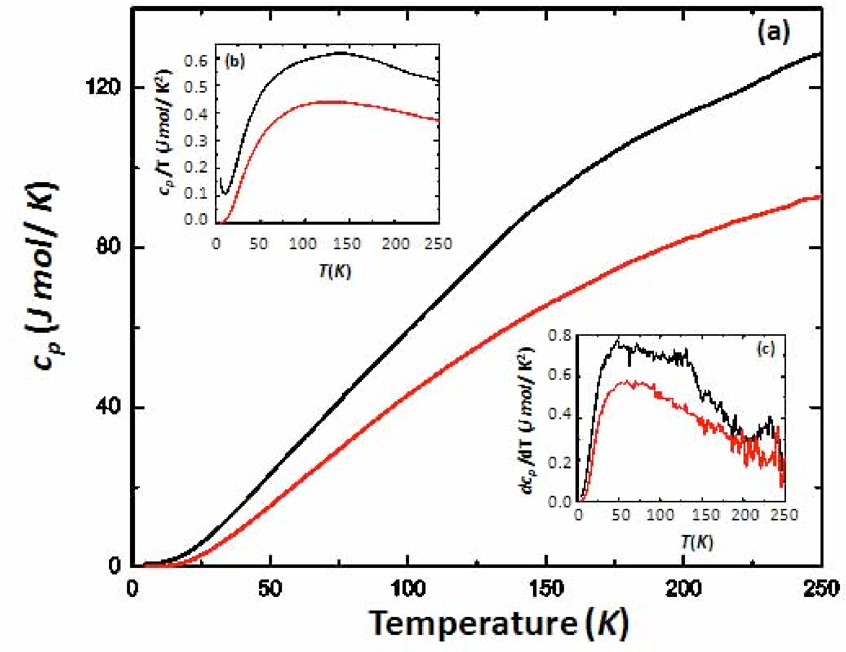

Figure 4.9 Temperature dependence of the heat capacity of SSFO.

Similar as the other rare-earth ferrite except LSFO, SSFO was a complicated sample: there was magnetic properties on both A-site and B-site. Hence, we also measured a nonmagnetic sample with similar lattice structure, LaGaO$_3$(LGO), as a standard. Fig. 4.9(a) shows $c_p(T)$ of SSFO and of LGO measured in the ranges 3 $\sim$ 270 K respectively. Compared to LGO, there were three weak singularities: $T < 10\ K$, $T \sim 150\ K$, and $T \sim 220\ K$. In order to check them, $c_p(T)/T$ and $dc_p\ (T)/dT$ were calculated, Fig. 4.9(b) and (c). In $c_p\ (T)/T$, we observed a pronounced short-range-order tail below 10 K, it should be the antiferromagnetic ordering of Sm^{3+} ions as the case of Nd^{3+} ions [11, 12, 13]; the singularities at 150 K and 220 K were still not prominent. However, they were much clearer in $dc_p\ (T)/dT$ as a bump around 220 K and a jump around 150 K. As discussed before, the bump, $\sim$ 220 K, was one CEF level of Sm^{3+} similar to the case of Nd^{3+} ions [11, 12]; the jump, $\sim$ 150 K, was the signal of charge-ordering of Fe^{3+}, which agreed with the resistivity measurement very well.

4.2.6 Powder Neutron Diffraction

Elastic neutron powder diffraction measurements were performed to determine the possible structural and magnetic order. The magnetic ordering transition temperature, magnetic structure, and the lattice structure can be accurately determined. The instrument was the High-Intensity Powder Diffractometer (HIPD) spectrometer at the Lujan Center, Los Alamos National Laboratory (LANL). HIPD is close to the neutron source (primary flight path = 9 *m*) which resulted in high counting rates. The beam size was 1 *cm* wide and 5 *cm* high. The detectors were located at ±153°, ±90°, ±40° and ±14°, each covering ±5°, therefore, the total momentum transfer range was $0.2 \sim 60$ Å^{-1}. We used standard closed-cycle refrigeration to acquire the neutron diffraction data at different temperatures. Well ground powder (typically $100 \sim 500$ μm) was transfered into the cylindrical vanadium sample can in the glove box filled with dry He gas.

A flat vanadium can was used for Sm-bearing compositions due to the high absorption of Sm. The data were analyzed by the GSAS and FullProf Suite refinement programs to determine the nuclear and magnetic structures [1, 2]. The fitting results of the lattice constants will be discussed in the following XRD section.

i) Powder Neutron Diffraction of RFeO$_3$ (R = La, Pr, Nd, Sm, and Y)

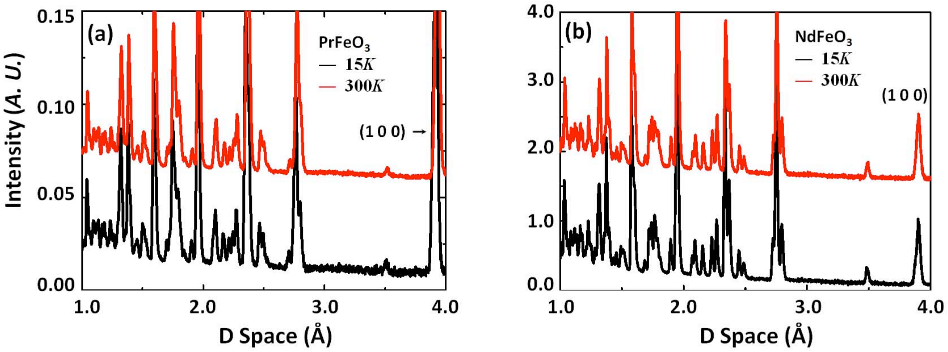

Figure 4.10 Temperature-dependence of PFO and NFO by powder neutron diffraction from 300 *K* to 15 *K*.

The reported T_N of PFO and NFO were around $\sim$ 680 *K*, hence there should be no big difference between base temperature and room temperature. We measured them at 15 *K* and 300 *K*, in Fig. 4.10(a) and (b). There was no big difference between the temperatures except that the intensities are lower in room temperature due to the Debye-Waller effects. The parent compounds are G-type antiferromagnetic and the magnetic peak (1 0 0) is labeled in Fig. 4.10.

ii) Powder Neutron Diffraction of $R_{1/3}$Sr$_{2/3}$FeO$_3$ (R = La, Pr, Nd, Sm, and Y)

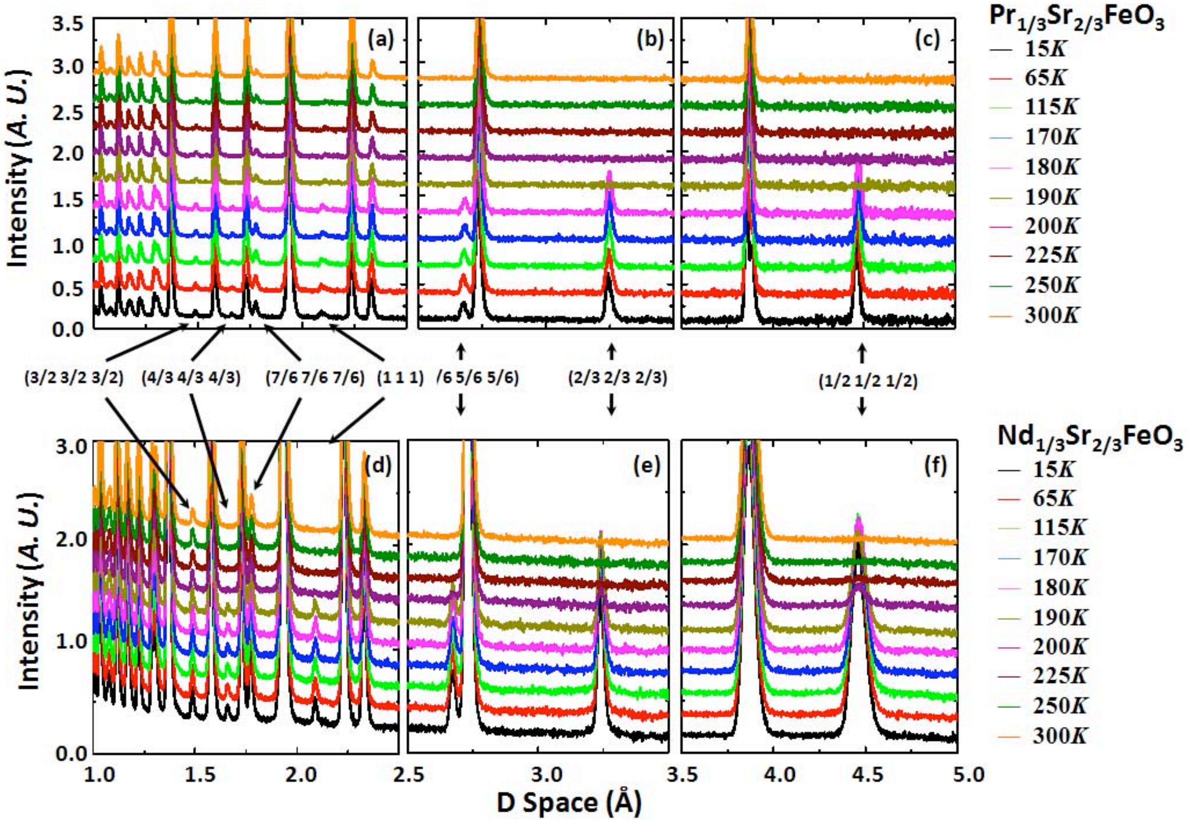

Figure 4.11 Temperature-dependence of PSFO, (a), (b), (c), and NSFO, (d), (e), (f), by powder neutron diffraction from 300 K to 15 K. The arrows show the magnetic Bragg peaks and will be discussed later.

In order to determine the Verwey temperature. PSFO and NSFO were measured at a series of temperatures: 15 K, 40 K, 65 K, 90 K, 115 K, 140 K, 145 K, 150 K, 155 K, 160 K, 165 K, 170 K, 175 K, 180 K, 185 K, 190 K, 200 K, 225 K, 250 K, 275 K, 300 K, Fig. 4.11. Several magnetic Bragg peaks showed up below $\sim$ 190 K for PSFO and below 200 K for NSFO. The temperature dependence of the magnetic order parameter for different Bragg peaks are plotted with the labeled phases in Fig. 4.12 and Fig. 4.13. We can see that the Verwey transition of NSFO was also around $\sim$ 190 K. Therefore, the T_V of NSFO and PSFO were very close to each other.

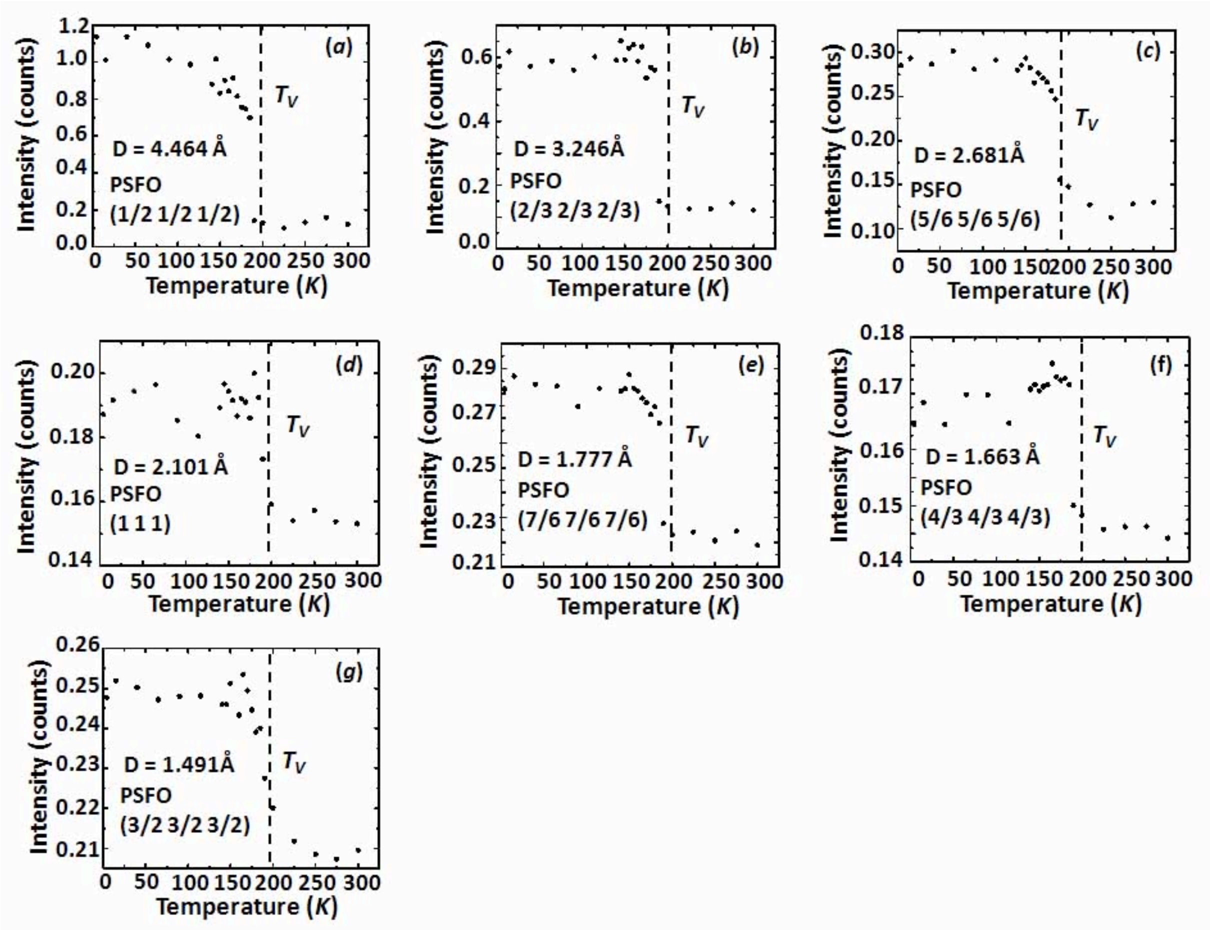

Figure 4.12 Temperature-dependence of PSFO by powder neutron diffraction from 300 *K* to 15 *K*.

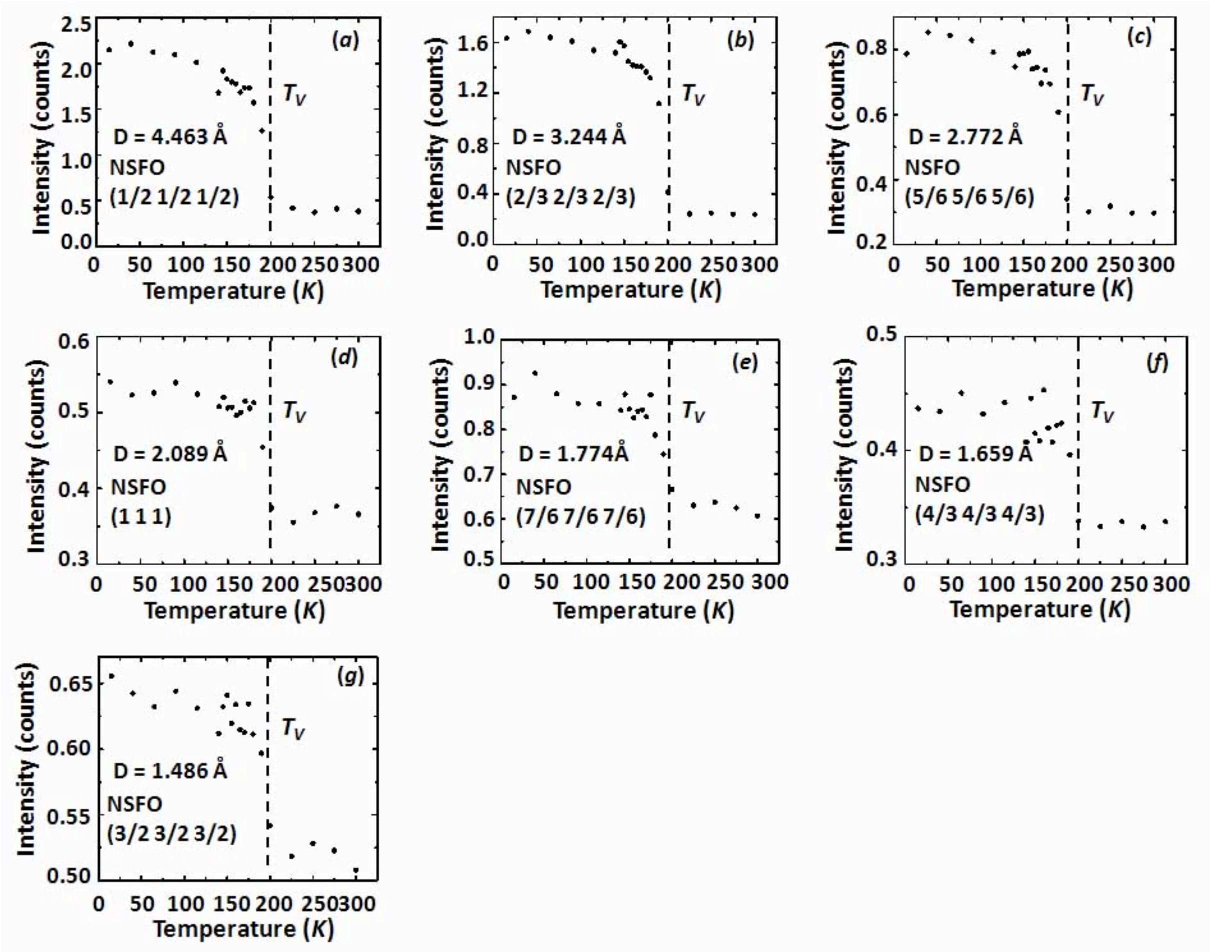

Figure 4.13 Temperature-dependence of NSFO by powder neutron diffraction from 300 *K* to 15 *K*.

Refer to the structure figure in chapter 1, Fig. 1.3, the Fe ions were antiferromagnetically ordered below the magnetic phase transition temperature into $\cdots\uparrow\downarrow\downarrow\downarrow\uparrow\uparrow\cdots$ along (100) direction. Therefore, the magnetic ordering vector should be $(\frac{n}{6}\frac{n}{6}\frac{n}{6})$ and the nuclear superlattice peaks

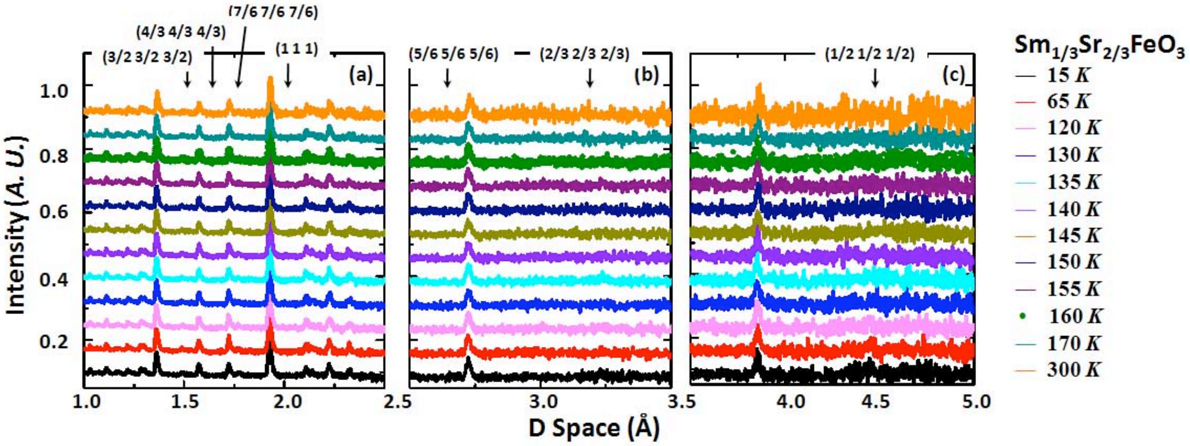

Figure 4.14 Temperature - dependence of SSFO, (a), (b), and (c), by powder neutron diffraction from 300 K to 15 K. There were different intensity steps of the temperatures between (a) and (c).

should appear ($\frac{n}{3}\frac{n}{3}\frac{n}{3}$).

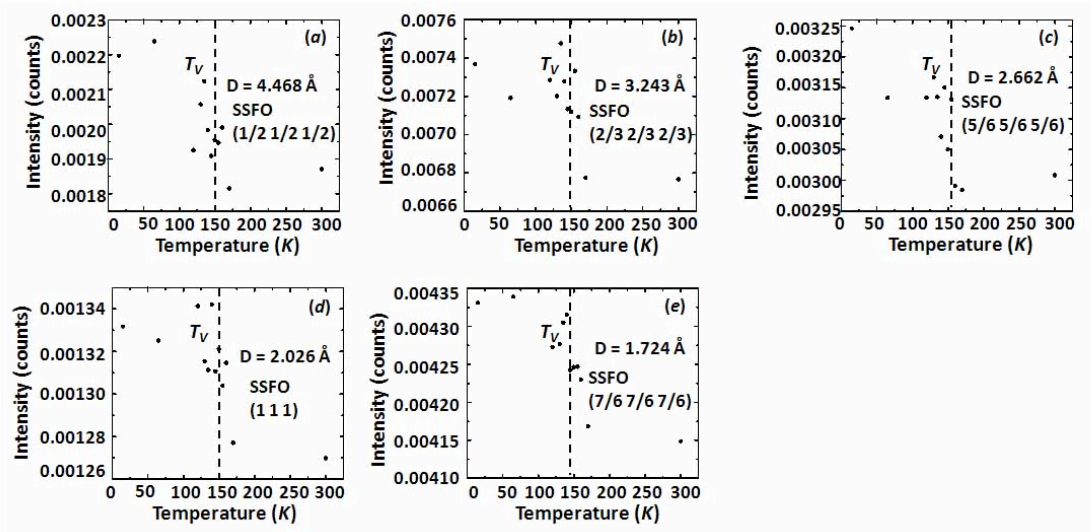

Figure 4.15 Temperature-dependence of NSFO by powder neutron diffraction from 300 K to 15 K.

Due to the high neutron absorption cross-section of Sm^{3+} ion, we measured the sample 3 times longer than PSFO. The magnetic ordering signals were still blurred , Fig. 4.14(a), (b), and (c): except the wavevector ($\frac{7}{6}\frac{7}{6}\frac{7}{6}$), Fig. 4.15(e), the intensities of the other magnetic peaks(bumps) were very hard to be recognized. If we integrated the area of those bumps, we could clearly observed the magnetic Bragg peaks was ordered, Fig. 4.15.

From above measurement, we could easily conclude that it is magnetic ordered. Because the wave vector of the CO superlattice peaks are the double of magnetic peak, it is difficult to observe evidence of CO state from our neutron data. The extra measurement would be needed: resonant x-ray scattering is a very good option [14].

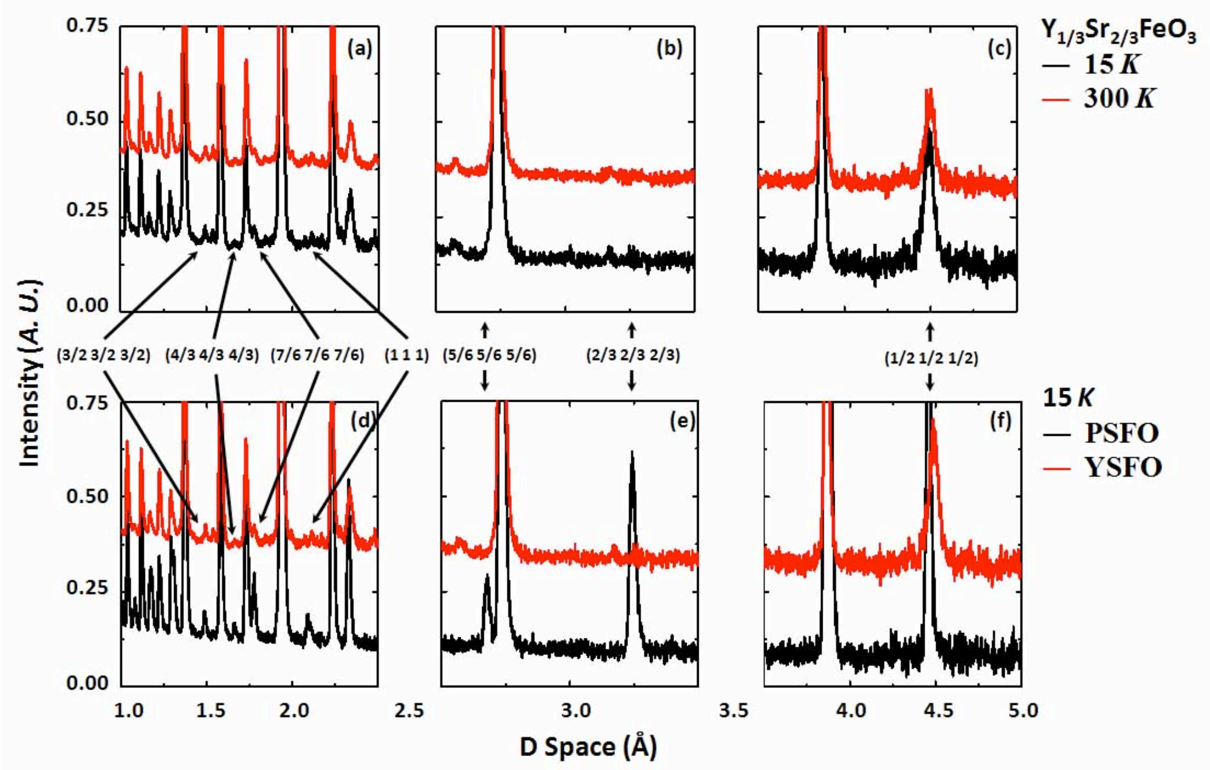

Figure 4.16 The powder neutron diffraction of YSFO at 300 *K* and 15 *K*, (a), (b), and (c); the powder neutron diffraction comparison of PSFO and YSFO at 15 *K*, (d), (e), and (f).

In Fig. 4.16(a), (b), and (c), we could not observe the intensities difference between 15 *K* and 300 *K* expect the Debye-Waller effects, therefore there was not observed magnetic ordering in our YSFO sample. In order to confirm this result, we compared YSFO with PSFO at 15 *K*, Fig. 4.16(d), (e), and (f): Some magnetic phase signals, $(\frac{n}{6}\frac{n}{6}\frac{n}{6})$, were lost. Therefore, it was very hard to confirm the magnetic ordering in YSFO.

4.2.7 Transmission Electron Microscopy

The first direct observation of CO in LSFO was obtained by the transmission electron microscopy (TEM) [15]. The measurement will help us observe the CO superlattice and check the sample quality.

The model of the machine is Philips CM-30 and the operation voltage is 200 *keV*. There were 4 major parts: the electron gun which could provide a beam of electrons exiting from the assembly at some given angle, the electron lens which could focus the parallel rays at some constant focal length, the vacuum system which increased the mean free path of the electron gas interaction, and the CCD camera which helped record the data. The experimental temperature could reach as low as 4 *K* by liquid He cooling system. However, the system was usually cooled by liquid nitrogen, which meant that the lowest experimental temperature was around ~ 80 *K*. In the *R*SFO system, the transition temperature was higher than 100 *K*, which means that liquid nitrogen system was good enough. Based on the Bragg′s law, the signal of the lattice structural refelections due to the space group would be observed as diffraction spots. For the CO compounds, a series of new spots which are the signal of the superstructural refelections will be observed below the Verwey transition temperature.

The TEM samples were made by: (i) grinding the sample into fine powders; (ii) mixing the ground powders with methanol and sieving the mixtures onto the sample support mesh “grid” ; (iii) gently tapping or shaking the holder to make the powders spread evenly and inverting the plate to dislodge the excess powder; (iv) repeating steps (iii) until enough powder adheres to the mesh; (v) cleanning the powders outside of the mesh.

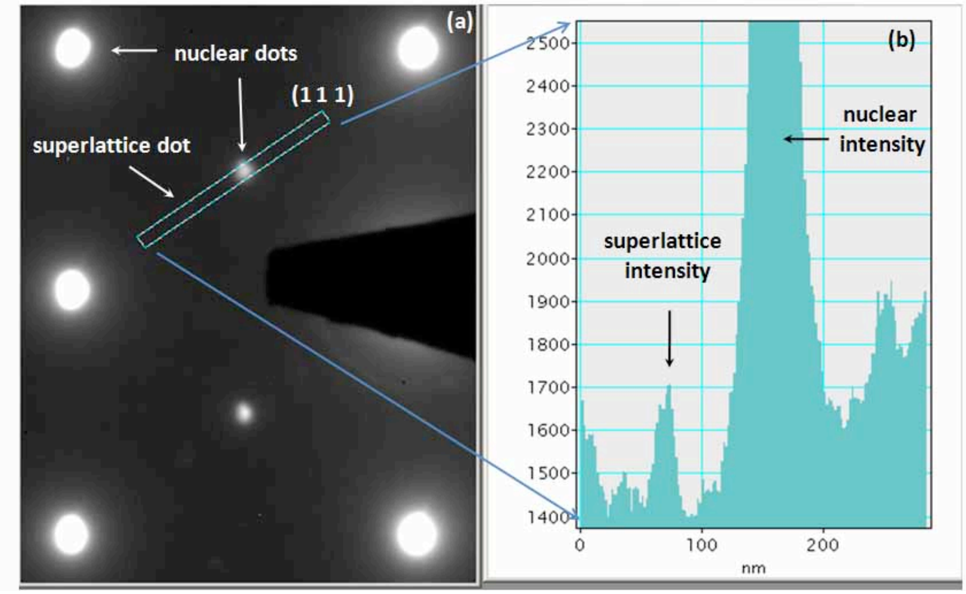

Figure 4.17 Transmission electron microscopy measurement of LSFO at ~ 100 *K*.

TEM of LSFO

TEM measurement of LSFO was carried out at around ~ 80 *K*, which was much lower than the Verwey transition temperature, $T_V \sim 210$ *K*. In Fig. 4.17(a), the big shining spots were the reciprocal lattice vectors in the simple cubic setting and indicated that the electron diffraction patterns is on [0 1 $\bar{1}$] zone axis of a single grain from the powder; beside the lattice vector points, there were a series of Bragg diffraction spots shown up along the $[1\ 1\ 1]_c$ direction and they were the signal of the superstructural reflections. The reflection signals in Fig. 4.17(a) were a little bit inconspicuous due to the powder condition sample, so a slice is cut and the relative intensities of the spots were plotted in Fig. 4.17(b) to help a lot to confirm the reflections. The strongest peak is signal of the simple cubic lattice and the small peak beside it is the magnetic superlattice. Those $(\pm\frac{1}{3}, \pm\frac{1}{3}, \pm\frac{1}{3})$ atomic displacements reflections were induced by CO: Fe^{3+} and Fe^{5+} species showed the ordering along the perovsikte $[1\ 1\ 1]_c$ direction with a sequence of $\ldots$ 335335 $\ldots$ in the real-space [6].

Bibliography

[1] GSAS http://www.ncnr.nist.gov/xtal/software/gsas.html

[2] FullProf http://www.ill.eu/sites/fullprof/

[3] D. Treves, Journal of Applied Physics 36 (1965) 1033

[4] W. C. Koehler, E. O. Wollan, and M. K. Wilkinson, Physical Review 118 (1960) 58

[5] M. Marezio, J. P. Remeika, and P. D. Dernier, Acta crystallographica B 26 (1970) 2008

[6] P. D. Battle, T. C. Gibb, and P. Lightfoot Journal of Solid State Chemistry 84 (1990) 271

[7] T. Mizokawa and A. Fujimori Physics Review Letter 80 (1998) 1320

[8] Y. Tomioka, Y. Tokura, and Chul Sung Kim Journal of Applied Physics 87 9 (2000) 4873

[9] O. Paetzold, Journal of Statistical Physics, 61 (1990) 495

[10] Y. Tomioka, Y. Tokura, and Chul Sung Kim, Journal of Applied Physics 87 (2000) 4873

[11] J. Bartolomé, E. Palacios, M. D. Kuząŕmin, F. Bartolomé, I. Sosnowska, R. Przenioslo, R. Sonntag, and M. M. Lukina, Physical Review B, 62(2000), 1058

[12] F. Bartolomé, J. Bartolomé, M. Castro, J. J. Melero, Physical Review B, 62(2000), 1058

[13] W. Schnelle, R. Fischer, and E. Gmelin, Journal of Physics D: Applied Physics, 34 (2001) 846

[14] J. Herrero-Martin, G. Subias, J. Garcia, J. Blasco, and M. C. SĞnchez, Physical Review B 79 (2009) 045121

[15] J. Q. Li, Y. Matsui, S. K. Park, and Y. Tokura, Physical Review Letters 79 (1997) 297

CHAPTER 5. Inelastic Neutron Scattering Study of *R*FeO$_3$ (*R* = La, Pr, Nd, Sm, and Y)

5.1 Introduction

The Sr doped compound $R_{1/3}$Sr$_{2/3}$FeO$_3$ (*R*: rare earth metal) (*R*SFO) is a complicate system, we will begin the work with relative simple case, parent compound *R*FeO$_3$ (*R*FO) and take it as a reference on the crystal electric field (CEF) excitations of magnetic rare earth ions and the magnetic exchange energy between Fe ions. The first systematic study of magnetism in *R*FO was done in 1965 [1]: D. Treves measured the lattice and magnetic properties of *R*FO to understand the magnetic behavior and its origin in these orthoferrites. *R*FO is an antiferromagnetic insulator with T_N around 700 *K*. Fig. 5.1 shows the lattice and magnetic structure of LFO: the black dots are the R^{3+} ions, the brown octahedra is composed of Fe^{3+} ions and O^{2-} aions, which occupy the center-site and corner-sites, respectively. The arrows are the spin directions of Fe^{3+} ions in LaFeO$_3$. In other *R*FO, the magnetic moments of Fe^{3+} ions are in different directions. However, each spin direction is opposite to the nearest neighbors, which is named as G-type antiferromagnet (AF) [2].

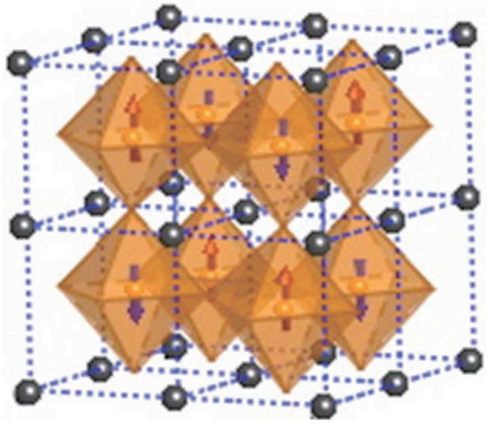

Figure 5.1 Crystal structure and magnetic ordering of LFO.

In this chapter, I will discuss the magnetic scattering calculation of Fe^{3+} ions in LFO by the Heisenberg model at first. Meanwhile, an analyzing method in **Q**-space is provided to analyze the different contributions of Fe^{3+} magnetic excitation, and the phonon to the total low-angle spectra of LFO. Based on the data analysis of LFO, crystal electric field (CEF) excitations of the magnetic R^{3+} ions is determined and compared to the fitting results from the Gaussian functions in E-space. Finally, the theoretical calculation and experimental measurement of the magnetic spectra of Fe^{3+} ions in *R*FO are presented [3, 4].

5.2 Sample Measurement and Data Reduction

Inelastic neutron scattering (INS) measurements were performed on the TOF instruments, Pharos and ARCS spectrometers. LFO, NFO and YFO were measured on Pharos while LFO, PFO, NFO, and SFO were measured on ARCS. LFO and NFO had been measured twice because we wanted to compare scattering from the same sample on different instruments.

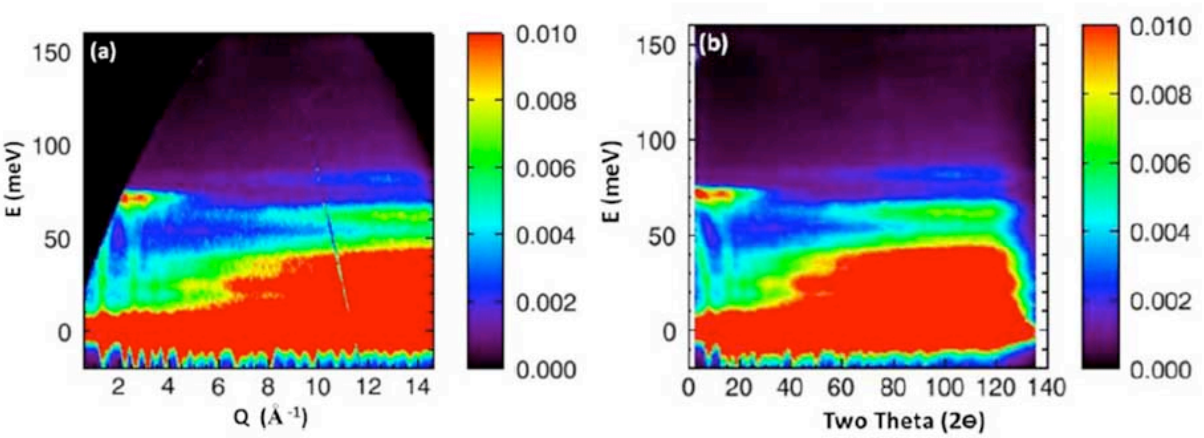

Figure 5.2 Inelastic neutron scattering intensity of $\mathrm{LaFeO_3}$ (a) versus momentum (Q) and energy transfer, (b) versus scattering angle and energy transfer on ARCS at $T = 10\ K$ and $E_i = 160\ meV$.

On ARCS, powders ($\sim 14\ g$) of *R*FO (*R*= La, Pr, and Nd) were packed in 5 aluminum foil slots, and loaded in an aluminum can whose size were approximately 4.5 $cm \times 6.5\ cm$. The sample thickness was around 0.5 *cm*. To estimate the sample density, the packing fraction was assumed as 0.7. (For SFO, 3.55 *g* sample was loaded by 4 slots in a 4 $cm \times 5\ cm$ aluminum can and the thickness was 0.4 *mm* to minimize the strong neutron absorption.) INS spectra were measured with incident energy (E_i) of 180 *meV*. On Pharos, around $\sim 50\ g$ of powders (LFO and NFO) were packed in a flat aluminum can (6 *cm*

× 6 *cm*) and the incident energy (E_i) was 120 *meV* and 160 *meV*. Sample cans oriented at 135° to the incident neutron beam for both instruments. Vacuum environment is important for the sample: it not only helps the cooling system to decrease the temperature quickly, but also reduces the background from the scattering by the atoms in the air. The measurement temperature was ~ 10 *K*. To achieve adequate statistics, the sample was run for approximately $\sim$ 24 hours on Pharos, and $\sim$ 5 hours on ARCS due to the different flux and sample quantities. The TOF data were reduced into $\hbar\omega$ and the scattering angle (2θ) histograms by DAVE and IDL software. Because of the position geometric effect of the detectors, the efficiencies of the detectors are different and the efficiency corrections are applied by the beam scientist.

Then, the scattering data was obtained at each point on a grid in Q-ω (2θ-ω) space, which were plotted in Fig. 5.2(a) and (b) respectively as discussed in chapter 3, Eq.(3.102).

Table 5.1 Sample masses and moles of *R*FO (*R* = La, Pr, Nd, Sm, and Y) on Pharos and ARCS.)

	Pharos		ARCS	
	mass (*g*)	mole (mol)	mass (*g*)	mole (mol)
$LaFeO_3$	40.81	0.1681	11.66	0.0480
$PrFeO_3$	- -	- -	17.93	0.0733
$NdFeO_3$	49.50	0.1995	17.45	0.0703
$SmFeO_3$	- -	- -	3.55	0.0140
$YFeO_3$	45.29	0.2350	- -	- -

5.3 Results and Discussion

5.3.1 Data Analysis

Based on the data reduction discussed in the section 4.5, the phonons are subtracted and the magnetic intensity for *R*FO (*R* = La, Nd, Pr, Sm, and Y) at 10 *K* is shown in Fig. 5.3. It is observed that i) there is an excitation peak around 70 *meV* in each sample and this peak shifts to lower energy direction from LFO to YFO; ii) there are more than one magnetic excitation peak in PFO, NFO, and SFO, which are due to the magnetic ions of R^{3+} (*R*: Pr^{3+}, Nd^{3+}, and Sm^{3+}); iii) in Fig. 5.3(a), SFO has a weak intensity because Sm has a strong neutron absorption, which we will further discuss later; iv) in Fig. 5.3(c), the magnetic peak intensity of YFO is a little bit higher than the relative peaks' intensity, the reasons are that the intensity units are arbitrary and the sample measurements for those two figures are taken on different instruments as mentioned above.

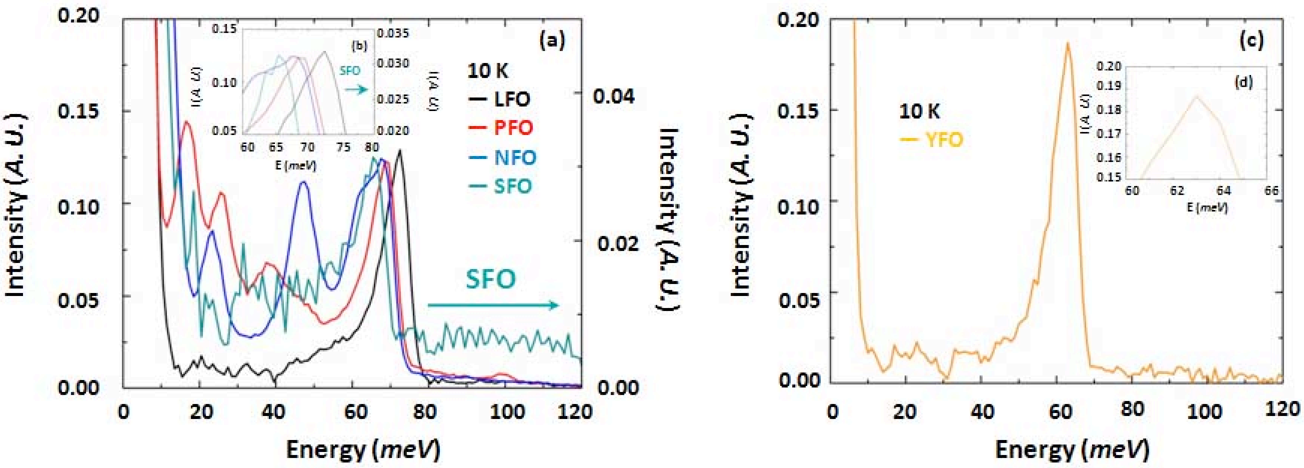

Figure 5.3 Comparison of the magnetic scattering measurement of *R*FO (*R* = La, Pr, Nd, and Sm) (a) and the enlarge plot of the peaks' positions (b) at $T = 10\ K$ on ARCS. The magnetic scattering measurement of YFO (c) and (d) the enlarge plot of YFO peak's position (d) at $T = 10\ K$ on Pharos.

From Fig. 5.3, it is hard to determine the contribution of Fe spin waves to the magnetic intensity of the Fe^{3+} magnetic peak in PFO, NFO, and SFO due to CEF excitations. In order to extract spin-wave scatterings for those magnetic ferrites, the CEF excitations need to be accounted for. The relative simple compound LFO will serve as an example at first to introduce the analysis of spin waves and exchange energies in LFO using the Heisenberg model simulations.

5.3.2 LaFeO$_3$

5.3.2.1) Heisenberg Model of Fe-ion Spin Waves

In LFO, nearest-neighbor (*NN*) $Fe^{3+}(3d^5)$, *S* = 5/2, spins are coupled by strong AF superexchange interactions ($J_{AF} < 0$). According to the INS studies of single-crystal TmFeO$_3$ [5], the spin waves can be approximated using a Heisenberg model Hamiltonian only with isotropic *NN* exchange interaction,

$$\mathbf{H} = -J_{AF} \sum_{\langle i,j \rangle} \mathbf{S}_i \cdot \mathbf{S}_j \, , \tag{5.1}$$

where $\mathbf{S}_i$ and $\mathbf{S}_j$ represent the spin vector on the *i*th and *j*th iron atom.

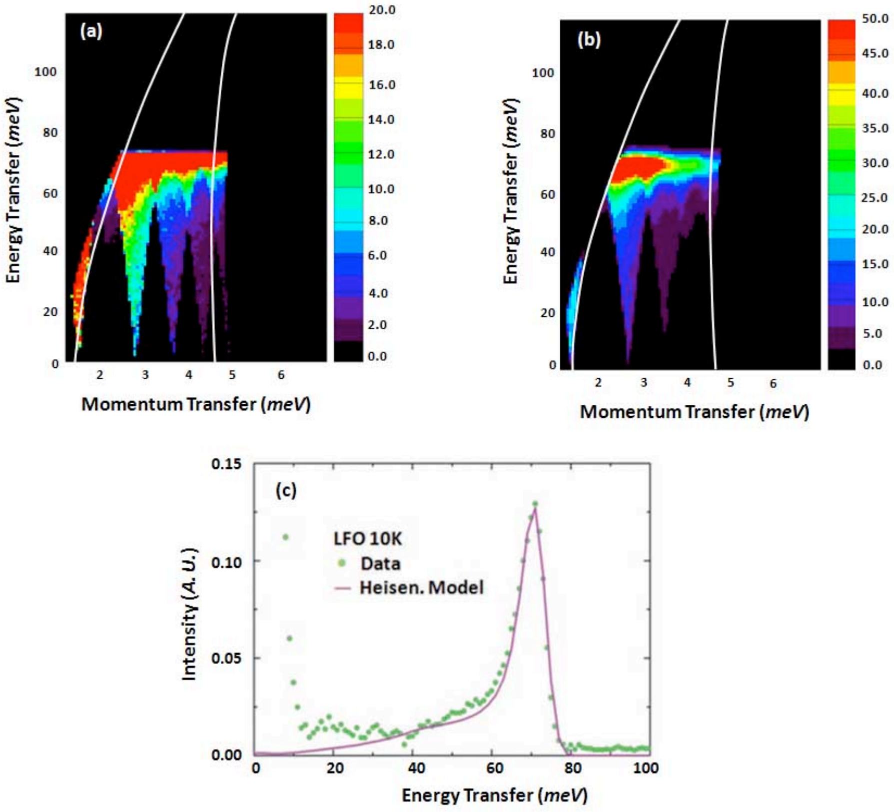

Figure 5.4 (a) The raw calculated neutron intensities, (b) the calculated intensities with the energy resolution, and (c) extracted angle-averaged magnetic intensity (dots) versus the intensity calculated from a Heisenberg model for the spin waves for LFO at T = 10 K on ARCS. In (a) and (b), the curved white lines indicate the low-angle summation regions leading to the corrected magnetic spectra.

From the theoretical calculation of spin-wave density-of-states (SWDOS), there is one magnetic peak observed in this G-type LFO magnetic structure and it is $6|J_{AF}|S^{3+}$, which has been in Fig. 3.6. Furthermore, the angle averaged coherent spin-wave scattering cross-section of a single crystal can be calculated, Fig. 5.4. With the inelastic neutron measurement, the energy is $\sim$ 71 *meV*, Fig. 5.4(c) (dots). Because S^{3+} = 5/2, the value of J_{AF} can be obtained from the position of the magnetic peak and it is $\sim$ -4.75 *meV*. However, the Heinsenberg model calculation result, Fig. 5.4(a), does not include effects of the instrument resolution. Usually, the an gaussian function is assumed as the resolution factor, and the final theoretical data is obtained from the convolution of a gaussian resolution function with the Heinsenberg model data, Fig. 5.4(b). In Fig. 5.4(c), the experimental data and calculations are comparable.

Since the intensity expression in energy frequency is complicated, defining the error-bar is not easy. Series of χ^2 with different J_{AF} are calculated,

$$\chi^2 = \sum_i (I_{exp.} - I_{calc.})^2 \,, \tag{5.2}$$

where $I_{exp.}$ and $I_{calc.}$ are the observed and calculated intensities, respectively.

J_{AF} is determined by the value with the lowest χ^2 and the upper/lower bound of this J_{AF} is decided by the ratio of the boundary and central χ^2, which is 2 in this case. For example, the relationship between J_{AF} and χ^2 is plotted in Fig. 5.5. $\chi^2_{4.75}$ is the lowest, and the lower(upper) boundary is - 4.74 ($\sim$ - 4.767). Since the boundary values are not symmetry to J_{AF} = - 4.75, the closest boundary is taken to keep the variance in the acceptable region. Therefore, J_{AF} = - 4.75 ± 0.01 *meV*.

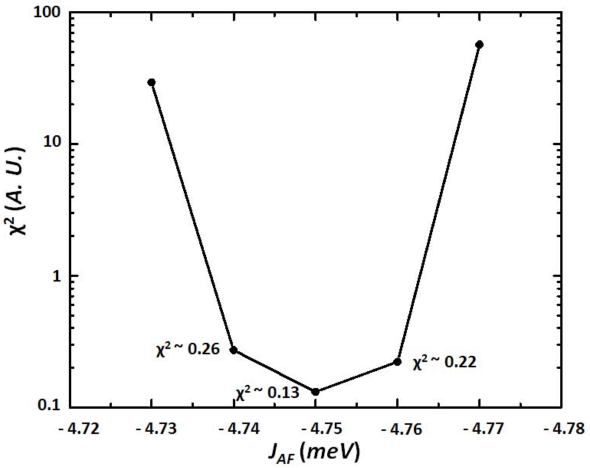

Figure 5.5 LFO error-bar estimation: χ^2 vs J_{AF} on ARCS at 10 *K*.

If we integrate the angle-averaged intensity in ω space, the total value will be,

$$N^{Fe}_{\Delta 2\theta_{1,2}}(\Delta\omega_{1,2}) = \int_{\omega_1}^{\omega_2} I^{Fe}_{\Delta 2\theta_{1,2}}(\omega) d\omega \,, \tag{5.3}$$

Although the unit of the total value is arbitrary, it is the energy integration on a uniform momentum region and I will call them as total state number for convenience. In order to determine the correct integrated intensity, I will check the result with the Q-dependence of the neutron scattering data in different energy transfer ranges (Q-cuts) in the following section.

5.3.2.2) Constant Energy Q-cuts

Since La^{3+} ion is non-magnetic, there is no CEF existed in magnetic spectrum and it will be easy to separate phonon from magnetic scattering. Furthermore, the lattice structure of LFO is similar to the other *R*FO, the phonon spectrum of LFO will be a reference to the others.

The integrated scattering function over a range of energies is defined as,

$$S_\omega(Q) = \int_{\omega-\Delta\omega}^{\omega+\Delta\omega} S_{tot}(Q,\omega)d\omega\,, \tag{5.4}$$

Then, the different contributions to INS can be separated in some ω-range. For LFO, the full structure factor, S_ω(Q), has three components: the pollycrystalline averaged spin wave scattering of *Fe*$^{3+}$, S_ω^{mag} (Q), the phonon contribution, S_ω^{ph} (Q), and the multiple scattering, S_ω^{multi} (Q).

$$S_\omega(Q) = S_\omega^{multi}(Q) + S_\omega^{ph}(Q) + S_\omega^{mag}(Q)\,, \tag{5.5}$$

The Q-cut of different energy transfer ranges 30.5-40.5 *meV*, Fig 5.5(c), is analyzed as an example: i) the multiphonon and other background contributions are treated as a constant background; ii) the one-phonon scattering is approximated as incoherent with the intensities varying as Q^2, section 3.3; iii) the spin wave scattering intensity follows the magnetic form factor, **F**(**Q**), section 3.4.

The normalized intensity from measurement, $\mathcal{I}_\omega$(Q), is defined by,

$$\mathcal{I}_{\Delta\omega_{1,2}}(Q) = \int_{\omega_1}^{\omega_2} \mathcal{I}_{tot}(Q,\omega)d\omega\,, \tag{5.6}$$

where $\mathcal{I}_{\Delta\omega_{1,2}}$(Q) is proportional to the scattering function, and ω_1 (ω_2) is the integration limit ω-$\Delta\omega$ (ω+$\Delta\omega$).

If we integrate the spectrum in Q-space, the total value from Q$_1$ to Q$_2$ will be,

$$\mathcal{N}_{\Delta\omega_{1,2}}^{Fe}(\Delta Q_{1,2}) = \int_{Q_1}^{Q_2} \mathcal{I}_{\Delta\omega_{1,2}}^{Fe}(Q)dQ\,, \tag{5.7}$$

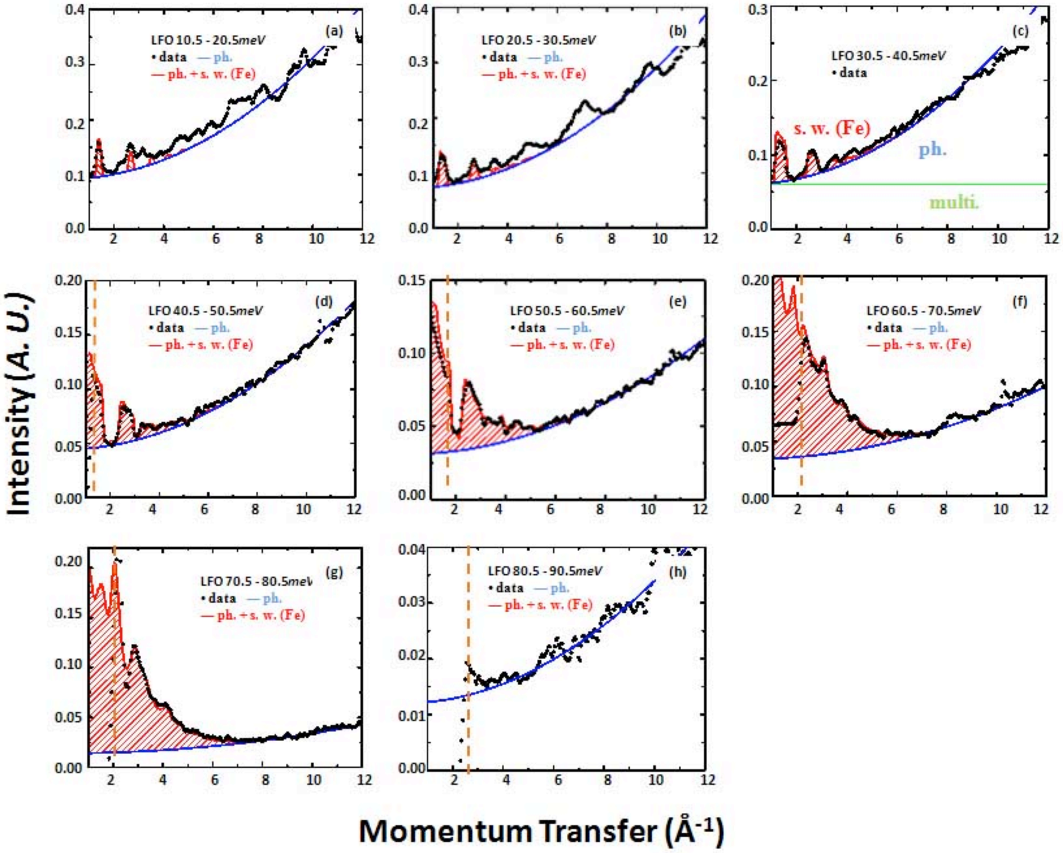

Figure 5.6 The Q-dependence of the neutron scattering data for different energy transfer ranges in LFO on ARCS at T = 10 K: (a) 10.5 - 20.5 meV, (b) 20.5 - 30.5 meV, (c) 30.5 - 40.5 meV, (d) 40.5 - 50.5 meV, (e) 50.5 - 60.5 meV, (f) 60.5 - 70.5 meV, (g) 70.5 - 80.5 meV, and (h) 80.5 - 90.5 meV. The black dots are the experimental data. The blue line it an estimate of the incoherent phonon background plus multiple scattering. The red column is the calculation of the polycrystalline averaged spin wave scattering plus background using the parameters in the text. The brown dash line in different energy transfer ranges ((d)-(h)) indicates the minimum Q obtainable for the experimental setup.

Similar as the total state numbers in E-cuts, $\mathrm{N}^{Fe}_{\Delta 2\theta_{1,2}}$ $(\Delta\omega_{1,2})$, this total value in Q-cuts, $\mathcal{N}^{Fe}_{\Delta 2\omega_{1,2}}$ $(\Delta Q_{1,2})$, is also named as the total state numbers for convenience. Actually, these two state numbers with the same Q and ω ranges need to agree with each other exactly.

Here, I am going to test this method on LFO. First, the data and calculations of $\mathcal{I}^{Fe}_{\Delta\omega_{1,2}}$(Q) were compared in Fig. 5.6. There were three things I want to mention: i) For the beginning region of the experimental data, the intensity suddenly drops to zero or low value especially at the high energy scale, the reason is the boundary data obtained by the detectors; ii) oscillations in experimental data and calculations are due to the coherent magnetic and phonon scattering, respectively; iii) there was no magnetic signal in the energy scale 80.5 - 90.5 meV, Fig. 5.6(h). The Q-cut fitting was very well. Second, I integrated the intensities in Energy-cuts and Q-cuts, and compared the state numbers from both cuts in Table 5.2.

Table 5.2 The integrate intensities of Fe^{3+} magnetic states of Energy - cuts and Q - cuts in LFO.

Energy Range (*meV*)	State number	
	S_{tth}	S_{ω}
10.5 : 20.5	0.089 ± 0.004	0.086 ± 0.006
20.5 : 30.5	0.163 ± 0.009	0.164 ± 0.011
30.5 : 40.5	0.209 ± 0.012	0.210 ± 0.015
40.5 : 50.5	0.274 ± 0.016	0.274 ± 0.019
50.5 : 60.5	0.473 ± 0.029	0.473 ± 0.034
60.5 : 70.5	1.442 ± 0.099	1.438 ± 0.104
70.5 : 80.5	1.596 ± 0.103	1.524 ± 0.116
80.5 : 90.5	−−	−−

From the comparison of these intensities, we found that the agreement among them were excellent except the starting and ending data which were due to the boundary effect. When the energies were larger than 80 *meV*, the phonon contribution would be dominant as we expected. Therefore, comparing the total state numbers in E-cuts and Q-cuts provides a method to check the numerical integrations, and determines the integrating constant for the different components to the E-cuts and Q-cuts. In the following sections, we were going to apply this method to the more complicated magnetic system, where crystal field (CF) signals from rare earth ions are included.

5.3.3 Crystal Field Excitations

CF is a phenomenon in rare earth and transition metal containing compounds that results in a splitting of the energy levels of the outermost electron shells, such as e_g-t_{2g} splitting the cubic of $3d$-orbital system. It is based on the fact that the electronic structure of center ion can be distorted by the surrounding ligands. The total contribution of the crystalline environment can be replaced by a field and the whole crystal system is replaced by a transition metal ion inside the imaginary field.

In a free ion, the outermost ($3d$ and $4f$) electrons are orbitally degenerate. CF can also be explained as the interaction between metal ions and surrounding ligands: the electrons in the orbitals of center ions and ligands repel each other by Coulomb force and the electronic clouds of ligands will come closer to some of the center ions while moving away from the others. As a result, the orbital degeneracy will partially or totally get lost resulting in split energy levels corresponding to different CF states. If rare earth is small, the splitting in transition metals is large. In addition, the Hund's third rule need to be modified in some special cases. These excitations between CEF states can be observed by neutron scattering and they are $\sim$ 10 *meV* for rare-earth containing compounds.

In magnetic rare-earth ferrites, rare-earth CEF excitations are also present in the same energy range as Fe spin waves. In order to extract Fe spin-waves, we must corned for the CEF contribution from the magnetic scattering. The CEF cross section can be written as,

$$\frac{d^2\sigma}{d\Omega d\omega} \propto [g_J F(\mathbf{Q})]^2 e^{-2W} \frac{k'}{k} S_{CF}(\mathbf{Q},\omega)\,, \tag{5.8}$$

where $\mathbf{Q}$ is the scattering vector, $\vec{k'}$ - $\vec{k}$, and $\hbar\omega$ is the energy transfer. g_J is Lande factor, $F(\mathbf{Q})$ is the magnetic form factor, k' and k are values of the initial and final neutron wavevectors, and e^{2W} is the Debye-Waller factor. $S_{CF}(\mathbf{Q}, \omega)$ is the response function of the system which is determined entirely by the temperature and CEF eigenstates,

$$S_{CF}(\mathbf{Q},\omega) = \sum_{i,j} \rho_i \mid \langle i \mid \mathbf{J}_\perp \mid j \rangle \mid^2 \delta(E_i - E_j - \hbar\omega)\,, \tag{5.9}$$

where $\mid i \rangle$ and $\mid j \rangle$ are the initial and final CEF eigenstates of the system with level energies E_i and E_j . $\mathbf{J}_\perp$ is the component of the total angular moment operator perpendicular to the scattering vector; ρ_i is the thermal population factor of the initial state. The observed excitation is between the levels which have non-zero matrix elements.

For rare earth ions, the spin - orbit coupling is usually stronger than CF potential, and the ground state is degenerate. Neither $\mathbf{S}_z$, nor $\mathbf{L}_z$ is conserved quantities. However, the total angular momentum **J** = **L** + **S**, remains a good quantum number. Therefore, the magnetic form factor is given by,

$$F(\mathbf{q}) = \langle j_0(q) \rangle + \langle j_2(q) \rangle \frac{J(J+1) + L(L+1) - S(S-1)}{3J(J+1) + S(S-1) - L(L+1)}, \tag{5.10}$$

where $\langle j_0 \rangle$ and $\langle j_2 \rangle$ are,

$$\langle j_0(s) \rangle = Aexp(-as^2) + Bexp(-bs^2) + Cexp(-cs^2) + D, \tag{5.11}$$

and,

$$\langle j_L(s) \rangle = (Aexp(-as^2) + Bexp(-bs^2) + Cexp(-cs^2) + D)s^2, \tag{5.12}$$

If $L \neq 0$, $s = 0$, $\langle j_L(s) \rangle = 0$; $s = \frac{\sin\theta}{\lambda}$ [6, 7].

5.3.3.1) Crystal Field Study of Nd^{3+} ions

The spherically symmetric ground state of Nd^{3+} is $^3H_4$ with 3 unpaired *f*-electrons, and the atomic structure is $^4I_{9/2}$. Thus, the *J* is half integer, 9/2, and the 10-fold degenerate ground state multiplet splits into (2 *J* + 1)/2 = 5 doublets due to he orthorhombic environment of Nd site. The non-zero matrix elements of the excited levels from the ground state are shown in Fig. 5.7. There are 5 energy levels and the transition energy is defined as E_{ij} where *i* and *j* are the numbers of energy levels.

Table 5.3 The magnetic form factors, $\langle j_0 \rangle$ and $\langle j_2 \rangle$, for Nd^{3+}.

Nd^{3+}	*A*	*a*	*B*	*b*	*C*	*c*	*D*
$\langle j_0 \rangle$	0.0540	25.029	0.3101	12.102	0.6575	4.722	-0.0216
$\langle j_2 \rangle$	0.6751	18.342	1.6272	7.260	0.9644	2.602	0.0150

The magnetic form factor of Nd^{3+} in NFO is calculated with the constants of Table 5.3 [6, 7] and plotted in Fig. 5.8.

In order to study excitations from the ground state CF level, the first experiment was carried out at 10 *K* at which the thermal population of excited CEF levels could be neglected. The ground

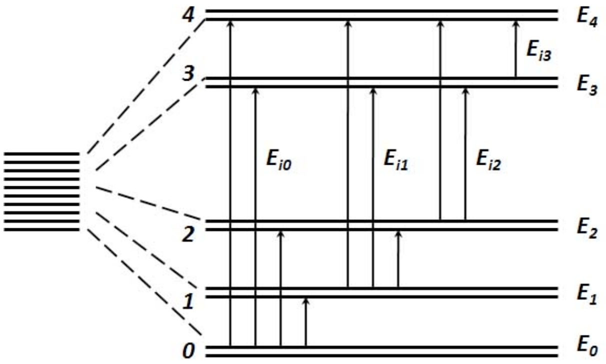

Figure 5.7 Crystal field splitting diagram in Nd^{3+} with distorted orthorhombic symmetry. E_{ij} is the transition energy from *i*th level and *j*th level.

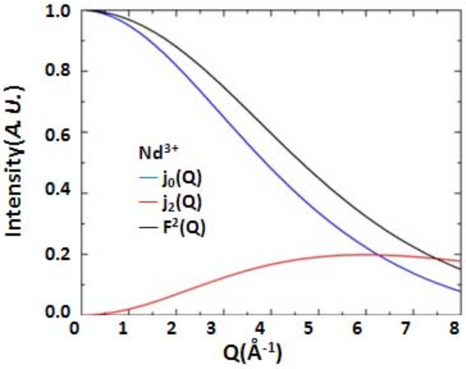

Figure 5.8 The magnetic form factor of Nd^{3+}.

state of Nd^{3+} in NFO splits into 5 Kramers doublets because of the CF, and there are 4 transitions as reported before: shown in $\sim$ 11 *meV*, 23 *meV*, 46 *meV* and 61 *meV* [8, 9], Fig. 5.9. Compared to LFO, the full structure factor of NFO, $S(\mathbf{Q}, \omega)$, has four components: the pollycrystalline averaged spin wave scattering of *Fe*$^{3+}$ in NFO, $S_{mag}(\mathbf{Q}, \omega)$, incoherent phonon background, $S_{phonon}(\mathbf{Q}, \omega)$, multiple scattering, $S_{multi}(\mathbf{Q}, \omega)$, and CF scattering of Nd^{3+}, S_{CF} $(\mathbf{Q}, \omega)$.

The CF scattering in NFO was obtained by subtracting the contribution of Fe spin wave scattering, S_{mag}, from the total magnetic data, as shown in Fig. 5.9. The CF peaks were fitted by Gaussian function. In order to determine the fitting constants of the gaussian function for CFE and the intensity of Fe^{3+} magnetic scatterings, the NFO Q-cut plots of the theoretical calculation and the experimental data were compared in Fig. 5.10.

Fig. 5.10(a) shows an example of different contributions to the Q-cut in the energy range

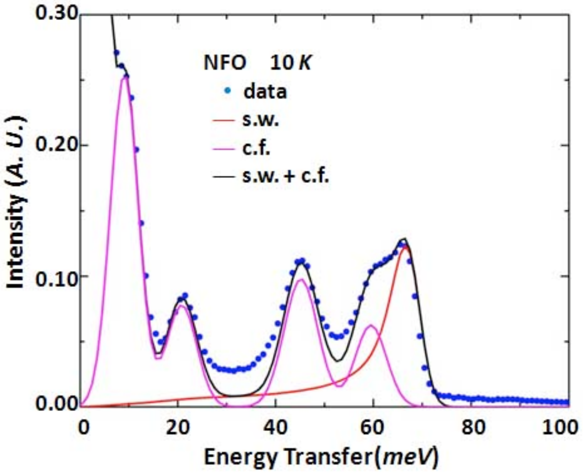

Figure 5.9 The theoretical calculation and magnetic scattering measurement of NFO at 10 *K* on ARCS. The experimental data are blue dots, the total simulating contribution is black line, the Heisenberg model and crystal field calculations are red line and magenta line, respectively.

10.5*meV*-20.5 *meV*. Because of the similar phonon spectra of LFO and NFO, the phonon-fitting from LFO, Fig. 5.6, was used as a reference for NFO. Furthermore, the initial Q-value boundary is increasing as the energy increases due to the limitation of the instrument, the brown dash lines in Fig. 5.10.

In Fig. 5.9, the calculated integrated-intensity of Heisenberg model of Fe^{3+} and the fitted CF excitations of Nd^{3+} are red and pink lines; In Fig. 5.10, the Q-cut magnetic scattering intensities of Fe and Nd ions are the zone between green and blue lines and the zone between red and green lines, respectively. In Table 5.4, the calculated integrated-intensity ratio of Heisenberg model of Fe^{3+} and the fitting excitations of Nd^{3+} were compared to the Q-cut magnetic scattering ratio between Fe^{3+} and Nd^{3+} ions.

Therefore, the positions and integrate intensities of the Nd^{3+} CFEs in NFO at 10 *K* were determined. The measured and calculated energies and transition intensities of CF are listed in Table 5.5. The intensities were normalized to the intensity of $\sim$ 9.54 *meV* transition, which was set as 100. They agreed very well at $\sim$ 21.17 *meV*and $\sim$ 45.75 *meV*. The peak at $\sim$ 60.6 *meV* was close to the magnetic signal of Fe^{3+} ion, therefore the intensity was very likely to have been interfered.

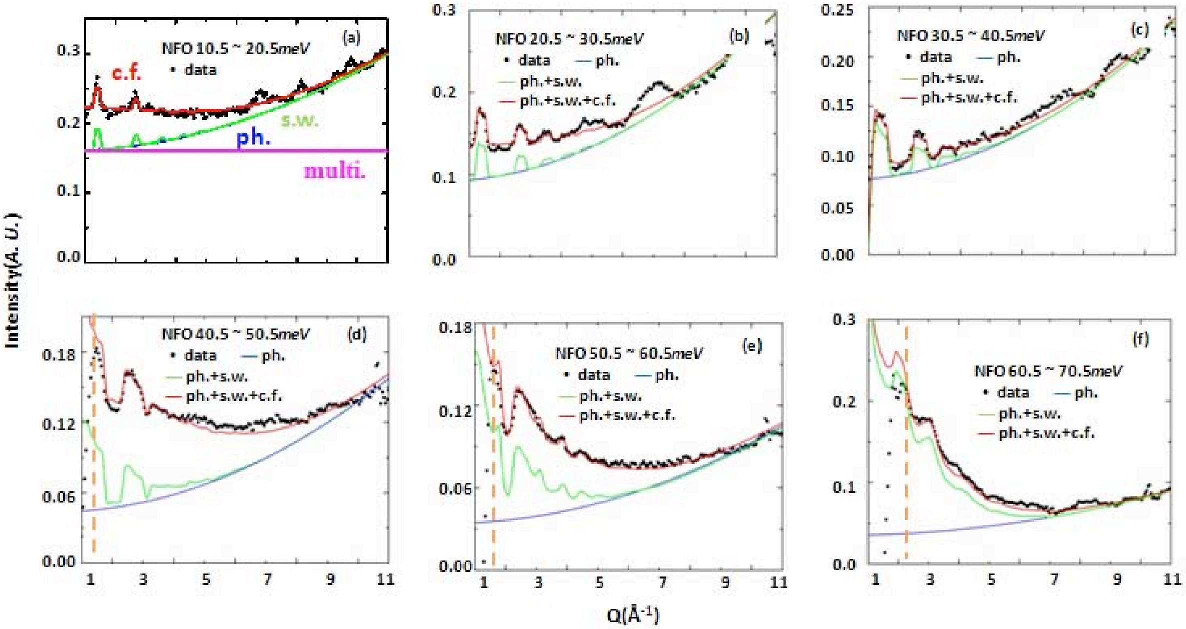

Figure 5.10 The Q - dependence of the neutron scattering data for different energy transfer ranges in NFO at T = 10 K. The brown dash line in some different energy transfer ranges ((d)-(f)) is the starting point of the experimental recording.

When the temperature increased to 300 K, no structure transition was found, and the Zeeman splitting of the ground state was 0.5 meV which was small compared to the CF splitting [10].

Table 5.4 The comparison of measured and calculated energies and transition intensities of Nd^{3+} in NFO CF at 10 K.

Energy Range	State number (S_{tth})		State number (S_ω)	
(meV)	spin-wave	C.F.	spin-wave	C.F.
10.5 : 20.5	0.073 ± 0.006	1.334 ± 0.019	0.074 ± 0.010	1.107 ± 0.008
20.5 : 30.5	0.127 ± 0.008	0.445 ± 0.006	0.127 ± 0.004	0.451 ± 0.005
30.5 : 40.5	0.163 ± 0.010	0.140 ± 0.001	0.165 ± 0.015	0.148 ± 0.002
40.5 : 50.5	0.236 ± 0.014	1.356 ± 0.020	0.250 ± 0.026	1.389 ± 0.010
50.5 : 60.5	0.488 ± 0.018	0.648 ± 0.009	0.495 ± 0.044	0.660 ± 0.007
60.5 : 70.5	1.621 ± 0.026	0.387 ± 0.004	1.667 ± 0.104	0.402 ± 0.005
70.5 : 80.5	0.121 ± 0.013	3.92e-4 ± 3e-5	0.251 ± 0.010	0.021 ± 0.001

Therefore, the CF structure was similar to that at 10 K except some thermal broadening: there are still 5 doublets splitting. However, the integrated intensities of transitions between excited states are changed by the thermal energy, $\sim k_BT$, according to the increased population of the excited states. For this reason, some new energy excitations may appear. For example, the integrated intensities of transitions from the ground state have decreased when the temperature changed from 10 *K* to 300 *K*, Fig. 5.11(b), due to depopulation of the ground state.

Table 5.5 The comparison of measured and calculated energies and transition intensities of Nd^{3+} in NFO CF at 10 *K*.

Energy levels	Energy (*meV*)		Integrated Intensities	
	calculated*	measured	calculated*	measured
0	0.0	0.0		
1	10.14	9.38 ± 0.08	100.00	100.0 ± 3.06
2	22.37	21.22 ± 0.13	29.31	30.85 ± 1.11
3	44.70	45.68 ± 0.07	46.05	41.77 ± 1.64
4	60.82	59.93 ± 0.13	$7.00^{\dagger}$	17.76 ± 1.26

† reported in reference [9].

The population of CF levels can be explained by Boltzmann statistics, the partition function and probability for each transition can be expressed as

$$Z_i = e^{\frac{\Delta E_{ij}}{k_B T}}\ , \ and\ P_i = \frac{Z_i}{\sum_i Z_i}\ , \tag{5.13}$$

where ΔE_{ij} is the transition energy between *i*th and *j*th levels.

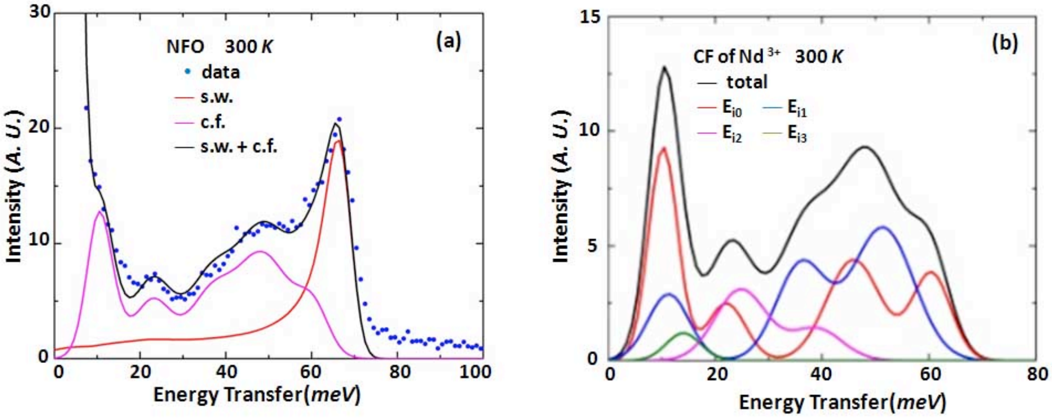

Figure 5.11 (a) Comparison of calculations and magnetic scattering measurement of NFO at 300 *K* on Pharos. The experimental data are blue dots, the total simulating contribution is black line, the Heisenberg model and crystal field calculations are red line and magenta line, respectively. (b) Total crystal field calculation (black line) from the contribution of E_{ij} series at 300 *K*.

The population from the ground level to *i*th level transition is,

$$M(i) \propto P_0(1 - P_i)\,, \tag{5.14}$$

At 300 *K*, several peaks were hard to recognize because they were much weaker and broader, except the one of $\sim$ 67 *meV*, which could be explained as the Fe^{3+} spin waves. The smeared broad peaks were not only due to the thermal broadening, but also due to the appearance of new CF excitation energies from the excited states. The possible positions of CF excitation peaks were listed in Table 5.6, E_{ij} means transition energy to the *i*th excited level from *j*th level. Because we do not know the transition matrix elements, we could not get the selection rules to determine the intensities of the transitions from every state. However, the 10 *K* observed transition, E_{i0}, should have a non-zero transition matrix element, which means that E_{i0} were allowed at least. Table 5.6 listed the statistical calculation of intensity of E_{i0} at 300 *K* from the measurements at 10 *K*.

As the scattering integrated intensities of Fe ions at 10 *K* and 300 *K*, Fig. 5.9 and Fig. 5.11(a), are similar, the total magnetic scattering difference between both temperatures comes from the changes to the CF, which means that there are CEF excitations present from other excited states at 300 *K*, Fig. 5.11(b).

Table 5.6 The comparison of the ground excitation transition intensities of NFO CF between 10 *K* and 300 *K* (PHAROS).

E_{i0}	Energy (*meV*)	Integrated Intensity (10 *K*)	Probability (10 *K* → 300 *K*)	Integrated Intensities 300 *K*	
				Calculated	Measured
E_{00}	0.0				
E_{10}	9.38 ± 0.08	42.67 ± 1.28	0.30	12.80 ± 0.38	11.71 ± 0.34
E_{20}	21.22 ± 0.13	13.16 ± 0.47	0.34	4.47 ± 0.16	4.35 ± 0.13
E_{30}	45.68 ± 0.07	17.82 ± 0.70	0.39	6.95 ± 0.28	9.89 ± 0.38
E_{40}	59.93 ± 0.13	7.58 ± 0.54	0.40	3.03 ± 0.22	7.65 ± 0.30

5.3.3.2) Crystal Field Study of Pr^{3+} ions

CF levels of Pr^{3+} in the environment of orthorhombically distorted perovskite material are shown in Fig. 5.12. Although many experimental and theoretical studies on Pr^{3+} in perovskite oxide have been done [11, 12], we still could not have a clear scheme on the CF of Pr^{3+} ions.

For PFO, CF of Pr^{3+} is a little bit different from CF of Nd^{3+} in NFO. There are 2 unpaired

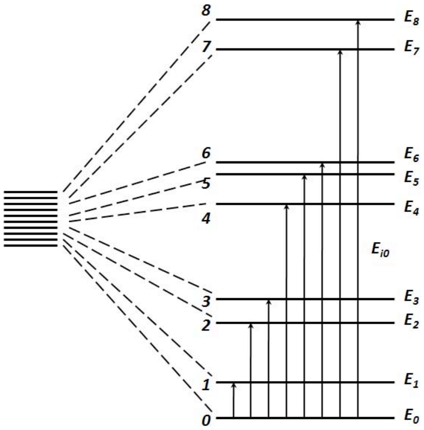

Figure 5.12 Crystal field splitting diagram in Pr^{3+} with distorted orthorhombic symmetry. E_{ij} is the transition energy from *i*th level and *j*th level.

f-electrons and the atomic structure is $^3H_4$. Since the structure of PFO is distorted orthorhombicly and $J = 4$, the ground state multiplet splits into ($2J + 1 = 9$) singlets. The dipole allowed transitions from the ground state are shown in Fig. 5.12. There are 9 energy levels and the transition energy is defined as E_{ij}, where *i*th and *j*th are the numbers of the energy levels.

Table 5.7 The magnetic form factors, $\langle j_0 \rangle$ and $\langle j_2 \rangle$, for Pr^{3+}.

Pr^{3+}	*A*	*a*	*B*	*b*	*C*	*c*	*D*
$\langle j_0 \rangle$	0.0504	24.9989	0.2572	12.0377	0.7142	5.0039	-0.0219
$\langle j_2 \rangle$	0.8734	18.9876	1.5594	6.0872	0.8142	2.4150	0.0111

Based on Eq. (5.10), (5.11), and (5.12), the magnetic form factor of Pr^{3+} in PFO is calculated and plotted in Fig. 5.13 with the constants of Table 5.7 [6, 7].

The INS spectra of PFO sample at 5 *K* exhibited two well resolved inelastic lines ($\sim$ 16.8 *meV* and 25.1 *meV*) and three broad inelastic features ($\sim$ 39*meV*, 88.5*meV*, and 99.5 *meV*). In addition, there were two reported CF excitations which were very hard to be observed, 5 and 65 *meV* [12], due to the energy resolution and strong magnetic scattering of Fe spin waves, Fig. 5.14(a). The former is very close to the elastic line and very hard to be separated from the peak of elastic energy; the latter one is very close to the spin-wave peak of Fe in PFO.

It is possible that other peaks exist around $\sim$ 55 or $\sim$ 77 *meV* which would give a better fitting result, Fig. 5.14(b) or (c). In order to check the second blur peak, $\sim$ 65 *meV*, and the extra peaks

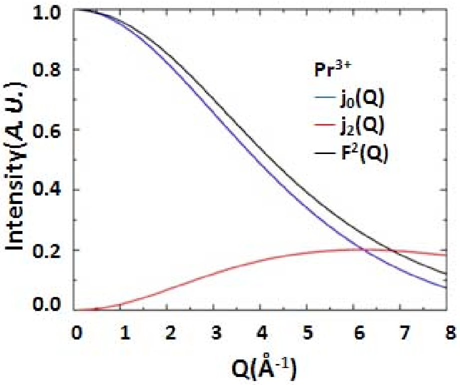

Figure 5.13 The magnetic form factor of Pr^{3+} in $PrFeO_3$.

around ~ 55 and ~ 77 *meV*, the series of Q-cuts for PFO are plotted.

Similar as the CFEs analysis of NFO, the Q-cuts were fitted to determine the integrated intensities at different energy excitations, Fig. 5.15, and Fig. 5.15(a) shows each contributions to the low-energy region 20.5 *meV*-30.5 *meV*.

In Fig. 5.14, the calculated integrated intensity of Heisenberg model of Fe^{3+} and the fitting CF excitations of Pr^{3+} were red and pink lines; In Fig. 5.15, the Q-cut magnetic scattering intensities of Fe and Pr ions are the zone between green and blue lines and the zone between red and green lines, respectively. Both integrated intensities were compared in Table 5.8.

From the Q-cuts data fitting, Fig. 5.15, we found: i) When the energies were higher than 40 *meV*, it was very convenient to represent the phonon contributions of PFO from the phonons of LFO. Because lattice contribution from O^{2-}, which was very close in both LFO and PFO, was the main origin of phonon scattering in those energy ranges; ii) When the energies were less than 40 *meV*, the phonon fitting of PFO would include the contribution from rare-earth metal ions and could not simply get from the phonon of LFO due to the different scattering cross sections between La^{3+} and Pr^{3+}. However, the phonon of LFO is still not a bad reference.

Based on the comparison of these intensities listed in Table 5.8: i) due to the limitation of the instrument, the initial Q-value boundary is increasing with increasing energy, the brown dash lines in Fig. 5.15; ii) in the energy ranges between 10.5 *meV* and 50.5 *meV*, the integrated intensities of CF of Pr^{3+} and the spin wave of Fe^{3+} from the energy-cuts and Q-cuts agreed with each other very well except the bothering from the boundary effect; iii) in the Q-cuts from 50.5 - 60.5 *meV*, 60.5 -

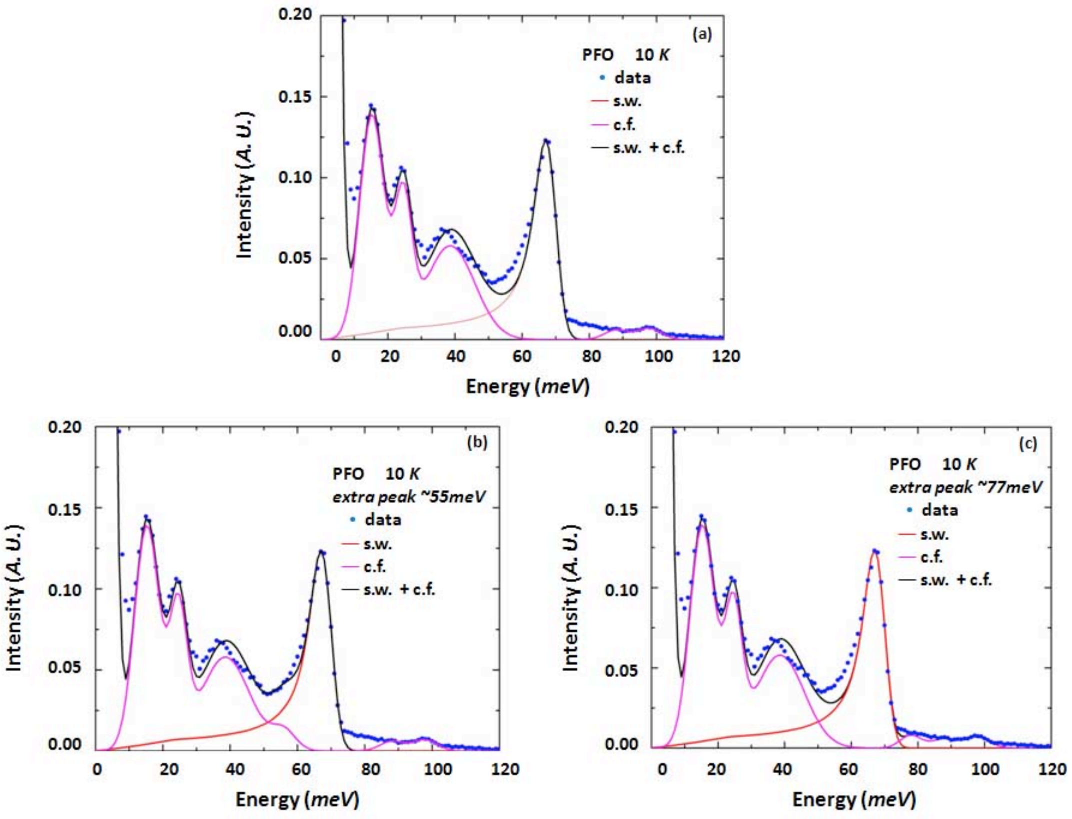

Figure 5.14 (a) The theoretical calculation and magnetic scattering measurement of PFO at T = 10 K (blue dots) on ARCS, and total contribution(black line) of Heisenberg model calculation (green line) with J_{AF} = -4.55 meV and crystal field calculation (red line); (b) the theoretical calculation and magnetic scattering measurement of PFO at T = 10 K with an extra peak $\sim$ 55 meV; (c)the theoretical calculation and magnetic scattering measurement of PFO at T = 10 K with an extra peak $\sim$ 77 meV.

70.5 meV, and 65.5 - 75.5 meV, the integrated intensities of CF did not include an excitation at $\sim$ 55 meV, and the agreement was good which meant that no CEF excitation is likely near 55 meV; iv) in the Q-cuts from 70.5 - 80.5 meV, the CF agreement was not very good. If we added another new peak around $\sim$ 75 meV, it would better the case, Fig. 5.14(c); v) in the Q-cuts from 80.5 - 90.5 meV and 90.5 - 100.5 meV, there was not any magnetic scattering from Fe^{3+}, and CF scattering of Pr^{3+} was the only contribution to the magnetic scattering, which agreed with energy-cuts very well.

Therefore, the final CFEs of Pr^{3+} ion were determined and listed in Table 5.9. The CEF of Pr^{3+} in $PrGaO_3$ (PGO) was also compared because it had a similar Pr^{3+} CEF scattering as PFO

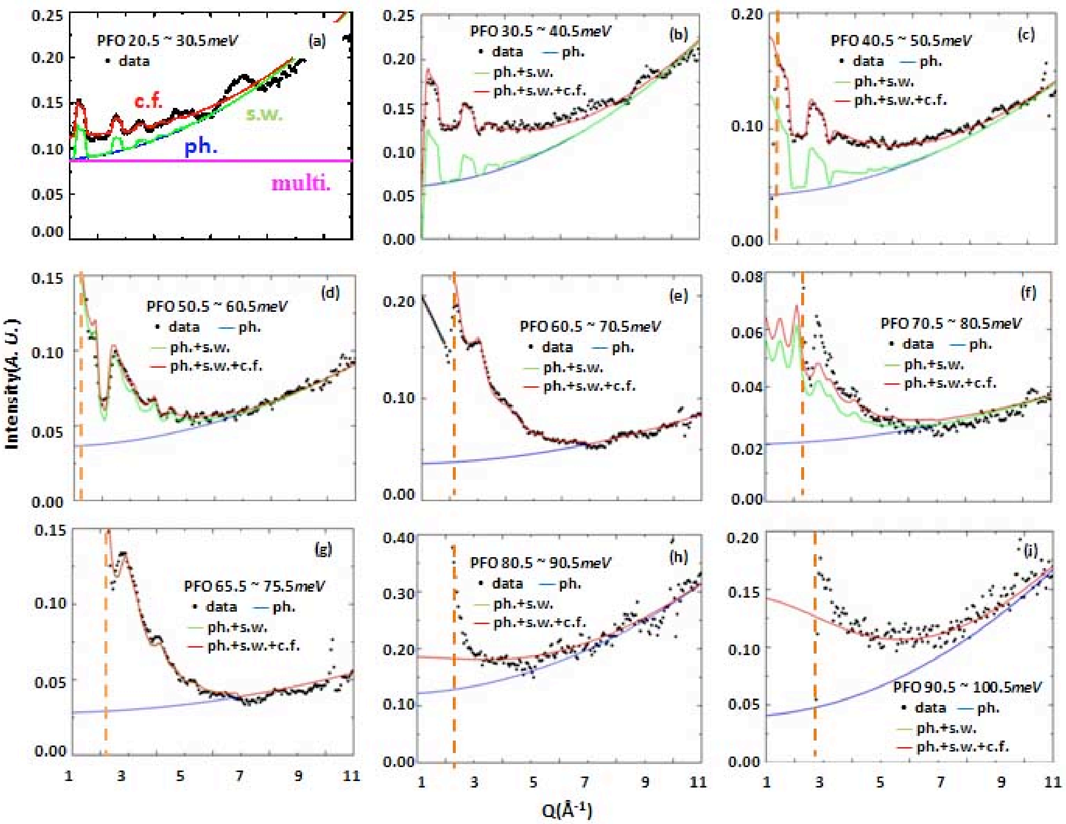

Figure 5.15 The Q - dependence of the neutron scattering data for different energy transfer ranges (Q-cuts) in PFO at $T = 10\ K$. The brown dash line in some different energy transfer ranges ((d)-(i)) is the starting point of the experimental recording.

and was the only theoretical calculation on CFE of Pr^{3+} in perovskite oxides, *Pnma* [11, 12].

There are three things I want to point out in table 5.9. First, the peak around $\sim 65\ meV$ was too weak to be observed in our measurement, although it had been mentioned in K. Feldmann's measurement on PFO and A. Podlesnyak's measurement on PGO [11, 12]. However, we also found that K. Feldmann *et. al.* did not report the spin-wave excitation of Fe^{3+} ions [11]. The magnetic peak they argued as CFE around $\sim 60\ meV$ was much like the signal of Fe^{3+}, which should have been around $\sim 67\ meV$ in our data. Second, the observed $\sim 67\ meV$ of PGO is not found in the measurement of PFO. It is probable that the calculated peaks $\sim 67\ meV$ moved to low energy part and combined with the CFE peak $\sim 37\ meV$, which was very broad in our data; and there was also the possibility of the different structural distortion between PFO and PGO which should not give such big difference. Another option for the $\sim 67\ meV$ peak was that it moved to

Table 5.8 The integrated intensities of Fe^{3+} magnetic states and CF of E-cuts and Q-cuts in PFO.

Energy Range	State number (S_{tth})		State number (S_{ω})	
(meV)	spin-wave	C.F.	spin-wave	C.F.
10.5 : 20.5	0.098 ± 0.010	2.187 ± 0.033	0.102 ± 0.022	2.106 ± 0.049
20.5 : 30.5	0.163 ± 0.015	1.278 ± 0.021	0.155 ± 0.025	1.217 ± 0.012
30.5 : 40.5	0.208 ± 0.018	0.718 ± 0.020	0.208 ± 0.030	0.783 ± 0.008
40.5 : 50.5	0.297 ± 0.024	0.491 ± 0.014	0.296 ± 0.034	0.479 ± 0.007
50.5 : 60.5	0.615 ± 0.041	0.049 ± 0.013	0.628 ± 0.041	0.050 ± 0.001
60.5 : 70.5	2.039 ± 0.082	6.07e-4 ± 3e-5	2.086 ± 0.119	0.025 ± 0.001
65.5 : 75.5	1.420 ± 0.069	5.66e-5 ± 3e-6	1.664 ± 0.084	0.028 ± 0.001
70.5 : 80.5	0.242 ± 0.019	0.002 ± 1e-4	0.614 ± 0.022	0.024 ± 0.001
80.5 : 90.5	– –	0.094 ± 0.005	– –	0.091 ± 0.004
90.5 : 100.5	– –	0.138 ± 0.010	– –	0.135 ± 0.002

the high energy part which resulted the new peak of ~ 75 *meV*. However, that peak was too close to the boundary of Fe^{3+} spin wave excitation and the signal was so blurred, it was too dangerous to make such kind of assumption. Thus, the CF excitations ~ 67 *meV* were still not clear and need to be studied further. Third, it was the first time to observe the peak around ~ 100 *meV*, which was forbidden in $PrGaO_3$. It could be explained by that the distortion in PFO was stronger than that in PGO, therefore the matrix element needed to be revised.

Table 5.9 The comparison of measured and calculated energies of Pr^{3+} in PGO and PFO CF at 10 *K*.

Energy levels	$PrGaO_3$			$PrFeO_3$	
0	0.0	0.0	0.0	0.0	0.0
1	5.6^{a}	5.1 ± 0.1^{a}	4.7 ± 0.1^{b}	2.0 ± 0.1^{b}	$--^{c}$
2	16.0^{a}	16.0 ± 0.2^{a}	10.7 ± 0.3^{b}	14.7 ± 0.4^{b}	15.2 ± 0.1^{c}
3	23.4^{a}	21.5 ± 0.2^{a}	20.0 ± 0.4^{b}	23.2 ± 0.5^{b}	24.7 ± 0.1^{c}
4	32.9^{a}	38.0 ± 0.2^{a}	37.0 ± 1.0^{b}	36.0 ± 1.0^{b}	36.6 ± 0.5^{c}
5	67.4^{a}	$--^{a}$	65.0 ± 2.0^{b}	58.0 ± 2.0^{b}	$--^{c}$
6	69.3^{a}	67.0 ± 2.0^{a}	$--^{b}$	$--^{b}$	$--^{c}$
7	89.5^{a}	86.0 ± 2.0^{a}	$--^{b}$	$--^{b}$	88.1 ± 0.5^{c}
8	113.1^{a}	$--^{a}$	$--^{b}$	$--^{b}$	97.9 ± 0.3^{c}

† *a* reported in reference [11]; *b* reported in reference [12]; *c* is from our work.

5.3.3.3) Crystal Field Study of Sm^{3+} ions

There are 5 electrons in the 4*f* shell of Sm^{3+}. According to Hund's rule, the resulting free-ion electronic ground state is ${}^6H_{5/2}$. Similar to Nd^{3+} in NFO, the ground state multiplet of Sm^{3+} splits into 3 doublets, as shown in Fig. 5.16.

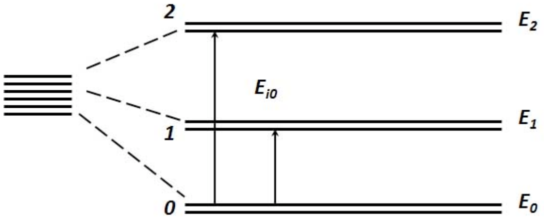

Figure 5.16 Crystal field splitting diagram in Sm^{3+} with distorted orthorhombic symmetry. E_{ij} is the transition energy from *i*th and *j*th level.

Table 5.10 The magnetic form factors, $\langle j_0 \rangle$ and $\langle j_2 \rangle$, for Sm^{3+}.

Sm^{3+}	*A*	*a*	*B*	*b*	*C*	*c*	*D*
$\langle j_0 \rangle$	0.0288	25.207	0.2973	11.831	0.6954	4.212	-0.0213
$\langle j_2 \rangle$	0.4707	18.430	1.4261	7.034	0.9574	2.439	0.0182

The magnetic form factor of Sm^{3+} is calculated from the listed constants in the Table 5.10 [6, 7].

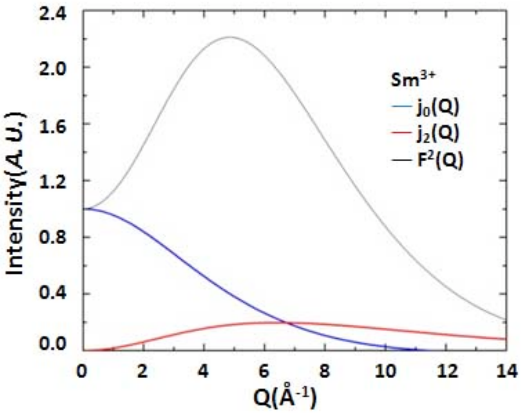

Figure 5.17 The magnetic form factors, $\langle j_0 \rangle$ and $\langle j_2 \rangle$, for Sm^{3+}.

Because of the strong neutron absorption of Sm^{3+}, the signal was very low in the reduced data. It was very hard to get accurate background information from the empty can and phonons. From Fig. 5.18(dots), we can clearly see that there is a wide shoulder around $\sim$ 20 *meV*, a broad peak around $\sim$ 30 *meV*, a bump from 40 $\sim$ 60 *meV*, and a sharp peak around $\sim$ 65 *meV*. Two of the first three could come from the CF of Sm^{3+}, the other one might originate from the remaining of

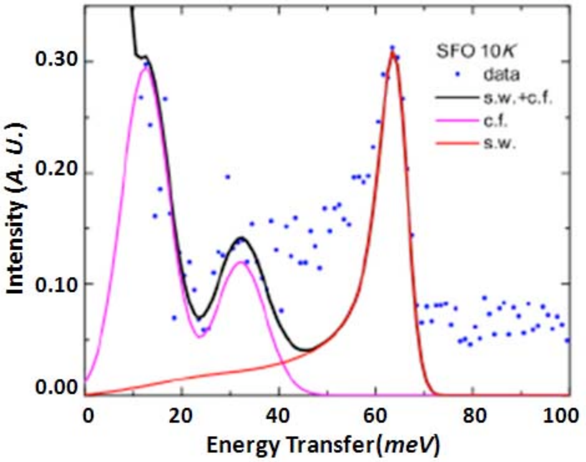

Figure 5.18 The theoretical calculation and magnetic scattering measurement of SFO at 10 *K* on ARCS. The experimental data are blue dots, the total simulating contribution is black line, the Heisenberg model and crystal field calculations are red line and magenta line, respectively.

empty can and phonons; the last one, ∼ 65 *meV*, was the magnetic signal of the Fe^{3+} spin wave which could be discussed in the following section and calculated by *NN*s Heisenberg model.

Table 5.11 The comparison of measured and calculated energies and transition intensities of Sm^{3+} in SFO CF at 10 *K*.

Energy Range	State number (S_{tth})		State number (S_{ω})	
(*meV*)	spin-wave	C.F.	spin-wave	C.F.
10.5 : 20.5	0.025 ± 0.003	0.507 ± 0.034	0.027 ± 0.003	0.509 ± 0.053
15.5 : 25.5	0.035 ± 0.004	0.254 ± 0.016	0.035 ± 0.004	0.255 ± 0.021
20.5 : 30.5	0.042 ± 0.005	0.171 ± 0.010	0.044 ± 0.005	0.178 ± 0.014
25.5 : 35.5	0.049 ± 0.005	0.232 ± 0.014	0.048 ± 0.005	0.249 ± 0.021
30.5 : 40.5	0.056 ± 0.006	0.203 ± 0.012	0.057 ± 0.006	0.207 ± 0.018
40.5 : 50.5	0.087 ± 0.008	0.018 ± 0.001	0.087 ± 0.008	0.018 ± 0.002
50.5 : 60.5	0.224 ± 0.019	6.06e-5 ± 4e-6	0.244 ± 0.024	6.86e-4 ± 1e-4
60.5 : 70.5	0.439 ± 0.033	5.58e-9 ± 3e-10	0.438 ± 0.036	7.07e-4 ± 1e-4

Up to now, there has been no previous work on CEF of Sm^{3+} in SFO. Based on the research of $SmMnO_3$ (SMO) by infrared spectra [13], there were two CEF excitations around ∼ 16 *meV* and ∼ 37 *meV*, which we could find in Fig. 5.18. Since the magnetic and lattice structure of SFO is pretty similar to SMO, the CEF excitation spectra of Sm^{3+} in these two compounds should be similar. Then, the bump from 40-60 *meV* should be the result of the remaining of empty can and phonons. In order to prove this assumption, Q-cuts were plotted in Fig. 5.19.

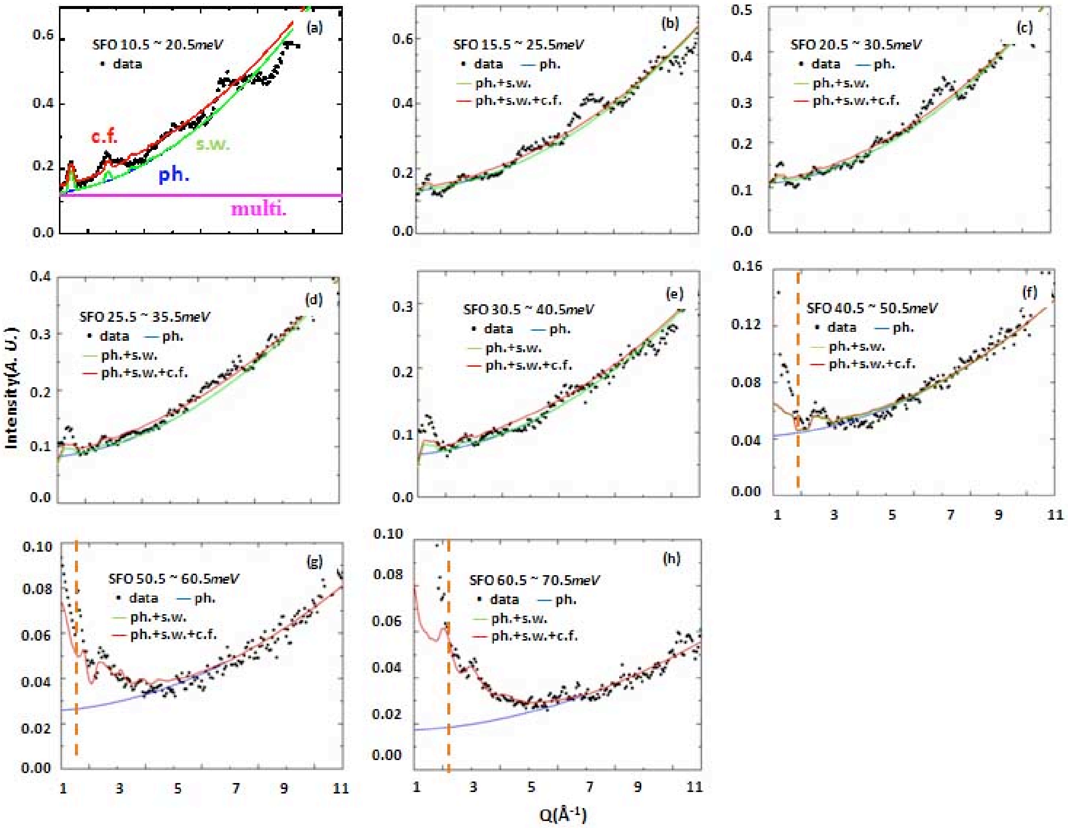

Figure 5.19 The Q-dependence of the neutron scattering data for different energy transfer ranges in SFO at $T = 10$ K. The brown dash line in some different energy transfer ranges ((f)-(h)) is the starting point of the experimental recording.

Then, the Q-cuts in Fig. 5.19 could be fitted and Fig. 5.19(a) is an example of the fitting with different components to the total scattering function of 10.5 $meV \sim 20.5$ meV.

Based on Table 5.11, the relative state numbers in E-cuts and Q-cuts were compared: from 10.5 meV to 40.5 meV, CF was included in the total fittings; from 40.5 meV to 60.5 meV, CF was not included in the total fittings. The fitting results were very good. So we could assign the wide shoulder around ~ 20 meV and the broad peak around ~ 30 meV to the CFE of Sm^{3+} in SFO, and the bump from $40 \sim 60$ meV should arise from poorly subtracted empty can and phonons.

5.4 Heisenberg Model of Fe-ion Spin Waves

From above discussion, the contribution of CEF excitations of the rare-earth ions, R^{3+}, to the magnetic signal have been studied and it provides a chance to more accurately analyze the spin-wave spectra

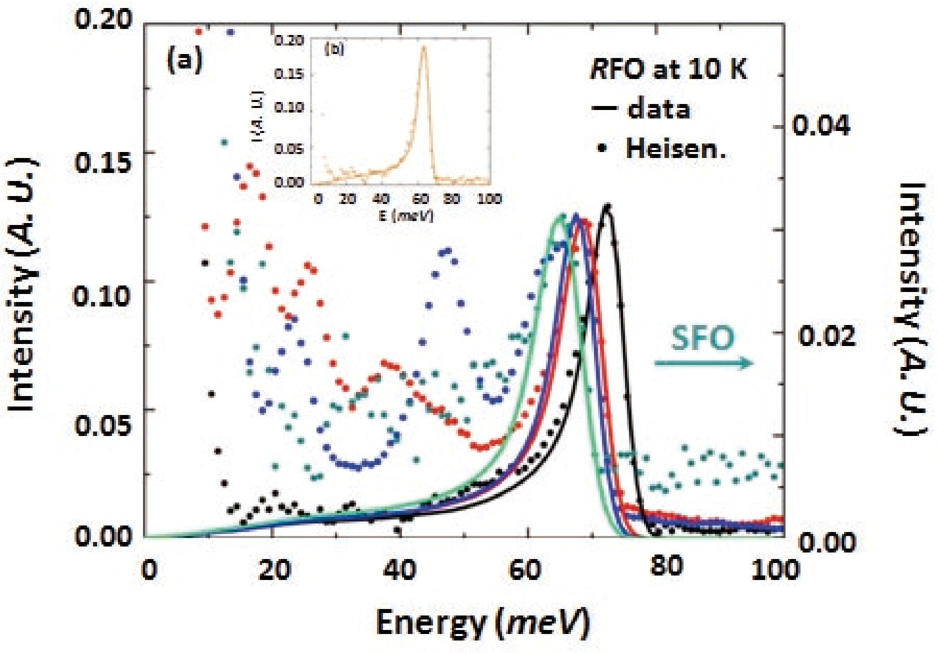

Figure 5.20 (a) The Heisenberg model calculation for *R*FO (*R* = La, Pr, Nd, and Sm) with J_{AF} = -4.75 *meV*(LFO), J_{AF} = -4.55 *meV*(PFO), J_{AF} = -4.45 *meV*(NFO), and J_{AF} = -4.32 *meV*(SFO). (b) The Heisenberg model calculation for YFO with J_{AF} = -4.19 *meV*.

of Fe^{3+} ion in *R*FO. If it is assumed that there is no coupling between *R* and Fe spins, *R*FO is expected to have the similar magnetic dynamics of Fe^{3+} ion as LFO, as shown in Fig. 5.5 and 5.20, then the peak in the SWDOS of Fe ions in PFO, NFO, SFO, and YFO appears at $\sim$ 69 *meV*, $\sim$ 67 *meV*, $\sim$ 64 *meV*, and $\sim$ 63 *meV*. The former two are consistent with the findings from the report of K. Feldmann *et al.* [8] and R. Przenioslo *et al.* [9], while the latter two have never been reported before. Therefore, the Heisenberg model is applied: the peak in the SWDOS should appear at an energy of $6|J_{AF}|S^{3+}$, where S^{3+} is a constant, 5/2. J_{AF} should be -4.55 ± 0.01 *meV* (PFO), -4.45 ± 0.01 *meV* (NFO), -4.34 ± 0.01 *meV* (SFO), and -4.18 ± 0.01 *meV* (YFO), respectively. The error-bars are determined by the χ^2 method in LFO part, section 5.3.2. The series exchange energies of *R*FO are listed in Table 5.12. The model calculation and experimental data were compared in Fig. 5.20, and the integrated-intensity agreement of *R*FO is reasonable as CF intensity included.

In fact, we can get a rough exchange energy in mean field theory (MFT): there are 6 *NN*s which have the same spin moments as the center ion's. The exchange energy can be expressed as,

$$J_{AF} = \frac{3k_B T_N}{zS(S+1)}, \tag{5.15}$$

where *S* represents the spin and z is the total number of *NN* (z=6).

Table 5.12 Antiferromagnetic exchange energies and integrated intensities of *Fe*$^{3+}$ magnetic states of rare-earth orthoferrites.

	$LaFeO_3$	$PrFeO_3$	$NdFeO_3$	$SmFeO_3$	$YFeO_3$
Néel Temperature(*K*)*	738	707	693	675	643
AFM exchange energy (*meV*)					
Heisenberg model	4.75 ± 0.01	4.55 ± 0.01	4.45 ± 0.01	4.32 ± 0.02	4.18 ± 0.01
MFT	3.74	3.58	3.51	3.42	3.26
Integrated Intensity	1.71	1.70	1.70	0.62	1.70

∗ reference 1.

As listed in Table 5.12, the MFT calculation implies a linear relationship between the exchange energy (J_{AF}) and *Néel* temperature (T_N). Therefore, the ratio of spin-wave excitation should be the same as the ratio of T_N, and we can easily get *R*FO (*R* = Pr, Nd, Sm and Y) from ∼ -4.75 meV (LFO).

Furthermore, the integrated areas of the five samples were compared. The similar numbers of *R*FO (*R* = La, Pr, Nd, and Y) prove that the *Fe*$^{3+}$ ion states of this series compounds were very similar. The SFO was different because the proper absorption constant is needed to correct the strong neutron absorption of *Sm*$^{3+}$.

5.5 Summary

We applied INS to study the compounds, *R*FeO_3 (*R* = La, Pr, Nd, Sm, and Y), and the magnetic excitation from Fe^{3+} ion can be fitted by the linear Heisenberg model. Due to the lattice distortion, the AF exchange energies and T_N were decreasing with the *R*-site substitution from La to Y, which agreed with the results of mean field theory. With the help of Q-cuts fitting, the CEFs of the magnetic ions, Pr^{3+}, Nd^{3+}, and Sm^{3+}, were fitted and they agreed with the theoretical calculation very well.

Bibliography

[1] D. Treves, Journal of Applied Physics 36 (1965) 1033

[2] W. C. Koehler, E. O. Wollan, and M. K. Wilkinson, Physical Review 118 (1960) 58

[3] G. L. Squires, *Introduction to the theory of thermal neutron scattering*, Cambridge University Press. 1996

[4] R. J. McQueeney, *Lattice effects in high-temperature superconductors*, UMI, 1997

[5] S. M. Shapiro, J. D. Axe, and J. P. Remeika, Physical Review B 10 (1974) 2014

[6] P. J. Brown, *Magnetic form factors*, chapter 4.4.5; A. J. C. Wilson, ed. *International tables for crystallography*, vol. C, pp. 391-399

[7] S. W. Lovesesy, *Theory of neutron scattering from condensed matter*, vol. 2, Clarendon Press, Oxford, 1984; W. Marshall, and S. W. Lovesesy, *Theory of thermal neutron scattering*, Chapter 6, Oxford University Press 1971

[8] A. Podlesnyak, S. Rosenkranz, F. Fauth, W. Marti, A. Furrer, A. Mirmelstein, and H. J. Scheel, Journal Physics: Condensed Matter 5 (1993) 8973-8982

[9] R.Przenioslo, I. Sosnowska, M. Leowenhaupt, and A.Taylor, Journal of Magnetism and Magnetic Materials 140-144 (1995) 2151-2152

[10] M. Loewnhaupt, Physica B 163 (1990) 479-482

[11] K. Feldmann, K. Hennig, L. Kaun, B. Lippold, M. M. Lukina, S. Matthies, W. Matz, and E. Warming, Physica Status Solidi B 72 (1975) 817

[12] A. Podlesnyak, S. Rosenkranz, F. Fauth, W. Marti, H. J. Scheel, and A. Furrer, Journal Physics: Condensed Matter 6 (1994) 4099-4106

[13] V. Nekvasil, S. Jandl, A. A. Mukhin, V. Yu. Ivanov, and A. M. Balbashov, Journal of Applied Physics 105 (2009) 07E113

CHAPTER 6. Inelastic Neutron Scattering Study of $R_{1/3}$Sr$_{2/3}$FeO$_3$ (*R* = La, Nd, Pr, and Sm)

6.1 Introduction

The INS study of the parent compound *R*FO served as a model system to extract the magnetic exchange energy from INS data after accounting for phonons, CF excitations and other background contributions. For the Sr-doped compounds, we are interested in the effect of CO on the spin excitations. Obtaining the exchange parameters J_F and J_{AF} allow us to test the validity of the suggestion that CO of LSFO is driven by magnetism [1, 2]. Due to the smaller rare-earth ionic size, the *R*-site substitution from La to Sm leads to narrower bandwidths, which should increase the importance of Coulomb interactions [3].

In this chapter, I will discuss LSFO at first and show that the magnetic energy plays an important role in the CO in LSFO: the magnetic energy alone can stabilize the CO state. Then, I will discuss the substituted compounds with other rare-earths, the role of Coulomb interactions in CO transition should be more and more important due to the narrower bands and larger charge-transfer (CT) gap.

Similar to *R*FO parent compounds, the analysis of the magnetic scattering in *R*SFO (*R* = Nd, Pr, Sm, and Y) is much more complicated than LSFO due to the presence of the unpaired electrons in R^{3+}. To isolate the contribution of Fe ions in *R*SFO, we must simultaneously fit both the CEF excitations from R^{3+} and the spin wave excitations from Fe. In chapter 5, we have studied the crystal electric field (CEF) excitations of the parent compounds, *R*FO. Since the environment of R^{3+} in *R*FO is similar in *R*SFO, we can assume that the CEF of R^{3+} in *R*SFO should not change much with Sr^{2+} doping other than an obvious decrease in intensity by 1/3 of CEF excitation [4, 5]. Therefore, the contribution of Coulomb interactions can be tested.

6.2 Data Measurement

INS measurements were performed on Pharos spectrometer at Lujan Center of LANL and ARCS at SNS of ORNL. LSFO, NSFO and YSFO were measured on Pharos while LSFO, PSFO, NSFO, and SSFO were measured on ARCS. LSFO and NSFO had been measured on each instrument to compare scattering from the same sample. As two similar TOF spectrometers, Pharos and ARCS both measure the scattered intensity S(Q, ω) over a wide range of momentum ($\hbar$Q) and energy transfers ($\hbar\,\omega$).

Table 6.1 Sample masses and moles of *R*SFO (*R* = La, Pr, Nd, Sm, and Y) on Pharos and ARCS.

	Pharos		ARCS	
	mass (*g*)	mole (mol)	mass (*g*)	mole (mol)
$La_{1/3}Sr_{2/3}FeO_3$	40.13	0.192	13.53	0.0649
$Pr_{1/3}Sr_{2/3}FeO_3$	- -	- -	22.37	0.1069
$Nd_{1/3}Sr_{2/3}FeO_3$	38.84	0.185	14.22	0.0676
$Sm_{1/3}Sr_{2/3}FeO_3$	- -	- -	4.15	0.0185
$Y_{1/3}Sr_{2/3}FeO_3$	58.01	0.275	- -	- -

On ARCS, powders of *R*SFO (*R* = La, Pr, Nd, and Y) were packed in 4 aluminum foil slots, and loaded in an aluminum can. INS spectra was measured with incident energy (E_i) of 180 *meV*. On Pharos, powders were packed in a flat aluminum can and E_i was 160 *meV*, Table 6.1. The samples were oriented at 135° to the incident neutron beam on both instruments, and run for approximately $\sim$ 24 hours on Pharos and $\sim$ 3 hours (except SSFO) on ARCS due to the different flux. The large absorption cross section of Sm^{3+} ion limited the loaded mass of the SSFO powders, hence ARCS with superior flux was the only suitable instrument to measure SSFO and it was measured $\sim$ 6 hours.

Similar to *R*FO, the TOF data were reduced into $\hbar\omega$ and scattering angle (2θ) histograms after applying the corrections for detector efficiencies, empty can scattering, and instrumental background. The full spectrum for LSFO at $T = 10\ K$ as a function of 2θ and ω is shown in Fig. 6.1(a). The data summed over the high angle range of 2θ = 70 - 90° contain only phonon scattering, Fig. 6.1(b), while the data within the low angle range of 7 - 30° contain scattering from both phonons and spin-waves, Fig. 6.1(c). Magnetic scattering in LSFO sample was obtained by subtracting the high angle data from low angle data after scaling by a constant factor at each temperature described in section 3.6, as shown in Fig. 6.1(c). The final magnetic scattering of LSFO is compared with LFO in Fig. 6.1(d): the single peak in LFO

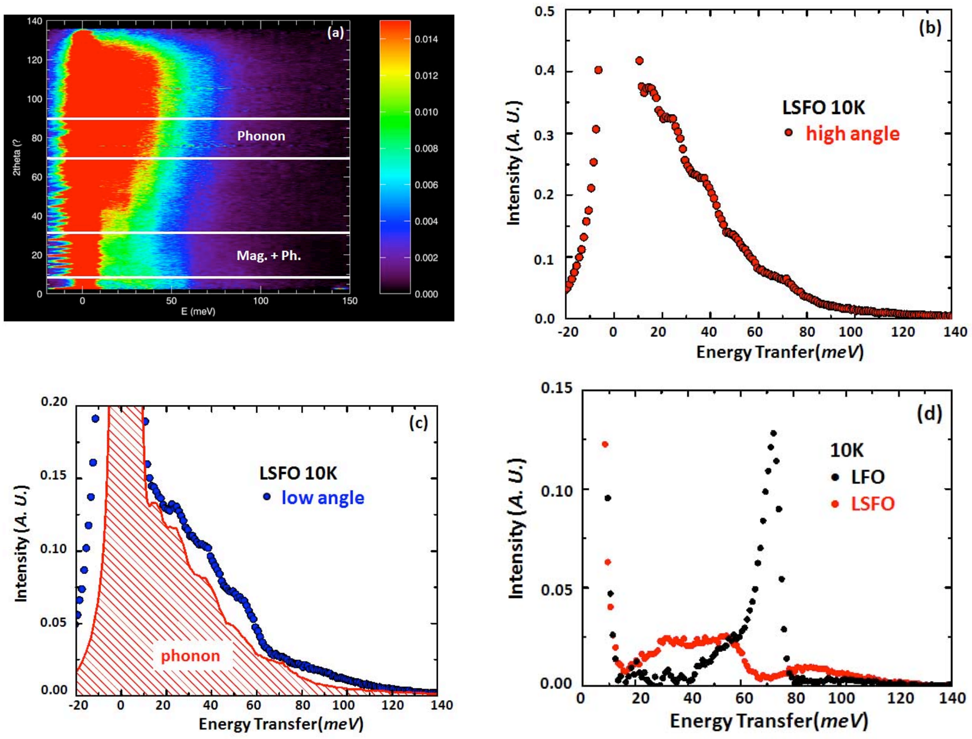

Figure 6.1 (a) Inelastic neutron scattering intensity of LSFO (color scale) versus scattering angle and energy transfer at $T = 10\ K$ and $E_i = 180\ meV$ on ARCS. Horizontal white lines delineate regions where phonon and magnetic scattering are isolated. (b) Neutron intensity summed over the angle range from 70 - 90° originating from phonons (red dots). (c) Neutron intensity summed over the low angle range from 7 - 30° (blue dots) and phonon background from scaled from high angle sum (red hatched region) (d) Isolated magnetic scattering from LSFO (red dots) and LFO (black dots).

splits into a low and high energy band with Sr doping (we will discuss the origin of this splitting in detail below); and the residual phonon intensities at $\sim$ 20 and 30 meV are presented in both samples as well.

6.3 Results and Discussion

Fig. 6.2 shows the DOS of spin-wave excitations of RSFO (R = La, Nd, and Pr): there were no magnetic signals higher than $\sim$ 140 meV and the high energy excitation spectrum, > 90 meV, were very similar for each composition. There are clearly two magnetic energy bands in LSFO and PSFO; although there appears to be only one single broad band in NSFO. Suggesting that the low energy band in LSFO and PSFO moved toward to high energy band and into the gap between them. We now describe the

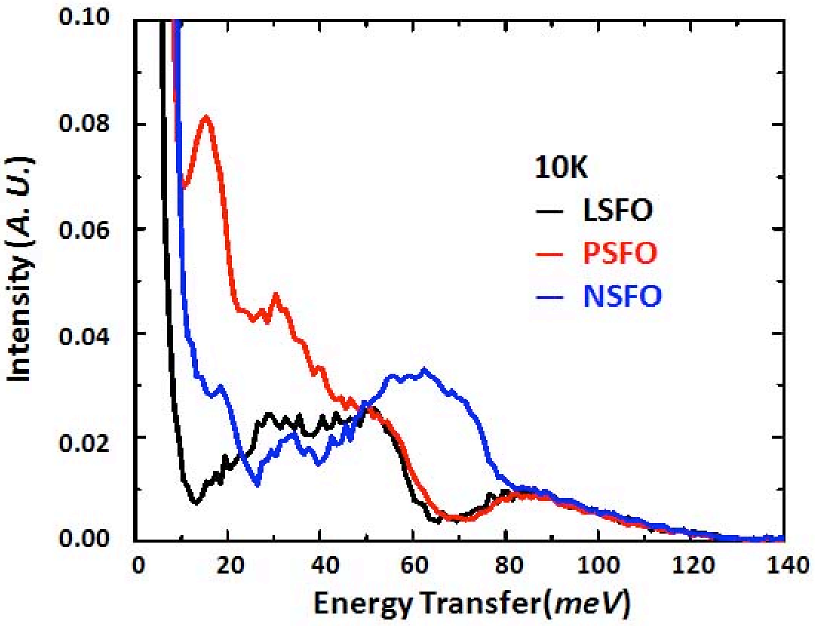

Figure 6.2 Inelastic neutron scattering intensity of *R*SFO (*R* = La, Pr, and Nd) versus scattering angle and energy transfer at T = 10 K and E_i = 180 meV.

analysis in details as in *R*FO, the magnetic excitations of *R*SFO (*R* = Pr and Nd) are complicated by the presence of CEFs on the rare earth metals.

6.3.1 $\mathbf{La_{1/3}Sr_{2/3}FeO_3}$

Figure. 6.3(a) shows the temperature dependence of the magnetic scattering in LSFO. As the temperature was raised, the $\sim$ 85 meV spin wave band gradually shifts to lower energies and becomes strongly damped just below the transition. Spin wave damping might be caused by magnon - magnon interactions near T_V, $\sim$ 210 K. However, as the Verwey transition is first order transition, it is also possible that the charge fluctuations cause damping since the optical gap measured by infrared reflectivity closes rapidly near T_V [3]. Spin wave scattering is replaced by broad paramagnetic scattering above T_V. The intensities at $\sim$ 20 and 30 meV appear at all temperatures, which also confirms the argument that part of the low energy intensity has its origin in the residual phonon scattering. From the measurement below T_V, the energy band, which begin around $\sim$ 85 meV, could not be fully measured with the incident energy $E_i \sim$ 120 meV, so the neutron spectra are also measured with incident energy of 300 meV. In Fig. 6.3(b), there were no magnetic excitations higher than 140 meV, and the two magnetic spin-wave peaks are clearly

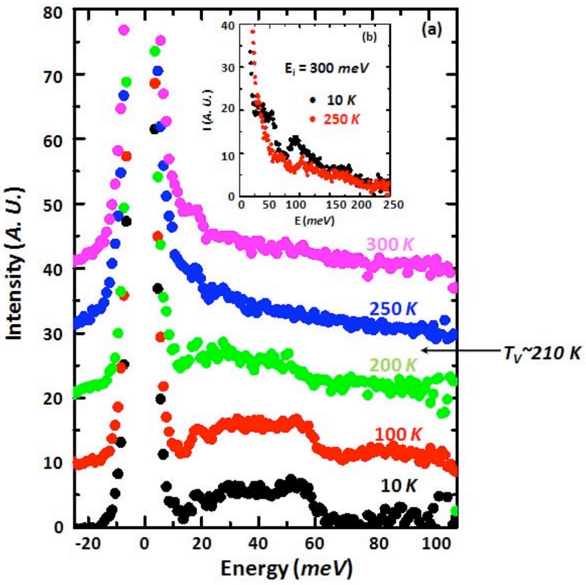

Figure 6.3 (a)Temperature dependence of the magnetic scattering from LSFO with E_i = 120 *meV* on Pharos. (b) Magnetic scattering from LSFO up to high energies with E_i = 300 *meV* at *T* = 10 *K* and *T* = 250 *K* on Pharos.

shown when compared to the data above T_V at 250 *K*.

Previous studies on *R*FO showed that the experimental data agreed very well with the Heisenberg-model calculation of spin-waves on Fe site. However, the magnetic structure and exchange interactions are more complicated in *R*SFO. As discussed in section 4.2.6; There are two different kinds of Fe ions, Fe^{3+} and Fe^{5+}, and two related exchange interactions; antiferromagnetic interaction between Fe^{3+}-Fe^{3+} and ferromagnetic interaction between Fe^{3+}-Fe^{5+}, Fig. 6.4. We constructed a *NN* Heisenberg model Hamiltonian to fit the data and using LFO as a reference. The Hamiltonian for those spin waves is

$$\mathbf{H} = -J_{AF} \sum_{\langle i,j \rangle} \mathbf{S}_i^{3+} \cdot \mathbf{S}_j^{3+} - J_F \sum_{\langle i,j \rangle} \mathbf{S}_i^{3+} \cdot \mathbf{S}_j^{5+} \, , \tag{6.1}$$

where sums are over each pair-type, the *i*th and *j*th iron atom; $\mathbf{S}_i$ and $\mathbf{S}_j$ represent the spin vector on them.

Because of the small charge-transfer gap in LSFO, some fraction of doped holes in LSFO reside on oxygen. The F superexchange exists between Fe^{3+} and nominal Fe^{5+} whether the holes are on iron or oxygen. When the holes are on iron, F exchange occurs between half-filled and empty e_g orbitals. When a single hole is on oxygen, sharing of the spin-polarized oxygen electron leads to F exchange. For

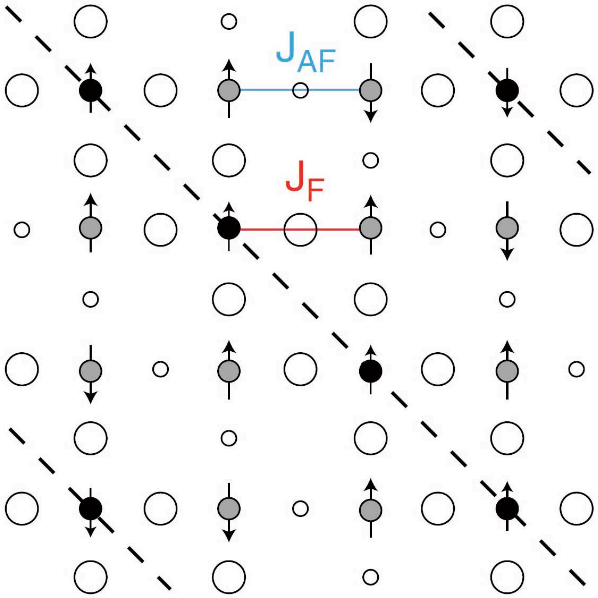

Figure 6.4 Schematic diagram of oxygen hole density and iron spins in the (001) plane of LSFO. Open circles denote oxygen and circle radius represents hole density. Black (gray) circles are nominal Fe^{5+} (Fe^{3+}) ions. The dashed line indicates a metal-centered domain wall.

the same reason, the presence of oxygen holes between Fe^{3+} pairs will reduce J_{AF} as compared to the parent insulator LFO.

Table 6.2 The different fitting exchanges with different spin values of Fe ions in Heisenberg Model.

Model	$J_{AF}(meV)$	$J_F(meV)$	S^{3+}	S^{5+}	J_F/J_{AF}
1	-2.5	5	5/2	5/2	2
2	-3.5	5.1	5/2	2	1.5
3	-4.7	5.2	5/2	3/2	1.1

The spin values of Fe ions are also decided by the holes' position: if the hole is on the oxygen ion, the Fe oxidation state is lower and the spin of Fe ions would be larger.

We tried several model with different values of S^{5+}. Table 6.2 lists three different parameters in the Heisenberg Model and Fig. 6.5(b) shows the experimental data and calculation result with the different fitted exchange energies. Based on the comparisons in Table 6.2 and Fig. 6.5, i) The antiferromagnetic exchange energies J_{AF} changes with the different S^{5+}, but the ferromagnetic exchange energies J_F are insensitive to the value of S^{5+}; ii) The models look the same. It is hard to determine the spin state of S^{5+} from INS. However, a combination of neutron diffraction and Mössbauer measurements had estimated

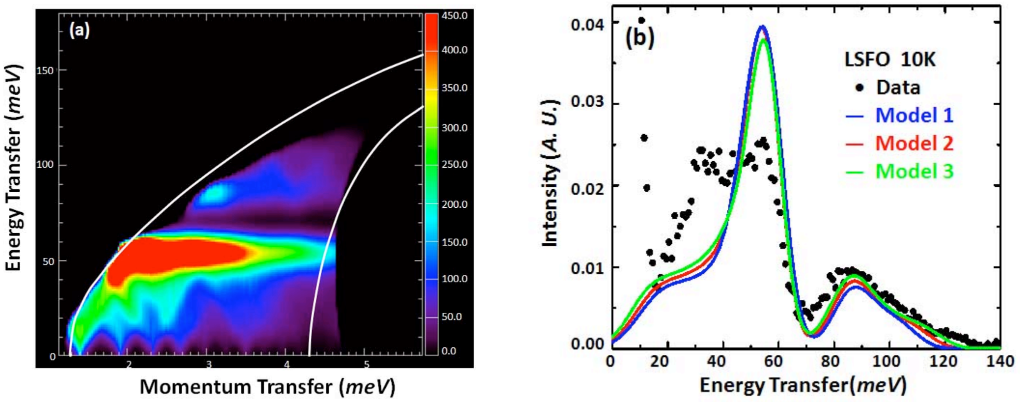

Figure 6.5 (a) The calculated (left) neutron intensities of model 2 and (b) extracted angle-averaged magnetic intensity (dots) versus the intensity calculated from Heisenberg models for the spin waves with different spin values on Fe^{5+} ions for LSFO on ARCS. The curved white lines indicate the low-angle summation regions (3° - 30°) leading to the corrected magnetic spectra.

the iron valences to be ~Fe$^{3.4+}$ and ~Fe$^{4.2+}$ due to hybridization with oxygen [6]. Since Model 2 ($S^{3+} \approx 5/2$ and $S^{5+} \approx 2$) is the closest to the measured moment sizes with the data, J_{AF} = - 3.5 *meV* and J_F = 5.1 *meV* ($|J_F/J_{AF}|$ = 1.5), as shown in Fig. 6.5(a), which is the calculated angle averaged the coherent spin-wave scattering cross-section.

Unlike LFO, the LSFO *NN* Heisenberg model calculations do not show quantitative agreement with the data, Fig. 6.5(b). In particular, the model does not capture the observed spectral weight near 35 *meV*. However, the critical ratio $|J_F \ / \ J_{AF}|$ is determined by the splitting between the upper (>70 *meV*) and lower energy (<60 *meV*) bands. The *NN* model calculations show that there are two peak energies with a maximum energy on MCDW: i) For F-like spin waves, the interactions exist between Fe^{3+} and Fe^{5+}, so the local excitation energy originates mainly from the *NN*s of Fe^{3+} and Fe^{5+} ions; ii) For AF-like spin waves, the interaction exist mainly between Fe^{3+} and Fe^{3+}, and the local excitation energy originates from the *NN*s of Fe^{3+} ions. The rough calculation of the magnetic spectrum is expressed as,

$$\begin{aligned} &High-energy\,transfer:\ F-like\,band\,,\ E_F = 3J_F(2S^{3+}+S^{5+})\,,\\ &Low-energy\,transfer:\ AF-like\,band\,,\ E_{AF} = 3\mid J_{AF}\mid S^{3+}+3J_FS^{5+}\,, \end{aligned} \tag{6.2}$$

Since the high energy band consists of F-like spin waves with $\sim$ 110 *meV* and the low energy band is AF-like spin waves with $\sim$ 55 *meV*, J_F = 5.1 *meV* and J_{AF} = -3.5 *meV*.

In previous chapter, chapter 5, we have discussed the error-bar of J_{AF} in *R*FO. With the similar method, we will estimate the error-bar of LSFO. Compared to the fitting of *R*FO, the fitting result of LSFO is very rough. There are two peaks, but the angle averaged DOS cannot give much details on the accurate positions and intensities. Furthermore, there are 3 variables in the Heisenberg model Hamiltonian, Eq(6.1), S^{5+}, J_{AF} and J_F. Hence, just the gap region of LSFO is analyzed with two fixed variables, and the error-bar of the third is obtained. Therefore, the fitting parameters of LSFO are, S^{5+} = 2.0 $\pm$ 0.1, S^{3+} = 2.5, J_F = 5.1 $\pm$ 0.1 *meV* and J_{AF} = -3.5 $\pm$ 0.2 *meV*, which results in the ratio $|J_F\ /\ J_{AF}| > 1.5$.

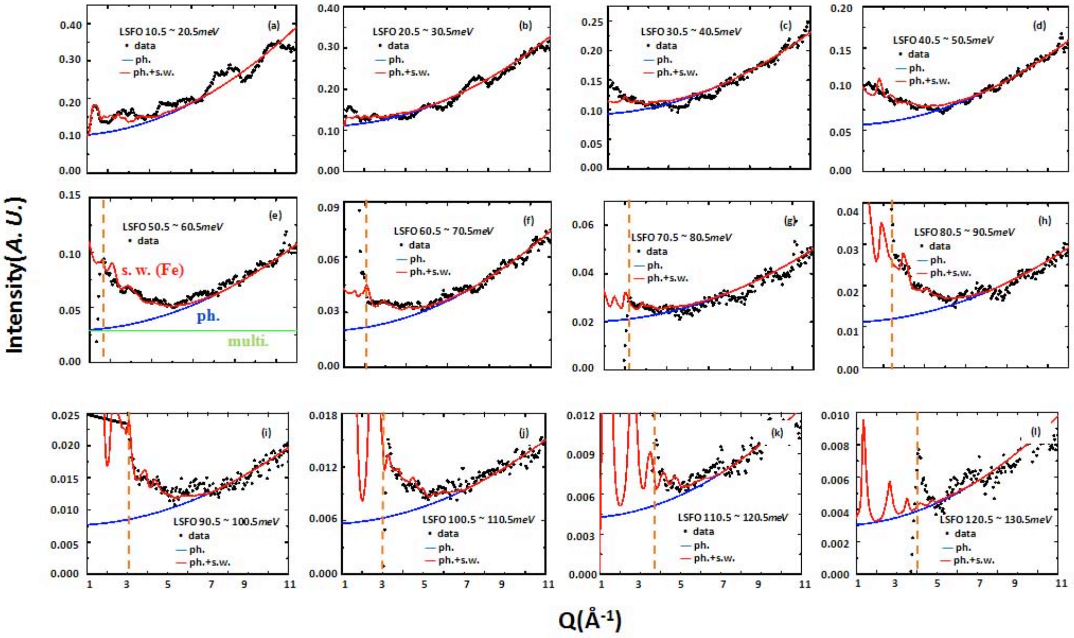

Figure 6.6 The Q-dependences of different energy transfer ranges for LSFO with 10 *meV* step: (a) 10.5 - 20.5 *meV*, (b) 20.5 - 30.5 *meV*, (c) 30.5 - 40.5 *meV*, (d) 40.5 - 50.5 *meV*, (e) 50.5 - 60.5 *meV*, (f) 60.5 - 70.5 *meV*, (g) 70.5 - 80.5 *meV*, (h) 80.5 - 90.5 *meV*, (i) 90.5 - 100.5 *meV*, (j) 100.5 - 110.5 *meV*, (k) 110.5 - 120.5 *meV*, and (l) 120.5 - 130.5 *meV*. The black dots are the experimental data. The blue line it an estimate of the incoherent phonon background plus multiple scattering. The red line is the calculation of the polycrystalline averaged spin wave scattering plus background using the parameters in the text.

With the same fitting parameters in Heisenberg model, we calculated the Q-cut of LSFO, Fig. 6.6, and the energy transfer range 50.5-60.5 *meV*, Fig. 6.6(e), is discussed as an example. Table 6.3 compares the different calculated state numbers from E-cut and Q-cut in LFO, and the related parameters of energy

Table 6.3 The integrated intensities of Fe^{3+} magnetic states of Energy - cuts and Q - cuts in LSFO.

Energy Range	State number	
(meV)	S_{tth}	S_{ω}
10.5 : 20.5	0.168 ± 0.007	0.191 ± 0.007
20.5 : 30.5	0.212 ± 0.009	0.217 ± 0.008
30.5 : 40.5	0.271 ± 0.013	0.267 ± 0.011
40.5 : 50.5	0.552 ± 0.024	0.516 ± 0.021
50.5 : 60.5	0.817 ± 0.034	0.796 ± 0.031
60.5 : 70.5	0.211 ± 0.014	0.211 ± 0.010
70.5 : 80.5	0.069 ± 0.003	0.068 ± 0.002
80.5 : 90.5	0.177 ± 0.009	0.177 ± 0.010
90.5 : 100.5	0.143 ± 0.006	0.140 ± 0.008
100.5 : 110.5	0.084 ± 0.003	0.087 ± 0.004
110.5 : 120.5	0.033 ± 0.001	0.033 ± 0.001
120.5 : 130.5	0.003 ± 3.0E-4	0.003 ± 2.0E-4
130.5 : 140.5	2.62E-5 ± 1.0E-6	$--$

resolution and the Heisenberg Model are determined.

Next-nearest-neighbor (*NNN*) exchange may affect the results as they will modify the zone boundary and optical spin wave energies, leading to shifting and broadening of peaks in the SWDOS. If *NNN* interactions widen the splitting of the high and low energy bands (as would occur, for example, by the presence of ferromagnetic Fe^{3+}-Fe^{3+} *NNN* exchange), then the *NN* model may overestimate the ratio $|J_F/J_{AF}|$. *NNN* exchange can only be determined reliably by dispersion measurements and are presently hampered by the lack of large single crystals. However, studies of *NNN* Heisenberg models for LSFO indicate that $|J_F/J_{AF}| > 1$ unless *NNN* exchanges are very large (greater than $\sim 20\%$ of the *NN* exchange). Such large *NNN* interactions are not expected for either LFO or LSFO based on INS studies of single crystals of similar cubic perovskites such as $TmFeO_3$ [7], YVO_3, $LaMnO_3$, and $Pr_{0.5}Sr_{0.5}MnO_3$ [8], and even the hole doped A-type AF metal $Nd_{0.45}Sr_{0.55}MnO_3$ [9].

The similar 35 meV signal was also observed in LFO, Fig. 6.1(d). In order to check the assumption that this additional intensity comes from the phonon or empty can background, the Q-cut of LSFO was useful. In Fig. 6.6(c), we could clearly find the total fitting of phonon and spin-wave was good in the Q-cut, 30.5 $meV \sim$ 40.5 meV, and the total state number agreed very well in the E- and Q-cuts for that energy scale. Therefore, there was a possible explanation that the 35 meV signal was not the magnetic energy excitation.

The $\sim 30\%$ reduction of J_{AF} in LSFO as compared to LFO was consistent with oxygen hole density between Fe^{3+}-Fe^{3+} pairs as expected from the small charge-transfer gap. Based on this, we proposed that the MCDW was a charge density wave, with appreciable hole density in the AF region between the domain walls. Fig. 6.4 illustrated this scenario with schematic drawing of iron and oxygen positions in the [001] plane of LSFO. Oxygens surrounding Fe^{5+} are depicted as having significant hole density, while oxygens between Fe^{3+}-Fe^{3+} pairs have smaller hole density. Despite having hole density on oxygen, the magnetic domain wall is still centered on the nominal Fe^{5+} metal sites (i.e., it is not an oxygen centered domain wall).

The measured exchange ratio $\mid J_F \,/\, J_{AF} \mid > 1$ implies that magnetic interactions alone are sufficient for stabilizing the observed [111] CO structure. It should be noted that for holes that are primarily on iron, the [111] structure also has the minimum Coulomb energy. However, the oxygen character of the doped holes and their delocalization, as indicated by the presence of doped holes between domain walls, would strongly reduce the Coulomb energy. Thus, it appeared plausible that the Verwey transition in LSFO occurs without a dominant influence from Coulomb interactions.

6.3.2 $\mathbf{Pr_{1/3}Sr_{2/3}FeO_3}$

In order to test the role that the intersite Coulomb interactions play in the CO, we studied a series of *R*SFO (*R*: rare earth) samples. Because the ionic radius of Pr^{3+} was closer to La^{3+} than the other rare earth ions, the magnetic properties of Fe ions in PSFO should be the most similar to the LSFO and are discussed first. Based on the diffraction characterizations, we learned that the lattice structure of PSFO is distorted more from ideal perovskite than LSFO. The net effect is to produce the narrower bands and larger CT gap [3], thus Coulomb interactions are more weekly screened and should be more important with Pr^{3+} substituting on La^{3+}. Given that (1 1 1) has lowest electrostatic energy, this should increase T_V. The observed describe of T_V with rare earth substitution suggests that Coulomb interactions are unimportant. In that case, the magnetism should be modified by rare earth substitution.

Fig. 6.7(a) shows the temperature dependence of the magnetic scattering from PSFO. Similar as LSFO, the ~ 85 *meV* spin wave band gradually shifts to lower energies and becomes strongly damped just below the transition as the temperature was raised, $T_V \sim 200$ *K*. Fig. 6.7(b) compares the low and high energy spectra of the magnetic excitations as the temperature just above and below T_V (210 *K* and 170 *K*). Due to the small temperature difference of 40 *K* between these two data, we could approximately

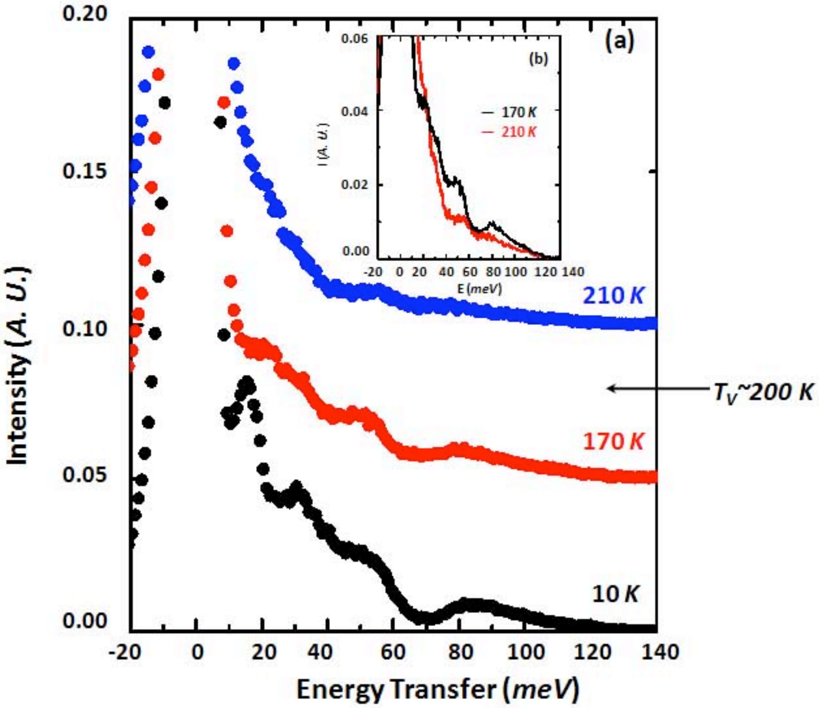

Figure 6.7 (a)Temperature dependence of the magnetic scattering from PSFO with E_i = 160 *meV* on ARCS; (b) Magnetic scattering from PSFO at T = 170 *K* and T = 210 *K*.

assume that they had the same CFE, therefore, the observed magnetic energy gap should originate from Fe ions in PSFO.

Unlike nonmagnetic La^{3+} ions, the magnetic properties of Pr^{3+} ion complicates the study of Fe magnetism in PSFO, so we first discuss how we correct for the CEF excitations of Pr^{3+}.

6.3.2.1) *Crystal Electric Field Excitation*

Based on our previous studies on PFO in section 5.3.3.2, the CEFs of Pr^{3+} were detectable by INS. We assume that the environment of Pr^{3+}-site does not change a lot in PSFO with Sr^{2+} ion doped and the CEF of Pr^{3+} in PSFO would be similar to the PFO. However, 2/3 of Pr^{3+} has been substituted by nonmagnetic ions, Sr^{2+}, the integrated intensity amounts of Pr^{3+} in PSFO should be 1/3 of Pr^{3+} in PFO.

The magnetic scattering intensities of PFO and PSFO were compared in Fig. 6.8(a), the magnetic peak around $\sim$ 67 *meV* in PFO, which was the magnetic excitation signal of Fe^{3+} ions, split into high and low energy bands similar as LFO and LSFO. The CFEs of PSFO were fitted by

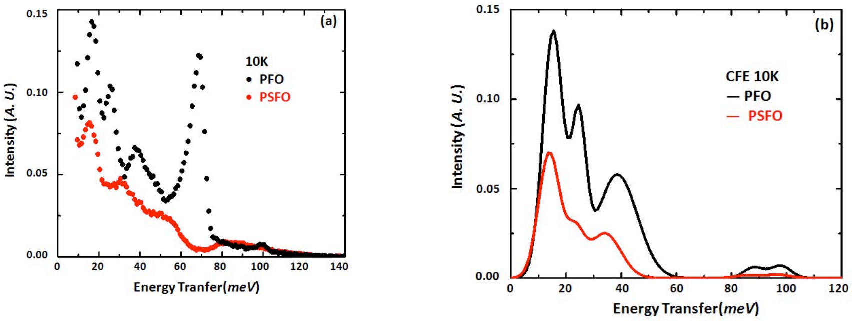

Figure 6.8 (a) The magnetic scattering intensity of PFO (black dots)and PSFO (red dots) at T = 10 K; (b) the fitted CEF intensities in PFO (black line)and PSFO (red line) at T = 10 K.

a series of gaussian functions using a similar method as the fitting of PFO, Fig. 6.8(b). In order to confirm the separation of CFEs of Pr^{3+} ions and magnetic excitations of Fe^{3+} ions, both E- and Q-cuts were used. The total integrated intensities from the same E-range/Q-range in both cuts were compared, Table 6.4 [10]. The agreement was good and the fittings were reasonable, excluding the 10.5 meV - 20.5 meV Q-cut which was affected by the elastic tail. The model calculation of Fe^{3+} ions will be discussed in the following section.

Table 6.4 The integrated intensities of Fe^{3+} magnetic states and the CEFs states of Energy-cuts and Q-cuts in PSFO.

Energy Range (meV)	State number (S_{tth})		State number (S_{ω})	
	spin - wave	C.F.	spin - wave	C.F.
10.5 : 20.5	0.154 ± 0.001	1.285 ± 0.083	0.250 ± 0.014	0.750 ± 0.048
20.5 : 30.5	0.203 ± 0.003	0.626 ± 0.009	0.203 ± 0.006	0.622 ± 0.005
30.5 : 40.5	0.279 ± 0.009	0.502 ± 0.014	0.278 ± 0.008	0.502 ± 0.012
40.5 : 50.5	0.535 ± 0.021	0.108 ± 0.005	0.533 ± 0.019	0.105 ± 0.03
50.5 : 60.5	0.676 ± 0.006	0.002 ± 1E-5	0.672 ± 0.008	0.002 ± 1E-5
60.5 : 70.5	0.259 ± 0.021	−−	0.253 ± 0.019	−−
70.5 : 80.5	0.088 ± 0.005	0.004 ± 1E-6	0.088 ± 0.002	0.004 ± 1E-6
80.5 : 90.5	0.153 ± 0.002	0.034 ± 0.001	0.152 ± 0.003	0.036 ± 0.001
90.5 : 100.5	0.135 ± 0.001	0.041 ± 0.001	0.136 ± 0.001	0.043± 0.001
100.5 : 110.5	0.081 ± 0.001	0.010 ± 0.001	0.081 ± 0.001	0.011 ± 0.001
110.5 : 120.5	0.034 ± 0.02	3.51E-5 ± 1E-6	0.033 ± 0.013	−−
120.5 : 130.5	0.005 ± 2E-4	−−	−−	−−
130.5 : 140.5	2.06E-4 ± 1E-5	−−	−−	−−

The fitted CEFs of Pr^{3+} in PSFO and PFO are compared in Table 6.5 [11]. The positions of

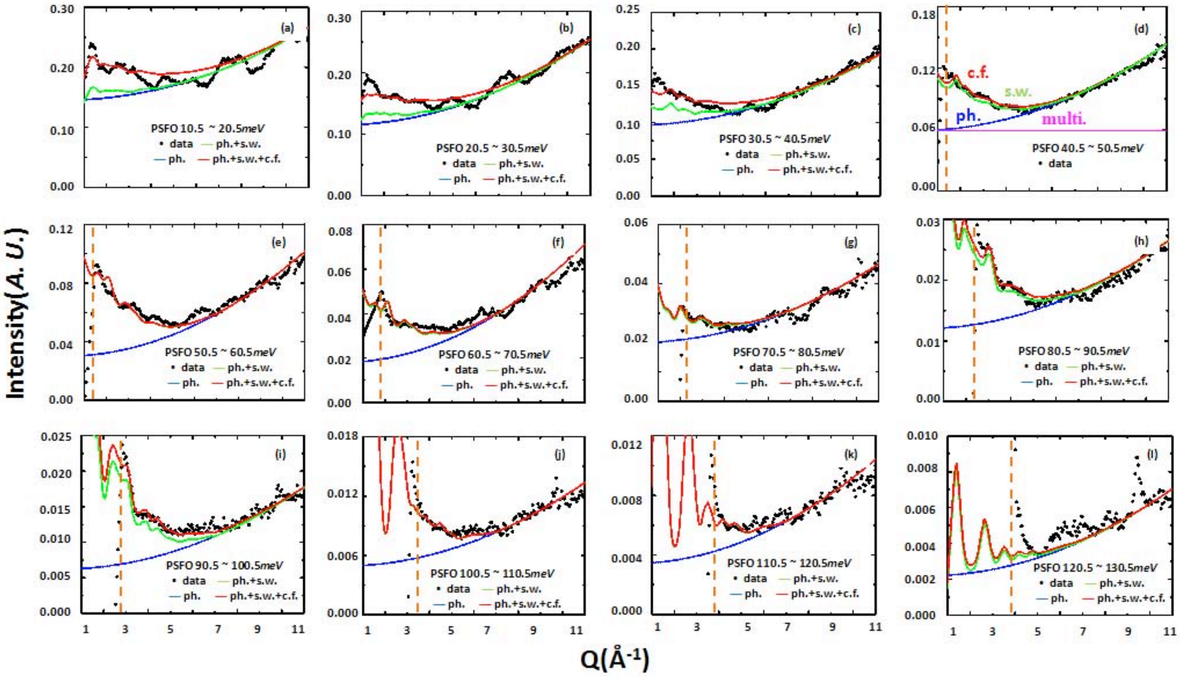

Figure 6.9 The Q - dependences of different energy transfer ranges for PSFO with 10 *meV* step: (a) 10.5 - 20.5 *meV*, (b) 20.5 - 30.5 *meV*, (c) 30.5 - 40.5 *meV*, (d) 40.5 - 50.5 *meV*, (e) 50.5 - 60.5 *meV*, (f) 60.5 - 70.5 *meV*, (g) 70.5 - 80.5 *meV*, (h) 80.5 - 90.5 *meV*, (i) 90.5 - 100.5 *meV*, (j) 100.5 - 110.5 *meV*, (k) 110.5 - 120.5 *meV*, and (l) 120.5 - 130.5 *meV*. The black dots are the experimental data. The blue line it an estimate of the incoherent phonon background plus multiple scattering. The red column is the calculation of the polycrystalline averaged spin wave scattering plus background using the parameters in the text. The brown dash line in some different energy transfer ranges ((d)-(l)) is the starting point of the experimental recording.

CFEs had shifted a little, ~ 1 *meV*, but this shift is within the error bar. The integrated intensity ratio of Pr^{3+} in PSFO was not exactly 3 times of the CFE in PFO, especially E_{20} and E_{60}, but it was still acceptable. Because the excitations of E_{10} (5.9 *meV*) and E_{20}(13.9 *meV*) were very close to the elastic peak, the reported CFE of E_{10} was not observed and the integrated intensity ratio of E_{20} in PFO and in PSFO was far from 3; because the integrated intensity of E_{60}(77.6 *meV*) was small even in PFO, it was hard to be observed in PSFO. Here I also wanted to mention one thing: although the integrated intensity ratio of E_{70} (85.9 *meV*) and E_{80}(96.9 *meV*) agreed very well with PFO, the integrated intensities were small and the fitting could be affected not only by the multiple-phonon, but also magnetic scattering from Fe in those energy regions.

Table 6.5 The integrated intensities of Pr^{3+} CFE states in PFO and PSFO.

E_{i0}	PFO		PSFO			PFO/PSFO
	E. (*meV*)	area	E. (*meV*)	area	ratio	
E_{10}	−−	−−	−−	−−	−−	−−
E_{20}	15.2 ± 0.1	1.29 ± 0.04	13.9 ± 0.3	0.68 ± 0.01	1.00 ± 0.01	1.88 ± 0.06
E_{30}	24.7 ± 0.1	0.53 ± 0.02	23.3 ± 0.2	0.19 ± 0.01	0.28 ± 0.01	2.89 ± 0.19
E_{40}	36.6 ± 0.5	1.06 ± 0.03	34.1 ± 0.1	0.36 ± 0.01	0.53 ± 0.01	2.94 ± 0.12
E_{50}	−−	−−	−−	−−	−−	
E_{60}	−−	−−	−−	−−	−−	
E_{70}	88.1 ± 0.5	0.054 ± 0.01	85.9 ± 0.4	0.018 ± 0.003	0.02 ± 0.01	3.00 ± 0.40
E_{80}	97.9 ± 0.3	0.063 ± 0.007	96.9 ± 0.4	0.021 ± 0.002	0.03 ± 0.01	3.00 ± 0.40

6.3.2.2) *Heisenberg Model Calculation*

The exchange interactions between Fe sites in PSFO were determined in a similar method as LSFO. However, the environment of Fe ions is changed with the La^{3+} ion in LSFO replaced by the Pr^{3+} ion in PSFO. Because the quantities of the *R*-site substitution were small, one - third, and the ionic size of Pr^{3+} was close to the size of La^{3+}, the structure of Fe-O perovskite does not change significantly from LSFO to PSFO [3]. We would still apply the *NN* Heisenberg model Hamiltonian for those spin waves in PSFO and use LSFO as a reference.

In LSFO, there are two magnetic energy bands with an energy gap in the range from 60 *meV* - 70 *meV*. In PSFO, the similar energy bands and gap are observed within the error bar, Fig. 6.2. Since the high magnetic energy band cutoff of LSFO and PSFO are in close agreement and this energy is determined primarily by the F exchange energy, we assume that J_F is same in both compounds. Furthermore, since the low magnetic energy band is determined by both J_F and J_{AF}, the values of J_{AF} in both compounds are similar.

However, the total magnetic energy in Heisenberg Model was not just determined by exchange energies, the ionic spins were another factor. In LSFO, we assigned $S^{3+} \approx 5/2$ and $S^{5+} \approx 2$ based on the iron valences Mössbauer measurements, $\sim$Fe$^{3.4+}$ and $\sim$Fe$^{4.2+}$. With La^{3+} replaced by Pr^{3+}, the charge-transfer gap and the electronic bandwidth do not change a lot [3]. In addition, the oxygen deficiency in PSFO was comparable in LSFO based on the results of GSAS fitting [12] and titration discussed in section 4.2.2. Hence, the S^{5+} is not expected to change and is kept as 2. We can understand the result of PSFO using the case of LSFO, the same parameters as LSFO:

J_{AF} = - 3.5 ± 0.2 *meV* and J_F = 5.1 ± 0.1 *meV*. So $|J_F/J_{AF}|$ is larger than 1.

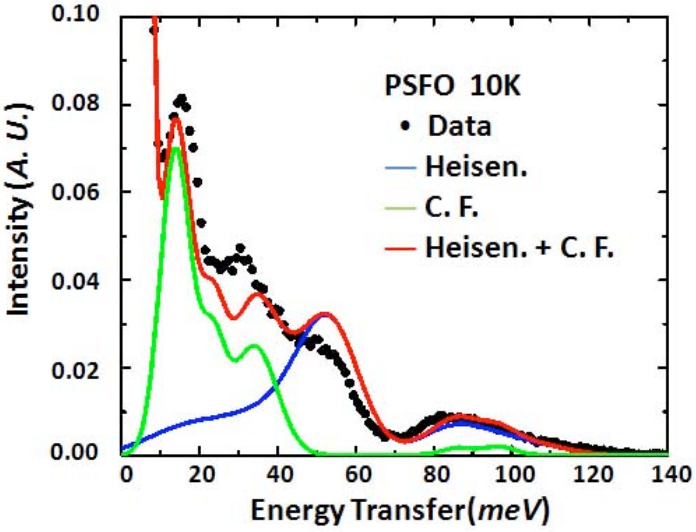

Figure 6.10 Comparison of PSFO magnetic scattering data at $T \sim 10\ K$ (dots) and the total simulating (red line) with the Heisenberg model calculation (blue line) and the CEF excitations (green line) summed from 2θ 3-30°..

The total fitting result including CEF of Pr^{3+} and magnetic excitations of Fe ions were compared to the experimental data, Fig. 6.10. The fitting was not very good in the region 15 *meV* to 35 *meV* which was due to the residual phonon signals that are also observed in LSFO.

Compared to the J_{AF} is - 4.55 *meV* in PFO, there was $\sim 20\%$ reduction of J_{AF} in PSFO. Therefore, we still could propose that the MCDW was a charge density wave, with appreciable hole density in the AF region between the domain walls.

6.3.3 $\mathbf{Nd_{1/3}Sr_{2/3}FeO_3}$

The Nd^{3+} is even smaller and the studies on the Fe magnetism in NSFO could perhaps provide some useful information and check the regularities based on the former discussion on LSFO and PSFO. From the diffraction characterization section 3.2.6, the lattice structure of NSFO is distorted more from ideal perovskite than the PSFO, so NSFO should have even narrower bands and larger CT gap than PSFO [3], and the Coulomb interactions should be even more important.

Fig. 6.11(a) shows the temperature dependence of the magnetic scattering from NSFO. In contrast to PSFO and LSFO, we observed only one energy band instead of the split low and high energy bands.

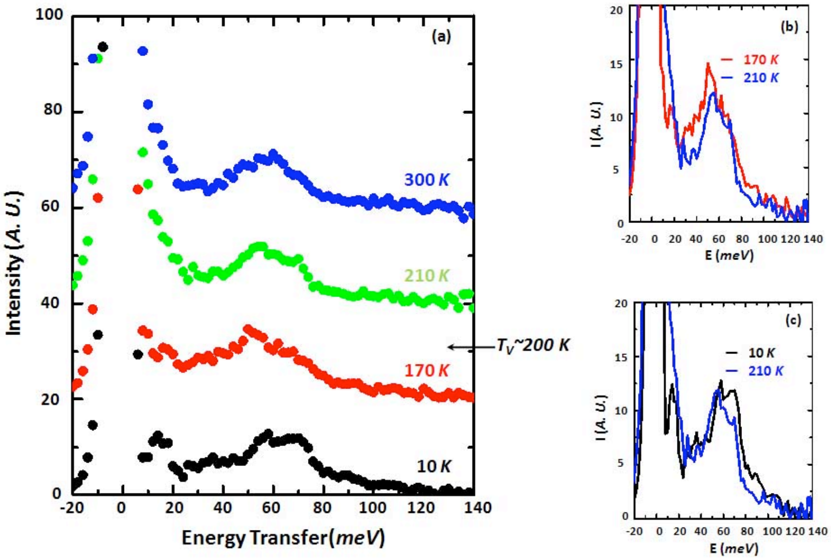

Figure 6.11 (a)Temperature dependence of the magnetic scattering of NSFO with $E_i = 160\ meV$ on Pharos, LANSCE; (b) The comparisons of magnetic scatterings of NSFO at T = 170 K and T = 210 K; (c) The comparisons of magnetic scatterings from NSFO at T = 10 K and T = 210 K.

There were two possible reasons: i) there is a strong CEF excitation of Nd^{3+} around 60 meV (E_{40}), which is making the gap region; ii) the low energy band observed in LSFO and PSFO moved to higher energies, then the high band appears as a tail in the total magnetic scattering as temperature is raising. The magnetic scattering tail, 80 meV - 140 meV, gradually shifts to lower energies and the magnetic spectrum is strongly damped just below the transition as the temperature raised, which was similar to PSFO and LSFO.

In order to test the first scenario, the magnetic scattering data at 210 K and 170 K are compared in Fig. 6.11(b), just above and below T_V = 200 K. It is hard to observe intensity difference in the range from 60 meV - 80 meV at the two temperatures, which means that there should be a gap. Perhaps the 40 K temperature difference will excite more electrons to higher energy CEF levels, the intensity of 60 meV at 210 K should be stronger than 170 K. In addition, the signal of Fe magnetic scattering is weaker at the temperatures just below T_V. Hence, the magnetic scattering between 10 K and 210 K are compared, there is a big intensity difference at 60 meV-80 meV and no gap exists, Fig. 6.11(c). Furthermore, significant CEF exists between 20 meV - 80 meV from 300 K data. Therefore, CEF correction seems much more important in NSFO than PSFO. We need to carefully account for the CEFs from Nd^{3+} before studying the magnetic excitations of Fe ions.

6.3.3.1) *Crystal Field Excitation*

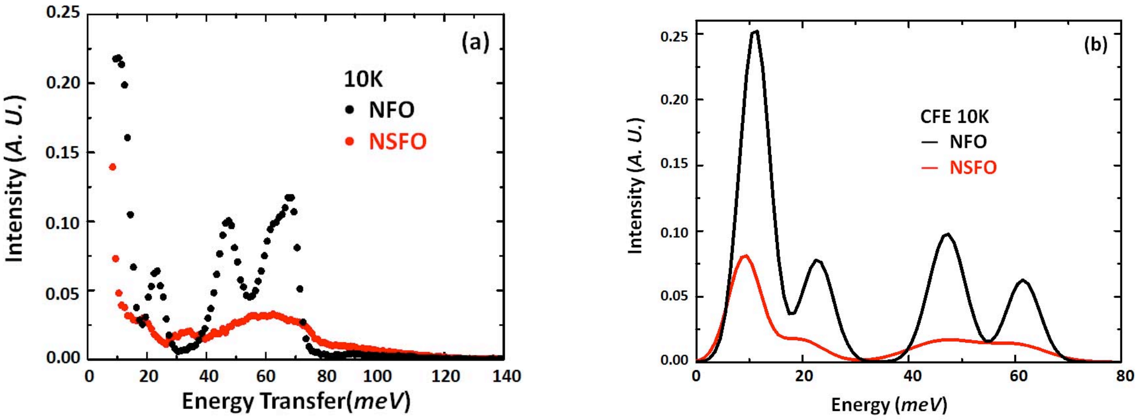

Figure 6.12 (a) The magnetic scattering intensity of NFO (black dots)and NSFO (red dots) on ARCS at $T = 10\ K$; (b) the CFEs of NFO (black line)and NSFO (red line) at $T = 10\ K$.

Similar as PSFO, we still keep the assumption that the environment of Nd^{3+}-site does not change much in NSFO, and the CEF excitation of Nd^{3+} in NSFO would be similar to the NFO. Again, only 1/3 of Nd^{3+} ions were left after substitution by nonmagnetic Sr^{2+} ions, the integrated intensity amounts of Nd^{3+} in NSFO should be around 1/3 of Nd^{3+} in NFO.

Table 6.6 The integrated intensities of Fe^{3+} magnetic states and the CEFs states of Energy - cuts and Q - cuts in NSFO.

Energy Range (meV)	State number (S_{tth}) spin - wave	State number (S_{tth}) C.F.	State number (S_{ω}) spin - wave	State number (S_{ω}) C.F.
10.5 : 20.5	0.116 ± 0.005	0.487 ± 0.029	0.115 ± 0.005	0.455 ± 0.025
20.5 : 30.5	0.161 ± 0.008	0.114 ± 0.006	0.158 ± 0.011	0.112± 0.009
30.5 : 40.5	0.178 ± 0.009	0.058 ± 0.004	0.181 ± 0.015	0.058 ± 0.003
40.5 : 50.5	0.240 ± 0.011	0.306 ± 0.015	0.233 ± 0.014	0.309 ± 0.018
50.5 : 60.5	0.376 ± 0.015	0.291 ± 0.0012	0.382 ± 0.016	0.284 ± 0.014
60.5 : 70.5	0.525 ± 0.021	0.116 ± 0.006	0.529 ± 0.022	0.118 ± 0.007
70.5 : 80.5	0.339 ± 0.014	0.005 ± 2E-4	0.346 ± 0.015	0.005 ± 3E-4
80.5 : 90.5	0.160 ± 0.008	6.87E-5 ± 3E-6	0.164 ± 0.006	– –
90.5 : 100.5	0.149 ± 0.006	– –	0.144 ± 0.005	– –
100.5 : 110.5	0.094 ± 0.003	– –	0.098 ± 0.005	– –
110.5 : 120.5	0.056 ± 0.001	– –	0.053 ± 0.004	– –
120.5 : 130.5	0.020 ± 0.001	– –	0.020 ± 0.005	– –
130.5 : 140.5	0.001 ± 4E-5	– –	– –	– –

The magnetic scattering intensities of NFO and NSFO are compared in Fig. 6.12(a). (Except experimental data of Fig. 6.11, all data in this section were measured by ARCS, SNS.) The CEF excitations of NSFO in energy-space were fitted by a series of gaussian functions based on the same method used to fit NFO. In order to confirm the magnetic excitation contribution from CEFs of Nd^{3+} ions and magnetic excitations of Fe^{3+} ions, E- and Q-cuts were plotted. The total integrated intensities from the same E- and Q-range in both cuts were compared, Table 6.6 [10]. Hence, the parameters of CEF excitation gaussian functions can be fitted.

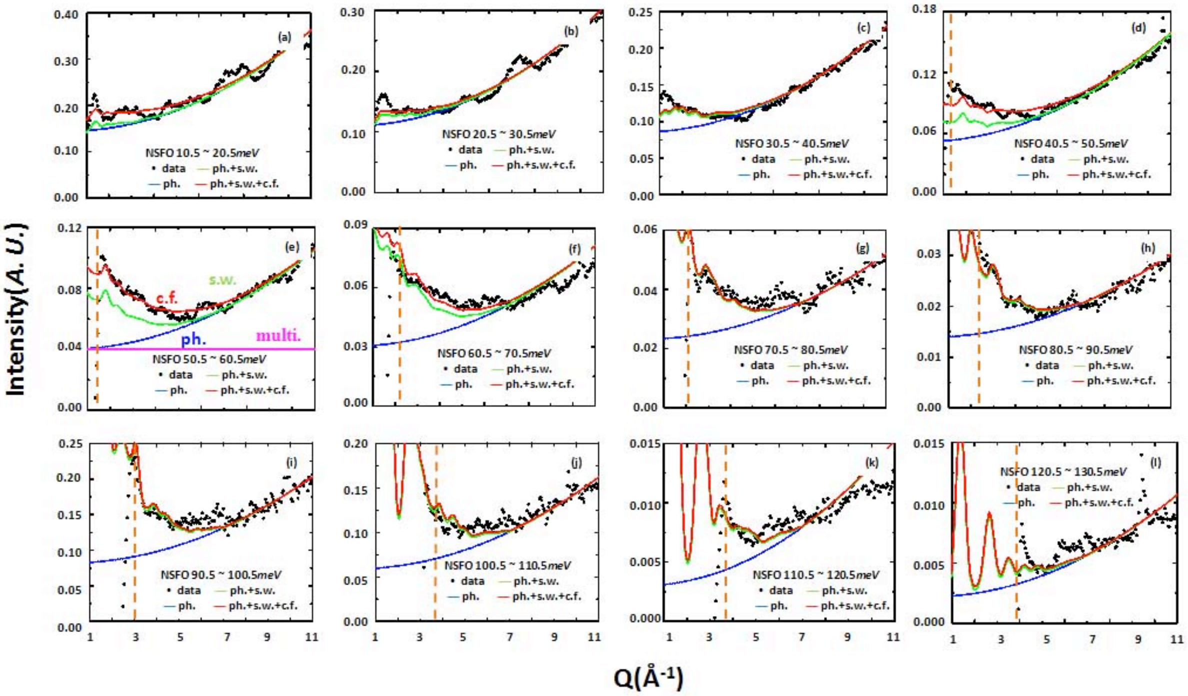

Figure 6.13 The Q-dependencies of different energy transfer ranges for NSFO at 10 *K* with 10 *meV* step: (a) 10.5 ∼ 20.5 *meV*, (b) 20.5 ∼ 30.5 *meV*, (c) 30.5 ∼ 40.5 *meV*, (d) 40.5 ∼ 50.5 *meV*, (e) 50.5 ∼ 60.5 *meV*, (f) 60.5 ∼ 70.5 *meV*, (g) 70.5 ∼ 80.5 *meV*, (h) 80.5 ∼ 90.5 *meV*, (i) 90.5 ∼ 100.5 *meV*, (j) 100.5 ∼ 110.5 *meV*, (k) 110.5 ∼ 120.5 *meV*, and (l) 120.5 ∼ 130.5 *meV*. The black dots are the experimental data. The blue line it an estimate of the incoherent phonon background plus multiple scattering. The red column is the calculation of the polycrystalline averaged spin wave scattering plus background using the parameters in the text. The brown dash line in some different energy transfer ranges ((d)-(l)) is the starting point of the experimental recording.

The fitted CEF excitations of Nd^{3+} in NSFO were compared to NFO, Table 6.7 [13, 14]. The positions of the excitations had shifted a little, $\sim$ 2 *meV*, which could be counted in error bar. The integrated intensity ratio of Nd^{3+} in NSFO was very close to 3 times in NFO, so the CEF assumption of NFO and NSFO are similar as assumed.

Table 6.7 The integrated intensities of Nd^{3+} CFE states in NFO and NSFO.

E_{i0}	NFO		NSFO			NFO/NSFO
	E (*meV*)	area	E (*meV*)	area	ratio	
E_{10}	9.05 ± 0.07	1.82 ± 0.05	9.58 ± 0.43	0.61 ± 0.06	1.00 ± 0.12	3.01 ± 0.31
E_{20}	20.8 ± 0.11	0.60 ± 0.04	19.2 ± 0.2	0.20 ± 0.03	0.33 ± 0.04	3.02 ± 0.42
E_{30}	45.2 ± 0.10	0.85 ± 0.09	46.9 ± 0.39	0.28 ± 0.03	0.46 ± 0.05	3.02 ± 0.45
E_{40}	59.5 ± 0.21	0.50 ± 0.09	60.9 ± 0.38	0.16 ± 0.03	0.27 ± 0.06	3.06 ± 0.78

6.3.3.2) *Heisenberg Model Calculation*

After according for CEF excitations, we now treat the Fe spin waves. From above discussion, LSFO and PSFO show two magnetic energy bands with an energy gap of 60 *meV* $\sim$ 75 *meV*. For the magnetic excitation of all three samples agreed with each other almost exactly above 85 *meV*. However, no energy gap was observed in NSFO and it is possible that the low energy band moves to higher energy and connects the unchanged high energy band. Since the high magnetic energy cutoff is determined by the ferromagnetic exchange energy, we begin by assuming that the J_F was same in those compounds. With J_F as a constant, J_{AF} is main factor for determining the position of low energy band.

The total fitting results of NSFO including CEF of Nd^{3+} and magnetic excitations of Fe ions were compared to the experimental data with $J_{AF} \sim$ -5.5 *meV*, Fig. 6.14. The fitting was not very good in the region 15 *meV* to 35 *meV* which is the energy range where residual phonon signals are observed similar to LSFO and PSFO.

The ratio of J_F and $\mid J_{AF} \mid$ in *R*SFO (*R* = La, Pr, and Nd) are concluded in Table 6.8 and plotted in Fig. 6.15: Compared to LSFO and PSFO, the $|J_F/J_{AF}| < 1$ in NSFO. This contradicts the theoretical calculation of T. Mizokawa, *et al.*. However, T. Mizokawa, *et al.* got the result, $\mid J_F/J_{AF} \mid > 1$, based on the assumption that J_{55} equals J_{AF}. However, $|J_{55}|$ should be quite small, since it originates from t_{2g} π-bonds. Assuming $|J_{55}| = 0$, the phase line is given by $|J_F/J_{AF}| >$ 1/2.

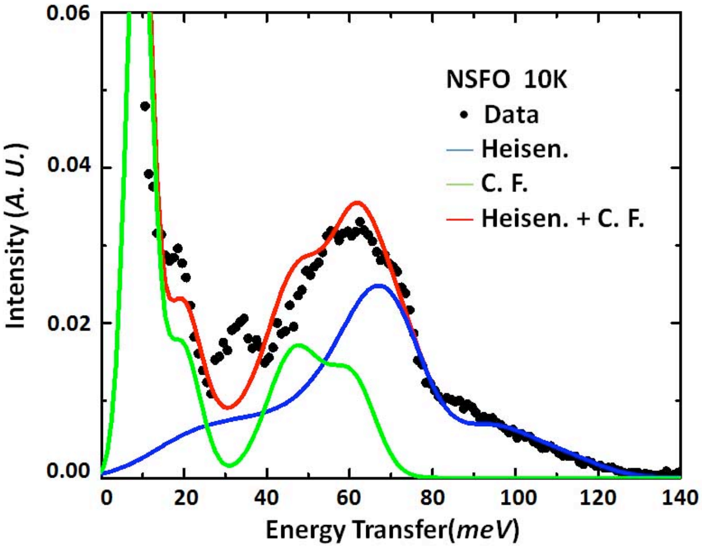

Figure 6.14 Comparison of NSFO magnetic scattering data at $T \sim 10\ K$ (dots) and the total simulating (red line) with the Heisenberg model calculation (blue line) and the CEF excitations (green line) summed from 2θ 3-30°.

Table 6.8 The spin momenta and exchange energies in *R*SFO.

	$La_{1/3}Sr_{2/3}FeO_3$	$Pr_{1/3}Sr_{2/3}FeO_3$	$Nd_{1/3}Sr_{2/3}FeO_3$
spin momenta			
S^{3+} (meV)	2.5	2.5	2.5
S^{5+} (meV)	2.0 ± 0.1	2.0 ± 0.1	2.0 ± 0.1
exchange energy			
J_{AF} (meV)	-3.5 ± 0.2	-3.5 ± 0.2	-5.5 ± 0.3
J_F (meV)	5.1 ± 0.1	5.1 ± 0.1	5.1 ± 0.1

Unlike LSFO and PSFO, $|J_{AF}|$ increased by 20% compared to the parent compound. Based on Table 6.9, we surmise that the increasing $|J_{AF}|$ in NSFO is due to increase in the CT gap and not the lattice distortion. The CT gap of NSFO is larger than LSFO and PSFO, hence electron will be more localized and the magnitude of AF exchange energy of NSFO is the largest in these three compounds. The lattice becomes more distorted going from LFO to NFO, which makes the larger $|J_{AF}|$ for LFO than NFO.

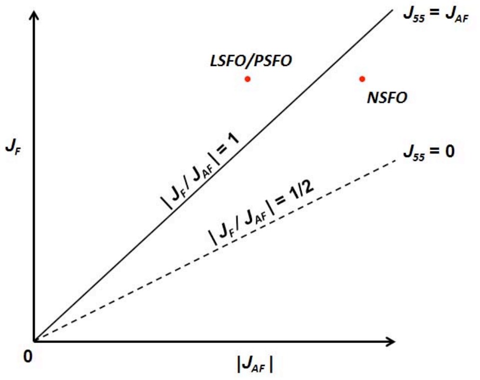

Figure 6.15 The $|J_F/J_{AF}|$ ratio in *R*SFO (*R* = La, Pr, and Nd) at 10 *K*.

6.4 Summary

We have investigated the magnetic property relevant to the CO transition for polycrystals of *R*SFO, where *R* = La, Pr, and Nd. There were several observed remarkable *R*-dependent features: (i) the CEFs of magnetic rare-earth ion in *R*SFO could be fitted using the parent *R*FO as a reference; (ii) With change of *R* from La to Nd, T_V shifts to lower temperature from LSFO to PSFO; (iii) the magnetic energy spectra of LSFO and PSFO were similar, which had two energy bands with a large gap, while the two bands merge in NSFO; (iv) the maximum magnetic energy spectra of *R*SFO are all the same; (v) the AF exchange energies between Fe^{3+} and Fe^{3+} ions, $|\ J_{AF}\ |$, and the ferromagnetic exchange energies between Fe^{3+} and Fe^{5+} ions, J_F, were estimated by linear Heisenberg Model: $|J_{AF}|$ has no effect on the lattice distortion and is most consistent with charge transfer gap and J_F was nearly constant; (vi)compared to *R*FO, the values of $|J_{AF}|$ were changing from 30$\%$ reduction (La) to 20$\%$ enhancement (Nd).

All these results indicate that the CO stability of *R*SFO decreases with the decrease of the *R*-site ionic radius or the decrease of the *p*-*d* hybridization effect. Therefore, the CO of LSFO and PSFO is mainly driven by the magnetic energy, even $|J_{55}|$ reach the maximum limit $|J_{AF}|$; the CO of NSFO can also be stabilized by the magnetic energy with a relative small limit for $|J_{55}|$, maybe the Coulomb energy effect on CO is unnegligible.

Table 6.9 The structural properties and exchange energies in *R*FO and *R*SFO.

	$\mathrm{LaFeO_3}$	$\mathrm{PrFeO_3}$	$\mathrm{NdFeO_3}$
space group	*Pnma*	*Pnma*	*Pnma*
bond length(Å)			
Fe - O(1)	2.002	2.004	2.005
Fe - O(2)	2.004	2.006	2.007
Fe - O(2)	2.005	2.015	2.017
bond angle			
∠ Fe - O(1) - Fe	157.6°	153.3°	151.2°
∠ Fe - O(2) - Fe	157.5°	152.4°	151.4°
exchange energy			
J_{AF} (*meV*)	- 4.90	- 4.55	- 4.45
	$\mathrm{La_{1/3}Sr_{2/3}FeO_3}$	$\mathrm{Pr_{1/3}Sr_{2/3}FeO_3}$	$\mathrm{Nd_{1/3}Sr_{2/3}FeO_3}$
space group	$R\bar{3}c$	$R\bar{3}c$	$R\bar{3}c$
bond length(Å)			
Fe - O	1.940	1.941	1.939
R - O	2.7413	2.7377	2.7329
bond angle			
∠ Fe - O - Fe	173.2°	170.5°	169.3°
charge transfer gap			
Δ(*meV*)	62	58	85
exchange energy			
J_{AF} (*meV*)	- 3.5	- 3.5	- 5.5
J_F (*meV*)	5.1	5.1	5.1

Bibliography

[1] T. Mizokawa and A. Fujimori, Physics Review Letter 80 (1998) 1320

[2] R. J. McQueeney, J. Ma, S. Chang, J.-Q. Yan, M. Hehlen, and F. Trouw, Physical Review Letter 98 (2007) 126402

[3] S. K. Park, T. Ishikawa, Y. Tokura, J. Q. Li, and Y. Matsui, Physical Review B 60 (1999) 10788

[4] D. Treves Journal of Applied Physics 36 (1965) No. 3 1033

[5] M. Loewnhaupt Physica B 163 (1990) 479-482

[6] P. D. Battle, T. C. Gibb, and P. Lightfoot, Journal of Solid State Chemistry 84 (1990) 271

[7] S. M. Shapiro, J. D. Axe, and J. P. Remeika, Physical Review B 10 (1974) 2014

[8] C. Ulrich, G. Khaliullin, J. Sirker, M. Reehuis, M. Ohl, S. Miyasaka, Y. Tokura, and B. Keimer, Physical Review Letter 91 (2003) 257202; K. Hirota, N. Kaneko, A. Nishizawa and Y. Endoh, Journal of the Physical Society of Japan 65 (1996) 3736; V. V. Krishnamurthy, J. L. Robertson, R. S. Fishman, M. D. Lumsden, and J. F. Mitchell, Physical Review B 73 (2006) 060404

[9] H. Yoshizawa, H. Kawano, J. A. Fernandez-Baca, H. Kuwahara, Y. Tokura, Physical Review B 58 (1998) R571

[10] P. J. Brown, *Magnetic form factors*, chapter 4.4.5; A. J. C. Wilson, ed. *International tables for crystallography* vol. C, pp. 391-399

[11] A. Podlesnyak, S. Rosenkranz, F. Fauth, W. Marti, H. J. Scheel and A. Furrer Journal Physics: Condensed Matter 6 (1994) 4099-4106

[12] http://www.ncnr.nist.gov/xtal/software/gsas.html

[13] K. Feldmann, K. Hennig, L. Kaun, B. Lippold, M. M. Lukina, S. Matthies, W. Matz, and E. Warming, Physics Status Solidi B 72 (1975) 817

[14] A. Podlesnyak, S. Rosenkranz, F. Fauth, W. Marti, A. Furrer, A. Mirmelstein, and H. J. Scheel Journal Physics: Condensed Matter 5 (1993) 8973-8982

CHAPTER 7. Electron-Lattice Interaction on $R_{1/3}$Sr$_{2/3}$FeO$_3$

7.1 Introduction

In our previous work on $R_{1/3}\mathrm{Sr}_{2/3}\mathrm{FeO}_3$ (*R*SFO), we have studied the contributions of the magnetic energy and Coulomb interaction to the CO in *R*SFO: the magnetic energy alone can stabilize the CO state of LSFO and PSFO; the effect of the Coulomb interaction is expected to show up gradually from LSFO to NSFO. Another possible factor to drive the CO which has discussed in the theoretical review chapter is the electron-lattice interaction which will be considered in this chapter. Based on the temperature-dependent phonon spectrum of *R*SFO, especially above and below T_V, we can make some general statements regarding the importance of electron-lattice interaction.

In order to understand the phonon spectrum, the simple Harmonic oscillator and anharmonicity will be reviewed at first in this section [1]; then, the experimental data will be shown and the damping will be fitted by the convolution method; at last, the shell model is applied to interpret the density-of-states (DOS) of *R*SFO [2, 3].

7.2 Harmonic Oscillators and Anharmonicity

7.2.1 Classical Harmonic Oscillator

As a model for the vibrational motion in crystals, the harmonic oscillator is applied to describe phonon dispersions, Fig. 7.1. The natural frequency of a classical one-dimensional harmonic oscillator of mass *M* and force-constant *k* is

$$\omega = \sqrt{\frac{k}{M}}, \tag{7.1}$$

Its potential energy is

$$E_p(x) = \frac{1}{2}kx^2 = \frac{1}{2}M\omega^2 x^2\,, \tag{7.2}$$

Since the kinetic energy equals the average potential in equilibrium,

$$\bar{E}_{p(x)} = \bar{E}_{k(x)} = \frac{1}{2}k_B T\,, \tag{7.3}$$

such that the mean-squared displacement $\bar{x^2}$ only depends on the temperature *T* and the force constant *k*,

$$\bar{x^2} = \frac{k_B T}{M\omega^2} = \frac{k_B T}{k}\,, \tag{7.4}$$

7.2.2 Harmonic Phonons

Since each phonon mode with some (**q**j) behaves as a simple harmonic oscillator, we can apply these ideas to the behaviour of harmonic lattice vibrations. Assuming the natural frequency of a quantum harmonic oscillator is ω, the thermal occupation factor of phonons, which are bosons, at temperature *T* is,

$$n(\hbar\omega, T) = \frac{1}{exp(\hbar\omega/k_B T) - 1}\,, \tag{7.5}$$

where k_B is the Boltzmann constant.

In thermal equilibrium, if a harmonic phonon with frequency $\omega = \omega_{qj}$, the energy is

$$E(qj) = (n(qj) + 1/2)\hbar\omega_{qj}\,, \tag{7.6}$$

with $n(qj) = n(\hbar\omega(qj))$. The total energy of a harmonic crystal is,

$$E_{harm}(T) = \sum_{qj} E(qj) = 3N\int_0^{\omega_{max}} \hbar\omega(n(\hbar\omega, T) + 1/2)g(\omega)d\omega\,, \tag{7.7}$$

where $g(\omega)$ is the DOS.

Based on the above discussions, the frequency does not depend on the vibration amplitude of the oscillator and the DOS has the same property, but the total energy of the oscillator is temperature depen-

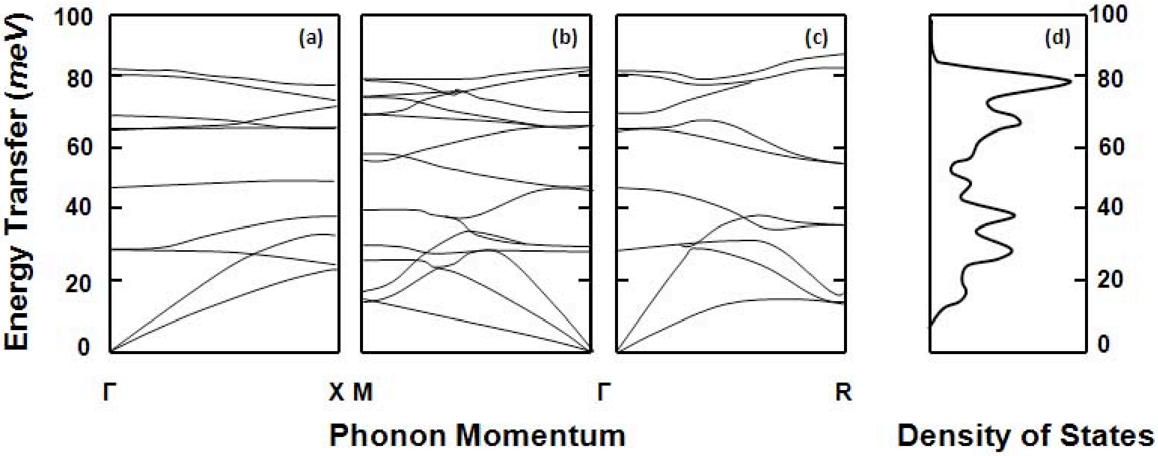

Figure 7.1 The phonon dispersion of LFO from (0 0 0) to (1 0 0) (a), from (1 1 0) to (0 0 0) (b), and from (0 0 0) to (1 1 1) (c); (d) The density-of state of LFO at T = 10 *meV*.

dent.

7.2.3 Anharmonicity

In the theory of harmonic oscillator presented above, the phonon frequency does not depend on the temperature and the amplitudes of the vibrations. However, it is just an ideal condition and the harmonic approximation is based on the proposition that the nuclei displacements from the equilibrium positions are small and the higher orders of the potential expansion are negligible. Although these conditions have been verified in many solids at low temperature, they tend to become invalid as the amplitude of the displacements increases at high temperatures. Then, the harmonic approximation leads to the thermal expansion and the finite thermal conductivity in the absence of phonon-phonon scattering [2, 3].

In anharmonic model, the phonon frequencies depend on the vibration amplitudes, and by Eq. (7.4), the temperature. Technically, the anharmonicity arises when the potential $V(r) \neq r^2$ for large r. The total energy of the system will be much more complicated than the harmonic case. Because the anharmonicity is often a small effect, usually the system is approximated to a harmonic oscillator and the anharmonicity is added as a perturbation term. Then, the ‘renormalized’ phonon frequencies will have some shifts

$$\tilde{\omega}(qj) = \omega(qj) + \Delta(qj) - i\Gamma(qj)\,, \tag{7.8}$$

where $\omega(qj)$ is the harmonic frequency of mode (qj), the term - $i\Gamma(qj)$ expresses the phonon damping, and $\Delta(qj)$ is the correction of the phonon frequencies, including the anharmonic potentials.

Usually, the phonon width Γ is small and the energy shift Δ is the main perturbation term. In fact, the measured frequencies in a neutron scattering experiment are those shifted frequencies. In the case of weak anharmonicity ($\Gamma/\omega \ll 1$), we will still label the state as a phonon state (qj) due to the long lifetime.

The anharmonic model is based on the detailed information related to the interatomic potentials which are obtained from a Taylor expansion of the potential. However, this lattice information of the sample is not easy to obtain from experimental data, and the phenomenological models, such as shell model, are harmonic approximations based on the data fitting. Thus, fitting the phonon data to fully anharmonic theoretical models is very difficult.

As the simplest case to the peakwidth, the thermal broadening due to anharmonicity has been studied a lot: when the temperature increases, the atomic motions become more vigorous and will have a large mean-squared displacement that leads to increased sampling of the anharmonic portion of the potential.

7.3 Phonon Spectra of *R*FeO$_3$

When the measured data are reduced to the magnetic contribution in previous chapters, we used high angle data as a measure of phonons. The high angle data is related to phonon density-of-states (DOS). Similar to the analysis of the magnetic energy of *R*SFO, we are going to take the phonon spectrum of *R*FO as a good reference and study them first. Since parent compounds *R*FO are insulators, only the anharmonic phonon-phonon interactions cause temperature dependent effects. The doped compounds *R*SFO are semiconductors and the phonon shift or broadening can arise from both phonon-phonon and electron-lattice interactions. Therefore, understanding the lattice dynamics of the parent compound helps to isolate the effect of electron-lattice interaction of *R*SFO.

7.3.1 Temperature dependence of LFO

Since the crystal structures in this series of samples are stable and there is no structure transitions, the phonon spectra of LFO will be discussed as an example of a system where weak anharmonic interactions are present. The raw high angle and the related phonon DOS data (dots) are shown in Fig. 7.2 for LFO. The elastic peak signal is shadowed by brown region and will not be included in the discussion. The high angle data are nearly temperature independent except for broadened signals at high temperature. Because there is no phase transition in LFO, the broadening is the result of the lattice anharmonicity [4].

We analyze the anharmonic broadening by simulating the high temperature phonon data by using the base temperature signal where anharmonic is expected to be small.

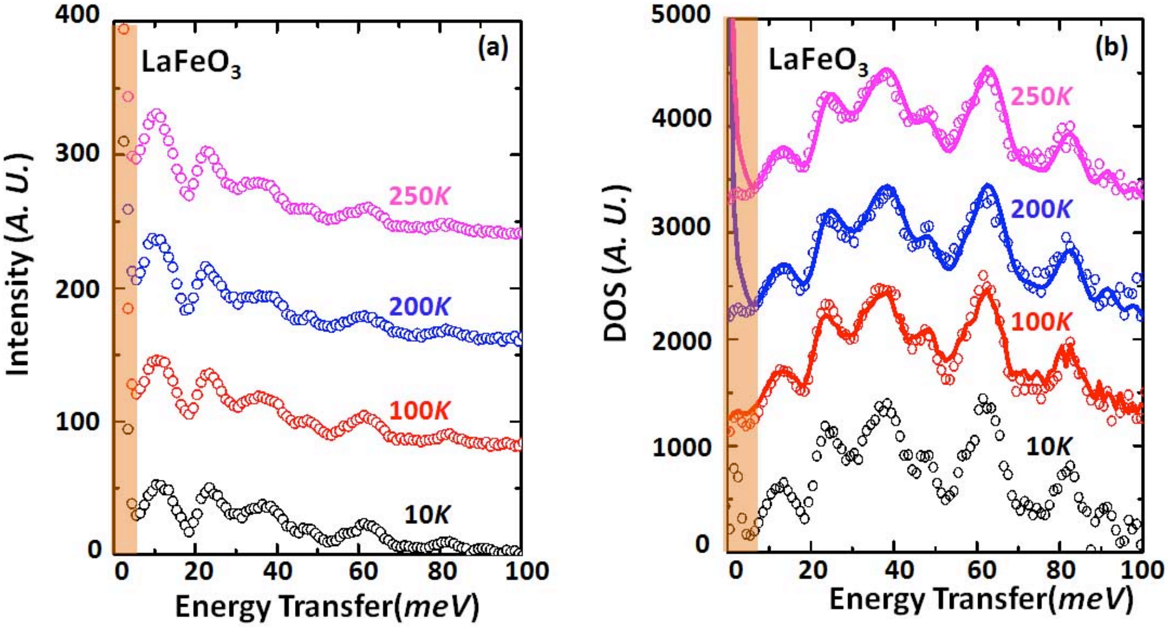

Figure 7.2 (a) High - angle(70° - 90°) scattering data of LFO on Pharos at 10 K (black), 100 K (red), 200 K (blue), and 250 K (pink); (b) Phonon scattering data (circle) and convolution fitting (line) for LFO at relative temperatures. The shadowed by brown region is the part of the elastic peak signal.

In the case of LFO phonon DOS, anharmonic broadening is introduced by a convolution of the base temperature data set (f) with a continuous probability distribution (g). Usually, the bell-shaped Gaussian and Lorentzian distribution are used. Compared to Lorentzian function, the Gaussian distribution has much narrower tail and shaper intensity, so we used Gaussian distribution in this section,

$$g(x) = Aexp(-\frac{(x-\mu)^2}{2\sigma^2}) \ , \tag{7.9}$$

where A is the amplitude, μ is the center of the function, and σ is the half width of the peak.

Therefore, the convolution is typically viewed as a modified version of the original functions and the sign is expressed as '$*$',

$$(f * g)[\omega] = \sum_{\omega'=-\infty}^{\infty} f[\omega']g[\omega - \omega'] = \sum_{\omega'=-\infty}^{\infty} f[\omega - \omega']g[\omega'] \;, \tag{7.10}$$

where both f and g are the functions of ω (ω'); the coefficients of the product are given by the convolution of the original coefficient sequences and extended with zeros where are necessary to avoid undefined terms.

The fitting results(lines) are shown in Fig. 7.2(b). The convolution fitting data agree with the measurement very well and the full width at half maximum(FWHM) of the broadening function is increasing with temperature as we expected, Fig. 7.3. Hence, the convolution gives us a quantitative estimate of the anharmonic contribution.

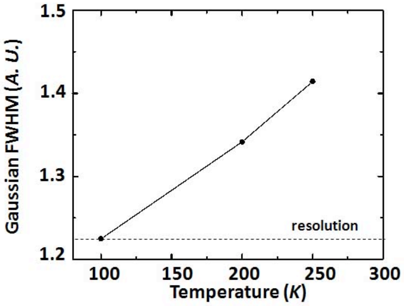

Figure 7.3 The full width at half maximum (FWHM) at 100 *K*, 200 *K*, and 250 *K*.

7.3.2 The Phonon DOS of RFO (R = La, Pr, Nd, and Sm) at 10 K

In this section, the effect of *R*-ion substitution on the phonons of these iron oxides will be discussed. In Fig. 7.4(a), the brown shadow region shows the signals of the elastic peaks and will not be presented in the DOS figure, Fig. 7.4(b). From Fig. 7.4, we can learn that the DOS of LFO, PFO, and NFO are pretty close at the high energy region (higher than 50 *meV*), which is the energy region consisting primarily of oxygen vibrations. Although the data share similar features at the low energies (less than 50 *meV*), the intensities are different. This is partially due to the different cross-section of *R*, *La* $\sim$ 9.7 barn, *Pr* $\sim$ 2.7 barn, *Nd* $\sim$ 16.6 barn, and *Sm* $\sim$ 39 barn. As the transfer energy is less than 20 *meV*, the experimental data agree with the cross-section prediction: the intensity of PFO is the smallest and the intensity of SFO is the largest.

The phonon DOS signal of SFO is detrimentally affected by the strong neutron absorption of Sm:

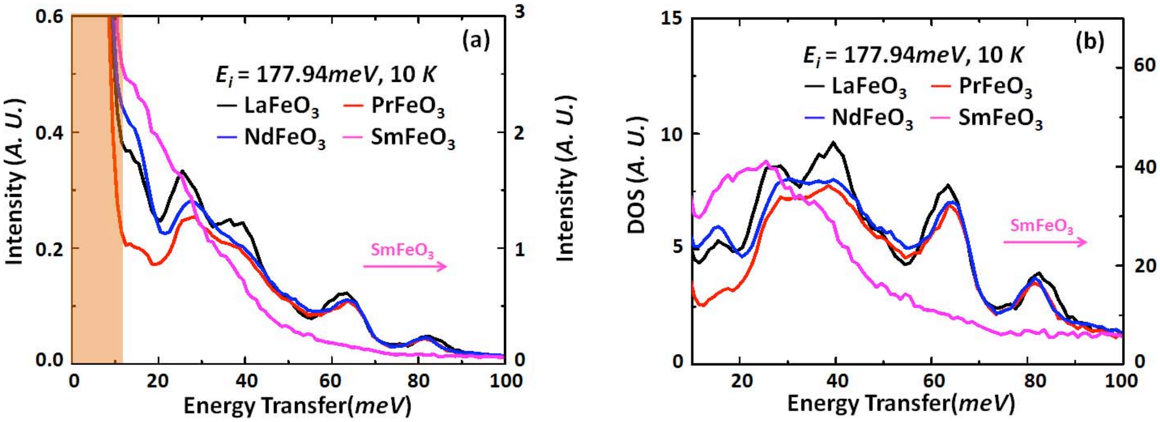

Figure 7.4 High-angle scattering (a) and phonon DOS (b) data of *R*FO (*R* = La, Pr, Nd, and Sm) on ARCS at 10 *K*.

although the 40 *meV* peak is still detectable, the 60 *meV* and 80 *meV* peaks are just very weak bumps.

7.4 Lattice Dynamical Model

To better understand the phonon DOS and contribution of different atomic vibrations to different energy ranges, we develop a lattice dynamical model. The frequency of harmonic oscillator model, ω, is determined by the mass of the atoms and the force-constants between them in the crystal, but it is just an ideal example and much simpler compared to a real dynamical lattice. In order to understand the more accurate lattice interaction between the atoms, the dispersion/DOS is fitted. There are a lot of models describing these vibrating modes, the choice of the model depends on the type of binding between the atoms. Because *R*FO is an ionic crystal, we shall consider only two phenomenological models: the rigid ion and shell models.

7.4.1 Rigid Ion Model

For the rigid ion model, the ionic system consists of charged atoms. The Coulomb potential energy between two atoms (*lk*) and (*l′ k′*) with charge $Z_k e$ and $Z_{k'} e$ at the site *r*(*lk*) and *r*(*l′ k′*) respectively can be expressed as

$$\Phi_C(lk, l'k') = \frac{Z_k Z_{k'} e^2}{\mid r(lk) - r(l'k') \mid}, \tag{7.11}$$

In order to stabilize the lattice, a short-range repulsive force is included by the exponential Born-Mayer potential,

$$\Phi_R(lk, l'k') = b(lk, l'k')exp(\frac{-\mid r(lk) - r(l'k') \mid}{\rho(l'k')}), \tag{7.12}$$

where $b(lk,l'\ k')$ and $\rho(l'\ k')$ describe components of the repulsive interaction.

Thus, the total potential will be

$$\Phi(lk, l'k') = \Phi_C(lk, l'k') + \Phi_R(lk, l'k'), \tag{7.13}$$

The force between atoms is expressed by the force constant matrix

$$\Phi_{\alpha\beta}(lk, l'k') = \frac{\partial^2\Phi(lk, l'k')}{\partial r_\alpha \partial r_\beta} \mid_{r=|r(lk)-r(l'k')|}, \tag{7.14}$$

where r_α and r_β mean the directions of α and β.

Then, the classical motion equation are

$$m_k\ddot{u}_\alpha(lk) = -\sum_{l'k'\beta} \Phi_{\alpha\beta}(lk, l'k')u_\beta(l'k'), \tag{7.15}$$

where m_k is the mass of atom (*lk*), $u_\alpha(lk)$ and $u_\beta(l'\ k')$ are the displacements of (lk) on α direction and $(l'k')$ on β direction respectively.

Due to the motion correlation between (*lk*) and $(l'\ k')$ and Fourier transform of the force matrix, the dynamical matrix of the atoms (*lk*) and $(l'\ k')$ in reciprocal space **q**, $D_{\alpha\beta}(kk', \mathbf{q})$, will be defined as [4]

$$D_{\alpha\beta}(kk', \mathbf{q}) = \frac{1}{\sqrt{m_k m_{k'}}} \sum_{l'} \Phi_{\alpha\beta}(0k, l'k')e^{i\mathbf{q}\cdot(\mathbf{r}(l'k')-\mathbf{r}(0k))}, \tag{7.16}$$

where $m_{k'}$ is the mass of atom $(l'\ k')$.

Therefore, the dynamical matrix is the result of a summation over the above two potentials. However, the evaluation for this periodic system is very complicated. The Coulomb energy is conditionally convergent, i.e. it just converges under certain specific additional conditions for an infinite 3-D material. Because the interaction between ions decays as the inverse power of *r* and the number of interacting ions increases with $4\pi r^2$ as the surface area of a sphere, it is hard to decide which term will be dominant.

In order to solve the problem, Ewald method is usually applied. In 1921, Ewald assumed that the point charge at the atomic sites were replaced by extended charge distributions, such as spheres or gaussians [6]. Then, the direct lattice sum is split into a direct lattice sum and a reciprocal lattice sum. If the charge density parameter (i.e. radius or gaussian width) is selected properly, both terms will converge rapidly to a value which is independent of it. Hence, the Coulomb contribution to the dynamical matrix of atoms (*lk*) and (*l′ k′*) can be broken up into the direct and reciprocal terms,

$$C_{\alpha\beta}(kk', \mathbf{q}) = C^{(d)}_{\alpha\beta}(kk', \mathbf{q}) + C^{(r)}_{\alpha\beta}(kk', \mathbf{q})\,, \tag{7.17}$$

For the short-ranged potential(Born-Mayer potential), the contribution to the dynamical matrix is

$$R_{\alpha\beta}(kk', \mathbf{q}) = \sum_{l'} \Phi^{(R)}_{\alpha\beta}(0k, l'k') e^{i\mathbf{q}\cdot(\mathbf{r}(l'k') - \mathbf{r}(k))}\,, \tag{7.18}$$

where the force constant matrix, $\Phi^{(R)}_{\alpha\beta}(lk, l'k')$, is given for non-diagonal elements ($k \neq k'$) as

$$\begin{aligned} \Phi^{(R)}_{\alpha\beta}(lk, l'k') = & \frac{(r(lk) - r(l'k'))_\alpha (r(lk) - r(l'k'))_\beta}{\mid r(lk) - r(l'k') \mid^2} \\ & \times [G(lk, l'k') - F(lk, l'k')] - \delta_{\alpha\beta} G(lk, l'k') \end{aligned}\,, \tag{7.19}$$

and for diagonal ($l\ k = l'\ k'$) elements as

$$\Phi^{(R)}_{\alpha\beta}(lk, lk) = -\sum_{l'k'} \Phi^{(R)}_{\alpha\beta}(lk, l'k')\,, \tag{7.20}$$

For central forces, *F* and *G* are the radial and tangential parts, respectively.

$$\begin{aligned} F(lk, l'k') &= \frac{\partial^2 \Phi(lk, l'k')}{\partial r^2} \mid_{r = |r(l'k') - r(lk)|} \\ G(lk, l'k') &= \frac{1}{r} \frac{\partial \Phi(lk, l'k')}{\partial r} \mid_{r = |r(l'k') - r(lk)|} \end{aligned}\,, \tag{7.21}$$

Based on the above formulas, the matrix notation of the dynamical matrix in the rigid ion model is

$$\mathbf{D} = \mathbf{m}^{-1/2}(\mathbf{R} + \mathbf{ZCZ})\mathbf{m}^{-1/2}\,, \tag{7.22}$$

where $\mathbf{Z}$ is a diagonal matrix containing the ionic charges and $\mathbf{m}^{-1/2}$ is a diagonal matrix containing the square root of the atomic masses. Therefore, the rigid ion model requires only the charges of the ions and two short-range force constants for close atomic pairs as parameters.

7.4.2 Shell Model

The shell model is an extension of the rigid ion model: the electronic polarizability of the constituent ions are allowed. In the shell model, a massless shell with charge $\mathbf{Y}_k$ around the ionic core is introduced and can move independently due to the polarizability. Between the shell and core, there is a spring with force constant $\mathbf{K}_k$ which bounds them together. The parameters of the rigid ion model replaced by the shell-core springs, the deficiencies of the rigid ion model is solved: the frequencies of various longitudinal optical (LO) phonon mode and the optical-frequency dielectric constant are in better agreement with data.

Although the shell model is very similar to the rigid ion model, the final dynamics matrix still need to be revised due to the introducing of the shell charge. Since the shells can be considered as massless and the motion follows the cores adiabatically, the dynamical matrix of the shell model governs only the core motion

$$\mathbf{D} = \mathbf{m}^{-1/2}(\mathbf{R} + \mathbf{ZCZ} - (\mathbf{R} + \mathbf{ZCY})(\mathbf{S} + \mathbf{YCY})^{-1}(\mathbf{R} + \mathbf{YCZ}))\mathbf{m}^{-1/2}\,, \tag{7.23}$$

where $\mathbf{Y}$ is a diagonal matrix of shell charges and the matrix $\mathbf{S}$ augments the short-ranged matrix $\mathbf{R}$ according to the formula

$$\mathbf{S}_{\alpha\beta}(kk', q) = R_{\alpha\beta}(kk', q) + \delta_{\alpha\beta}\delta_{kk'}\mathbf{K}_k\,, \tag{7.24}$$

7.4.3 Ground State Phonon DOS of ABO$_3$

From the discussion in the above section, the shell model is introduced to analyze the ground state phonon DOS. The force constants can be determined by the interatomic potential which includes the long-range Coulomb and short-range ionic interactions. If there are two atoms k and k' with the effective charges, $Z(k)$ and $Z(k')$, and the relative radii, $R(k)$ and $R(k')$, the potential energy between the two atoms with r distance can be expressed as [6],

$$V(r) = (\frac{e^2}{4\pi\epsilon_0})[\frac{Z(k)Z(k')}{r}] + aexp[\frac{-br}{R(k)+R(k')}], \tag{7.25}$$

where *a* and *b* are constants, and equal 1822 *eV* and 12.364 respectively [7].

Then, the radial and tangential force constants for this central force are

$$\begin{aligned} F(k,k') &= \frac{\partial^2 V(r)}{\partial r^2} \mid_{r=|r(k')-r(k)|} \\ G(k,k') &= \frac{1}{r}\frac{\partial V(k,k')}{\partial r} \mid_{r=|r(k')-r(k)|} \end{aligned}, \tag{7.26}$$

The distance between two ions, *r*, can be calculated by the lattice structure. For the program code of Ames Laboratory, the effective charge and force constants, *Z*, *F* and *G*, are the parameters.

Example 1. The Phonon DOS of LaMnO$_3$ *at 10 K*

Before calculating the phonon DOS of LFO by shell model, the program code is tested on the LaMnO$_3$ (LMO), whose phonon DOS has been calculated previously [8].

The crystal structure of LMO has been studied using x-ray and neutron diffraction techniques, both at ambient temperature and pressure [7-14]. Below $\sim$ 800 *K*, LMO was found to have an orthorhombic structure with *Pnma* symmetry [14].

In 2007, E. G. Rini *et al.* applied the shell model, Eq. 7.12, to calculate the lattice dynamics by the computer program DISPR [15] with the following 7 optimized parameters: *Z*(Mn) = 1.62, *Z*(La) = 1.68, *Z*(O) = -1.1, *R*(Mn) = 1.0801 , *R*(La) = 1.7474 , *R*(O) = 1.7976 , oxygen shell charge is -2.24*e*, and the shell-core force constant is 142 eV/^{2} [6]. The calculation of phonon DOS is shown in Fig. 7.5 (black line).

Based on the parameters of the shell model in E. G. Rini *et al.*, the radial and tangential force constants can be calculated, Appendix E. If we apply them in the shell model program code of Ames Laboratory, the result is shown in Fig. 7.5 (red line) and agree with calculating of E. G. Rini.

Example 2. The Phonon DOS of LaFeO$_3$ *at 10 K*

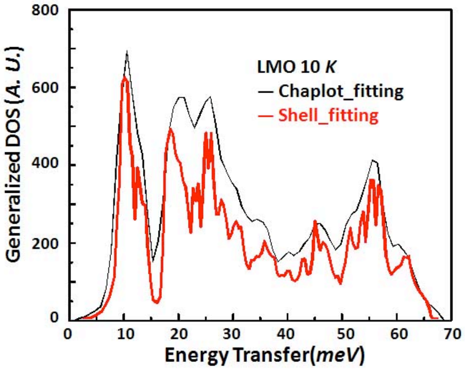

Figure 7.5 Comparison of LMO fittings in the shell model with the parameters of S. L. Chaplot (black line) and Ames Laboratory (red line) at 10 *K*.

LFO has an orthorhombic unit cell (space group *Pnma*) and four f.u./ unit cell. It has five atoms in the asymmetric unit, so there are 20 atoms. The structure has two oxygen ions O1 and O2 with different site symmetry. La and O1 occupy crystallographic sites 4*c*; the other oxygen atom, O2, is at the general position 8*d*; Fe is at 4*a* position. The model parameters are listed in Appendix F. 17 pairwise force constants are selected. The calculated partial DOS for the various atoms for LFO are plotted in Fig. 7.6(a),

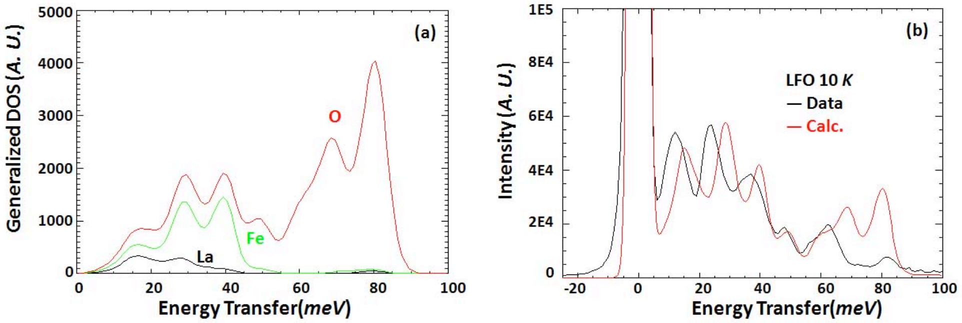

Figure 7.6 (a) The calculated partial DOS for the various atoms, La, Fe, and O, for LFO; (b) the comparison of the experimental data and the total calculation DOS of LFO at 10 *K*.

It is clearly shown that the partial phonon DOS of La is just on the energy range 0 - 45 *meV*, while the energy range of Fe is 0 - 55 *meV* and on O is 0 - 95 *meV*. Compared on the basis of neutron intensity, La has the weakest contribution. Hence, the high energy phonon DOSs (larger than ∼ 55 *meV*) are almost entirely the vibration modes of O atom, and the low energy phonon DOSs (less than ∼ 55 *meV*) has contributions from all atoms.

The total phonon DOS will be summed by the atom ratio in the chemical formula, Fig. 7.6(b), and the elastic peak is included. Compared to the experimental data, it was clearly found that the shapes of the calculation and measured data are roughly same. However, the energy excitations of calculated phonon DOS are a little bit higher than the data in the low energy region; although the energy excitations of calculated phonon DOS are same as the data in the high energy region, the intensities are much higher. Therefore, the precise analysis needed to be implemented by adjusting the fitting parameters, and the number and magnitude of force constants.

7.5 Phonon Spectra of $R_{1/3}Sr_{2/3}FeO_3$

Similar to the phonon spectra of *R*FO, the high angle data of *R*SFO can be reduced to phonon DOS related function. The temperature dependence phonon spectra of *R*SFO will be presented and effects of electron-lattice interaction will be deduced. Then the phonon spectra of *R*SFO at 10 *K* will be compared and compared to data of the parent compounds *R*FO.

7.5.1 Temperature dependence of LSFO

Fig. 7.7(a) shows the temperature dependence of the high-angle scattering data of LSFO. As we expected, the thermally broadened signal is also found. However, there are some features of the DOS that appear to depend on the Verwey transition temperature, T_V = 210 *K*. Fig. 7.7(b) shows two effects that appear above T_V: 1) the signal at $\sim$ 50 *meV* broadened; 2) the peak at $\sim$ 70 *meV* moved toward the low energies. In order to confirm whether these phenomena are due to anharmonicity or electron-lattice coupling, we need to analyze the DOS of the phonon spectra at several temperatures.

In above section, the temperature dependence of phonon spectra of LFO was understood as anharmonic broadening obtained by the convolution method. Although many details of lattice dynamics of LFO and LSFO have been changed due to Sr^{2+} doping, the parent compound is still a good reference. Since both LSFO and LFO have the same energy resolution due to the same incident energy, 120 *meV*, the same gaussian function can be applied to account for thermal broadening.

The convolution data of LSFO are shown in Fig. 7.7(b). Below the transition temperature, T_V, the fitting data agree with the measurement data very well; Above the transition temperature, the bump at $\sim$ 50 *meV* is much broadening and the peak at $\sim$ 70 *meV* is shifted. In order to observe the Verwey

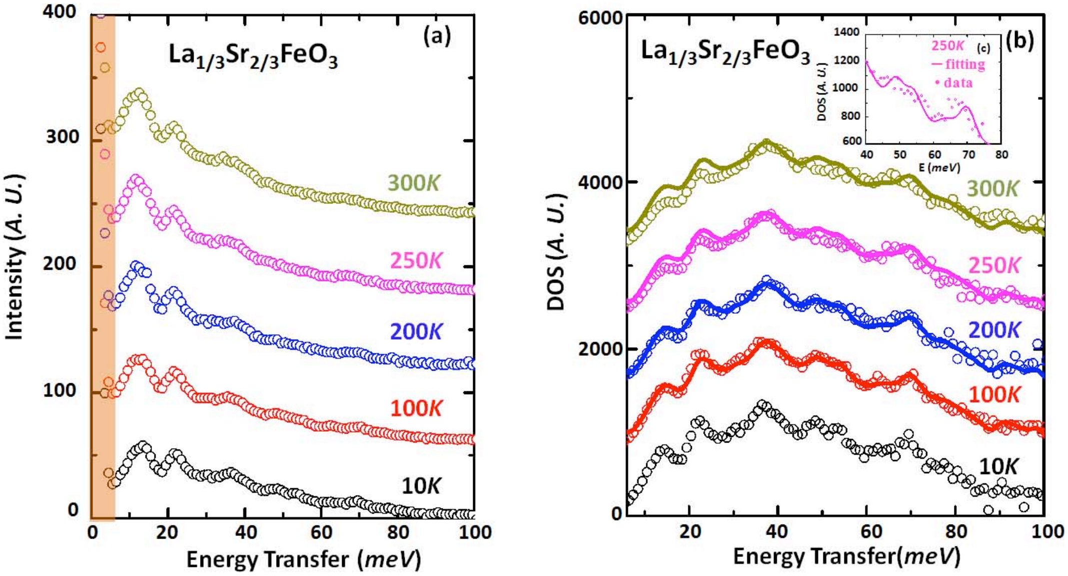

Figure 7.7 (a) High - angle(70° - 90°) scattering data of LSFO on Pharos with E_i = 120.0 *meV* at 10 *K* (black), 100 *K* (red), 200 *K* (blue), 250 *K* (magneta), and 300 *K* (dark yellow); (b) Phonon scattering data (circle) and convolution fitting (line) for LSFO at relative temperatures; (c) the comparison of convolution fitting and measurement data at 250 *K* from 40 *meV* to 80 *meV*.

transition effect on the phonon, the calculation and measurement data are compared at 250 *K*, which is just above the transition temperature, Fig. 7.7(c). Therefore, the shifts in vicinity of T_V is likely due to electron - lattice interaction caused by CO. Actually, this phenomenon is similar to the temperature-dependence Raman spectra of $La_{1-x}Ca_xMnO_3$ as discussed before, the related atomic motions are i) O2 antistretching to MnO_6 bending ($A_g(1)$ to $A_g(3)$) and in-phase O2 ‘scissorslike’ ($B_{2g}(2)$) for the phonon DOS differences of 50 *meV* and 65 *meV* excitations; ii) in-plane O2 stretching ($B_{2g}(1)$) for the phonon DOS at $\sim$ 75 *meV* excitations [16, 17].

Another thing I want to mention is that the low energy phonon spectra even do not agree with the fitting data, and the difference is bigger and bigger with the increasing of the temperature. However, the difference is just limited to the intensity, not the energy positions, and these energy regions are mainly related to the La and Fe ions (partial phonon DOS in section 7.4.2). The possible explanation are the anisotropy of Fe ions and the changing ionic environment of La^{3+}/Sr^{2+}.

7.5.2 Temperature dependence of RSFO (R = Pr and Nd)

A similar analysis of the phonon DOS were performed on other *R*SFO compounds. Fig. 7.8(a) and Fig. 7.9(a) show the high-angle scattering data of *R*SFO (*R* = Pr and Nd). Similar to LSFO, a general thermal broadening is found. Near the verwey transition temperature, we observe similar features: 1) the signal at $\sim$ 50 meV broadened; 2) the peak at $\sim$ 70 meV moved toward the low energies.

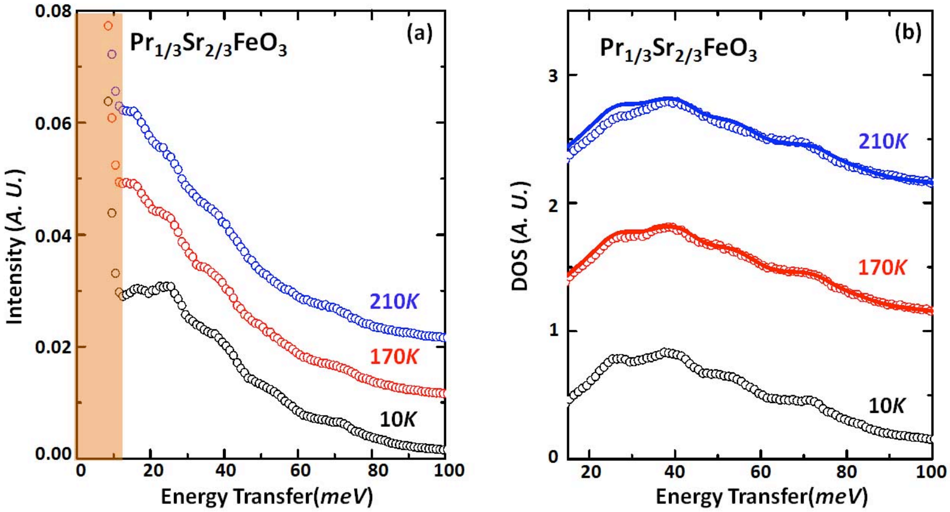

Figure 7.8 (a) High-angle(70° - 90°) scattering data of PSFO on ARCS with E_i = 177.94 meV at 10 K(black), 100 K(red), and 210 K(blue); (b) Phonon scattering data (circle) and convolution fitting(line) for PSFO at relative temperatures.

As the discussion in the former section, the DOS of phonons of *R*SFO (*R* = Pr and Nd) at different temperatures are fitted by the data at base temperature, the thermal broadening is introduced by convoluting with the gaussian functions, Fig. 7.8(b) and Fig. 7.9(b). The broadening at $\sim$ 50 meV and the shifting at $\sim$ 70 meV, and the differences between the phonon DOSs at 170 K(just below T_V) and 210 K (just above T_V) are more and more significant with the decreasing ionic size. Furthermore, the simulating intensities at the low energy phonon DOSs are worse and worse.

Fig. 7.10 shows the FWHM of the relative gaussian functions for *R*SFO (*R* = La, Pr, and Nd). Compared the FWHM of this series of compounds, we could clearly learned that the LSFO has the smallest value and PSFO has the largest. Thus, the energy resolution of LSFO is the best and PSFO is the worst due to the different initial energies of LSFO (120 meV), NSFO (160 meV), and PSFO (177.94meV). The broadening parameter of LSFO is also compared to LFO, they agree with each other

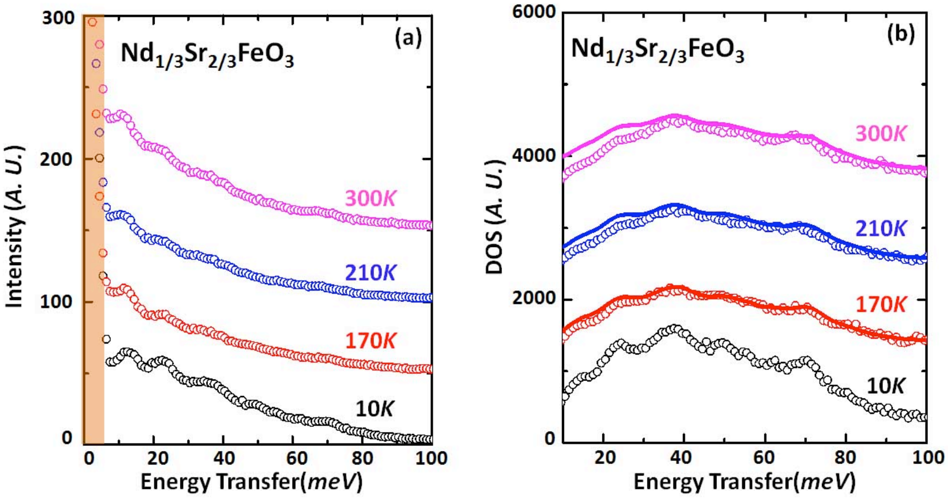

Figure 7.9 (a) High - angle(70° ∼ 90°) scattering data of NSFO on Pharos with E_i = 160.0 *meV* at 10 *K*(black), 100 *K*(red), 210 *K*(blue), and 300 *K*(magneta); (b) Phonon scattering data (circle) and convolution fitting(line) for NSFO at relative temperatures.

as we expected due to the same initial energies for LSFO and LFO.

7.5.3 The Phonon DOS of RSFO (R = La, Pr, Nd, and Sm) at 10 *K*

The high-angle scattering and phonon DOS data of *R*SFO (*R* = La, Pr, Nd, and Sm) at 10 *K* are plotted in Fig. 7.11. In LSFO, PSFO, and NSFO, the shapes and the intensities of the scattering data are pretty close to the energy region of oxygen vibrations at high energies (higher than 50 *meV*); the data are pretty similar at the low energy part (less than 50 *meV*), while the intensities are different as the ionic size of *R*-site decreases from La^{3+} to Nd^{3+}. One possible reason is the different ionic size of R^{3+} and the relative structures, another is the cross-section of the *R*, *La* ∼ 9.7 barn, *Pr* ∼ 2.7 barn, *Nd* ∼ 16.6 barn, *Sm* ∼ 39 barn. Hence, the contribution of R^{3+} to the intensity can not be ignored at low temperature, which is similar to what we have observed in *R*FO. For the Sr doped Sm sample, it has a little bit different: although the high-energy signals are still weak as SFO, the low-energy data are observable due to the smaller absorption, one-third of SFO. Although the high energy signals are still faint by using higher E_i = 290.95 *meV*, it looks like that they are better than the low incident energy data. The side effect for this bigger incident energy procedure is the worse energy-resolution, it is hard to discuss the low energy data. Therefore, we must combine the low and high incident energy data and analyze them quantitatively.

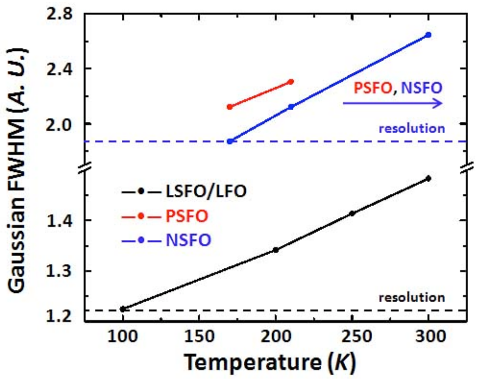

Figure 7.10 The comparison of the full width at half maximum(FWHM) of the convoluting gaussian functions for the anharmonic broadening of *R*SFO (*R* = La, Pr, and Nd) as a function of temperature.

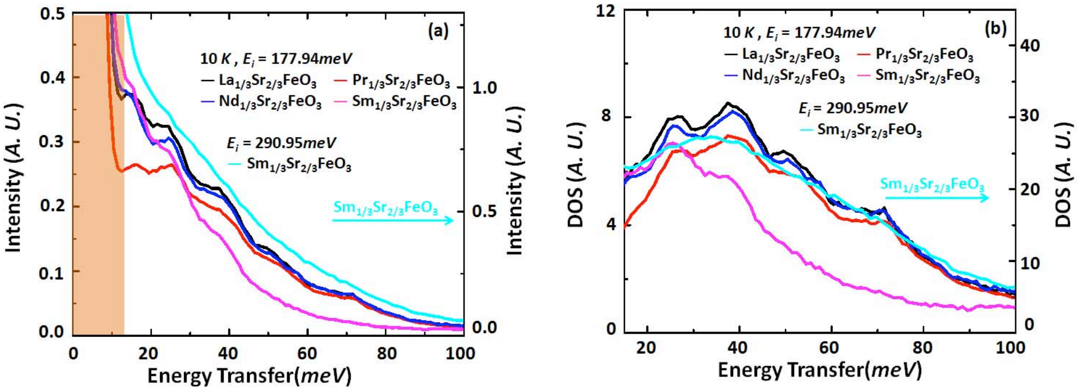

Figure 7.11 High-angle scattering (a) and phonon DOS (b) data of *R*SFO (*R* = La, Pr, Nd, and Sm) at 10 *K*.

The high energy phonon DOSs of LSFO, PSFO and NSFO agree with each other very well; the low energy phonon DOSs have the similar shapes. In SSFO, E_i = 177.94 meV, the interference of Sm absorption is more significant: the agreement of the $\sim$ 20 meV and 30 meV peaks are pretty good; the signal of the $\sim$ 40 meV peak is detectable; the $\sim$ 50 meV and 70 meV peaks are too faint to be nominated. As E_i = 290.95 meV, the signal intensities are good, but the bad resolution masks the identification of parts in phonon DOS. Compared to the NSFO measurement with the same incident enrgy, 290.95 meV, similar phonon DOS is observed. Hence, the SSFO just can be analyzed quantitatively, not as the qualitative discussion in LSFO, PSFO, and NSFO.

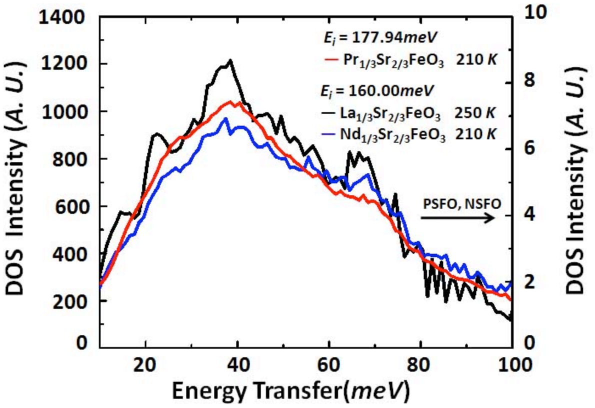

Figure 7.12 Phonon DOS data of LSFO(black) and NSFO(blue) on Pharos with E_i = 160.0 *meV* at 250 *K* and 210 *K* respectively, and PSFO(red) on ARCS with E_i = 177.94 *meV* at 210 *K*.

7.5.4 The Phonon DOS of SFO (R = La, Pr, and Nd) at 250/210 *K*

At 250/210 *K*, which are just above the transition temperatures, the Phonon DOS of *R*SFO (*R* = La, Pr, and Nd) are compared in Fig. 7.12. Because they have the similar lattice structure, $R\bar{3}c$, the DOS spectra of these three compounds are expected to agree with each other. At the transfer energy from 10 *meV* to 40 *meV*, the intensities are different because of the different cross-section of *R* and the lower intensity of NSFO compared to LSFO is perhaps due to the stronger partial DOS contributions from Fe and O, which are similar as the phonon DOS at 10 *K*. At the energy region from 40 *meV* to 70 *meV*, the different intensities are due to the lattice effect on O-site with *R*-site ion substitution.

7.6 The Comparison of the Ground State of Phonon of *R*FO and *R*SFO

The high-angle scattering and phonon DOS data of the parent and Sr doped compounds are compared in Fig. 7.13. (Since the high-angle scattering data has similar results of the phonon DOS data, we will just compare the DOS data following.) As *R* = La, Pr, and Nd, we could get the similar comparison results with the Sr doped: i) the $\sim$ 15 *meV* excitation is much broader and a little bit harden; ii) at $\sim$ 25 *meV* and 40 *meV*, the intensities drop a little bit and the excitation is slightly soften; iii) the $\sim$ 50 *meV* excitation is more significant; iv) the $\sim$ 65 *meV* and $\sim$ 80 *meV* excitations broaden and shift to the low energies; v) a new excitation shows up at $\sim$ 75 *meV*. Based on the phonon-phonon/lattice-lattice discussion of the partial phonon DOS in sections 7.2 and 7.4, the low energy excitation (less than $\sim$ 45 *meV*) signals are

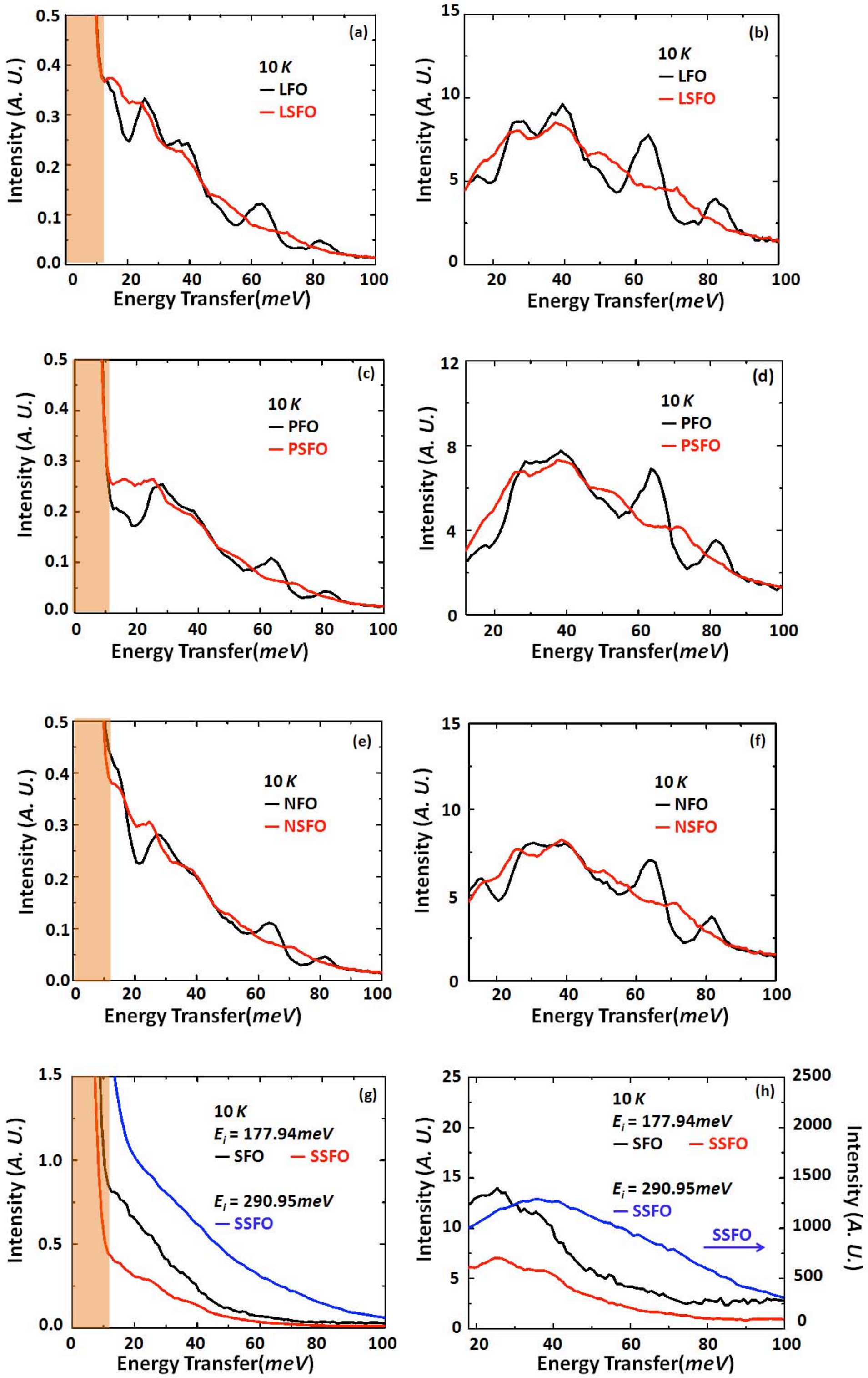

Figure 7.13 High - angle scattering(a), (c), (e), (g) and phonon DOS(b), (d), (f), (h) data comparison of *R*FO and *R*SFO (*R* = La, Pr, Nd, and Sm) at 10 *K*.

the result of the total contribution of metal and oxygen ions, and the high energy excitation (larger than ~ 45 *meV*) signals is just the result of oxygen ions. With the Sr ions doped, the doped hole changes Fe^{3+} ions in *R*FO into Fe^{3+} and Fe^{5+} ions in the ordered *R*FO, thus the environment of O ions changes a lot which leads to the difference of the partial DOS of oxygen ions. As discussed in the previous section, section 7.5.1, the Raman spectra of LMO and Ca-doped compounds, $La_{1-x}Ca_xMnO_3$, have the similar temperature dependence and it is related to the atomic motions of oxygen [16, 17]. Since the excitation frequency is determined by both the force constant and atomic mass, section 7.2, the partial phonon DOSs of heavy metal ions do not change a lot. Therefore, the electron-lattice interaction should play a role for the CO and O modes will be affected a lot.

7.7 Summary

After analyzing the temperature dependence of phonon spectra of LFO and *R*SFO, the thermal broadening in the phonon spectra due to lattice anharmonic can be accounted for. The remaining shifts in DOS of *R*SFO above and below T_V are very similar to the CO case of $La_{1-x}Ca_xMnO_3$, therefore the effect of electron-lattice interactions needs to be considered. In order to understand the electron-lattice interactions, the phonon DOSs of *R*SFO and the related parent compound were compared and the shell model is applied to calculate them. And O modes are most affected.

Bibliography

[1] G. L. Squires, *Introduction to the theory of thermal neutron scattering*, Cambridge University Press. 1996

[2] R. J. McQueeney, *Lattice effcts in high-temperature superconductors*, UMI, 1997

[3] O. Delaire, *The Phonon Entropy of Transition Metals and Alloys*: *Effects of Impurities and of a Martensitic Phase Transition*, http://resolver.caltech.edu/CaltechETD:etd-05262006-160244, 2006

[4] R. J. McQueeney, J. Ma, S. Chang, J.-Q. Yan, M. Hehlen, and F. Trouw, Physical Review Letter 98 (2007) 126402

[5] P. P. Ewald, Annals of Physics (Leipzig) 64 (1921) 253

[6] W. Cochran, *CRC Critical Reviews in Solid State Science*, March (1971)

[7] Mala N. Rao, S. L. Chaplot, N. Choudhury, K. R. Rao, R. T. Azuah, W. T. Montfrooij, and S. M. Bennington, Physical Review B 60 (1999) 12061

[8] E. G. Rini, Mala N. Rao, S. L. Chaplot, N. K. Gaur, and R. K. Singh, Physical Review B 75 (2007) 214301

[9] J. B. A. A. Elemans, B. V. Larr, K. R. V. D. Veen, and B. O. Looptra, Journal of Solid State Chemistry 3 (1971) 238

[10] B. C. Tofield and W. R. Scott, Journal of Solid State Chemistry 10 (1974) 183

[11] P. Norby, I. G. Krogh Andersen, E. Krogh Andersen, and N. H. Andersen, Journal of Solid State Chemistry 119 (1995) 191

[12] J. F. Mitchell, D. N. Argyriou, C. D. Potter, D. G. Hinks, J. D. Jorgensen, and S. D. Bader, Physical Review B 54 (1996) 6172

[13] Q. Huang, A. Santoro, J. W. Lynn, R. W. Erwin, J. A. Borchers, J. L. Peng, and R. L. Greene, Physical Review B 55 (1997) 14987

[14] J. Rodriguez-Carvajal, M. Hennion, F. Moussa, A. H. Moudden, L. Pinsard, and A. Revcolevschi, Physical Review B 57 (1998) R3189

[15] S. L. Chaplot, N. Choudhury, Subrata Ghose, Mala N. Rao, R. Mittal, and P. Goel, European Journal of Mineralogy 14 (2002) 291; S. L. Chaplot, Bhabha Atomic Research Centre, External Report No. BARC-972, 1978 (unpublished).

[16] M. N. Iliev, M. V. Abrashev, J. Laverdiere, S. Jandl, M. M. Gospodinov, Y.-Q. Wang, and Y.-Y. Sun, Physical Review B 73 (2006) 064302

[17] E. Liarokapis, Th. Leventouri, D. Lampakis, D. Palles, J. J. Neumeier, and D. H. Goodwin, Physical Review B 60 (1999) 12758

CHAPTER 8. SUMMARY AND DISCUSSION

8.1 Summary

Due to its special magnetic and transport properties, the transition-metal oxide (TMO) with strong electron correlation has received considerable attention. It has been widely recognized by researchers that CO arises from the coupling or the competition among Coulomb interaction, magnetic energy, and electron-phonon/electron-lattice interaction. In this thesis, we applies inelastic neutron scattering (INS) to study the exact driving force of the charge ordering (CO) in a series of $R_{1/3}\mathrm{Sr}_{2/3}\mathrm{FeO}_3$ (*R*: rare earth metal).

The magnetic exchange energy can be obtained from the magnetic spectra by INS measurement. We have shown that the magnetic energy is the dominant interaction to CO in $\mathrm{La}_{1/3}\mathrm{Sr}_{2/3}\mathrm{FeO}_3$, which agrees with the theoretical prediction conducted by T. Mizokawa, *et al.* [1]. We arrived at this conclusion by determining that the large ferromagnetic exchange energy (J_F) occurring between Fe^{3+}-Fe^{5+} pairs stabilizes the CO state. However, since the observed CO structure also minimizes the Coulomb energy, we cannot unambiguously confirm the dominance of the magnetic interaction. Therefore, we address this issue by examining other *R*SFO with different rare earths. Because of the smaller *R* ions, we expected the crystalline distortions to increase the charge-transfer (CT) gap and narrow the electronic bandwidth. The net result is to reduce electronic screening, thereby enhancing the Coulomb interaction and stabilizing the CO. Nevertheless there was a contrary observation that CO was destabilized with decreasing ion (*R*) size due to the reduction of T_N [2, 3]. This observation might support the magnetic mechanism, and should imply that the CO is suppressed due to weaker magnetic interactions in the smaller rare earth compounds. Hence, the INS spectra measurement of this series of compound were very important to test this scenario.

However, the crystal electronic field (CEF) excitation of the magnetic rare-earth ion contributes strongly to the magnetic spectra of *R*SFO. In order to account for the CEF signal from the total magnetic spectra and grasp the pure signal of Fe magnetic scattering, we first analyzed the parent compounds *R*FeO$_3$ (*R*: rare earth metal) by the assumption that the ionic environment of R^{3+} in *R*SFO is similar to *R*FO. The CEF excitation parameters are determined by fitting in both energy- and momentum-space. Simultaneously, calculations of the Fe spin-wave spectra of of *R*FO were performed using linear nearest-neighbor (*NN*) Heisenberg Model. In Table 8.1, the lattice distortion increases with the *R*-site substitution from La to Nd, so the superexchange will be weaker, which leads to smaller magnitude of the antiferromagnetic exchange energy J_{AF}. We also had unexpected observations during the analysis of the CEF of PFO and SFO: i) two unreported CEF excitations are observed ($E_{70} \sim 80$ *meV* and $E_{80} \sim 100$ *meV*); ii) we measured the CEF of SFO by INS for the first time and the result agrees with the infrared spectrum.

The characterization and the magnetic spectrum fitting results of *R*SFO are listed in Table 8,1: i) the lattice distortion increases with the *R*-site substitution from La to Nd, which is the same as *R*FO; ii) $|J_{AF}|$ is the same in LSFO and PSFO, and bigger in NSFO; iii) J_F is independent of *R* substitution; iv) the CT gap of NSFO is the largest among those three compounds [3]. Furthermore, the lattice distortion of the NSFO should be close to the lattice effect PSFO due to the geometric tolerance factor. Therefore, we can conclude that i) the magnetic energy is the main driving force to the CO state of LSFO and PSFO; ii) increased $|J_{AF}|$ destabilized the CO of NSFO and the contribution of magnetic energy to the CO is weaker. Maybe the Coulomb energy effect on CO is unnegligible.

The $|J_{AF}|$s of *R*FO and *R*SFO were compared. There was a $\sim 20\%$ increase of $|J_{AF}|$ in NSFO compared to NFO, and a 30% reduction in LSFO and a 20% reduction in PSFO compared to LFO and PFO, respectively. Since *R*FO is a typical insulator and *R*FSO is a semiconductor, we propose that the MCDW is a charge density wave with appreciable hole density in the AF region between the domain walls. Moreover, the distortion per cents of the lattice are listed in Table 8.2. In perovskite oxides with a (180° - ω) *M-O-M* bond, the bond-length modulation and bond angle enter the overlap integral *b* is expressed as [4],

$$b^2 \sim cos^2(\omega/2)/d^7 \,, \tag{8.1}$$

where *d* is the average bond length.

Therefore, there are two origins for the increased $|J_{AF}|$: i) the CT gap, which will increase the electron hopping energy between the interacting ions of the superexchange; ii) the lattice distortion,

Table 8.1 The structural properties and exchange energies in *R*FO and *R*SFO.

	$LaFeO_3$	$PrFeO_3$	$NdFeO_3$
space group	*Pnma*	*Pnma*	*Pnma*
bond length(Å)			
Fe - O(1)	2.002	2.004	2.005
Fe - O(2)	2.004	2.006	2.007
Fe - O(2)	2.005	2.015	2.017
bond angle			
∠ Fe - O(1) - Fe	157.6°	153.3°	151.2°
∠ Fe - O(2) - Fe	157.5°	152.4°	151.4°
geometric tolerance factor			
t	0.951	0.925	0.918
Fe-O-Fe overlap integral			
b^2	0.0074	0.0072	0.0071
exchange energy			
J_{AF} (meV)	- 4.90	- 4.55	- 4.45
	$La_{1/3}Sr_{2/3}FeO_3$	$Pr_{1/3}Sr_{2/3}FeO_3$	$Nd_{1/3}Sr_{2/3}FeO_3$
space group	$R\bar{3}c$	$R\bar{3}c$	$R\bar{3}c$
bond length(Å)			
Fe - O	1.940	1.941	1.939
R - O	2.7413	2.7377	2.7329
bond angle			
∠ Fe - O - Fe	173.2°	170.5°	169.3°
geometric tolerance factor			
t	0.999	0.997	0.996
Fe-O-Fe overlap integral			
b^2	0.0096	0.0096	0.0096
charge transfer gap			
Δ(meV)	62	58	85
exchange energy			
J_{AF} (meV)	- 3.5	- 3.5	- 5.5
J_F (meV)	5.1	5.1	5.1

which is the largest from NFO to NSFO compared the difference of LFO to LSFO and PFO to PSFO .

Table 8.2 The structure distortion from *R*FO and *R*SFO.

$Pnma \rightarrow R\bar{3}c$			
	LFO→LSFO	PFO→PSFO	NFO→NSFO
bond length(Å)			
ΔFe-O(1)(%)	0.062(3.1%)	0.063(3.1%)	0.066(3.3%)
ΔFe-O(2)(%)	0.064(3.2%)	0.065(3.2%)	0.068(3.4%)
ΔFe-O(2)(%)	0.065(3.2%)	0.074(3.7%)	0.078(3.9%)
bond angle			
Δ∠Fe-O(1)-Fe(%)	-15.6°(-10.2%)	-17.2°(-11.2%)	-18.1°(-12.0%)
Δ∠Fe-O(2)-Fe(%)	-15.7°(-10.0%)	-18.1°(-11.8%)	-17.9°(-11.8%)
Fe-O-Fe overlap integral			
Δ *b*	0.0022(29.7%)	0.0024(33.3%)	0.00158(35.2%)

To address the presence of the electron-phonon/electron-lattice, the temperature-dependence phonon spectra of *R*SFO were analyzed. There are two features that suggest some role for electron-phonon/electron-lattice couping based on phonon data as the temperature is above/below T_V: i) the phonon at $\sim$ 50 *meV* reduced; ii) the softening of $\sim$ 70 *meV* phonons. And it has been proved that those singularities do not come from thermal factor. Furthermore, the similar phonon phenomenon is observed in the temperature-dependence Raman spectra of $La_{1-x}Ca_xMnO_3$, which has been proved as the result of electron-lattice interaction, thus the electron-lattice interaction should have played some role in the CO state. Based on the partial phonon DOS, those two features belong to the oxygen phonon region which indicates that the CO state is relative to the oxygen phonons. Therefore, the electron-phonon/electron-lattice might be recognized from the environment of the oxygen phonons which is changed from a average valence environment, $Fe^{3.67+}$, into the ordered diacritical valence environments, Fe^{3+} and Fe^{5+}.

8.2 Future Work

Although the magnetic spectrum of *R*SFO have been studied very well, there is still an uncertainty about nature of excitations in region of 20 *meV*-30 *meV*. This signal might come from the residual phonons and empty-can, which are poorly subtracted. Unfortunately, density-of-state cannot provide enough information and the details of the magnetic dispersion need to be obtained. The single crystal data will help a lot, but there is no good one grown by the image-furnace technique for inelastic neutron scattering measurement due to the rigorous requirement of the high oxygen pressure currently.

Due to the strong neutron absorption of Sm in SSFO and SFO, the magnetic and phonon spectra are not analyzed very well. A more precise instrument with high revolution and flux needs to be applied.

There are still a lot of unfinished work in the phonon spectrum of *R*FO and *R*SFO, such as, developing the model for phonon dispersion and density-of-state, identifying modes that have strong electron-phonon/electron-lattice coupling, measuring the phonon spectra by a single crystal, and so on. With the help of *R*FO, the role of electron-phonon/electron-lattice interaction in the *R*SFO system will be determined.

Bibliography

[1] T. Mizokawa and A. Fujimori, Physics Review Letter 80 (1998) 1320

[2] V. P. S. Awana, S. X. Dou, I. Felner, I. Nowik, S. K. Malik, A. Mehta, R. Singh, A. V. Narlikar, and W. B. Yelon, Journal of Applied Physics 83 (1998) 7312

[3] S. K. Park, T. Ishikawa, Y. Tokura, J. Q. Li, and Y. Matsui, Physical Review B 60 (1999) 10788

[4] J.-S. Zhou and J. B. Goodenough, Physical Review B 77 (2008) 132104

APPENDIX A. Iodometric Titration

Standard Operating Procedures

- Ingredients:

0.075 *mol/l* $Na_2S_2O_3$

0.010 *mol/l* $KMnO_4$

0.075 *mol/l* KI

2.0 *mol/l* KI

1.0 *mol/l* HCl

1.0 *mol/l* H_2SO_4

Starch indicator solution

1. **Preparation of the Solutions:**

   Solutions containing HCl or KI may be light sensitive and should only be prepared as needed. If mixed before actual use, the solutions may contain free iodine and can no longer be trusted. The other solutions should be stable for extended periods.

   a) Prepare 0.075 *mol/l* $Na_2S_2O_3$

      i) Weigh out 4.6521*mg* $Na_2S_2O_3 \cdot 5\ H_2O$(Mm = 248.112 *mg/mol*); Place into a 250*ml* volumetric flask; Add some distilled H_2O and stir to dissolve.

      ii) Top off gradually with distilled H_2O to 250*ml* line, swirling throughout.

   b) Prepare 0.010 *mol/l* $KMnO_4$

      i) Weigh out 0.3952*mg* $KMnO_4$(Mm = 158.09 *mg/mol*); Pour into a 250*ml* volumetric flask; Add some stilled H_2O and stir to dissolve.

      ii) Top off gradually with distilled H_2O to 250*ml* line, swirling throughout.

c) Prepare 0.075 *mol/l KI*

- i) Weigh out 3.1125*mg KI*(*Mm* = 165.998 *mg/mol*); Pour into a 100*ml* beaker; Add some distilled H_2O and stir to dissolve; Transfer the solution into a 250*ml* volumetric flask and swirling throughout.
- ii) Top off gradually with distilled H_2O to 250*ml* line.

d) Prepare 2.0 *mol/l KI*

- i) Weigh out 33.1996*mg KI*. Pour into a 100*ml*beaker; Add some distilled H2O and stir to dissolve; Transfer the solution into a 100*ml* volumetric flask and swirling throughout.
- ii) Top off gradually with distilled H_2O to 100*ml* line.

e) Prepare 1.0 *mol/l HCl*

- i) Prepare 2.0 *mol/l HCl*
  - (1) Put about 250*ml* distilled H_2O into a 1000*ml* volumetric flask.
  - (2) Pour 165*ml* full strength *HCl*($\mathbf{12.1N}$) into the same flask and swirl.
  - (3) Top off gradually with distilled H_2O to 1000*ml* with distilled H_2O and swirl throughout.
- ii) Prepare 1.0 *mol/l HCl*
  - (1) Add about 25*ml* distilled H_2O into a 100*ml* volumetric flask.
  - (2) Pipette 8.3*ml* full strength *HCl* into the same flask using a pipette and swirl.
  - (3) Top off gradually with distilled H_2O to 100*ml* with distilled H_2O and swirl throughout.
  - (4) Alternatively, can dilute 50*ml* 2.0M *HCl* above with 50*ml* distilled water.

f) Prepare 1.0 *mol/l* H_2SO_4

- i) Put about 250*ml* distilled H_2O into a 1000*ml* volumetric flask. **DON'T ADD $\boldsymbol{H_2SO_4}$ FIRST**!
- ii) Pour the volume of full strength H_2SO_4 into the same flask and swirl.
- iii) Top off gradually with distilled H_2O to 1000*ml* with distilled H_2O and swirl throughout.

g) Prepare Starch indicator solution

- i) Weigh 1*mg* of soluble starch. Add a few drops of distilled H_2O and rub mixture into a paste.
- ii) Prepare 100*ml* boiling distilled H_2O and add starch paste and stir well.

iii) Boil this suspension for about 1min., then let it cool.

iv) Allow to settle, then decant fine suspension into covered flask or vial; the solution can be filtered somewhat if desired. Many want to keep refrigerated.

v) The starch indicator solution can spoil and should be prepared fresh when needed.

2. **Experimental Procedures:**

a) Demarcating the standard $Na_2S_2O_3 \cdot 5\ H_2O$: although the ratio of $Na_2S_2O_3$ to H_2O is nominally 1:5 in the bottle off of the shelf (for the 250 *ml* solution prepared as described above, the nominal molar concentration of $Na_2S_2O_3$ is 0.075 *mol/l*), we must experimentally verify the molar concentration of $Na_2S_2O_3$

i) Transfer 20 *ml KI* and 20 *ml* $KMnO_4$ solutions into a 250 *ml* Erlenmeyer flask.

ii) Add more than 4 *ml* 1*M* H_2SO_4 as acid environment.

iii) Add some starch solution as indicator, the color of the solution should be blue. It is advisable to calculate the approximate volume of $Na_2S_2O_3$ needed and to only add the starch solution when the titration is nearing the end point.

iv) Titrate with $Na_2S_2O_3$ solution, drop by drop, until the blue disappears; be sure to record initial and final titrant volumes. Stirring vigorously. When approaching endpoint, greenish tint will disappear, leaving only dark blue. When blue color disappears, a slight pinkish color may remain; if titration is continued, solution will be white, almost clear. Choose the endpoint consistently; since a ratio will be taken, differences in endpoint choice will roughly cancel. Record volume to titrant used (V_1). Patience pays when you approach the end point.

v) The volume of $Na_2S_2O_3$ solution used should be around 13 *ml*. Calculate the molar density of the $Na_2S_2O_3$ solution from the actual volume used.

b) Titrating the Sample (*The following steps are very important, don't mix it up!*)

i) Carefully weigh out enough sample to use up at least 10 *ml* of titrant and place into an Erlenmeyer flask. (250*ml* flask is recommended!!).

ii) Add some water inside the flask.

iii) Add the 2.0 *mol/l KI* solution.

iv) Add the 2*mol/l HCl*, they will help to dissolve the sample. If the sample doesn't dissolve very well, you can heat the solution, but remember to add some $Na_2S_2O_3$ to produce CO_2 as the environment (In fact in the CO_2 atmosphere, *HCl* can also be added at first, then *KI*).

v) Add the 1*mol/l* H_2SO_4 and starch; the color will be blue.

vi) Add some $Na_2S_2O_3$ in the cool solution as the environment (the ions Cu^+ and I^- can be oxidized by the oxygen easily in the acid environment).

vii) Use the standardized $Na_2S_2O_3$ solution to titrate. Remember to record the volume of titrant used.

viii) At last, remember to clean, dry and seal all glassware.

3. **Calculations:**

a) Molar concentration of $Na_2S_2O_3$. Mixing the *KI* and $KMnO_4$ solutions in an acidic environment (as in steps above) liberates free iodine via the reaction

$$2MnO_4^- + 15I^- + 16H^+ \longrightarrow 2Mn^{2+} + 5I_3^- + 8H_2O\,, \tag{A.1}$$

If N_{KMnO_4} is the total number of mols of $KMnO_4$ molecules in solution, then it follows from equation (1) that the number of free iodine molecules produced in the reaction is

$$N_{I_2} = \frac{5}{2} N_{KMnO_4}\,, \tag{A.2}$$

Adding $Na_2S_2O_3$ results in the following reaction,

$$I_2 + 2S_2O_3^{2-} \longrightarrow 2I^- + S_4O_6^{2-}\,, \tag{A.3}$$

From equations (2) and (3) it follows that

$$N_{Na_2S_2O_3} = 2N_{I_2} = 5N_{KMnO_4}\,, \tag{A.4}$$

is the number of mols of $Na_2S_2O_3$ required to turn all iodine molecules into iodide. Therefore, the molar concentration of the $Na_2S_2O_3$ solution must be

$$n_{Na_2S_2O_3} = \frac{5N_{KMnO_4}}{V_{Na_2S_2O_3}}\,, \tag{A.5}$$

where $V_{Na_2S_2O_3}$ is the volume of $Na_2S_2O_3$ used.

b) Titrating sample. First some definitions of symbols:

N: Total number of mols of sample to be titrated;

m: Mass of sample to be titrated;

M: Nominal molar mass of sample to be titrated;

$\nu + x$: Valence of the metal ion in sample and x is a number between 0 and 1;

$y + \delta$: Oxygen stochiometry of sample and d is a number between 0 and 1;

$V_{Na_2S_2O_3}$: Volume of $Na_2S_2O_3$ used to titrate sample;

$n_{Na_2S_2O_3}$: Molar concentration of the $Na_2S_2O_3$ solution;

$N_{Na_2S_2O_3}$: Total number of mols of $Na_2S_2O_3$ used to titrate sample;

T: metal ion in sample;

k: stoichiometry of metal in sample;

Two relations are readily obvious:

$$N = \frac{m}{M}\,, \tag{A.6}$$

and

$$N_{Na_2S_2O_3} = n_{Na_2S_2O_3} V_{Na_2S_2O_3}\,, \tag{A.7}$$

As in the case of $KMnO_4$ in equation (1), the metal ion in the sample liberates free iodine in the following reaction

$$2T^{\nu+x} + (2x)I^- \longrightarrow 2T^{\nu+} + xI_2\,, \tag{A.8}$$

Again, equation (3) is the reaction equation when $Na_2S_2O_3$ is added to the solution. From equations (3) and (8) we can find that

$$N_{Na_2S_2O_3} = xN\,, \tag{A.9}$$

Substituting equations (6) and (7) into equation (9) and rearranging gives

$$x = n_{Na_2S_2O_3} V_{Na_2S_2O_3} \frac{M}{m}\,, \tag{A.10}$$

The relationship between the valence of the metal ion (i.e. x) and the oxygen stoichiometry (i.e. δ) will vary from sample to sample based on the following. Oxygen has a valence of -2 and may be viewed as accepting electrons. In the oxide samples of interest to us, the number of electrons that O^{2-} accepts must be balanced by the combination of stoichiometry and valence of all the other ions. Therefore,

$$\sum(k_i\nu_i) + k(\nu + x) = 2(y + \delta)\,, \tag{A.11}$$

where k_i and ν_i are stoichiometry and valence of all other ions, respectively. Note that equation (11) assumes that the oxygen off stoichiometry only affects the valence of the metal ion of interest and no other ion.

Example 1: CuO

From the chemical formula of CuO, we know that $y = 0$ and $k = 1$. There are no other ions to consider. Then from equation (11), once the titration has been performed, the oxygen content is given by

$$\delta = \frac{(1 + x)}{2}\,, \tag{A.12}$$

Example 2: $LaFeO_3$

Again, from the chemical formula, $k = 1$ and $\nu = 2$. In addition, in this case we must consider

La which has stoichiometry k_{La} = 1 and valence ν_{La} = 3.

$$k_{La}\nu_{La} + k(\nu + x) = 3 + 2 + x = 2(y + \delta)\,, \tag{A.13}$$

Example 3: $La_{1/3}Sr_{2/3}FeO_3$

Based on the chemical formula, k = 1 and ν = 2. In addition, in this case we must consider La which has stoichiometry k_{La} = 1/3 and valence ν_{La} = 3, and Sr, which has stoichiometry k_{Sr} = 2/3 and valence ν_{Sr} = 2.

$$\sum(k_i\nu_i) + k(\nu + x) = 1/3 \times 3 + 2/3 \times 2 + 2 + x = 2(y + \delta)\,, \tag{A.14}$$

APPENDIX B. Sm^{3+} Absorption Calculation

The neutron absorption cross section of Samarium is large, 5922.56 barn, which is almost 150 times larger than the scattering cross section. In order to account for large absorption effects, we are going to calculate the transmission efficiency and use it to correct the neutron scattering signals.

The incident angle between the incident beam and the sample, ϕ, the scattering angle between the incident and scattering beams, 2θ, and the thickness of the sample, t, are the first three factors that we need to consider because it will decide the length of the neutron beam passed. Fig. B.1 shows the transmission sketch and A is a random point in the sample.

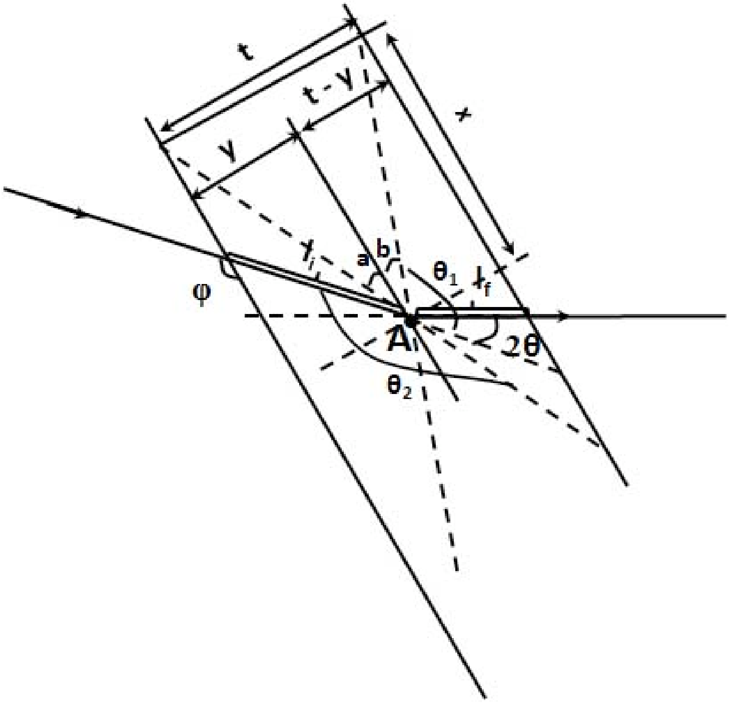

Figure B.1 The transmission sketch of Samarium sample. $l_i(l_f)$ is pathway of the the neutron beam passed(left) in the sample; x(y) is the distance of the point to the edge of the sample on the sample parallel(perpendicular) direction; a(b) is the angle of the point to the front(back) ending point on the sample parallel direction.

Assume

$$a = arctan(\frac{y}{x}), \quad b = arctan(\frac{t-y}{x})\,, \tag{B.1}$$

and

$$\theta_1 = \phi - b, \quad \theta_2 = \phi + a\,, \tag{B.2}$$

From Fig. B.2, we can easily find that the length that the the neutron beam passed in the sample, l_i, is

$$l_i = \frac{y}{sin(\pi - \phi)}\,, \tag{B.3}$$

The calculation of l_f is more complicated: there are 3 cases which are decided by the scattering angles.

i) $2\theta \leq \theta_1$

the scattered neutrons go through the can and detected by the detectors, which is shown in Fig. B.2

$$l_f = \mid \frac{t-y}{cos(\frac{\pi}{2} + 2\theta - \phi)} \mid\,, \tag{B.4}$$

ii) $\theta_1 \leq 2\theta \leq \theta_2$

The scattered neutrons go through part of the can and hit the frame of the empty can. So they are absorbed by Gd cover and can not be recorded by the detectors, Fig. B.3(a)

$$l_f = \frac{x}{cos(2\theta - \phi)}\,, \tag{B.5}$$

iii) $2\theta \geq \theta_2$

The scattered neutrons do not go through the can and go back to the front panel of the empty can. The detectors can not record the them, Fig. B.3(b)

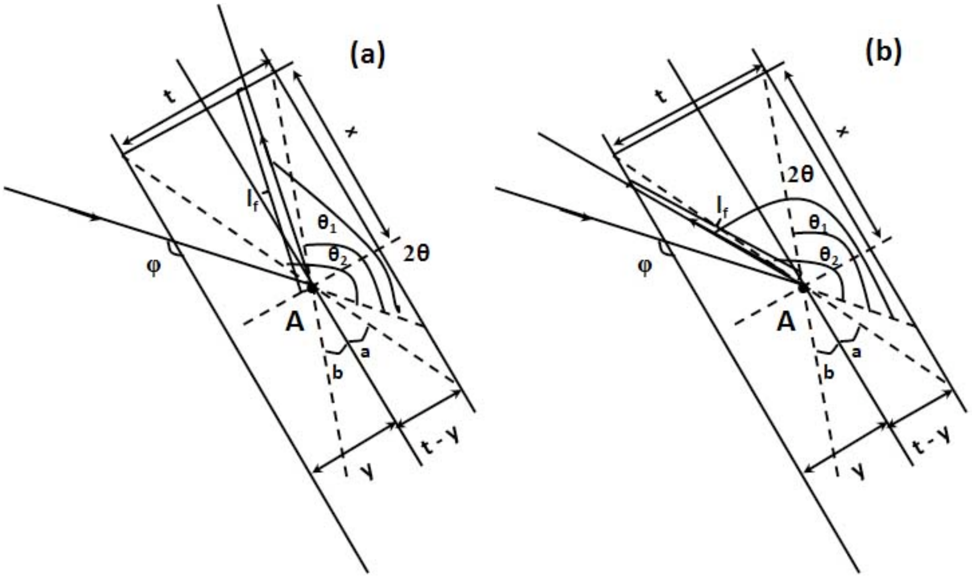

Figure B.2 The transmission sketch of Samarium sample.(a) $\theta_1 \leq 2\theta \leq \theta_2$, (b) $\theta_2 \leq 2\theta$.

$$l_f = \mid \frac{y}{cos(\frac{\pi}{2} - 2\theta + \phi)} \mid , \tag{B.6}$$

So we can calculate the transmission efficiency by the relationship

$$\mathbf{T} = \mathbf{I}\, exp[-l_i\,(\mu_{ai} + \mu_s) - l_f\,(\mu_{ae} + \mu_s)]\,, \tag{B.7}$$

where μ_{ai} and μ_{af} are the absorption efficiency at different energies, which are defined as following equations; μ_s is the scattering efficiency which is almost constant at different energies.

$$\begin{aligned} \mu_{ai} &= \mu_a \times \sqrt{\frac{25.3}{e_i}}, \\ \mu_{af} &= \mu_a \times \sqrt{\frac{25.3}{e_i - e}}, \\ \mu_s &= \mu_s \times \sqrt{\frac{25.3}{e_i}}, \end{aligned} \tag{B.8}$$

where the unit of energy is *meV* and the unit of efficiency is cm^{-1}.

The calculated transmission coefficients are angle and energy dependent, Fig. B.3. With the sample can oriented at 135° to incident beam, the weakest signal at 135° and the strongest signal at 45° because

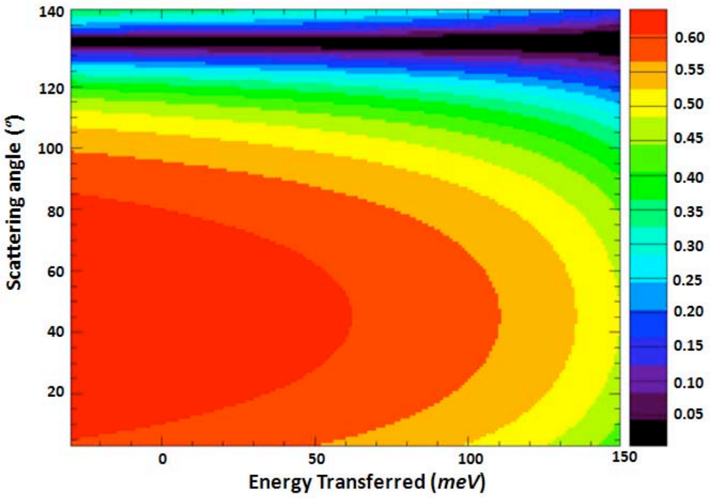

Figure B.3 The calculated neutron transmission coefficients.

of the dark angle position as we expected. For example, Fig. B.4(a) reveals the normalized integration along the scattering-angle direction in the energy region, 20.5 $\sim$ 30.5 *meV*, and the inset figures, Fig. B.4(b) and (c), exhibit the lowest and highest integrate angle position. We can clearly observe: i) the neutron absorbing coefficient is decreasing as the scattering angle going up to 45°(decided by the dark angle); ii) the absorption is stronger and stronger as the angle increasing toward 135°(dark angle position).

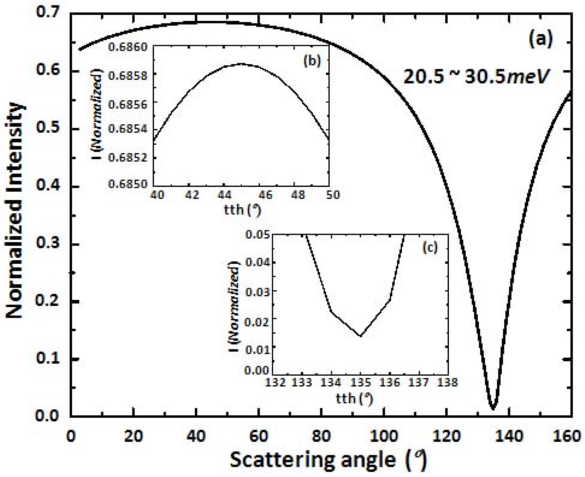

Figure B.4 (a)The total integrate transmission coefficient along the scattering - angle direction in the energy region, 20.5 - 30.5 *meV*; and the specific scattering - angle positions around 45° (b) and 135°(c).

The normalized integration over energy is shown in Fig. D.5. 7° - 30° and 70° - 90° are the angle ranges that I usually select for the low and high angle regions. As the tranferred energy increasing, the neutron transmission is decreasing. those two lines of the energy ranges have similar tendency, but different shape.

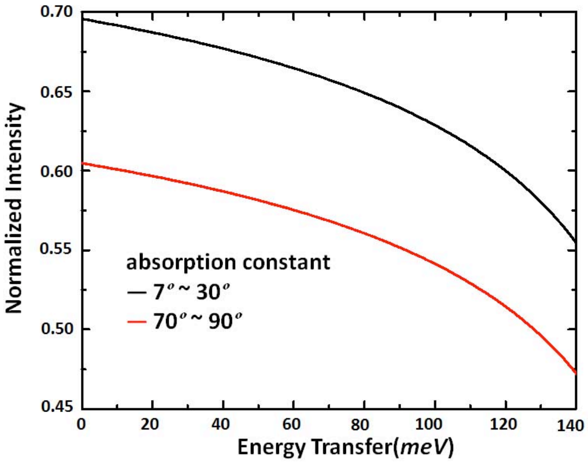

Figure B.5 The integrate transmission coefficient in the energy-space with the 2θ ranges: $7° \sim 30°$ and $70° \sim 90°$.

APPENDIX C. Data Reduction of SFO

In above discussion, we have calculated the absorption correction for the Sm containing samples. Actually, it is somewhat complicated to reduce the experimental data. The experimental data is the total signal including the sample and aluminum can scatterings, we have to subtract the can information from the raw data before we revised the Sm data with the absorption correction. Fig. C.1 shows the comparison of the experimental and empty can measurements in low-angle and high-angle region. We can clearly learn that the low-angle raw data contain a large contribution from the empty can signals above ~ 65 *meV* and the high-angle raw data are mainly empty can scattering above ~ 35 *meV*. The useful energy regions of the sample are different at low-angles and high-angles because the absorption of Sm^{3+} ion is scattering angle dependent. In Fig. C.1, the shapes of empty can scattering and total scattering are compared. Usually the absorption correction of the can must be applied as well in a data reduction process.

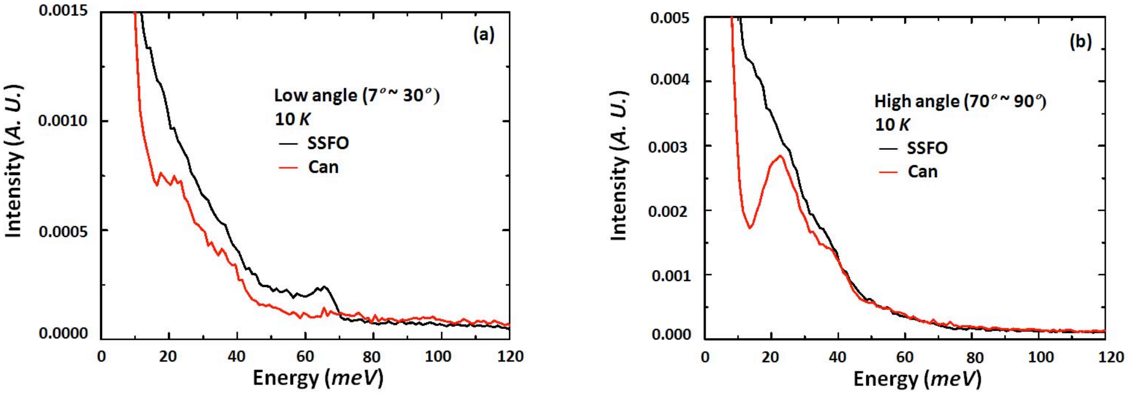

Figure C.1 Magnetic scattering intensities of SFO and SSFO with the Sm^{3+} absorption correction at $E_i = 177.94$ *meV* and $T = 10$ *K*.

From the studies on the other *R*FO (*R* = La, Pr, Nd, and Y) and CEFs, we know that magnetic excitation of Fe^{3+} results a peak near ~ 70 *meV*. The two CEFs of Sm^{3+} have energies less than ~ 50 *meV*, hence the low - angle data is useful, despite the absorption. However, the isolation of the magnetic scattering data also depends on the high - angle data, which has strong absorption effects higher than $\sim$ 35 meV. The other method to obtain the pure magnetic scattering peak need to be considered. From the X - ray diffraction characterization, we know that SFO has the similar lattice structure as the other *R*FO, the high - angle plot shall be similar to the others: Higher than 35 meV, there are phonon DOS peaks at 40 $meV \sim 50$ meV and 50 $meV \sim 60$ meV respectively. In the approximate magnetic scattering of SFO, Fig. E.1, there are uncleaned phonon signals included in the corresponding energy region. With the calculation of the Q - cuts in SFO, we also proved this assumption.

APPENDIX D. Data Reduction of SSFO

The basic data reduction method for SSFO is similar to the SFO in the previous chapter: we calculate transmission coefficient and multiply it to the sample data. Compared to SFO, the sample signal of SSFO should be better than the case of SFO since there is 2/3 less Sm^{3+}. However, the amount of SSFO sample that we have is less than the SFO because of the sensitive synthesis requirement (section 3.1), this case is still not simple.

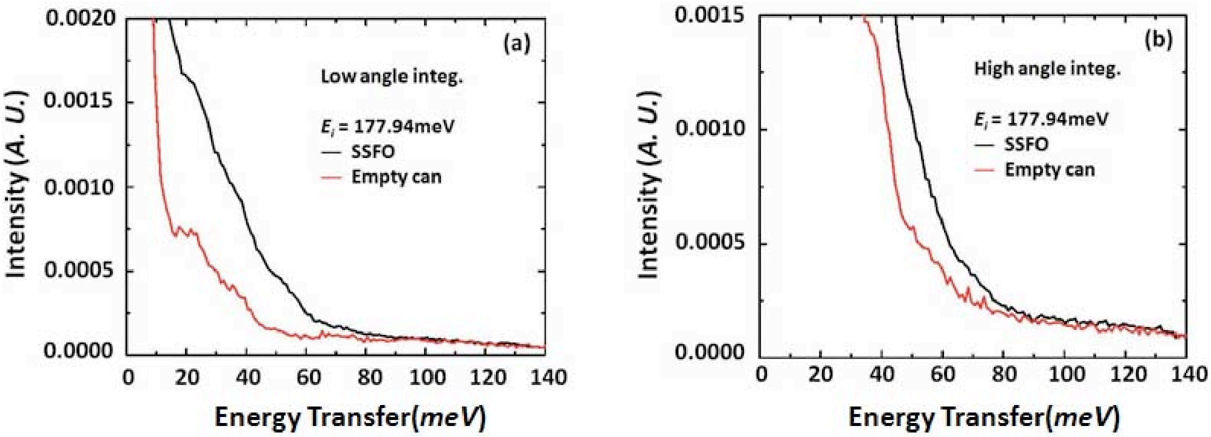

Figure D.1 The comparison of the low - angle (7° - 30°)(a) and high - angle (70° $\sim$ 90°)integration(b) of SSFO and empty can at 10 K and $\sim E_i = 180$ meV.

In order to check how strong the Sm^{3+} absorption is in SSFO, we compared the raw data of SSFO with the empty can measurement, Fig. D.1. We can clearly see that the the empty can signal is less than the total raw data of SSFO and can not be ignored. For energy transfer larger than 90 meV in both low-angle and high-angle integrated scattering regions, observed scattering comes entirely from the empty can. Therefore, high energy magnetic scattering signal is washed out by poor signal/noise and we can not make a conclusion whether the high energy magnetic excitations exist. In SFO: the interesting energy region for Fe^{3+} magnetic excitation is less than 65 meV. However, we do have a big trouble in SSFO:

the most interesting energy region between 50 $meV \sim 120$ meV is very difficult to analyze.

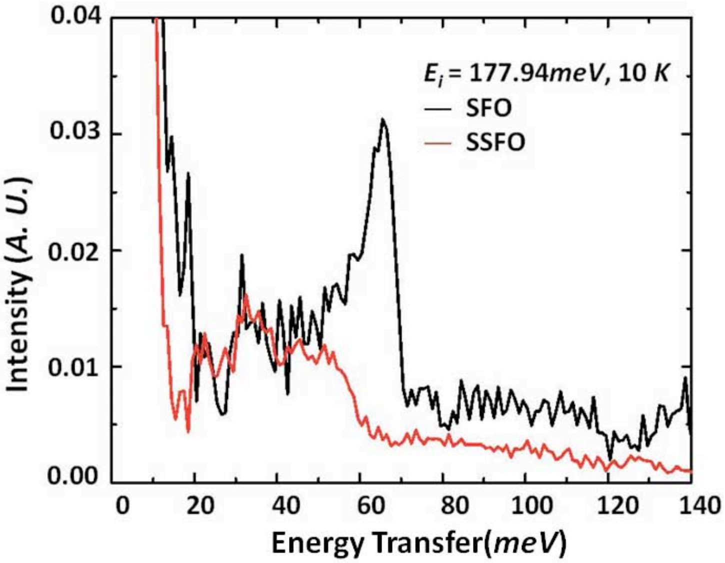

Figure D.2 Magnetic scattering intensities of SFO and SSFO with the Sm^{3+} absorption correction at E_i = 177.94 meV and T = 10 K.

Before we try to dig out the magnetic scattering data at energy higher than 65 meV, I am going to analyze the low energy magnetic spectrum first. Fig. D.2 shows the comparison of the magnetic spectrum of SFO and SSFO after the Sm^{3+} absorption correction. For SSFO, the peaks at $\sim$ 20 meV and 35 meV are the CFEs and the peak at $\sim$ 45 meV is the signal of residual aluminum can and phonon backgrounds. Although the Sm^{3+} quantity in SSFO is one third of SFO′s, the peak intensities at CFEs are not one third of SFO′s. This can be explained as the remaining sample can and phonon signals which exist in the other *R*SFO compounds.

Now, I turn to the high-energy part of the magnetic scattering spectrum. From the discussion in the previous chapters, we know that the neutron absorption is angle- and energy-dependent: if the scattering angle is constant, the absorption is larger at high energy transfer than low energy; if we rather fix the energy, the absorption increases with the scattering angle is up to 45°, and decreases as the angle is raised from 45° to 135°. Hence, there are two methods to solve the absorption problem: changing the integrating angle regions or the incident energy. Because the magnetic excitation signal decreases with the Q and the phonon signal is proportional to Q^2, we have to select the best low angle region to probe magnetic excitation and the best high angle region for phonons. Based on the other *R*SFO(*R* = La, Pr, and Nd) compounds, the low - angle and high - angle regions keep at 7° $\sim$ 30° and 70° $\sim$ 90°. Increasing

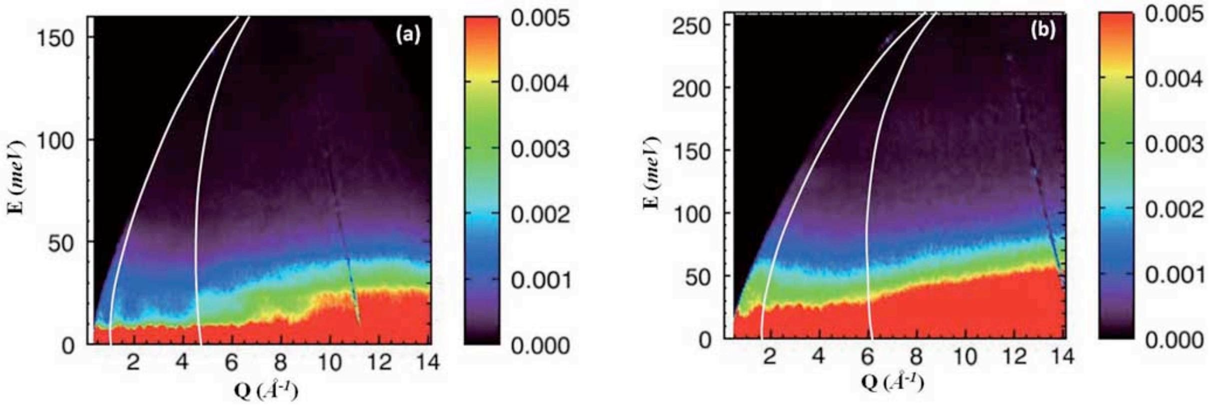

Figure D.3 Inelastic neutron scattering intensity of SSFO (color scale) versus scattering angle and energy transfer with $\sim E_i = 180\ meV$ (a) and $\sim E_i = 290\ meV$ (b) at $T = 10\ K$. The white lines delineate region where low scattering angle region is isolated.

the incident energy will lower the absorption and is a better option. The larger incident energy lowers the absorption cross-section and provides much more measurement signal, Fig. D.3. Comparing these two different measurement with the same integrating angle, more signal can be observed in the higher incident energy one.

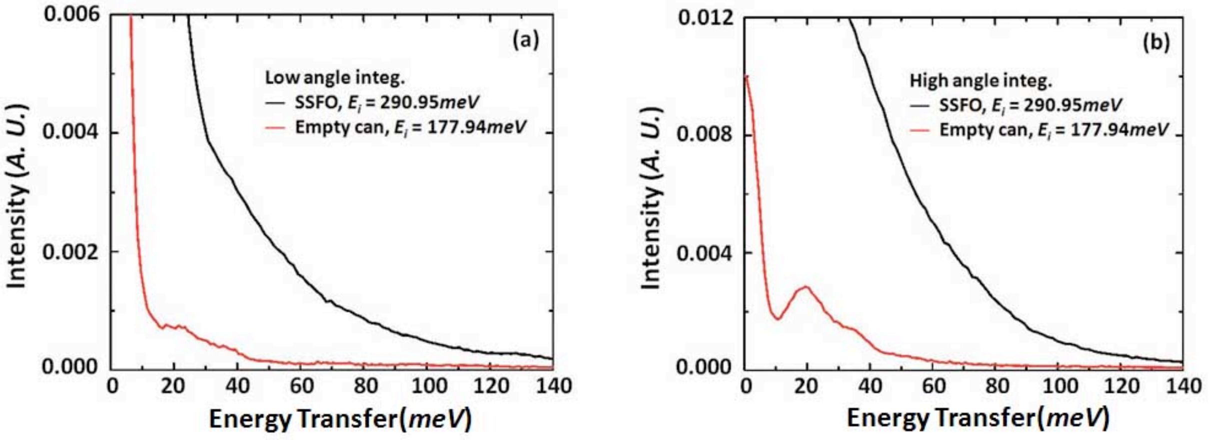

Figure D.4 The comparison of the low-angle (7° - 30°)(a) and high-angle (70° - 90°)integration(b) of SSFO with $E_i \sim 290\ meV$ and empty can with $E_i \sim 180\ meV$ at $10\ K$.

The only shortcoming for changing the incident energy is that the energy resolution is worse, so we must set up a reasonable incident energy. Fig. F.4 shows the comparison of raw data of SSFO with $E_i \sim 290\ meV$ and the data of empty can with $E_i \sim 180\ meV$, and there are signal left at high energy part

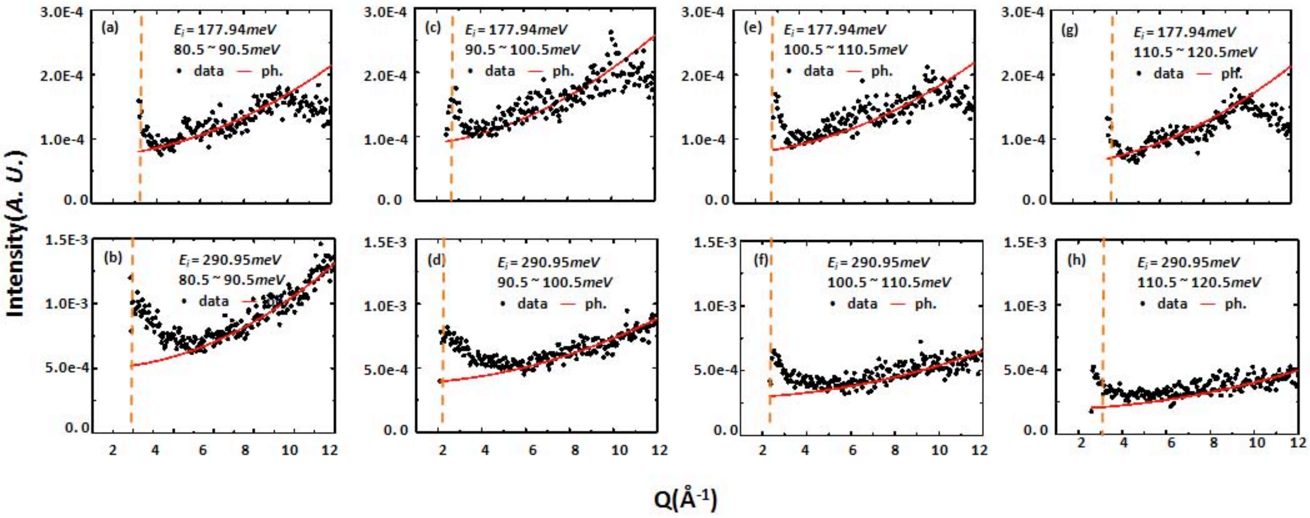

Figure D.5 The Q-cuts comparison of $E_i \sim 180$ meV((a), (c), (e), (g)) and ~ 290 meV((b), (d), (f), (h)) at 10 K. The brown dash line is the starting point of the experimental recording.

in both scattering angle regions. (The empty can was not measured with $E_i \sim 290$ meV, so we have to substitute it with the data at ~ 180 meV.) In addition, the Q-cut of SSFO at high energy regions with different E_i are compared in Fig. D.5. As $E_i \sim 290$ meV, there is magnetic signal at low Q; at $E_i \sim 180$ meV, it is hard to say the magnetic signal due to the boundary effect.

The magnetic scattering spectrum of SSFO with $E_i \sim 290.95$ meV is plotted in Fig. F.6 and compared to the spectrum with $E_i \sim 177.94$ meV. The low energy excitation signals with both incident energies agree with each other very well and the high energy excitation signals also show up, but it is still very hard to conclude whether or not the excitation gap exists.

Since it is hard to answer the gap question quantatively, we have to discuss it qualitatively. The low-angle and high-angle scattering spectrum of RSFO are compared in Fig. D.7(a) and (b). In the low-angle scattering spectrum, there is a drop in LSFO and PSFO, and a bump in NSFO at the magnetic gap region, 60 $meV \sim 80$ meV; In the high-angle scattering spectrum, there is a bump in LSFO, PSFO and NSFO at the same energy range. Therefore, the energy gap exists in LSFO and PSFO and is not observed in NSFO. The magnetic scattering in SSFO is more complicated due to the different incident energies, we will discuss them separately: i) $E_i \sim 177.94$ meV, the scattering intensities are very low in the low- and high-angle data when the transfered energy is larger than ~ 65 meV. We will not discuss it further. ii) $E_i \sim 290.95$ meV, there is neither a drop, nor a bump in the low-angle data at the gap region. Then, we

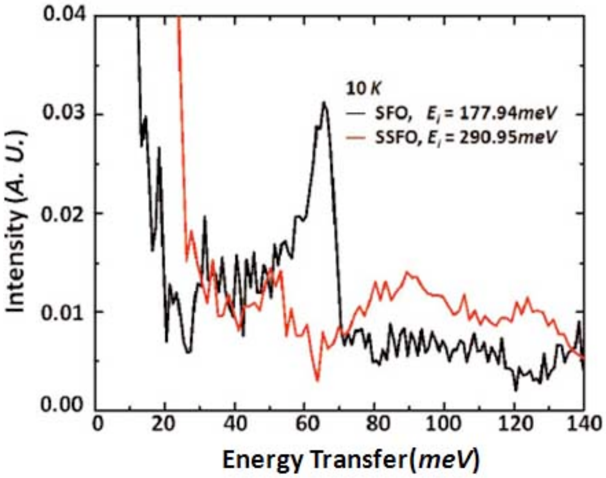

Figure D.6 Magnetic scattering intensities of SFO and SSFO with the Sm^{3+} absorption correction at T = 10 K with E_i = 177.94 meV(black) and 290.95 meV(red) respectively.

check the high-angle data. It is very disappointed to observe the disappeared bump at the gap region due to the energy resolution.(We compared it with the high angle data of NSFO at $E_i \sim$ 177.94 meV and 290.95 meV, Fig. D.7(c), it clearly shows the energy resolution effect) Because the lattice structures of *R*SFO(*R* = La, Pr, Nd and Sm) are similar, we assume the phonons are similar in them. Therefore the gap should not exist. SSFO is similar to NSFO, not to LSFO and PSFO.

Another way to prove the excitation gap is the Q-cut figures. Due to the absorption factor in SSFO, we can not compare the same energy scale data of LSFO and SSFO on the same scale. Therefore, we will calculate the magnetic contribution of Fe^{3+} from Q-cuts and compare the tendency of the integrated intensities with the other *R*SFO. We do not know the J_{AF} and J_F in SSFO, so the only factor we could fit is phonon. Fortunately, there is no contribution from Sm^{3+} CEF for transfered energy larger than 40 *meV*. The remaining part of the Q-cuts will be just the magnetic signal of Fe^{3+}, Fig. D.8.

Table D.1 The integrated intensities of Fe^{3+} magnetic states of Q - cuts in *R*SFO(*R* = La, Pr, Nd and Sm).

Energy Range	State number (S_ω)			SSFO	
(*meV*)	LSFO	PSFO	NSFO	E (meV)	S_ω
50.5 : 60.5	0.796	0.672	0.408	50.25 : 59.25	0.064
60.5 : 70.5	0.211	0.253	0.561	59.25 : 69.75	0.076
70.5 : 80.5	0.068	0.088	0.374	69.75 : 80.25	0.051
80.5 : 90.5	0.177	0.152	0.176	80.25 : 89.25	0.048

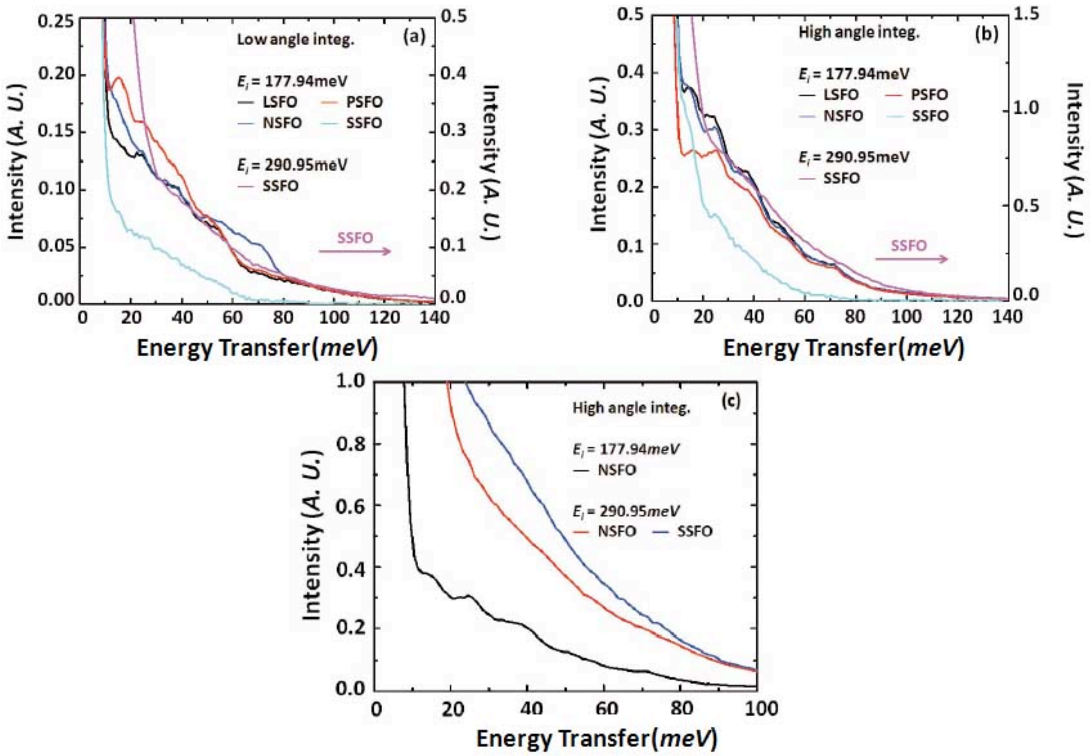

Figure D.7 Neutron intensity summed over the low angle range from 7 - 30°(a) and the high angle range from 70 - 90° in *R*SFO(*R* = La, Pr, Nd and Sm); (c) the high angle intensity comparison of NSFO (E_i = 177.94 *meV* and 290.95*meV*)and SSFO(E_i = 290.95 *meV*).

The integrated intensities were listed in Table D.1. The energy step size of SSFO is 1.5 *meV*, so the energy ranges of the Q-cut are not exact same as the others. And the values of integrated intensities are plotted in Fig. D.9: For LSFO and PSFO, the state numbers of Fe^{3+} are decreasing from 50.5 *meV* - 60.5 *meV* to 70.5 *meV* - 80.5 *meV* and then increasing in 80.5 *meV* - 90.5 *meV*, so the bottom of the energy gap is the cut 70.5 *meV* - 80.5 *meV*; For NSFO, the state numbers of Fe^{3+} are increasing from 50.5 *meV* - 60.5 *meV* to 60.5 *meV* - 70.5 *meV* and then decreasing after 60.5 *meV* - 70.5 *meV*, so the top of the energy band is the cut 60.5 *meV* - 70.5 *meV* and the energy gap does not exist. Because the tendency of the integrated intensities of SSFO is same as NSFO, we could conclude that there is no energy gap between the low and high energy bands in SSFO.

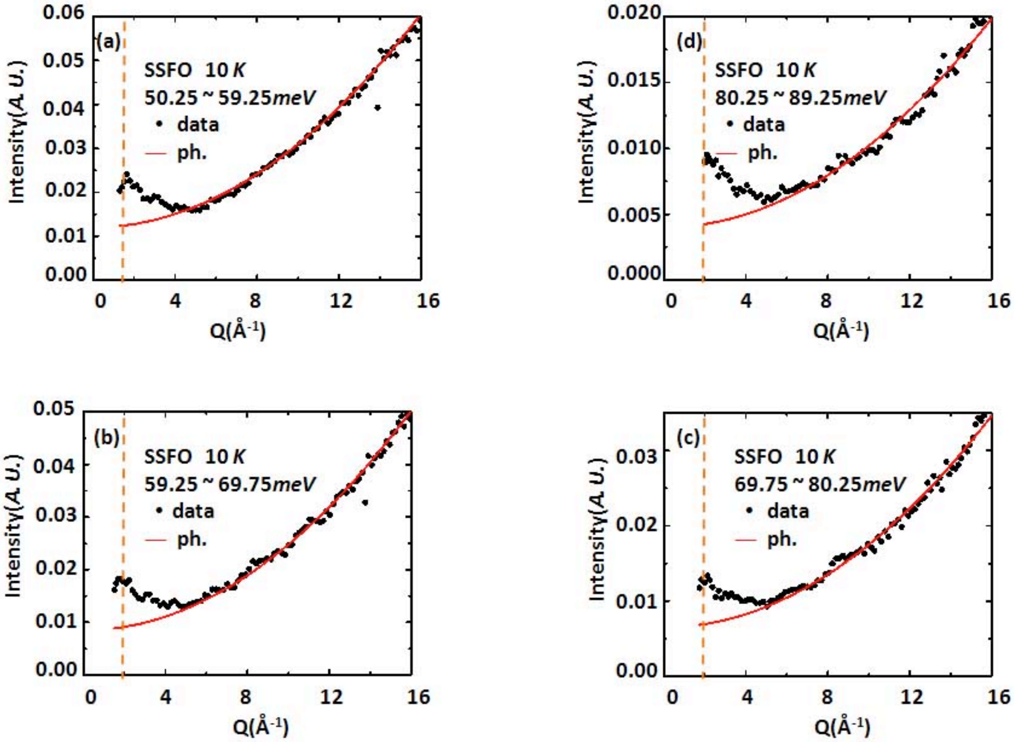

Figure D.8 The Q-dependencies of different energy transfer ranges for SSFO with $\sim 10\ meV$ step: (a) 50.25 - 59.25 meV, (b) 59.25 - 69.75 meV, (c) 69.75 - 80.25 meV, (d) 80.25 - 89.75 meV. The black dots are the experimental data. The red line it an estimate of the incoherent phonon background plus multiple scattering. The brown dash line is the starting point of the experimental recording.

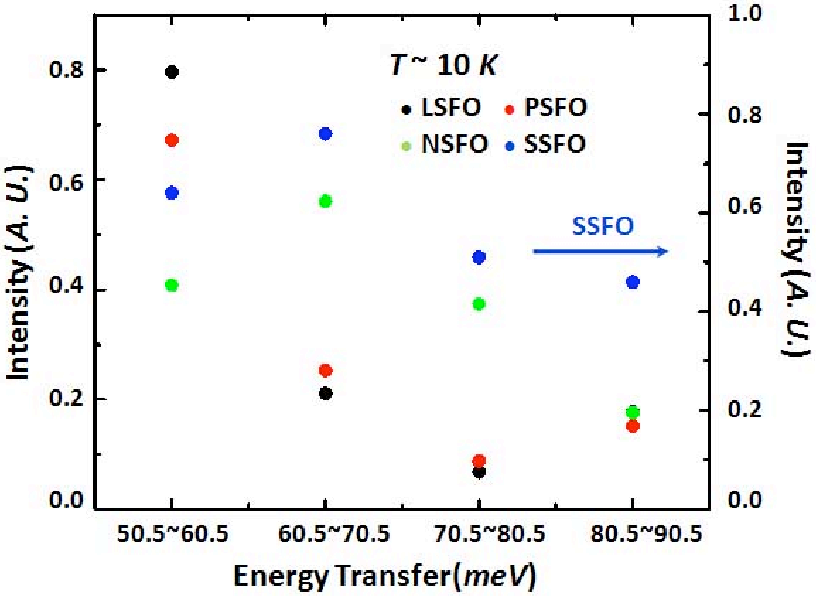

Figure D.9 The integrated intensities of different energy transfer ranges for *R*SFO with ∼ 10 *meV* step: 50.5 - 60.5 *meV*, 60.5 - 70.5 *meV*, 70.5 - 80.5 *meV*, and 80.5 - 90.5 *meV*. The black dots are the experimental data. The red line it an estimate of the incoherent phonon background plus multiple scattering.

APPENDIX E. $LaMnO_3$ orthorhombic perovskite model

Space group

Pnma

Lattice constants (Å)

5.616 7.789 5.503

Number of atoms in unit cell

20

The atom positions and labels of LMO.

Atom number	atom label	type	basis vector
1	La	1	0.541 0.25 0.007
2	La	1	-0.041 0.75 0.507
3	La	1	-0.541 0.75 -0.007
4	La	1	1.041 0.25 0.493
5	Mn	2	0. 0. 0.
6	Mn	2	0.5 0. 0.5
7	Mn	2	0. 0.5 0.
8	Mn	2	0.5 0.5 0.5
9	O1	3	0.476 0.25 0.577
10	O1	3	0.024 0.75 0.077
11	O1	3	0.524 0.75 0.423
12	O1	3	-0.024 0.25 -0.077
13	O2	4	0.292 0.041 0.206
14	O2	4	0.208 -0.041 0.706
15	O2	4	-0.292 0.541 -0.206
16	O2	4	0.792 0.459 0.294
17	O2	4	-0.292 -0.041 -0.206
18	O2	4	0.792 0.041 0.294
19	O2	4	0.292 0.459 0.206
20	O2	4	0.208 0.541 0.706

Shell model parameters for each atom of LMO

atom number	core charge (e^-)	shell charge (e^-)	spring constant between core and shell (*dyn/cm*)	atomic weight (*g/mol*)
1	1.68	0.0	1e30	138.9
2	1.68	0.0	1e30	138.9
3	1.68	0.0	1e30	138.9
4	1.68	0.0	1e30	138.9
5	1.62	0.0	1e30	54.94
6	1.62	0.0	1e30	54.94
7	1.62	0.0	1e30	54.94
8	1.62	0.0	1e30	54.94
9	-1.1	-2.24	2.27e6	16.0
10	-1.1	-2.24	2.27e6	16.0
11	-1.1	-2.24	2.27e6	16.0
12	-1.1	-2.24	2.27e6	16.0
13	-1.1	-2.24	2.27e6	16.0
14	-1.1	-2.24	2.27e6	16.0
15	-1.1	-2.24	2.27e6	16.0
16	-1.1	-2.24	2.27e6	16.0
17	-1.1	-2.24	2.27e6	16.0
18	-1.1	-2.24	2.27e6	16.0
19	-1.1	-2.24	2.27e6	16.0
20	-1.1	-2.24	2.27e6	16.0

Force pairs labels and vector joining pair followed by force tensor/constants for each shell (*dyn/cm*)

force between the pairs' labels	force vector direction	radial force constant (*F*)	tangential force constant (*G*)
1 9	0. 0. -1.	83773.	-10032.
1 12	1. 0. 0.	60779.	-7009.
1 9	0. 0. 0.	5841.	-530.
1 12	0. 0. 0.	4930.	-441.
1 13	0. 0. 0.	79503.	-9461.
1 16	0. 0. 0.	31970.	-3432.
1 17	1. 0. 0.	27032.	-2851.
1 14	0. 0. -1.	2757.	-234.
5 12	0. 0. 0.	100894.	-11757.
5 13	0. 0. 0.	91952.	-10600.
6 13	0. 0. 0.	91204.	-10504.
9 19	0. 0. 0.	22047.	-2283.
9 20	0. 0. 0.	21768.	-2251.
9 18	0. 0. 0.	17955.	-1820.
12 14	0. 0. -1.	17570.	-1778.
13 18	0. 0. 0.	19127.	-1952.
13 14	0. 0. 0.	18210.	-1849.

APPENDIX F. $LaFeO_3$ orthorhombic perovskite model

Space group

Pm$\bar{3}$*m*

Lattice constants (Å)

3.9 3.9 3.9

Number of atoms in unit cell

5

The atom positions and labels of LFO.

Atom number	atom label	type	basis vector
1	La	1	0. 0. 0.
2	Fe	2	0.5 0.5 0.5
3	O	3	0.5 0.5 0.
4	O	3	0.5 0. 0.5
5	O	3	0. 0.5 0.5

Shell model parameters for each atom of LFO

atom number	core charge (e^-)	shell charge (e^-)	spring constant between core and shell (*dyn/cm*)	atomic weight (*g/mol*)
1	2.2	0.0	1e30	138.9
2	2.0	0.0	1e30	55.85
3	-1.4	-2.0	1.6e6	16.0
4	-1.4	-2.0	1.6e6	16.0
5	-1.4	-2.0	1.6e6	16.0

Force pairs labels and vector joining pair followed by force tensor/constants for each shell (*dyn/cm*)

force between the pairs' labels	force vector direction	radial force constant (F)	tangential force constant (G)
1 3	0. 0. 0.	200000.	-30000.
2 3	0. 0. 0.	200000.	-25000.
3 4	0. 0. 0.	50000.	-10000.

$LaFeO_3$ orthorhombic perovskite model

Space group

Pnma

Lattice constants (Å)

5.564 7.880 5.564

Number of atoms in unit cell

20

The atom positions and labels of LFO.

Atom number	atom label	type	basis vector
1	La	1	0.0287 0.25 -0.002
2	La	1	0.4713 0.75 0.498
3	La	1	-0.0287 0.75 0.002
4	La	1	0.5287 0.25 0.502
5	Fe	2	0. 0. 0.
6	Fe	2	0.5 0. 0.5
7	Fe	2	0. 0.5 0.
8	Fe	2	0.5 0.5 0.5
9	O1	3	0.49 0.25 0.0105
10	O1	3	0.01 0.75 0.5105
11	O1	3	-0.49 0.75 -0.0105
12	O1	3	0.99 0.25 0.4895
13	O2	4	0.298 0.0206 0.729
14	O2	4	0.202 -0.0206 1.229
15	O2	4	-0.298 0.5206 -0.729
16	O2	4	0.798 0.474 -0.229
17	O2	4	-0.298 -0.0206 -0.729
18	O2	4	0.798 0.0206 -0.229
19	O2	4	0.298 0.4794 0.729
20	O2	4	0.202 0.5206 1.229

Shell model parameters for each atom of LFO

atom number	core charge (e^-)	shell charge (e^-)	spring constant between core and shell (*dyn/cm*)	atomic weight (*g/mol*)
1	1.68	0.0	1e30	138.9
2	1.68	0.0	1e30	138.9
3	1.68	0.0	1e30	138.9
4	1.68	0.0	1e30	138.9
5	1.62	0.0	1e30	54.94
6	1.62	0.0	1e30	54.94
7	1.62	0.0	1e30	54.94
8	1.62	0.0	1e30	54.94
9	-1.1	-2.24	2.27e6	16.0
10	-1.1	-2.24	2.27e6	16.0
11	-1.1	-2.24	2.27e6	16.0
12	-1.1	-2.24	2.27e6	16.0
13	-1.1	-2.24	2.27e6	16.0
14	-1.1	-2.24	2.27e6	16.0
15	-1.1	-2.24	2.27e6	16.0
16	-1.1	-2.24	2.27e6	16.0
17	-1.1	-2.24	2.27e6	16.0
18	-1.1	-2.24	2.27e6	16.0
19	-1.1	-2.24	2.27e6	16.0
20	-1.1	-2.24	2.27e6	16.0

Force pairs labels and vector joining pair followed by force tensor/constants for each shell (*dyn/cm*)

force between the pairs' labels	force vector direction	radial force constant (*F*)	tangential force constant (*G*)
1 9	0. 0. -1.	83773.	-10032.
1 12	1. 0. 0.	60779.	-7009.
1 9	0. 0. 0.	5841.	-530.
1 12	0. 0. 0.	4930.	-441.
1 13	0. 0. 0.	79503.	-9461.
1 16	0. 0. 0.	31970.	-3432.
1 17	1. 0. 0.	27032.	-2851.
1 14	0. 0. -1.	2757.	-234.
5 12	0. 0. 0.	100894.	-11757.
5 13	0. 0. 0.	91952.	-10600.
6 13	0. 0. 0.	91204.	-10504.
9 19	0. 0. 0.	22047.	-2283.
9 20	0. 0. 0.	21768.	-2251.
9 18	0. 0. 0.	17955.	-1820.
12 14	0. 0. -1.	17570.	-1778.
13 18	0. 0. 0.	19127.	-1952.
13 14	0. 0. 0.	18210.	-1849.